



Australian
National
University

Overcoming challenges of prototyping with single point incremental forming through formability and geometric accuracy analysis

Tegan Maree McAnulty

November 2017

A thesis submitted for the degree of
Master of Philosophy
of The Australian National University

© Copyright by Tegan Maree McAnulty 2017

Except where otherwise indicated, this thesis is my own original work.

Tegan Maree McAnulty
10 November 2017

To women tempted by STEM, may you never feel as if you can't do something like fall in love with a CNC milling machine and spend 4 years getting your steel caps dirty in an engineering workshop.

Acknowledgments

I would like to thank my supervisors, Dr Matthew Doolan, Professor Jack Jeswiet, and Mr Tony Baxter. Their support, advice, feedback, patience, guidance, opportunities, encouragement, experience, knowledge, and insights have been fundamentally essential in helping me complete this project.

Sincere thanks also go to the staff at Futuris and Excellerate Australia (formerly AutoCRC), without whom this project would never have existed. I am truly appreciative of their help and the various opportunities they facilitated throughout my degree.

Thank you to all my Building 31 colleagues. Particularly, Dave Adams - it was great to always have a SPIF expert handy and I am grateful for the insightful and nerdy discussions we had on this topic (among many others) which definitely helped me with my thesis. And Dave Tychsen-Smith - for your extensive technical support and equally extensive conversation themes.

Hamza, Vi Kie, Brendan V., Yimeng, Brendan M., Cameron, Tom, Ceilidh - even if work was stressful, you all made me love coming into the office every day. I just wish we'd started those baked-goods afternoon teas a year or so earlier!

There are also many other people at the ANU who have helped me along the way, whether that was assistance with equipment or general advice, and my thanks go to them.

Thanks of course to my family and family-in-law for their love and support and eventually learning to not ask me how my research is going. . . okay, they never really learnt.

To my friends and Girl Guides for providing regular distractions which always served to reset my stress levels and make me feel like a part of real life again.

And to Markus.

This research is supported by an Australian Government Research Training Program (RTP) Scholarship.

Abstract

With recent developments in rapid prototyping technologies, the automotive industry has been able to move away from costly and inefficient methods of prototyping. In fact, rapid prototyping techniques now exist for nearly all the components in a car, meaning time and money is saved in product development. One exception to this trend, despite their ubiquity in automotive applications, is formed sheet metal components.

Single point incremental forming (SPIF) is a sheet metal forming technique with a fast turnaround that uses little to no custom tooling. It is a promising method for filling the gap in rapid prototyping capability for sheet metal components. However, despite significant research over the last two decades, barriers to industrial viability still include the key issues of fracture occurring in the sheet metal, or a final part being rejected due to unacceptable dimensional error. These two issues are affected by SPIF process parameters, but the extent of their influences are not well understood. By investigating the effect of process parameters on material formability and geometric accuracy, this thesis seeks to address these issues.

Case studies emphasise the impact of formability and geometric accuracy on prototyping automotive components with SPIF. Also emphasised is the importance of effective support walls and optimal design of the forming surface that is used to generate toolpaths for forming components.

A systematic review of the literature regarding the first key issue, formability in SPIF, highlights significant inconsistencies in published research about the effects of process parameters. A hypothesis to explain this result presents the idea of non-linear effects and parameter interactions, which is supported by original experimental work. This shows the difficulty of empirical prediction of formability when, for example, a small change in one parameter may interact with another to significantly influence the outcome of the final part.

Identifying and following safe formability limits will minimise the likelihood of fracture for the forming surface of a component. Research in this thesis looks at the thickness distribution of variable wall angle conical frustum (VWACF) parts as a basis for defining a safe formability limit. However, experimental results show this is not viable due to irregular trends in the thickness distribution close to the fracture point of the VWACF.

The second key issue of geometric error in SPIF is approached by focusing on a

single mode of error, namely 'wall bulge', or springback in flat walls of components. Experiments studied how a variety of tool shapes and sizes affected its severity, and found a trade-off with 'pillowing', another mode of geometric error. At the same time as flat-ended tools reduce pillowing in the base, the experimental results show an increase in the amount of bulging in the walls.

The findings of this thesis demonstrate the impact that a single parameter change can have on multiple aspects of a component. Also highlighted are the complexities of the SPIF process that remain as barriers to industrial viability. This work contributes to overcoming these barriers and achieving efficient rapid prototyping of sheet metal components.

Publications

1. T. McAnulty, J. Jeswiet, and M. Doolan (2016). "Formability in single point incremental forming: A comparative analysis of the state of the art". In: *CIRP Journal of Manufacturing Science and Technology*. ISSN: 1755-5817. URL: <http://dx.doi.org/10.1016/j.cirpj.2016.07.003>
2. D. Adams, T. McAnulty, and M. Doolan (2015). "Experimental testing of an analytical model for membrane strains in single point incremental forming". In: *Key Engineering Materials*. Vol. 639. Trans Tech Publications, pp. 187–194. URL: <http://dx.doi.org/10.4028/www.scientific.net/KEM.639.187>

Contents

Acknowledgments	v
Abstract	vii
Publications	ix
Glossary	xxiii
1 Introduction	1
1.1 Background	1
1.2 Thesis aims and research question	2
1.3 Thesis outline	2
2 Literature Review	5
2.1 Single point incremental forming	5
2.2 Component production with SPIF	6
2.3 Formability in single point incremental forming	8
2.3.1 Introduction	8
2.3.2 Method	13
2.3.3 Results and Discussion	14
2.3.4 Conclusion	37
2.3.5 Analysed articles	39
2.4 Geometric accuracy in SPIF	40
2.5 Conclusion and proposed work	42
3 Research Methodology	45
3.1 Single point incremental forming process	46
3.1.1 Equipment for SPIF	46
3.1.2 Equipment setup and calibration	48
3.1.3 Preparation for SPIF process	48
3.1.4 SPIF process	50
3.1.5 Finishing operations	50
3.2 Formability assessment	51

3.3	Geometric accuracy measurement	52
3.4	Chapter summary	52
4	Case studies in prototyping parts using SPIF	55
4.1	Case study: Seat base	56
4.1.1	Forming strategies	56
4.1.2	Observations	63
4.1.3	Conclusions	67
4.2	Case study: Cushion pan	69
4.2.1	Forming strategies	69
4.2.2	Observations	73
4.2.3	Conclusions	75
4.3	Chapter summary	76
5	The thickness distribution of VWACF parts	79
5.1	Background	80
5.2	Method	82
5.2.1	Design of experiments	82
5.2.2	Test shape	83
5.2.3	Experimental procedure	85
5.2.4	Measuring the thickness distribution	85
5.3	Results and analysis	88
5.4	Discussion	94
5.4.1	General discussion	96
5.4.2	Significance of the results	98
5.4.3	Conclusions	98
5.5	Chapter summary	98
6	Variation of formability results in SPIF and the non-linearity and interactions of process parameters	101
6.1	Background	101
6.2	Method	102
6.2.1	Experimental Set 1	103
6.2.2	Experimental Set 2	103
6.2.3	Testing process	103
6.2.4	Analysis process	104
6.3	Results	107
6.4	Analysis	108
6.4.1	Experimental Set 1 parameter interactions	108

6.4.2	Experimental Set 2 parameter interactions	110
6.4.3	Non-linearity of parameters	111
6.5	Discussion	113
6.5.1	Parameter interactions	113
6.5.2	Non-linear parameter effects	115
6.5.3	Part failure and Contact Pressure	116
6.6	Conclusion	116
7	The impact of tool shape on wall bulge in flat-walled SPIF parts	119
7.1	Background	119
7.1.1	Hypothesis	120
7.1.2	This work	120
7.2	Method	121
7.2.1	Tool design	121
7.2.2	Test shape design	122
7.2.3	Experimental method	123
7.2.4	Strain analysis	125
7.2.5	Statistical analysis method	127
7.2.6	Formability assessment	127
7.3	Results and discussion	127
7.3.1	Wall bulge	129
7.3.2	Pillowing	132
7.3.3	Strains and material flow	134
7.3.4	Formability analysis	139
7.4	Chapter summary	141
7.4.1	Further work	142
8	Discussion	143
8.1	Summary of findings in this thesis	143
8.2	Formability	144
8.3	Geometric accuracy	145
8.4	SPIF in industry	147
8.5	Chapter summary	148
9	Conclusion	151
9.1	Formability	151
9.2	Geometric accuracy	152
9.3	Other insights from this work	153
9.4	Future work	153

9.4.1	Formability	153
9.4.2	Geometric accuracy	154
9.4.3	Broader research in SPIF	154
A	Case studies process parameters	169
B	Thickness distribution results of VWACF parts	171
C	Formability of VWACF test parts and statistical data analysis	189
C.1	Fracture depth of VWACF parts	190
C.2	Experimental Set 1 - R code	190
C.3	Experimental Set 2 - R code	192
D	Geometric accuracy results of truncated pyramid test parts	197

List of Figures

1.1	A standard product development cycle (Kalpakjian and Schmid, 2010a).	1
2.1	The initial tool movement of forming a part from a flat sheet with SPIF.	6
2.2	A comparison of methods used to assess the formability of a material in SPIF.	9
2.3	The Sine Law as applied to SPIF.	10
2.4	The main types of tools used in SPIF	11
2.5	Material thickness conclusions	15
2.6	Tool diameter conclusions	18
2.7	The toolpath of the straight groove test. Adapted from Li et al. (2014) .	21
2.8	Step down conclusions	23
2.9	Feed rate conclusions	25
2.10	Spindle speed conclusions	27
2.11	Total number of papers analysed for each parameter	34
2.12	Cross-section of an example SPIF part showing the characteristic errors of wall bulge and pillowing	41
3.1	CNC machine	46
3.2	CAD model of the SPIF forming rig, showing a formed component secured in the frame.	47
3.3	The forming rig with the location of the coordinate system's origin and axes highlighted.	48
3.4	Two examples of toolpath types used in SPIF. Adapted from Jeswiet, Micari, et al. (2005) and Filice, Fratini, and Micari (2002).	50
3.5	VWACF test shape with generic parameters	51
3.6	FARO Laser ScanArm V3 used to scan the surface of components for geometric accuracy analysis (FARO Technologies, 2012).	53
4.1	CAD model of the seat base component.	56
4.2	CAD model of the seat base SPIF surface, with holes and some features removed from the original to make it suitable for forming.	57
4.3	CAD model of the forming surface for the initial seat base test.	57

4.4	Tearing of the walls of the seat base when using single pass forming . . .	58
4.5	CAD model of the interim pass for the first attempt at forming the seat base.	59
4.6	Cross sectional CAD model of the interim and final passes for the seat base, showing key dimensions.	59
4.7	Left: Photograph of the component after two successful interim passes and 30% of the final pass, with fractures highlighted in red. Right: A close up of the fold-over failure.	59
4.8	CAD model of the forming surface for the third seat base attempt. The backing plate is in blue.	61
4.9	CAD model of the forming surface for the third seat base attempt, including the backing plate model. The draft angle analysis highlights in yellow the areas that are greater than 75° from the horizontal plane.	62
4.10	CAD model of the seat base highlighting the additions in red that became part of the forming surface for the first pass, where the part was formed from the top down.	62
4.11	Cross section of the CAD model showing the four interim passes used to progressively form the final geometry for the third attempt at the seat base. All but the red surface were formed with bottom-up multi-pass forming.	63
4.12	Photograph of the third attempt of the seat base component, successfully formed without cracks using bottom-up multi-pass SPIF	64
4.13	Detail of wrinkling resulting from the multi-pass forming of the first attempt for the seat base component.	65
4.14	CAD model of the second-last forming pass, with overlaid toolpath in yellow showing the peak in the trajectory of the tool.	66
4.15	Detail of the final formed seat base component, showing the folded-over lip created as a result of the multiple bottom-up re-forming passes.	66
4.16	Laser scanning results of the third iteration of the SPIF seat base, shown as a colour scale of positive (red) and negative (blue) deviations compared to the CAD model in the figure.	68
4.17	CAD model of the original cushion pan component.	69
4.18	CAD model of the cushion pan forming surface prior to removal of the central groove feature.	70
4.19	CAD model of the first design for the cushion pan SPIF surface.	70
4.20	Photograph of a failed cushion pan part highlighting the fracture locations in red.	71

4.21	CAD model of the final design of the cushion pan which successfully formed with SPIF.	72
4.22	The cushion pan component, successfully formed with SPIF.	72
4.23	View of the large support wall (Side B) where inwards bulging (negative error) occurred.	73
4.24	Bulging in the wall of the cushion pan as a proposed cause of unexpected fracture during forming.	74
4.25	Top view of geometric accuracy results after laser scanning and comparison with the CAD model. Note the inaccuracy in the large shallow area.	75
5.1	Explanation of the intersection point and how it is determined from the measured thickness of a VWACF part. (b) adapted from Figure 8, Hussain and Gao (2007).	80
5.2	Hemispherical and flat-ended tools used in the study.	83
5.3	VWACF test shape with geometric parameters	84
5.4	Set up of a height gauge and VWACF part used to measure depth increments and the fracture point.	87
5.5	Diagram showing the dial gauge setup used to measure the thickness along the cross section of the VWACF parts.	87
5.6	The thickness distribution of this test varies along the length of the part by more than $\pm 2.5\%$ compared to the sine law prediction. (a) Thickness distribution data, (b) Error plot including $\pm 2.5\%$ t_0 margins.	88
5.7	The measured thickness distribution closely follows the sine law prediction until the final fracture point. (a) Thickness distribution data, (b) Error plot including $\pm 2.5\%$ t_0 margins.	90
5.8	The measured cross-sectional thickness is decreased at the fracture point when compared to the sine law prediction. (a) Thickness distribution data, (b) Error plot including $\pm 2.5\%$ t_0 margins.	91
5.9	The measured thickness follows the prediction until approximately 5 mm before the fracture point, where positive deviation occurs. (a) Thickness distribution data, (b) Error plot including $\pm 2.5\%$ t_0 margins.	92
5.10	Rough external surface finish and internal galling of Test No. 10 and 14.	94
5.11	Results for Test No. 7 showing measured thickness distribution in Row (a) and corresponding error plots in Row (b). Note the variation between each test repeat.	95
5.12	Close up of part near the point of fracture. The surface is regular and free of microcracks.	97

6.1	VWACF test shape with geometric parameters	105
6.2	Height gauge measuring the lowest point of fracture on a VWACF part. Inset: detail of crack and gauge tip.	105
6.3	Effect of step down with varying tool shape: Experimental Set 1	109
6.4	The effect of thickness for different values of step down	111
6.5	The main effects of thickness and step down from Experimental Set 1	112
6.6	The effect of varying thickness on formability in Experimental Set 2	112
6.7	Effect of thickness with different tools for Experimental Set 1	114
6.8	Effect of thickness with different tools for Experimental Set 2	114
7.1	Hemispherical and flat-ended tool cross-sections, including dimensions.	120
7.2	Schematic of the ARAMIS digital image correlation system for determining surface strain.	126
7.3	Photo of a formed truncated pyramid component showing mottified internal surface. Inset: a reflective incrementally formed surface before treatment.	127
7.4	Top view of truncated pyramid test part. Colour scale from +5 mm (red) to -5mm (blue)	128
7.5	Cross-section deviation view of truncated pyramid test part. Colour scale from +5 mm (red) to -5mm (blue)	128
7.6	Maximum wall bulge plotted against tool flatness ratio	130
7.7	Maximum wall bulge plotted against tool shaft radius	131
7.8	Maximum base deviation ('pillow height') plotted against tool edge radius	133
7.9	Interpretation of Bambach SPIF strain model to explain pillowing using a hemispherical tool.	134
7.10	Translation of Bambach SPIF strain model to a flat-ended tool scenario.	135
7.11	Image from the stereoscopic camera in the ARAMIS system showing the stochastic pattern on the final formed T9 part.	136
7.12	Strain surface generated from the ARAMIS system showing sections which were exported. Thickness strain colour scale is shown on the left.	136
7.13	Cross-sectional strain for Tool 3 (R5r5) Tool 8 (R10r5), and Tool 9 (R10r10).	137
7.14	Cross-sectional strain for Tool 8, R10r5, and Tool 9, R10r10	138
7.15	Wall angle at fracture results from the VWACF formability tests, plotted against the tool flatness ratio (r/R). Raw data indicated by circles, average by diamond.	140
B.1	Test No. 1 - measured thickness distribution results and error plots for each test repeat.	172

B.2	Test No. 2 - measured thickness distribution results and error plots for each test repeat.	173
B.3	Test No. 3 - measured thickness distribution results and error plots for each test repeat.	174
B.4	Test No. 4 - measured thickness distribution results and error plots for each test repeat.	175
B.5	Test No. 5 - measured thickness distribution results and error plots for each test repeat.	176
B.6	Test No. 6 - measured thickness distribution results and error plots for each test repeat.	177
B.7	Test No. 7 - measured thickness distribution results and error plots for each test repeat.	178
B.8	Test No. 8 - measured thickness distribution results and error plots for each test repeat.	179
B.9	Test No. 9 - measured thickness distribution results and error plots for each test repeat.	180
B.10	Test No. 10 - measured thickness distribution results and error plots for each test repeat.	181
B.11	Test No. 11 - measured thickness distribution results and error plots for each test repeat.	182
B.12	Test No. 12 - measured thickness distribution results and error plots for each test repeat.	183
B.13	Test No. 13 - measured thickness distribution results and error plots for each test repeat.	184
B.14	Test No. 14 - measured thickness distribution results and error plots for each test repeat.	185
B.15	Test No. 15 - measured thickness distribution results and error plots for each test repeat.	186
B.16	Test No. 16 - measured thickness distribution results and error plots for each test repeat.	187
D.1	Part T1A geometric accuracy results - top view and cross-section view .	198
D.2	Part T1B geometric accuracy results - top view and cross-section view .	199
D.3	Part T2A geometric accuracy results - top view and cross-section view .	200
D.4	Part T2B geometric accuracy results - top view and cross-section view .	201
D.5	Part T3A geometric accuracy results - top view and cross-section view .	202
D.6	Part T3B geometric accuracy results - top view and cross-section view .	203
D.7	Part T4A geometric accuracy results - top view and cross-section view .	204

D.8	Part T4B geometric accuracy results - top view and cross-section view	. 205
D.9	Part T5A geometric accuracy results - top view and cross-section view	. 206
D.10	Part T5B geometric accuracy results - top view and cross-section view	. 207
D.11	Part T6A geometric accuracy results - top view and cross-section view	. 208
D.12	Part T6B geometric accuracy results - top view and cross-section view	. 209
D.13	Part T7A geometric accuracy results - top view and cross-section view	. 210
D.14	Part T7B geometric accuracy results - top view and cross-section view	. 211
D.15	Part T8A geometric accuracy results - top view and cross-section view	. 212
D.16	Part T8B geometric accuracy results - top view and cross-section view	. 213
D.17	Part T9A geometric accuracy results - top view and cross-section view	. 214
D.18	Part T9B geometric accuracy results - top view and cross-section view	. 215

List of Tables

2.1	Material Thickness: Summary of papers	17
2.2	Tool diameter summary of papers	19
2.3	Summary of Tool Type papers	20
2.4	Step down: Summary of papers	22
2.5	Step down: Summary of conclusions	24
2.6	Feed rate: Summary of papers	26
2.7	Spindle speed: Summary of papers	28
2.8	Tool diameter - Material thickness interaction with R/t ratio ‡	32
2.9	SPIF Experimental Parameter Framework	35
2.10	List of papers for systematic quantitative analysis with corresponding Reference ID	39
3.1	Constant SPIF experimental parameters	47
5.1	Parameter combinations for VWACF tests	85
5.2	Constant experimental parameters	86
5.3	Classification of results for VWACF tests	93
6.1	Tests and parameters for Experimental Set 1	104
6.2	Tests and parameters for Experimental Set 2.	106
6.3	Maximum wall angle results	108
6.4	Experimental Set 1 ANOVA results	109
6.5	Experimental Set 2 ANOVA results	110
7.1	Requirements for tool designs	121
7.2	Hemispherical and flat-ended tools	122
7.3	Constant experimental parameters	124
7.4	Linear correlations of parameters and maximum wall bulge	130
7.5	Linear correlations of parameters and maximum pillow height	133
7.6	Linear correlations of parameters and fracture angle	139
A.1	Process parameters used for forming the seat base (SB) and cushion pan (CP) components.	169

C.1 Raw data of the fracture depth of the VWACF parts 190

Glossary

CAD Computer-aided design

CAM Computer-aided manufacture

CNC Computer numerical control

DOE Design of experiments

SPIF Single point incremental forming

SQLR Systematic quantitative literature review

Tool geometry Describing the complete forming tool, including the parameters of tool shaft radius and tool end-shape.

Tool shape The end-shape of the tool. The most common shapes are hemispherical and flat.

Tool type The design of the forming tool, for example solid, where the tool is made from a single piece of material, or roller-ball, where a ball bearing is housed in the tip of a tool and allowed to rotate freely as it moves over the material.

VWACF Variable wall angle conical frustum

Introduction

1.1 Background

Sheet metal is a common material for products and components, particularly in the automotive industry. Futuris, the industry sponsor of this research, uses sheet metal in their interior automotive products, such as internal structures and frames for car seats. As a product manufacturer, Futuris follows a standard product development cycle, shown in Figure 1.1. The cycle includes phases for designing, prototyping, and mass-producing the product.

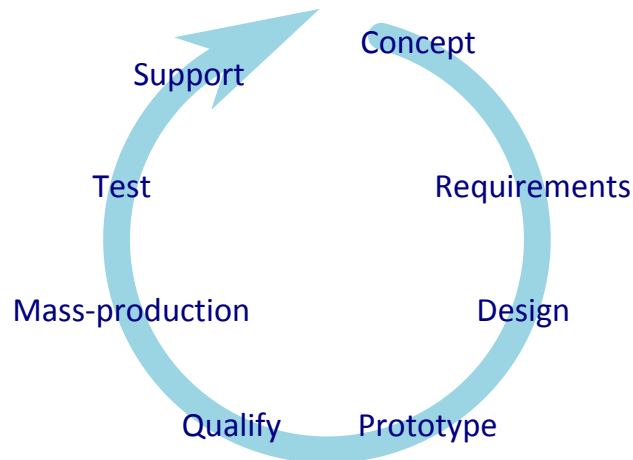


Figure 1.1: A standard product development cycle (Kalpakjian and Schmid, 2010a).

Sheet metal mass-production techniques are highly developed and efficient, though they typically involve a large initial investment. This means that low volume production runs are not economically viable, and alternative methods are needed for prototyping.

For plastic component prototypes, Futuris has made use of recently-developed 3D printing techniques to quickly manufacture prototypes of parts such as in-car cup

holders. However, for sheet metal products, no comparable rapid-prototype technique exists.

Currently, sheet metal component prototypes can be made with a prototype stamping mould that costs tens of thousands of dollars with a lead time of a few months, delaying progress on the product. Alternatively, a local workshop could produce the prototype using manual techniques, but while the cost is smaller, it compromises the final accuracy and is labour-intensive (Kalpakjian and Schmid, 2010b).

Single point incremental forming (SPIF), a dieless method of forming sheet metal, is a potential solution for rapid prototyping sheet metal. If implemented in an industrial situation, SPIF could reduce the cost per prototype and turnaround time. More thorough development may then be possible, which could result in safer products.

However, SPIF is not yet industrially viable. SPIF parts often fail due to fracture of the material (formability concerns) or they have unacceptable geometric accuracy, meaning more delays as additional test parts are manufactured (Behera, Sousa, et al., 2017).

1.2 Thesis aims and research question

This thesis aims to progress SPIF towards an industrially viable process where effective components can be produced that will not fail due to fracture and that will have an acceptable final geometric accuracy. To achieve this, the work undertaken will look at the effect of process parameters on material formability and geometric accuracy. A greater understanding will allow the best parameters to be selected for the situation to eliminate the aforementioned issues.

The research question for this thesis is as follows:

What are the effects and interactions of SPIF process parameters on the material formability during forming and geometric accuracy after forming?

1.3 Thesis outline

This thesis consists of nine chapters; the introduction, literature review, the research methodology, three experimental chapters, a discussion, and the conclusion.

Chapter 2 presents an in-depth introduction to SPIF as well as a review of the research literature around applied components, material formability, and geometric accuracy Chapter 3 describes the methodology used to answer the research question

of this thesis, including the process of forming parts with SPIF, and measuring the formability and geometric accuracy.

Chapter 4 presents two prototype component case studies. These two parts were manufactured with SPIF to provide insights into the contextual challenges for Futuris, the industry sponsor.

Chapter 5 introduces research carried out with the aim of determining safe formability limits in SPIF, to eliminate the risk of failure by fracture during forming. Chapter 6 continues the investigation into formability limits in SPIF by measuring the effect of, and relationships between, a number of process parameters.

Chapter 7 presents a novel study on geometric accuracy in SPIF. The effects of forming tools on a particular mode of geometric error are investigated to understand how to select the right tool in an industrial situation.

Chapter 8 discusses the findings of this thesis. The significance of the results, and the limitations of the research, are analysed from the perspective of the wider SPIF research knowledge, understanding, and industrial applicability. Chapter 9 summarises the conclusions from the previous research chapters and suggests directions for future work in this space.

Literature Review

This chapter presents an in-depth look at the topics introduced in Chapter 1, including a detailed description of single point incremental forming in §2.1.

The research literature surrounding SPIF is reviewed in a few specific areas. Firstly, case studies from the literature of components formed using SPIF are described, emphasising the challenges of failure by fracture and poor geometric accuracy.

Secondly, a quantitative literature review is presented in §2.3, based largely on a paper which has been published in the CIRP Journal of Manufacturing Science and Technology (McAnulty, Jeswiet, and Doolan, 2016). In this review, the reported effects of all fundamental SPIF process parameters on material formability are analysed, and insights are drawn from the results.

Finally, in §2.4 the literature on geometric accuracy in SPIF is reviewed to highlight the scope of the issue. A range of methods that have been proposed to improve outcomes for formed components are discussed.

Conclusions are then drawn based on the collected research, highlighting gaps in the literature. This leads to a statement on the the proposed experimental work for this thesis.

2.1 Single point incremental forming

Single point incremental forming (SPIF) is a technique for manufacturing sheet material components that has been in development for the last two decades (Echraf and Hrairi, 2011). A range of shapes are able to be produced with this technique, which also has the advantage of little to no custom tooling. A round-ended tool is used to incrementally form a sheet of material, clamped around the edge, into a cavity with no supporting die. This means the process is flexible and the equipment is not constrained to a single part shape (Jeswiet, Micari, et al., 2005).

Figure 2.1 is a diagram of SPIF, showing the generic round-ended forming tool and the raised frame and the clamp which holds the material in place. The toolpath

begins from the plane of the undeformed sheet and follows the periphery of the part. With each loop the generic tool presses further into the sheet by a specified amount, Δz (Figure 2.1).

Also shown is the single piece of custom tooling which can be used to improve the plastic forming mechanism of the sheet material. A backing plate is made from an inflexible material, with a cut-out that corresponds to the outer edge of the desired part. It is secured underneath the blank, and prevents any unwanted deformation in the flange of the component (Ambrogio, Cozza, et al., 2007).

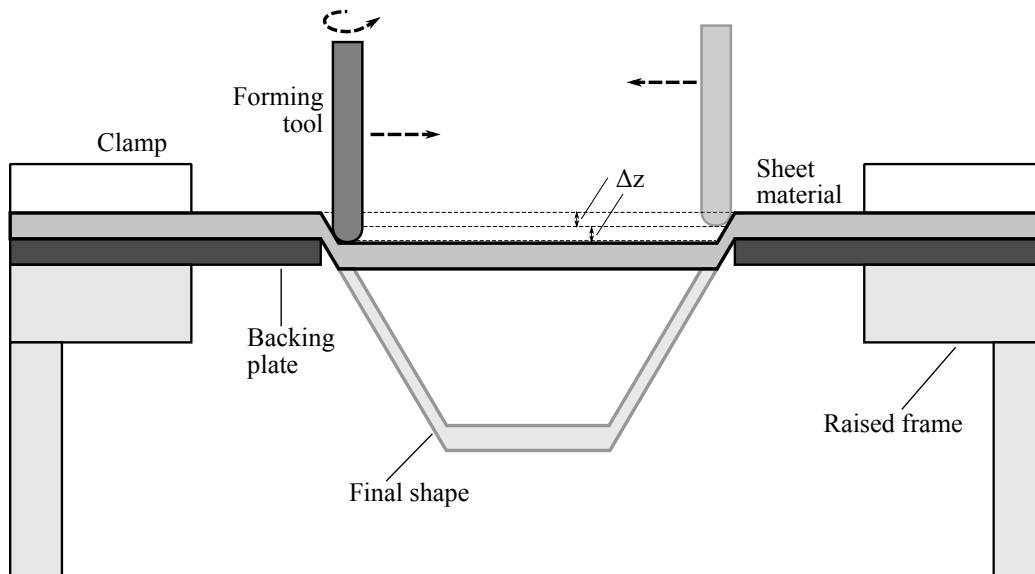


Figure 2.1: The initial tool movement of forming a part from a flat sheet with SPIF.

Due to the range of movement required for the tool, SPIF can be carried out in any 3-axis CNC mill or other machine with 3-axis movement capabilities. Furthermore, the development of more sophisticated computing technologies and CAD/CAM (computer-aided design/manufacture) software has expanded the possibilities of SPIF to more complex components.

2.2 Component production with SPIF

Across the literature, a number of researchers have presented case studies of various components made with SPIF. Understanding the lessons from these examples will inform both the production of the prototype case studies and the experimental investigations in this thesis.

Case studies can be carried out on scaled-down versions of a component, such

as the car door shell made by Palumbo and Brandizzi (2012), which the authors formed in a 140 mm² area. However, it is important to understand what may be significant differences in accuracy etc. between small and full-size versions of SPIF parts, therefore these types of investigations are an introduction to further research.

Applications of SPIF in the medical sector have also been widely investigated by researchers. Initially, Ambrogio, De Napoli, et al. (2005) made a customised ankle brace, with a geometric tolerance requirement of 1 mm that was unable to be completely achieved. More recently, patient-specific facial implants (Duflou, Behera, et al., 2013; Araujo et al., 2014) and cranial implants (Bagudanch, Lozano-Sánchez, et al., 2015; B. Lu, Ou, et al., 2016) have been manufactured, and in these instances geometric accuracy was also a problem, with deviations in one part up to 3 mm from the designed model (B. Lu, Ou, et al., 2016).

Insights to be gained from these medical applications include the topic of positioning the part within the forming space and the subsequent support wall generation. This was identified as a consideration that could mean the difference between success and failure, as seen in Araujo et al. (2014). Furthermore, springback of the part after cutting from the flange (B. Lu, Ou, et al., 2016) is a relevant issue for all components that have added support walls for forming, or a flange which does not form part of the final component.

In addition to geometric accuracy, formability can also be an issue for parts manufactured using SPIF. Jeswiet, Duflou, et al. (2005) made a solar cooker cavity but the first attempt fractured as it exceeded the formability limits. After changing the type of aluminium alloy used, the solar cooker cavity formed successfully, but if alternate material had not been readily available then the formability limit could have perhaps been increased by an improved combination of process parameters.

The literature shows several case studies which provide relevant guidance about key issues for forming components with SPIF. Geometric accuracy has been a concern, particularly in medical-related applications, and formability is also identified as a limiting factor.

While automotive-related components such as a car fender section (Bambach, Taleb Araghi, and Hirt, 2009), powertrain guards (Adams and Jeswiet, 2014a), and a motorbike seat and petrol tank (Jeswiet, Micari, et al., 2005) have been successfully formed with SPIF, they are not fully indicative of the geometric characteristics of the interior automotive parts produced by Futuris. Chapter 4 presents case studies of Futuris parts prototyped with SPIF, with features such as varying curvature radii and small details. These case studies will help to understand the unique challenges of interior automotive parts in order to better prepare for industrial application.

2.3 Formability in single point incremental forming

2.3.1 Introduction

Single point incremental forming (SPIF) is a method of manufacturing components from sheet material, with the advantage of little to no customised tooling and otherwise generic setup (T. J. Kim and Yang, 2000). This makes it ideal for producing sheet metal prototype components before investing in a stamping mould, or for one-off customised components.

SPIF is a type of incremental sheet forming (ISF), a class of processes which includes spinning and shear forming (Hagan and Jeswiet, 2003). SPIF has the advantage over a method such as spinning of being able to form asymmetric shapes. In the 2005 paper, Jeswiet, Micari, et al. succeeded in synthesising the current knowledge into a comprehensive review of the progress and state of the art of asymmetric ISF processes. More than a decade of research since then calls for an updated review of the progress and understanding of SPIF.

This work is a review of literature on single point incremental forming, specifically aiming to study the process parameters that influence the formability of the material during forming. Organising the results of this investigation will assist in creating straightforward parameter guidelines and instructions useful for future research and manufacturing real components with SPIF.

While commercial and industrial SPIF components have been made in the past, they can be so complex that 'trial and error' becomes the most feasible development technique, as using finite element analysis (FEA) would be too computationally expensive. Therefore, a significant challenge is how to develop SPIF into an industrial process using methods more sophisticated than trial and error.

The aim of this literature review is to collect relevant data from experimental papers and draw conclusions on maximising the formability of the material used in SPIF. The other aspects of SPIF that are not systematically covered in this review are forming forces, surface quality, geometric accuracy, and resultant material properties.

Formability is most commonly quantified by finding the maximum wall angle (Φ_{max}) to which the material can be formed before failure occurs (Jeswiet and Young, 2005), with respect to the horizontal plane. Typically a simple shape, such as a cone or pyramid, is used to determine this maximum wall angle. Multiple parts can be formed, each one with a steeper wall angle than the previous, until a part breaks (Shim and Park, 2001).

Another option is a shape where the wall angle changes from shallow to steep, for example the variable wall angle conical frustum (VWACF) reported in 2007 by Hussain, Gao, and Dar. If this part is used, only one test is needed to determine the

wall angle where failure occurs. In the same paper, Hussain, Gao, and Dar (2007) compared the VWACF results and results from straight-wall tests and found the latter overestimated Φ_{\max} by less than 4% due to its higher stiffness. Therefore, if the exact wall angle at fracture is required for straight wall parts, the VWACF results should be further tested with conical or pyramidal frustums.

A comparison of formability methods, namely the constant wall angle and VWACF methods, is visually described in Figure 2.2.

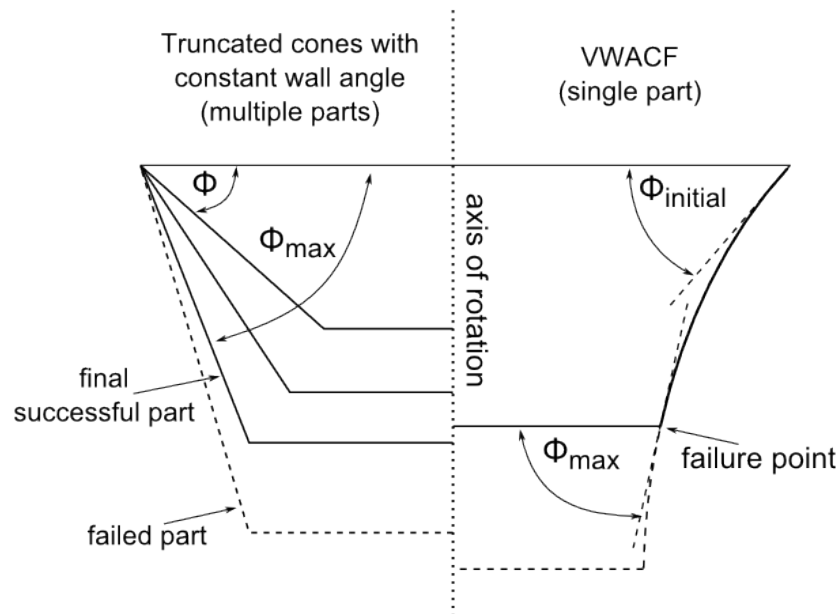


Figure 2.2: A comparison of methods used to assess the formability of a material in SPIF.

However, any formability test, if repeated accurately, should give consistent results such that the general effect of a process parameter can be determined. The general effect, further explained in §2.3.3, Results and Discussion, provides the data that is analysed in this literature review.

2.3.1.1 Material parameters

Many different materials have been used in SPIF, including a variety of metals (Jeswiet, Micari, et al., 2005), polymer sheets (Le, Ghiotti, and Lucchetta, 2008), and other sheet materials such as sandwich panels (Jackson, Allwood, and Landert, 2008), with a wide range of formability among them. This review will not examine formability limits of specific materials but will instead list them in the parameter analyses to allow comparison between experiments with the same material, for example PVC or

AA3003-O. Material type can be seen as the base upon which all other parameters are selected.

The thickness of the undeformed material blank is an important parameter and has significant effects on the SPIF process and final part, especially the force needed to deform the sheet which increases with increasing thickness (Arfa, Bahloul, and BelHadjSalah, 2013). Sheet thickness is also a factor in the sine law equation for shear forming, where the final thickness (t_f) of a part can be calculated from the initial thickness (t_i) and the wall angle from horizontal (Φ). The equation is $t_f = t_i * \sin(90 - \Phi)$ and has been shown to be accurate for SPIF parts formed in a single pass (Jeswiet, Hagan, and Szekeres, 2002). Figure 2.3 describes the sine law and its parameters.

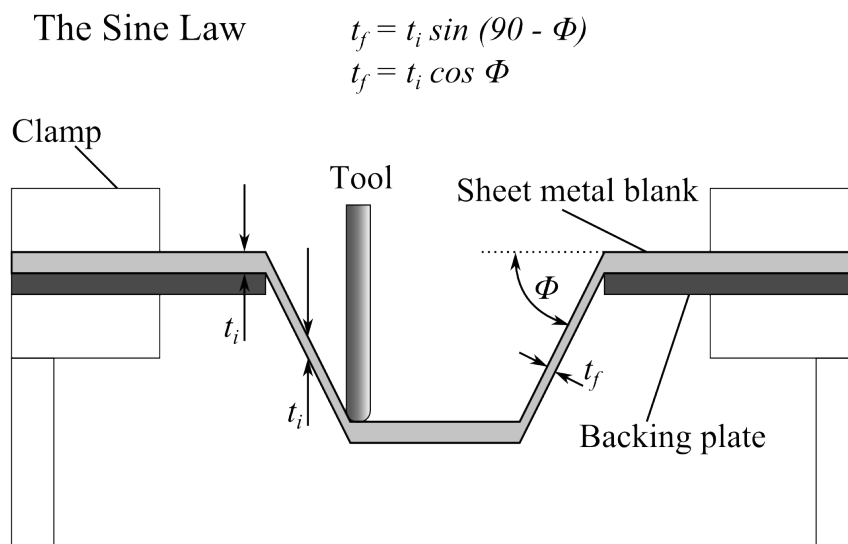


Figure 2.3: The Sine Law as applied to SPIF.

The absolute values of thickness are not important in this review, as unique material properties mean a 2 mm sheet of one material performs differently to a 2 mm sheet of a different material (Jeswiet, Micari, et al., 2005). Only the general effect of increasing or decreasing the thickness of the undeformed blank has been studied.

2.3.1.2 Tool parameters

The tool or punch used in SPIF to deform the sheet has traditionally been one of two types. Firstly, a solid hemispherical tool (Hagan and Jeswiet, 2003), and secondly, a tool with a ball bearing in a socket, allowing it to roll freely over the sheet (Shim and Park, 2001). As progress in SPIF and incremental forming in general developed, the types of tools expanded to include flat-ended and other shaped tools (Ziran et al.,

2010). Figure 2.4 shows the three main types of tools and their descriptive dimensions. The advantages of one type of tool over another have been a consistent area of research for some time, for example Y. H. Kim and Park (2002), and more recently Cawley, Adams, and Jeswiet (2013). Tool diameter and tool type are two parameters studied in this literature review.

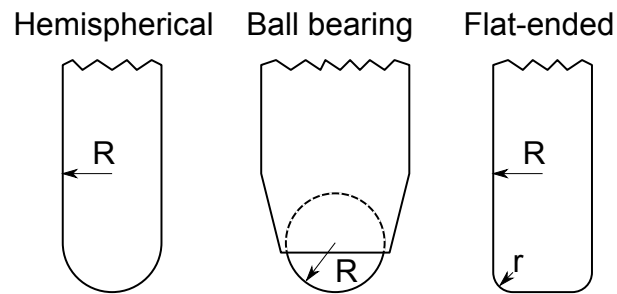


Figure 2.4: The main types of tools used in SPIF

The size and end-shape of the tool influence the mechanisms of the forming process. The size and shape of the area of contact between the tool and sheet can affect process aspects such as generated friction (Durante, Formisano, and Langella, 2011), observed forces (Centeno et al., 2014), and pressure (Silva, Skjoedt, et al., 2008).

The tools can be made from different materials, and the interaction between the tool material, blank material and lubrication influence the friction conditions seen during the process (Cavaler et al., 2010). Currently there have been no published journal papers examining the effect of different tool materials on formability in SPIF, therefore it is not able to be included in this literature review.

2.3.1.3 Toolpath parameters

The toolpath used in SPIF can be the equivalent of a machining operation such as Z-level finishing, though the tool does not cut the material. The motion of the tool is defined by the same parameters used in machining operations. Feed rate is the velocity of the tool as it moves over the sheet, typically defined in mm/min. Step down is how far the tool presses into the sheet with each circuit. Spindle speed is how fast the tool spins, specified in rotations per minute (rpm).

Toolpath parameters influence the generated friction by the movement and rotation of the tool (Durante, Formisano, Langella, and Capece Minutolo, 2009), and the feed rate and step down define the deformation rate of the material.

The relative rotation directions of the tool and toolpath determine the 'milling mode'; either conventional or climb milling, to use the standard machining terms.

If the tool and the toolpath are both moving clockwise or counterclockwise, it is conventional milling, and if they are rotating in different directions, it is climb milling. Climb milling is the most commonly used mode in SPIF, as the friction is reduced by the tool effectively 'rolling' over the sheet as it forms (Eyckens et al., 2010). Standard cutting tools typically rotate in a clockwise direction, which means that specifying toolpath direction might be enough for the reader to assume which milling mode is being used. However, for SPIF, it is necessary to define conventional or climb ('rolling') milling as the utilised machining mode.

2.3.1.4 Geometry

The shape of the incrementally formed part affects the strains and therefore the formability of the material. The geometry is an aspect which is not covered in this literature review due to the complexity of analysing the many different shapes and dimensions used across the studied papers.

In manufacturing a practical component, a draft angle analysis can be performed on the CAD model of the part to highlight which walls are steeper than a specified angle. Using the maximum wall angle for that material in the analysis will show whether there are any sections which may be too steep to form in a single SPIF pass. If there are no sections steeper than the permitted angle, it is likely that the part will succeed (Adams and Jeswiet, 2014a). The curvature of the walls of the part affects the types of strains developed during the process. For example, the strains generated in a conical frustum with a radius of curvature of 100 mm will be of a different type to those seen on the edge of a pyramidal frustum where the radius of curvature is only 10 mm (Filice, Fratini, and Micari, 2002; Fratini et al., 2004).

2.3.1.5 Experimental parameters

Since the process was first developed, research has been conducted into modifications of the basic SPIF process. For example, many different methods of heating the workpiece have been explored. Duflou, Callebaut, et al. (2007) used a laser to improve Φ_{\max} of TiAl6V4 sheets by more than 20°. The same Titanium alloy was heated up to 400°C with band heaters installed in the blank holder in Palumbo and Brandizzi (2012), and an improvement in formability was observed. The use of electric current through the tool and the sheet has been explored in recent years, also applied to TiAl6V4 (Fan et al., 2010) and other materials such as AA6061-T6 (Adams and Jeswiet, 2014b) with resulting formability improvements. As this literature review studies process parameters for basic SPIF, parameters relevant to hot SPIF and electric SPIF are not examined.

2.3.1.6 This work

This review will investigate the research literature to find what has been said about the effects of SPIF process parameters on formability. The results are hypothesised to show an optimal operating range for each SPIF parameter. The optimal operating range is a function of other parameters, which are interdependent in various combinations.

2.3.2 Method

This literature review is undertaken as a ‘systematic quantitative literature review’. This type of literature review is defined in Pickering and Byrne (2014). The process has been tested by multiple students and researchers, and produces repeatable and high quality results.

This technique is highly applicable to the area of SPIF parameters due to the quantitative nature of the data input. Furthermore, as will be seen in the tabulated results, it allows effective comparisons of parameter values between multiple papers. The selected parameters that have been studied in this review are universal to every single pass SPIF process, and more specialised processes such as applying electric current or external heat are not addressed.

Many papers have been published in the area of formability in SPIF, however the inclusion criteria highlighted below are used to select a high quality collection of papers that are a good representation of the wider field.

Details of the process steps as they relate to this literature review are shown below.

Topic

Formability in single point incremental forming.

Literature review research questions

What does the literature say about the effects of process parameters on formability and ‘techniques’ for improving formability? Is there consistency between conclusions?

What materials, parameter values and test shapes were used for the SPIF formability tests?

Keywords searched

SPIF / single point incremental forming

ISF / incremental sheet forming

ISMF / incremental sheet metal forming

Spifability

Formability

Forming limit
FLD, FLC
Maximum strain
Wall angle
Parameter interaction

Databases searched

Scopus
Science Direct
ProQuest
Web of Science

Criteria for inclusion of papers

Published journal article
Original research
Not a review paper
Varies SPIF process parameters
Uses standard SPIF, not multi-pass, electro SPIF, externally heated etc.
Presents results on formability limits for single pass SPIF

Categories

Summary of the categories which were used in the literature database:
Bibliographic information
Values of process parameters
Material used
Experimental setup
Test geometry
Type of analysis
Results of analysis
Most effective combination of parameters

2.3.3 Results and Discussion

The following results explain the main factor effects presented in the papers from this literature review. Four conclusions are discussed with respect to the effect of the factor on formability; specifically how the variation of that parameter increases the formability. These conclusions are:

1. **Increasing** the value of the parameter causes an increase in formability,

2. **Decreasing** the value of the parameter causes an increase in formability,
3. The parameter has **no effect** on formability, or
4. The value of the parameter should be **optimised** to obtain the greatest increase in formability.

An analysis on key parameter interactions is presented after the results of the main factor effects.

For this review, there were 35 papers found which fulfilled the requirements outlined in the method. In the data tables the papers are referenced, for ease of understanding, by the name of the first author, the year, and the numerical reference ID. This allows for clear differentiation between papers, for example, Hussain, 2010 [15] and Hussain, 2011 [16]. All papers and their corresponding reference IDs can be found in Table 2.10. Where details are missing about a parameter value for a particular paper, it is noted as N/A in the results tables. After the results of each parameter are presented, a discussion is carried out for that parameter. Finally, the cumulative results are discussed in §2.3.3.11.

2.3.3.1 Material thickness

A total of 15 papers from this literature review varied the material thickness to determine the effect on formability in SPIF. Of these, the majority (10) found the formability to increase with thicker sheets. The results are graphically represented in Figure 2.5 and details are given in Table 2.1.

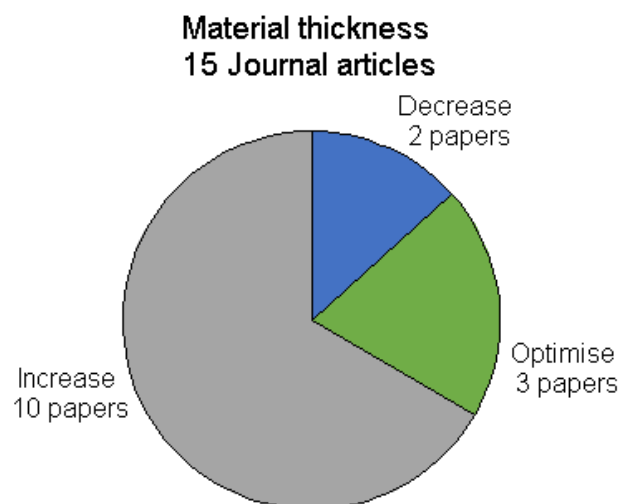


Figure 2.5: Material thickness conclusions

Out of the papers which tested variation of material thickness, only Bagudanch, Garcia-Romeu, et al. (2015) noted more than one repeat of each test. It is important to repeat tests when results are close together to determine significance, as in Fang et al. (2014) where results were only 0.5 mm apart. They measured the failure depth of a 1 mm sheet as 36 mm, and the failure depth of the 2.5 mm sheet as 35.5 mm. As these two thicknesses are significantly different, it may have provided more insight to also test a mid-point between the two, for example 1.5 or 2 mm thickness. It may be the case that a peak in formability was present rather than formability decreasing with thickness.

Hussain, Gao, and Hayat (2011a) examined the influence of the tool radius (R) : thickness (t) ratio on failure, which is linked to formability limits. The material is tested at two thicknesses, 0.7 and 2.6 mm, which is quite a large range - the largest difference between two successive thicknesses. They conclude that optimisation of $R : t$ ratio is needed to maximise the success of parts.

PVC was tested in 5 papers (Martins et al., 2009; Marques, Silva, and Martins, 2012; Silva, Alves, and Martins, 2010; Bagudanch, Garcia-Romeu, et al., 2015; Franzen et al., 2009) and the majority concluded that an increase in sheet thickness improved the formability of the material. On the other hand, Franzen et al. (2009) found a slight trend towards increased formability with the thinner sheet. However, the uncertainty in the experiment requires greater work to definitively compare the results against those from the other polymer papers.

Thickness optimisation Any kind of non-linear trend in formability is not observable in papers with only two levels of material thickness, and will therefore be categorised in either *Increase* or *Decrease*. For example, Jeswiet and Young (2005) plotted a linear trend of thickness against maximum wall angle. The equation for this trend is shown in Table 2.1.

To define thorough operating margins, investigation into the lowest and highest limits of formable sheet thicknesses for every material would be required. However, thick sheets present opportunities to make stronger parts with more satisfactory final thicknesses, such as for usable prototypes. In this case, having the knowledge to understand any trade-offs between, for example, sheet thickness and maximum wall angle, would allow the designer to choose the thickest sheet which still allows the part to be formed without failure.

Table 2.1: Material Thickness: Summary of papers

Papers	Material	Thickness [mm]	Test repeats
Conclusion: Increase material thickness to increase formability			
Jeswiet, 2002 [18]	AA3003-O	0.8, 1.3, 2.1	N/A
Jeswiet, 2005 [19]	AA3003-O	1.21 [#]	N/A
	AA5754-O	1.02 ^{##}	N/A
Ham, 2006 [13]	AA3003-O	0.81, 1.2, 2.1	N/A
Martins, 2009 [27]	PA, PC, PE, POM, PVC	2, 3	N/A
Manco, 2010 [25]	AA6082-T6	1, 2	1
Silva, 2010 [31]	PVC	2, 3	N/A
Marques, 2012 [26]	PA, PC, PET, PVC	2, 3	N/A
Shanmuganatan, 2013 [30]	AA3003-O	1, 1.25	N/A
Golabi, 2014 [11]	SS304	0.5, 0.7	N/A
Bagudanch, 2015 [4]	PVC	1.5, 2	3
Conclusion: Optimise material thickness to increase formability			
Ham, 2007 [13]	AA5182	0.93, 1, 1.5	N/A
	AA5754	0.93, 1, 1.45	N/A
	AA6451	0.8, 0.9, 1.545	N/A
Hussain, 2011 [16]	AA1060	0.7, 2.6	N/A
Hussain, 2013 [17]	AA2024-O	0.9, 1.4, 1.95, 3	2
Conclusion: Decrease material thickness to increase formability			
Franzen, 2009 [10]	PVC	2, 3	N/A
Fang, 2014 [9]	AA1100	1, 2.5, 4	1

$$^{\#} \Phi_{max} = 8.5t_0 + 60.7$$

$$^{##} \Phi_{max} = 3.3t_0 + 58.3$$

2.3.3.2 Tool diameter

Tool diameter was the most tested parameter in this literature review, with a total of 23 papers examining its effect on formability. Of these, 7 saw an increase in formability when the tool diameter was decreased, however 10 papers showed the opposite effect and 6 concluded that optimisation was necessary to maximise formability. These results are shown in Figure 2.6. All the tools in these papers were solid hemispherical tools.

Table 2.2 shows the details of each paper, with additional information about material type, thickness, and number of test repeats.

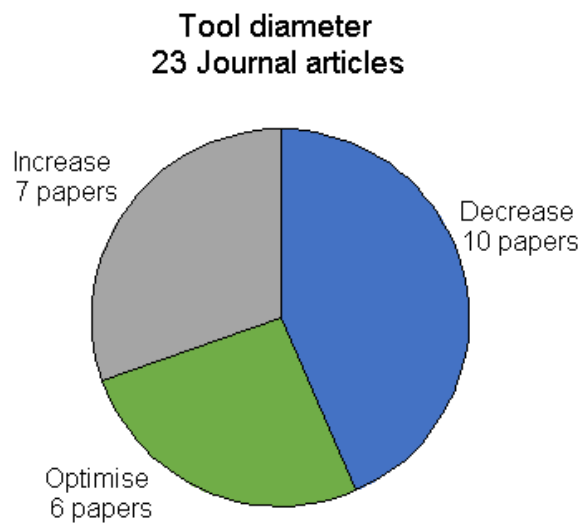


Figure 2.6: Tool diameter conclusions

Taking into account only the collected data on tool diameter, there is no clear consensus about the effect this parameter has on formability. An explanation is still not apparent if the results are grouped by material type (e.g. polymers, aluminium alloys, other materials). However, the 6 papers in the 'Optimise' category provide strong evidence that other parameters should be taken into account as they test a large number of different tools, over a wide range of materials and thicknesses.

For example, Hussain, Khan, et al. (2013) varied both thickness and tool diameter in a design of experiments and concluded that the diameter of the tool should be chosen based on a specific ratio with the thickness of the material. Al-Ghamdi and Hussain (2014) also drew conclusions about optimal ratios between tool size and material thickness for 7 different material types. From the results in Strano (2005), the author emphasises that reducing the tool diameter while maintaining a given sheet thickness will increase the likelihood of tearing from concentrated stress.

Table 2.2: Tool diameter summary of papers

Papers	Diameter [mm]	Material	Test repeats
Conclusion: Decrease tool diameter to increase formability			
Ham, 2006 [12]	4.7625, 12.7	AA3003-O	N/A
Ham, 2007 [13]	9.525, 12.7, 19.05	AA6451, AA5182, AA5754	N/A
Hussain, 2008 [14]	8, 12, 16	Commercially Pure Ti	2
Martins, 2009 [27]	10, 15	POM, PE, PA, PVC, PC	N/A
Petek, 2009 [29]	10, 16	DC05	3
Durante, 2011 [8]	5, 10, 15	AA7075-O	N/A
Silva, 2011 [32]	8, 12, 20, 30, 50	AA1050-H111	2
Marques, 2012 [26]	8, 10, 12	PET, PA, PVC, PC	N/A
Shanmuganatan, 2013 [30]	2.5, 5, 10	AA3003-O	N/A
Centeno, 2014 [6]	6, 10, 20	SS304	3
Conclusion: Optimise tool diameter to increase formability			
Kim, 2002 [20]	5, 10, 15	AA1050-O	N/A
Ambrogio, 2006 [2]	10, 12, 18, 20	AA1050-O	N/A
Ziran, 2010 [35]	4, 6, 10	AA3003-O	N/A
Hussain, 2010 [15]	6, 8, 11, 14, 16	AA2024-O	1
Hussain, 2013 [17]	7, 10.24, 13.5, 20	AA2024-O	2
Al-Ghamdi, 2014 [1]	2.2, 3.6, 4.4, 5.4, 6.6, 7.8	AA2024-O, AA2024-T6, AA1060-O, AA1060-H24, AA5083-O, Steel DS, Cu H59	2
Conclusion: Increase tool diameter to increase formability			
Strano, 2005 [33]	2.2, 3, 6.4	AA1050-O	N/A
Le, 2008 [21]	6, 12	PP	3
Franzen, 2009 [10]	10, 15	PVC	N/A
Silva, 2010 [31]	10, 15	PVC	N/A
Li, 2014 [22]	10, 20, 24.5, 30	AA7075-O	N/A
Golabi, 2014 [11]	6, 14	SS304	N/A
Bagudanch, 2015 [4]	6, 10	PVC	3

Table 2.3: Summary of Tool Type papers

Papers	Types of tool	Results
Kim, 2002 [20]	Solid hemispherical, roller ball tool	Roller ball tool had improved formability over stationary solid hemispherical tool using the straight groove test.
Ziran, 2010 [35]	Solid hemispherical, flat-ended tool	Flat ended tool with dimensions 10R3 improved formability over a hemispherical 10 mm tool (10R5), a 10R1 tool and 10R2 tool.
Durante, 2011 [8]	Solid hemispherical, roller ball tool	No difference in formability between roller ball tool and stationary solid hemispherical tool using a VWACF test.
Li, 2014 [22]	Solid hemispherical, roller ball tool	Roller ball tool had improved formability over stationary solid hemispherical tool using the straight groove test.
Lu, 2014 [24]	Solid hemispherical, roller ball tool, oblique roller ball tool	Roller ball tool had improved formability and surface finish over stationary solid hemispherical tool.

The implications of the research papers discussed in this section include the finding that tool size should not be selected without considering material thickness and material type. In addition, there is an optimal range for the ratio of tool diameter to material thickness - too large or small has detrimental effects on the formed part. Findings from this literature review specifically on the interaction between tool diameter and material thickness are presented and analysed in §2.3.3.8.

2.3.3.3 Tool type

A small number of papers compared different types of tools to determine their effect on formability. A summary of the results from each of these papers is shown in Table 2.3.

Y. H. Kim and Park (2002) and Li et al. (2014) both used a straight groove test to measure the formability of materials. The straight groove test simply involves the forming tool moving back and forth in a straight line, with progressively increasing depth. Figure 2.7, adapted from Li et al. (2014), shows the toolpath in the Z-X plane. Other researchers, including Durante, Formisano, and Langella (2011), have noted that this type of test is not indicative of the actual deformation in SPIF.

This is supported by Li et al. (2014) using the straight groove test and finding an increase in formability with increasing tool diameters while other similar tests

showed the opposite, for example Durante, Formisano, and Langella (2011) and Silva, Nielsen, et al. (2011). The other common issue with these investigations comparing tool types is that roller ball tools were compared to stationary hemispherical tools, i.e. 0 rpm spindle speed. It will be shown in §2.3.3.6 that increased spindle speed is advantageous, therefore the comparison is of limited usefulness.

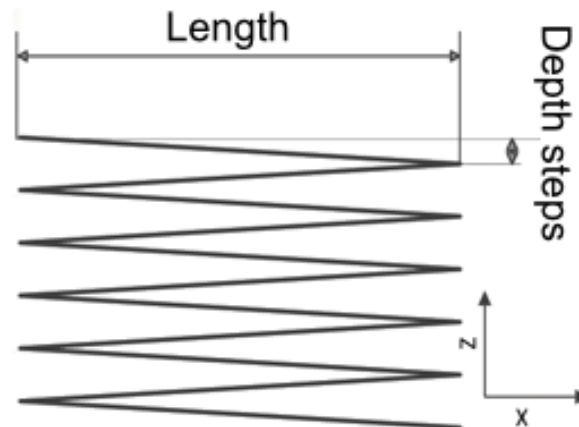


Figure 2.7: The toolpath of the straight groove test. Adapted from Li et al. (2014)

Traditionally tools in SPIF have been purely hemispherical and it is only within the last decade that research has been exploring the applications of tools with non-conventional cross sections (Cawley, Adams, and Jeswiet, 2013). Ziran et al. (2010) compared flat and hemispherical tool shapes, and found that formability was increased when using one particular flat ended tool shape, but decreased for other flat tool shapes. This area should be investigated more thoroughly with flat-ended and tools with other cross sections, having an effect not only on formability but also surface finish and forces (Cawley, Adams, and Jeswiet, 2013). This could help indicate which tool to use in a particular application.

2.3.3.4 Step down

There were 18 papers found that varied step down to determine the effect on formability. A majority of papers (13) concluded that decreasing the step down improves the forming limits of the material, and 7 papers conducted tests which presented results to the contrary. Figure 2.8 and Table 2.4 show the outcomes and papers.

Two papers found different results for the two materials they tested (Obikawa, Satou, and Hakutani, 2009; Davarpanah et al., 2015) so each material is counted individually making a total of 20 data points in the pie chart.

Hussain, Gao, Hayat, and Dar (2010) also found a different result than the majority

Table 2.4: Step down: Summary of papers

Papers	Material	Step down [mm]	Test repeats
Conclusion: Increase step down to increase formability			
Liu, 2013 [23]	AA7075-O	0.2, 0.5	N/A
Bagudanch, 2015 [4]	PVC	0.2, 0.5	3
Davarpanah, 2015 [7] *	PLA	0.2, 0.4, 0.6, 0.8, 1	4
Conclusion: Optimise step down to increase formability			
Ambrogio, 2006 [2]	AA1050-O	0.3 - 2	N/A
Obikawa, 2009 [28] *	Al foil, 50 μm	6, 12, 25, 50, 100, 200, 400 μm	N/A
Hussain, 2010 [15]	AA2024-O	0.08, 0.36, 0.78, 1.2, 1.48	1
Davarpanah, 2015 [7] *	PVC	0.2, 0.6, 1, 1.4, 1.8	4
Conclusion: Decrease step down to increase formability			
Kim, 2002 [20]	AA1050-O	0.1, 0.3, 0.5	N/A
Strano, 2005 [33]	AA1050-O	0.2, 0.4, 0.6, 0.8, 0.9, 1.2, 1.9	N/A
Ham, 2006 [12]	AA3003-O	0.127, 2.54	N/A
Ham, 2007 [13]	AA5754	0.0508, 0.127, 0.254	N/A
Hussain, 2008 [14]	Pure Ti	0.2, 0.75, 1.3	2
Le, 2008 [21]	PP	0.2, 1	3
Obikawa, 2009 [28] *	Al foil, 12 μm	1.5, 3, 6, 12, 25, 50, 100 μm	N/A
Petek, 2009 [29]	DC05	0.1, 0.5, 1, 3	3
Durante, 2011 [8]	AA7075-O	0.2, 0.4, 0.6	N/A
Shanmuganatan, 2013 [30]	AA3003-O	0.2, 0.4, 0.6, 0.8	N/A
Centeno, 2014 [6]	SS304	0.2, 0.5	3
Golabi, 2014 [11]	SS304	1, 1.5, 2	N/A
Ambrogio, 2015 [3]	AA5754, Ti6Al4V	0.1 - 0.5	N/A

* Multiple conclusions from one paper

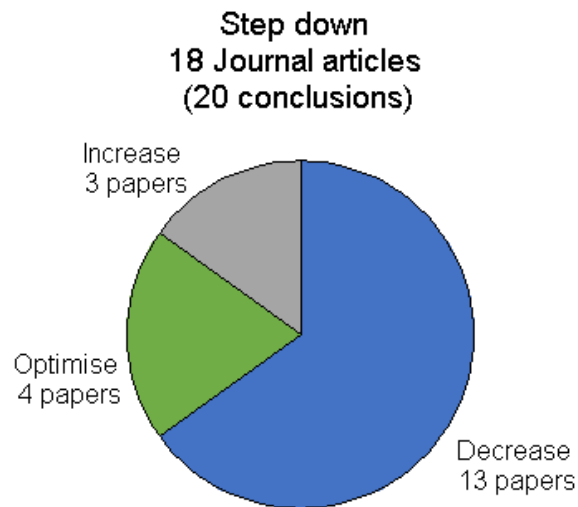


Figure 2.8: Step down conclusions

of papers, concluding that an optimum step down is required for maximum formability. From their experiments conducted using a central composite rotational design (CCRD) response surface method, the formability was improved using particular combinations of tool diameter and step down. This interaction is discussed in §2.3.3.8.

An interesting result was found in Liu, Li, and Meehan (2013), where truncated cones formed to a greater angle with 0.5 mm step down than 0.2 mm step down. However, the authors note that this is unusual and further testing would be required to confirm or disprove the results.

In their paper on incremental micro-forming, Obikawa, Satou, and Hakutani (2009) studied two different types and thicknesses of aluminium foils, and noted a peak in formability when step down was varied with the thicker foil. No such peak was observed for the thinner foil.

Theories behind the effect of step down on formability were proposed in some of the papers in this study. Table 2.5 summarises these theories.

Decreasing the step down has been shown to increase the formability, but also has a significant impact on forming time. It may be necessary in some situations to optimise process speed and formability (e.g. maximum wall angle) in which case the relative formability improvement per millimetre, for example, would need to be quantified.

Table 2.5: Step down: Summary of conclusions

Papers	Reason for conclusion
Conclusion: Decrease step down to increase formability	
Hussain, 2008 [14]	For Titanium, increasing the step down causes the deformation mechanism to include 'pulling' at the sheet. This caused deformation that was no longer localised.
Le, 2008 [21]	Higher friction is seen with larger step downs which leads to wrinkling and tearing of the thermoplastic sheet.
Durante, 2011 [8]	Increasing the tool-sheet contact area through increasing the step down leads to reduced formability.
Centeno, 2014[6]	A smaller step down results in more progressive deformation, beneficial to the formability.
Conclusion: Optimise step down to increase formability	
Ambrogio, 2006 [2]	A step down that is too small would result in increased wear.
Obikawa, 2009 [28]	Very small step down values caused normal and frictional stresses to be repeatedly applied to the same parts of the material. It is proposed that this exacerbates defects in the material and results in early failure.
Conclusion: Increase step down to increase formability	
Bagudanch, 2015 [4]	Attributed to the 'rheological properties of thermoplastic materials'. It is likely that the effect is not absolute and with further experimentation the conclusion would be 'Optimise'.

2.3.3.5 Feed rate

A total of 7 papers varied the feed rate of the tool and observed the effect on formability (Table 2.6). There was no majority conclusion, but the most common conclusion was that decreased feed rate increased the formability, shown in Figure 2.9.

Interestingly, Hussain, Gao, Hayat, and Dar (2010) showed that feed rate has different effects on AA2024 whether it is annealed or has been aged. Specifically, for the aged sheet it was beneficial to form at a slower feed rate, however no effect was noted with the annealed sheet. Each of these conclusions is counted separately in the pie chart.

Ambrogio and Gagliardi (2015) measured the process temperature of SPIF at high speeds using a lathe. An optimum value of feed rate maximised the generated temperature and increased the formability of the material. The upper and lower limits of the tests were quantitatively specified, but not the implied midpoint.

Heating of the sheet at lower feed rates was reported as the reason for increased formability in Ham and Jeswiet (2006). Low feed rates increase the time for frictional heating of a point between the sheet and the spinning tool, where forming occurs. Another proposal for why lower feed rates increased formability, from Hussain, Gao, and Zhang (2008), was that work hardening (detrimental to incremental forming) increases as the tool moves faster.

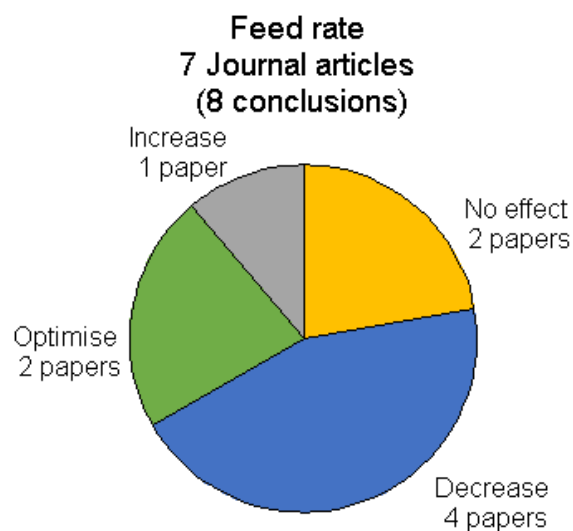


Figure 2.9: Feed rate conclusions

Bagudanch, Garcia-Romeu, et al. (2015) found that the failure depth of PVC variable wall angle pyramidal frustum (VWAPF) samples was positively affected by increased feed rate, and the parts fractured approximately 3 mm further at a feed of

Table 2.6: Feed rate: Summary of papers

Papers	Material	Feed rate [mm/min]	Test repeats
Conclusion: Increase feed rate to increase formability			
Bagudanch, 2015 [4]	PVC	1500, 3000	3
Conclusion: Optimise feed rate to increase formability			
Ambrogio, 2015 [3]	AA5754, Ti6Al4V	5000 - 500,000	N/A
Conclusion: Decrease feed rate to increase formability			
Ham, 2006 [12]	AA3003-O	1270, 2540	N/A
Le, 2008 [21]	PP	1000, 3000	3
Hussain, 2008 [14]	Titanium	1200, 2600, 4000	2
Hussain, 2010 [15] *	AA2024-T4	600, 1200, 2100, 4500	1
Conclusion: No significant effect of feed rate on formability			
Hussain 2010 [15] *	AA2024-O	373, 1200, 2437, 3674, 4500	1
Golabi, 2014 [11]	SS304	600, 1200	N/A

* Multiple conclusions from one paper

3000 mm/min compared to 1000 mm/min. This margin is small, but the results are reliable due to 3 repeats of each test. As the only paper which found increasing feed rate to cause an increase in formability, it would be interesting to extend the tests to values as high as 5000 or 10,000 mm/min, for example. At such high feeds, there may be detrimental effects to formability or surface finish which would result in a revision of the conclusion to 'Optimise'.

It has been shown that the influence of feed rate depends on the material being formed.

In addition to step down, feed rate impacts the process time. Therefore, optimisation would be required if a trade-off between forming time and increased formability was necessary. Knowledge of the effect of feed rate on the particular material would be required, as well as the relative increase in formability per decrease in feed rate.

2.3.3.6 Spindle speed

There were a total of 8 journal articles found which examined the effect of spindle speed on formability, listed in Table 2.7. A majority found that increasing the spindle speed caused an increase in formability. Figure 2.10 shows the proportions of each conclusion.

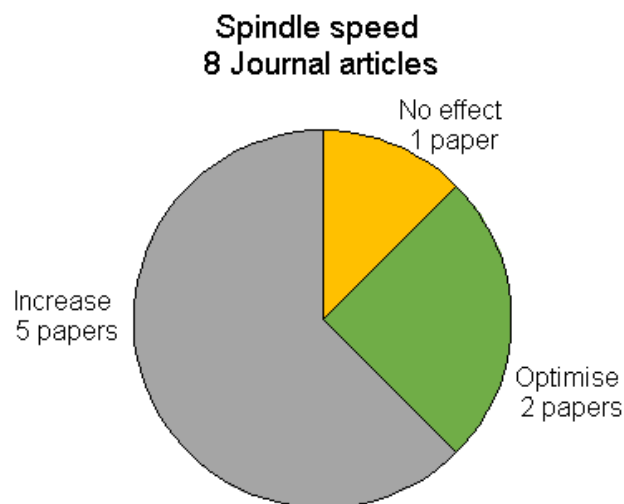


Figure 2.10: Spindle speed conclusions

Three papers, Buffa, Campanella, and Fratini (2013), Obikawa, Satou, and Hakutani (2009), and Davarpanah et al. (2015), tested multiple materials and found the same effect for each, though each had differing conclusions.

In their experiments using AA3003-O, Ham and Jeswiet (2006) found a spindle

Table 2.7: Spindle speed: Summary of papers

Papers	Material	Spindle speed [rpm]	Test repeats
Conclusion: Increase spindle speed to increase formability			
Ham, 2006 [12]	AA3003-O	100, 600	N/A
Le, 2008 [21]	PP	200, 700	3
Xu, 2013 [34]	AA5052-H32	0, 250, 500, 750, 1000, 2000, 3000, 4000, 5000, 6000, 7000	N/A
Buffa, 2013 [5]	AA1050-O, AA1050-H24, AA6082-T6	100, 2000, 4000, 6000, 8000, 10,000	N/A
Bagudanch, 2015 [4]	PVC	1000, 2000 †	3
Conclusion: Optimise spindle speed to increase formability			
Obikawa, 2009 [28]	Al foil, 0.05 mm	0, 5000, 10,000, 20,000	N/A
	Al foil, 0.012 mm	0, 2500, 5000, 10,000, 20,000, 25,000	N/A
Davarpanah, 2015 [7]	PVC, PLA	0, 1250, 5000, 7000	4
Conclusion: No effect of spindle speed on formability			
Petek, 2009 [29]	DC05	0, 40 †	3

† Free rotation of the tool was also tested

speed of 600 rpm produced a greater number of successful parts than 100 rpm. Frictional heating of the metal sheets is said in their paper to be the reason for the increased rate of success.

Xu et al. (2013) used a 50 mm upper-diameter VWACF and a 10 mm diameter hemispherical tool to test 11 different spindle speeds between 0 and 7000 rpm. The resulting graph of maximum wall angle vs. spindle speed climbed steadily as the speed increased, apart from a local minimum at 1000 rpm. Overall, the formability increased approximately 15° between 0 and 7000 rpm. They propose that the friction conditions change in stages as the spindle speed increases, and at high values of rpm the friction heating causes the material to soften and advantageous microstructural changes to occur.

Buffa, Campanella, and Fratini (2013) tested three different materials over a large range of spindle speeds. The chosen materials are typically hard to form at room temperature, but formability improved by approximately 10° over the range. The increase is attributed to changes in the crystal structure and grain growth as the high speeds cause heating in the sheet.

Obikawa, Satou, and Hakutani (2009) studied incremental micro-forming of thin aluminium foil, less than one fifth of a millimetre thick. They used a hemispherical tool of 1 mm diameter, and tested the largest range of spindle speeds among the papers in this review, 0 to 25,000 rpm. They found a peak in the major strain at failure for both materials at a midpoint in the range of spindle speeds.

Davarpanah et al. (2015) varied spindle speed over the same range as Xu et al. (2013), to whom they refer in their introduction as having shown the effect of spindle speed on SPIF of metals. They examine the effect of spindle speed on PVC cones with 40 mm major diameter and 5 mm diameter tool, finding wall angle to increase with spindle speed. Due to the large part - tool diameter ratio, there was a margin of error of $\pm 4^\circ$ in the calculation. However, the results showed that an optimum value of spindle speed produced the best results when taking into account surface roughness in addition to formability.

Based on the results from these 8 papers, it seems clear that increasing the spindle speed above 0 rpm will likely result in an increase in formability. From the two 'Optimise' papers (Obikawa, Satou, and Hakutani, 2009; Davarpanah et al., 2015), the upper bound will be found when the friction between the tool and the sheet is too high and damage to the surface begins to occur.

These papers also conclusively show that there would be no instance where stationary tools should be used, as the minimum friction was seen when the tool was free to rotate or with a roller ball tool, though this provides no friction heating benefits (Buffa, Campanella, and Fratini, 2013). Stationary tools are detrimental to

both formability and surface quality, demonstrated in Obikawa, Satou, and Hakutani (2009), Xu et al. (2013), and Durante, Formisano, and Langella (2011).

2.3.3.7 Spindle rotation direction

Only two papers in this study undertook research using both climb and conventional milling directions.

Obikawa, Satou, and Hakutani (2009) incorporated this aspect into their tests on aluminium foil. The range of 0 - 25,000 rpm spindle speed was tested in both conventional and climb milling directions, denoted by -25,000 rpm to 25,000 rpm. At high spindle speeds, there was little difference found between the two rotation directions.

Durante, Formisano, and Langella (2011) incrementally formed parts with a solid hemispherical tool rotating in a clockwise and counter clockwise direction, and compared the results to those of a stationary (0 rpm) tool and a roller ball tool. The rotation direction did not have a significant effect on formability, only on the final surface finish and the forces. The solid hemispherical tool produced an inferior surface finish to a roller ball tool, but the solid tool spinning at 600 rpm in climb (rolling) milling produced the lowest process force.

The conclusion to be made from the results in this section and the previous section on spindle speed is that for the majority of materials the forming tool should be rotated at relatively high speeds to maximise the formability. As such the rotation direction will not influence the outcome with any significance, though climb will still remain the most common milling mode as the tool is rolling over the sheet and minimises sliding friction. Additionally, it could be argued that there would be no situation where conventional milling would be helpful.

2.3.3.8 Interactions

The following sections describe some main two-factor parameter interactions and discuss their significance.

Feed rate - Spindle speed interaction Feed rate and spindle speed play a key role in the friction and associated heat generated during the SPIF process. Two papers studied the interaction of both parameters, and both used polymers for their tests. Results for polypropylene sheets in Le, Ghiotti, and Lucchetta (2008) showed improved formability for certain combinations of feed rate and spindle speed, finding a large interaction between the two.

Bagudanch, Garcia-Romeu, et al. (2015) found no influence on formability for the feed-speed interaction, however did show a statistically significant effect on surface roughness. They used similar feed rates (1500 mm/min and 3000 mm/min) but different values of spindle speed (free rotation and 2000 rpm). The free tool rotation would have resulted in low spindle speeds of 50 - 160 rpm. Therefore it would be interesting to test a mid-point spindle speed to compare with results from Le, Ghiotti, and Lucchetta (2008).

There is scope for understanding the effect of this interaction on materials other than polymers, to control the friction conditions, and develop an upper and lower operating margin of the ratio of feed rate: spindle speed [rot/mm].

Tool diameter - Material thickness interaction As mentioned briefly in §2.3.3.2: Tool diameter, there is evidence to show that the interaction of material thickness and tool diameter plays a large role in the formability of the material, and even whether or not the part will form at all. A small tool with a thick sheet can cause a large amount of damage to the surface, and render the part useless (Hussain, Gao, and Hayat, 2011a). Table 2.8 shows additional information for the papers listed in Table 2.2: Tool diameter summary of papers

Another example of the benefit of this interaction was shown in Ham and Jeswiet (2006), where the maximum wall angle increased by 13° from large tool/thin sheet to small tool/thick sheet.

Hussain, Khan, et al. (2013) varied sheet thickness and tool diameter and found an optimal combination could increase the maximum wall angle by nearly 20°. They present a graph of wall angle against the ratio of tool radius and sheet thickness (R/t_0) showing a peak in formability.

Silva, Alves, and Martins (2010) tested different thicknesses of PVC sheets and analysed the results of maximum wall angle taking into account tool radius. A small interaction was seen, causing the maximum wall angle to be positively affected by the combination of thick sheet and large tool.

Bagudanch, Garcia-Romeu, et al. (2015) carried out a full factorial with ANOVA and found that the interaction of sheet thickness and tool diameter was insignificant for formability but did have an effect on the final surface roughness.

Manco and Ambrogio (2010) also performed an ANOVA and found that the interaction in question did not have a significant effect on the minimum thickness observed in the tests

Understanding this interaction would allow the tool to be chosen based on the particular material and sheet thickness, in the case where the latter is a product requirement, for example. Silva, Alves, and Martins (2010) highlight that it is much

Table 2.8: Tool diameter - Material thickness interaction with R/t ratio ‡

Papers	Min R/t	Max R/t	Range	Material	Thickness
Conclusion: Decrease tool diameter to increase formability					
Ham, 2006 [12]	1.1299	7.84	6.71	AA3003-O	0.81, 1.2, 2.1
Ham, 2007 [13]	3.08	11.91	8.82	AA6451	0.8, 0.9, 1.545
	3.18	10.24	7.07	AA5182	0.93, 1.15, 1.5
	3.28	10.24	6.96	AA5754	0.93, 1, 1.45
Hussain, 2008 [14]	4.04	8.08	4.04	Commercially Pure Ti	0.99
Martins, 2009 [27]	1.67	3.75	2.08	POM, PE, PA, PVC, PC	2,3
Petek, 2009 [29]	5	8	3	DC05	1
Durante, 2011 [8]	2.5	7.5	5	AA7075-O	1
Silva, 2011 [32]	4	25	21	AA1050-H111	1
Marques, 2012 [26]	1.33	3	1.67	PET, PA, PVC, PC	2, 3
Shanmuganatan, 2013 [30]	1	5	4	AA3003-O	1, 1.25
Centeno, 2014 [6]	3.75	12.5	8.75	SS304	0.8
Conclusion: Optimise tool diameter to increase formability					
Kim, 2002 [20]	8.33	25	16.67	AA1050-O	0.3
Ambrogio, 2006 [2]	2.5	10	7.5	AA1050-O	1, 2
Ziran, 2010 [35]	2	5	3	AA3003-O	1
Hussain, 2010 [15]	3	8	5	AA2024-O	1
Hussain, 2013 [17]	1.17	11.11	9.94	AA2024-O	0.9, 1.4, 1.95, 3
Al-Ghamdi, 2014 [1]	1.1	3.9	2.8	(See Table 2.2)	1
Conclusion: Increase tool diameter to increase formability					
Strano, 2005 [33]	1.83	5.33	3.5	AA1050-O	0.6
Le, 2008 [21]	1	2	1	PP	3
Franzen, 2009 [10]	1.67	3.75	2.08	PVC	2, 3
Silva, 2010 [31]	1.667	3.75	2.083	PVC	2, 3
Li, 2014 [22]	4.92	14.76	9.84	AA7075-O	1.016
Golabi, 2014 [11]	6	14	10.5	SS304	0.5
Bagudanch, 2015 [4]	1.5	3.33	1.83	PVC	1.5,2

‡ R/t = tool radius over thickness ratio. Range is difference between Max and Min.

more practical to vary the tool size over a large range than it is to vary the sheet thickness.

Tool diameter - Step down interaction A number of the papers in this study provided results on the interaction of tool diameter and step down, and differing conclusions were found among them.

In Hussain, Gao, Hayat, and Dar (2010), the results were analysed using an ANOVA and the interaction in question had a p-value below 0.05. It also had the most influence on the maximum wall angle out of all the tested main factor effects and interaction effects. Le, Ghiotti, and Lucchetta (2008) saw a significant interaction between tool diameter and step down, where a small tool and a large step down value caused the maximum wall angle to decrease.

On the other hand, Ham and Jeswiet (2006) and Bagudanch, Garcia-Romeu, et al. (2015) found no significant interaction. Findings from the former may be attributable to the small values of step down utilised in the paper, varied from 0.0508 mm - 0.254 mm.

Based on the conclusions from these papers, it is uncertain how important this interaction is. In the case of Hussain, Gao, Hayat, and Dar (2010) the improvement in maximum wall angle was approximately 3°, smaller than the 13° improvement seen with the tool diameter - material thickness interaction in Ham and Jeswiet (2006). More research would need to be conducted to confirm this, and the combined effect of material type should also be taken into account.

This also extends into an interaction of tool edge radius and step down - for flat ended tools which are defined by a shaft radius and an edge radius (see Figure 2.4). Is the interaction the same for a hemispherical tool that has the same radius as the edge of a flat-ended tool, even if the flat ended tool is thicker than the hemispherical tool? This question is an area that would need to be investigated.

Step down - Material thickness interaction Ham and Jeswiet (2006) and Bagudanch, Garcia-Romeu, et al. (2015) also both assessed the step down - thickness interaction using an ANOVA, finding it to be statistically insignificant.

A medium influence of step down and blank thickness on the value of minimum thickness was observed in Manco and Ambrogio (2010), and Hussain, Gao, and Hayat (2011a) found the interaction to have no influence on the failure modes analysed in their paper.

The combined effect of step down and material thickness is therefore probably not very large, however more research would need to be conducted to determine whether

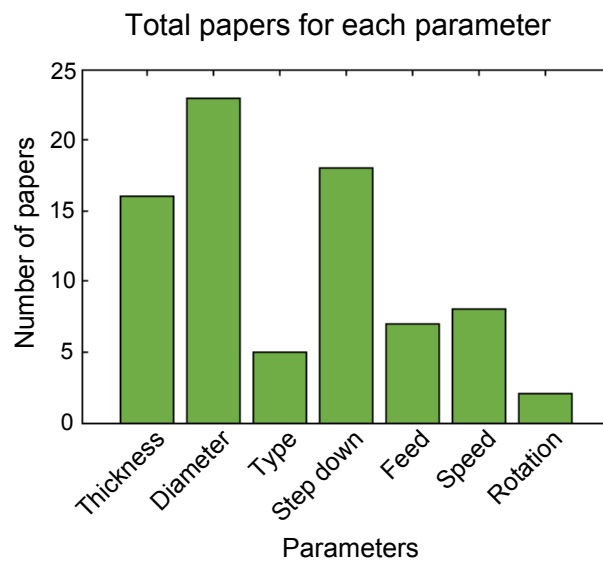


Figure 2.11: Total number of papers analysed for each parameter

or not there is an optimal range of step down based on the thickness of the formed material.

2.3.3.9 Parameter comparison

The bar graph in Figure 2.11 compares the total number of papers that were found for each individual parameter in this literature review. Tool diameter ('Diameter') had the largest amount of research conducted, followed by step down and material thickness ('Thickness'). Very few papers tested spindle rotation direction ('Rotation') or tool type ('Type'). There are a few possible reasons for low volumes of research. The parameter could have little to no effect, as has been found with spindle rotation direction, or it could be a relatively new development, for example using different tool types. It could also be due to a lack of awareness about the full breadth of possibilities for the parameter, such as tool type (only using hemispherical tools) or spindle speed (using non-rotating tools).

There is potential for a great deal more published research on some of the parameters. Future work could investigate tool shapes more thoroughly, continuing on from Ziran et al. (2010) and others including Cawley, Adams, and Jeswiet (2013). It would also be useful to improve understanding of feed rate, spindle speed, and friction and the role they play in increasing formability through induced heating.

Table 2.9: SPIF Experimental Parameter Framework

SPIF Parameter
Material type
Material thickness
Material properties
Tool diameter
Tool shape
Tool material
Step down
Feed rate
Spindle speed
Lubrication details
Number of test repeats
Spindle rotation direction
Toolpath type (e.g. spiral)
Test geometry details
Forming machine type
Backing plate details

2.3.3.10 SPIF parameters in the literature

This quantitative assessment of the literature allowed an insight into the experimental information written into these studied journal articles. Many of the papers from this review did not mention, for example, the number of test repeats carried out, the material properties, or the value of spindle speed. It is particularly important to mention all experimental details for a parameter such as feed rate, missing from 23% of papers in this review. Feed rates of 100 mm/min and 3000 mm/min may have significantly different effects on the outcome due to effects such as the heating produced by friction.

The amount of missing parameters meant that a full comparison of the experiments was not possible. This highlights a need for greater awareness of the full breadth of parameters which have an effect on the SPIF process, or on the significance of the findings in the paper.

A framework for crucial experimental information is proposed in Table 2.9. For any basic SPIF research, not taking into account variations such as heat- or electrically-assisted SPIF, these parameters provide important information for the reader.

2.3.3.11 Final discussion

This section provides some perspectives on the cumulative results of this work.

Differing conclusions among papers All the parameters in this literature review were found to have varying effects among the papers that studied them. This provides strong evidence for the hypothesis of this work mentioned in §2.3.1.6, which is that the parameters are interdependent and therefore do not have consistent effects across all situations.

The most significant discrepancies were found when analysing the conclusions on the effect of tool diameter, despite having the largest number of journal articles which studied the parameter. The analysis shows that a large range of tool diameters were utilised among the collected papers, and also highlights the significant interaction of tool diameter and material thickness, in addition to the possible interaction with step down. It is for these reasons that the large number of differing conclusions for tool diameter is not unusual. However, it does provide scope for future research to take these interactions into account so that we may see more consistent conclusions about their combined effect, and therefore make confident parameter choices in SPIF.

Hussain, Gao, Hayat, and Dar (2010) produced important results showing that the effect of feed rate is material-dependent, which provides an explanation for the four separate conclusions found in the literature analysis for feed rate. Heating of the sheet was commonly seen in the tests using high spindle speed, so the effect of this parameter would also vary depending on the material and thermal properties of the sheet.

Process mechanics Forming mechanisms in SPIF have been investigated in the literature, and two significant papers have presented models for predicting fracture in SPIF and discussed theories on deformation mechanisms and fracture occurrence.

Silva, Skjoedt, et al. (2008) proposed a theoretical framework which could explain the influence of thickness, tool diameter, step down, feed rate and spindle speed. They show that suppression of neck formation occurs in SPIF, resulting in forming limit diagrams being inapplicable for predicting failure in the process.

Malhotra et al. (2012) developed a model to predict fracture in truncated cones and VWACF parts, and also discussed necking in what they termed the 'noodle' theory, where high formability limits are a result of necks forming locally in the material but never developing enough to result in fracture.

Investigation into the process and deformation mechanisms offers insight into the results of this literature review, but fails to address all the inconsistencies in the experimental findings. Further investigation into the mechanics of deformation is required to understand how the interactions between the different process parameters may influence the deformation mechanisms and, by extension, the formability limits.

2.3.3.12 Future directions in SPIF

The overarching aim of SPIF research is to allow a component to be successfully formed on the first attempt, or at least minimise the amount of trial and error required. Among the papers in this literature review there are several ideas presented to help achieve this aim. A recurring proposal to achieve this has been the prediction of limit strains, for example with forming limit diagrams (FLDs) which are used to determine limit strains in stamping operations. Papers including Al-Ghamdi and Hussain (2014), Centeno et al. (2014), and Jeswiet and Young (2005) have discussed this possibility. Similarly, the maximum wall angle was determined early on (seen in Ham and Jeswiet (2006)) as a way to predict the success of the part before forming by comparing the wall angles to previously determined limits.

In-line force monitoring to predict failure (Petek, Kuzman, and Kopac, 2009), prediction of thinning (Shanmuganatan and Senthil Kumar, 2013), prediction of catastrophic forming defects (Hussain, Gao, and Hayat, 2011a) and basic success limits for a cone determined from experimentation (Golabi and Khazaali, 2014) are also proposed as tools to improve component development using SPIF. Additionally, in their paper from 2011, Silva, Nielsen, et al. take a fundamental approach to understanding formability limits and failure mechanisms, which is a step towards more generic solutions that are not limited by the extent of experimental campaigns.

2.3.4 Conclusion

The parameters that control the SPIF process have been varied and tested in experiments since the early days of development (Y. H. Kim and Park, 2002). A systematic literature search (Pickering and Byrne, 2014) was carried out to find journal articles that have varied these process parameters and studied the effect on material formability.

The details and outcomes from the 35 relevant papers were quantitatively recorded in a database, and results for material thickness, tool diameter, tool type, step down, feed rate, spindle speed, spindle rotation direction, and parameter interactions were analysed. These are the parameters that are necessary to control for every SPIF process, from single pass SPIF to laser-assisted SPIF. This is why only these most basic parameters, and not others such as the temperature of an external heat source, were studied in this review.

The results of these analyses showed that material thickness should be optimised based on the type of material, despite most papers concluding that formability increased with thickness. Optimisation is necessary because very large thicknesses, beyond the values tested in most of the papers, would begin to be too challenging to

form due to the large forces required, and formability would be decreased, as seen with 4 mm thick AA1100 in Fang et al. (2014). The effect of material thickness is consistent throughout the literature examined in this review, though specific results for each material may differ.

The type and thickness of the material should also be a consideration in optimisation of tool diameter, in order to achieve maximum formability. The research presented in this review, however, shows conflicting results about the impact of changing the tool diameter, likely due to this parameter affecting the process in a number of ways such as friction conditions, forming force and stress at the tool-sheet interface.

Tool type was also studied but only one paper was found to have looked at formability with different shapes of tools. More research would be needed to understand when non-hemispherical tools might be beneficial to formability and other outcomes in SPIF, for example surface finish or forces.

The consensus in the literature for step down was that formability improved with decreasing values, however it should be optimised if reduced process time is a requirement. Some papers found that polymers seemed to be affected by too-small step downs more than metals, and the formability was subsequently reduced. This indicates that material should be taken into account when choosing this variable, and it has also been shown that there may be interactions with material thickness and tool diameter.

Feed rate and spindle speed should both be optimised depending on the material type, with the former also necessarily requiring a trade off with process time. The variation in conclusions for feed rate is explainable by material dependence, shown in Hussain, Gao, Hayat, and Dar (2010), possibly stemming from the material's strain-rate sensitivity. Spindle speed was generally recognised to be a major factor in the heat generated from friction, and if heating benefits are desired, optimisation is necessary to prevent surface damage from excessive friction between the tool and sheet.

A small number of papers included data on parameter interactions, and these have also been studied in this literature review. There is an important interaction between feed and speed as they have a large effect on the friction conditions between tool and sheet. By extension, they also influence the frictional heating, which may be beneficial or detrimental to the process, depending on other parameters such as material type.

Thickness and the diameter of the tool have an important interaction that can cause significant surface damage if the ratio is extreme, studied in Hussain, Gao, and Hayat (2011a). Therefore, as mentioned, the tool diameter should be chosen based on the thickness of the material, because it is easy to change to obtain a wide range of tool diameters but sheet thickness is usually not as simple to adjust. Step down has possible but unsubstantiated interactions with both material thickness and tool

diameter.

In conclusion, it has been shown that SPIF parameters are not independent and are highly interdependent. A framework for the experimental parameters used in SPIF has been presented to ensure effective comparisons between research in the future.

2.3.5 Analysed articles

A list of the journal articles used for the systematic quantitative analysis in this chapter, along with the corresponding reference IDs, can be found in Table 2.10.

Table 2.10: List of papers for systematic quantitative analysis with corresponding Reference ID

Citation	Ref. ID
Al-Ghamdi and Hussain (2014)	[1]
Ambrogio, Filice, and Micari (2006)	[2]
Ambrogio and Gagliardi (2015)	[3]
Bagudanch, Garcia-Romeu, et al. (2015)	[4]
Buffa, Campanella, and Fratini (2013)	[5]
Centeno et al. (2014)	[6]
Davarpanah et al. (2015)	[7]
Durante, Formisano, and Langella (2011)	[8]
Fang et al. (2014)	[9]
Franzen et al. (2009)	[10]
Golabi and Khazaali (2014)	[11]
Ham and Jeswiet (2006)	[12]
Ham and Jeswiet (2007)	[13]
Hussain, Gao, and Zhang (2008)	[14]
Hussain, Gao, Hayat, and Dar (2010)	[15]
Hussain, Gao, and Hayat (2011a)	[16]
Hussain, Khan, et al. (2013)	[17]
Jeswiet, Hagan, and Szekeres (2002)	[18]
Jeswiet and Young (2005)	[19]
Y. H. Kim and Park (2002)	[20]
Le, Ghiotti, and Lucchetta (2008)	[21]
Li et al. (2014)	[22]
Liu, Li, and Meehan (2013)	[23]
B. Lu, Fang, et al. (2014)	[24]
Manco and Ambrogio (2010)	[25]
Marques, Silva, and Martins (2012)	[26]
Martins et al. (2009)	[27]
Obikawa, Satou, and Hakutani (2009)	[28]
Petek, Kuzman, and Kopac (2009)	[29]
Shanmuganatan and Senthil Kumar (2013)	[30]
Silva, Alves, and Martins (2010)	[31]
Silva, Nielsen, et al. (2011)	[32]
Strano (2005)	[33]
Xu et al. (2013)	[34]
Ziran et al. (2010)	[35]

2.4 Geometric accuracy in SPIF

Geometric accuracy has long been identified as an area of development in SPIF and has been studied extensively in the literature. SPIF components, made out of sheet material, are subject to mechanisms like springback that lead to geometric error, and a component which may not be fit for purpose.

In SPIF, there are some common modes of geometric error seen in formed parts. One mode is bending in the unformed flange of the sheet, studied in Ambrogio, Costantino, et al. (2004). However, the addition of a simple backing plate to support the flange during forming can resolve this issue.

Another type of error in SPIF is upwards bulging in the flat base of the part, named the 'pillow effect' by Ambrogio, Cozza, et al. (2007). Bulging in the base of the part (pillowing) has been studied by a number of authors.

In the original paper on the pillow effect, Ambrogio, Cozza, et al. (2007) studied geometrical errors in SPIF parts. Truncated pyramids were formed with varying process parameters and the pillow height (amount of geometric error in the base) was measured in each. The authors developed empirical equations from the results to predict the geometrical errors based on inputs of the selected parameters. The applicability of their investigation is limited by the specific test shape, but nonetheless it is a comprehensive first look at the phenomenon of pillowing in SPIF.

Further research includes work by Hussain, Gao, and Hayat (2011b), looking at pillowing in conical frustums. The severity of the error increased with sheet thickness and reduction in wall angle. Results from this study were supported with later work by Vanhove and Duflou (2015) where low wall angles had a strong influence on the severity of the pillowing. Al-Ghamdi and Hussain (2015) showed that pillow height peaks as part depth increases.

In some circumstances it may not be feasible to change the wall angle or forming depth of the part in an attempt to improve geometric accuracy, so optimising process parameters is more practical. A recent paper, Isidore et al. (2016), studied tool end-shape and the effect on pillow height using small truncated pyramids with low wall angles (100 mm² area, 12 mm depth). Two hemispherical tools with shaft radius 5 mm and 7 mm were used, with corresponding flat-ended tools of constant 1 mm edge radius.

The results showed flat-ended tools decrease bulging in the base of SPIF parts, agreeing with previous research conducted by Ziran et al. (2010). The FEA results indicated that stresses in-plane and normal to the sheet cause pillowing through buckling and bending of the sheet respectively.

A third mode of geometric error found in SPIF components is wall bulge, where

flat walls bulge inwards after forming. This type of error was seen in pyramid parts from Ham and Jeswiet (2008), Bambach, Taleb Araghi, and Hirt (2009), and Vanhove, Verbert, et al. (2010). Similar error was also seen in the walls of parts from Behera, Lauwers, and Duflou (2014) and termed the ‘Tent effect’, and ‘horizontal springback’ in a paper by H. Lu et al. (2016). Figure 2.12 shows the difference between these two error types, wall bulge and pillowing.

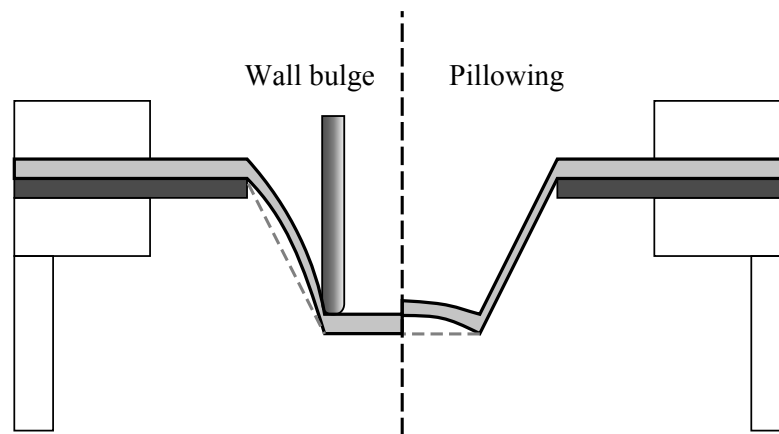


Figure 2.12: Cross-section of an example SPIF part showing the characteristic errors of wall bulge and pillowing

Research has been carried out to develop ways to improve geometric accuracy in SPIF. Previous studies have found that complicated multi-pass forming methods can help (Bambach, Taleb Araghi, and Hirt, 2009), as can increasing the wall angle of a part (Hussain, Gao, and Hayat, 2011b; Vanhove and Duflou, 2015), though this may not be a feasible solution in some cases. Individual parameters such as tool size and sheet thickness can have some effect, as discussed in the review paper by Gatea, Ou, and McCartney (2016).

Bambach, Taleb Araghi, and Hirt (2009) discuss a wall bulge study that tested an over-forming strategy to compensate for the bulging. The amount of deviation from this type of wall bulge error was able to be reduced by over-forming, but it was not eliminated.

The authors subsequently investigated multi-pass strategies to eliminate wall bulge error and achieve the desired geometry. Progressively forming a shape with more than one forming pass can improve the geometric accuracy by reducing the absolute deformation in each pass. As the elastic recovery (springback) is influenced by the amount of deformation, the springback is reduced when less deformation occurs in one pass. The results in Bambach, Taleb Araghi, and Hirt (2009) confirm this theory.

Notably, wall bulge error was more severe in the larger of the two sizes of truncated pyramids formed in the paper. Therefore, wall bulge is an important consideration for larger parts or prototypes such as automotive components.

Complex methods of toolpath adjustment are another area of investigation for reducing overall error in SPIF. For simple incremental forming, the toolpath follows the desired part surface exactly, but researchers such as Verbert, Duflou, and Lauwers (2007) have developed algorithms where areas of the part are ‘over-formed’ to compensate for elastic springback in the sheet of material. The algorithm classifies sections of a model to allow toolpath adjustment based on typical types of inaccuracy.

Behera, Verbert, et al. (2013) also developed a complex toolpath compensation method which requires a formed SPIF part to be scanned with a coordinate measuring machine (CMM) and the geometric error forms the algorithm input. The algorithm required a number of preliminary steps to be trained sufficiently. An offset toolpath is calculated for the component which compensates for the error and in their paper, and a later work (Behera, B. Lu, and Ou, 2016), the toolpath was shown to be effective. While this method produces accurate results, the requirement of using a CMM to scan an initial formed part does increase the complexity compared to a simple method such as adjusting process parameters.

Pillowing and wall bulge are two modes of geometric accuracy which have previously been studied in the literature. Among other parameters which have been shown to influence error, flat-ended tools can greatly reduce pillow height without the need for other adjustments (Isidore et al., 2016). Improving wall bulge in a SPIF part can be achieved through complicated toolpath adjustments.

No work has yet been done around the effect of flat-ended tools on wall bulge, which would be useful to understand for assisting with tool choice in industrial production situations. Selecting a particular tool is a simple way to significantly influence the outcome of a SPIF part (Hussain, 2014), in the same way that a machinist would change the type or size of tool in a milling process.

2.5 Conclusion and proposed work

This chapter has presented a number of insights into the process of SPIF in the context of component production. The understanding of the state of the art also indicates areas with scope for further study.

A fundamental framework for experimental parameters in SPIF is provided after important details were not consistently reported across the research literature. This framework aims to ensure SPIF experiments can be accurately replicated, and comprehensively understood to facilitate future meta analyses and literature comparisons.

Across both areas of the literature, the end-shape of the forming tool was the subject of limited research. However, the research that had been carried out suggested that a simple change in tool may have a significant effect on the final part. As an overarching theme, this thesis will consider the effect of tool shape on these two key areas of formability and geometric accuracy.

There is a lack of consistency between research papers about the effect of some process parameters on formability. The lack of consistency may be influenced in part by non-linear parameter effects as well as interaction effects, as hypothesised in §2.3.1.6 of the formability literature review. This thesis will further investigate non-linear parameter effects on formability, and the significance of parameter interactions including the promising area of tool shape.

Geometric accuracy of the SPIF process has been a widely-researched topic due to the importance of accurate components in practical applications. Relevant studies have included complex full-surface analysis methods for improving overall accuracy. Work has also been undertaken which focuses on characteristic modes of error and reducing their severity through process parameter selection.

This literature review identified wall bulge as a mode of error which had not been extensively studied, and could affect larger parts, such as automotive components, more severely. A similar mode - pillowing in the base of a part - has been successfully reduced by simply changing the tool shape from hemispherical to flat-ended. This thesis will explore the effect of tool shape on wall bulge, aiming to assess whether this type of inaccuracy can also be decreased with an informed selection of SPIF tool.

Research Methodology

This Research Methodology chapter summarises the approach taken to answer the thesis research question. It also describes the methods used in the experimental chapters.

The first section in this chapter (§3.1) presents information that is foundational to the work in this thesis: the technical process of manufacturing sheet metal components with SPIF. All physical experiments will follow this procedure.

The subsequent sections in this chapter relate directly to answering the research question, reiterated below (from §1.2).

Research Question:

What are the effects and interactions of SPIF process parameters on the material formability during forming and geometric accuracy after forming?

This question can only be answered by effectively measuring both material formability and geometric accuracy so that changes due to process parameters are clear.

In §3.2, the measurement process for formability in SPIF is presented. This process is applied to the experiments in Chapter 5 and Chapter 6, which both focus on understanding formability and process parameters.

Measuring geometric accuracy of formed components is achieved by the procedure in §3.3. This is applied to the experimental campaign in Chapter 7 that aims to determine the best tool shape for minimising geometric error.

By precisely measuring the effect of SPIF process parameters using the techniques in §3.2 and §3.3, the following experimental chapters will be able to answer the research question of this thesis. Future work can draw on the resulting conclusions and maximise the chance of forming successful and accurate components with SPIF.

3.1 Single point incremental forming process

As discussed in Chapter 2, single point incremental forming (SPIF) is a method of forming sheet material which can be carried out on any 3-axis milling machine, and uses little to no custom tooling. A sheet of material is clamped around the edges, held in a raised frame. A smooth-tipped forming tool rotates at a set speed and presses into the sheet, following the outside profile of the desired part and moving downwards in small increments with each circuit.

At a basic level, any component requiring negative forming (i.e. forming in a downwards direction only) can be produced on a SPIF setup.

3.1.1 Equipment for SPIF

The milling machine used to form all components was a DMG DMU 85 monoBLOCK 5-axis CNC milling machine, shown in Figure 3.1.



Figure 3.1: CNC machine

A forming rig is used to secure the sheet material and is mounted in the CNC machine. The design of the forming rig was adapted from Russell (2008). A CAD model of the rig is given in Figure 3.2, showing an example component held in the frame by low-profile forming rig clamps. These clamps bolt into the forming rig and secure the sheet material and the backing plate during forming.

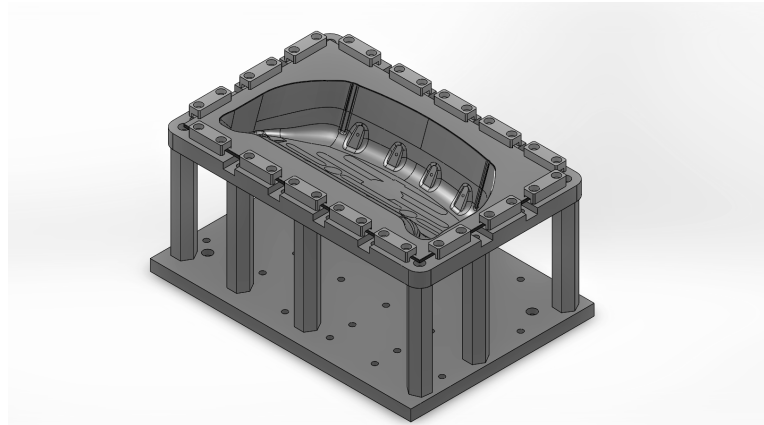


Figure 3.2: CAD model of the SPIF forming rig, showing a formed component secured in the frame.

A customised backing plate, which sits underneath the sheet material, can support the undeformed periphery of the part and improve the final outcome by reducing unwanted deformation. The customised backing plate is made from steel plate or a similar inflexible material. The experiments in this thesis used mild steel plate of 8 mm thickness for backing plates (Table 3.1). The backing plate can be clamped by itself in the forming rig and easily machined in-place to increase accuracy for the later forming operations.

Solid forming tools with various cross-sectional shapes were used consistently for the work carried out in this thesis, due to their simplicity and versatility, as described in §2.3.1.2. Ball-bearing and other types of tools were not used in these experiments.

To prevent surface damage, lubrication between the forming tool and the sheet material is required. Unless otherwise specified, the experiments in this thesis used deep-drawing oil (Table 3.1).

Table 3.1: Constant SPIF experimental parameters

Forming rig maximum dimensions		Value
Width (X-axis)		500 mm
Depth (Y-axis)		300 mm
Height (Z-axis)		250 mm
Process detail		Description
Lubrication type		Deep drawing oil Lamson Heavydraw 1290
Machine type		DMG DMU 85 CNC machine
CAD software		SolidWorks
CAM software		HyperMILL

3.1.2 Equipment setup and calibration

To prepare the equipment for forming a SPIF part, the forming rig is installed in the CNC machine and calibrated to establish the coordinate system. Its origin and axes in relation to the forming rig are shown in Figure 3.3. The origin is defined by three metal dowel pins which are mounted in the upper frame of the forming rig, and allow a rectangular backing plate and sheet material to be precisely aligned against them. The corner forms the origin point of the X- and Y-axis, with the Z-axis origin set to the top of the sheet material.

Any forming tool must also be installed in the machine and calibrated to set the length, shaft radius, and edge radius.

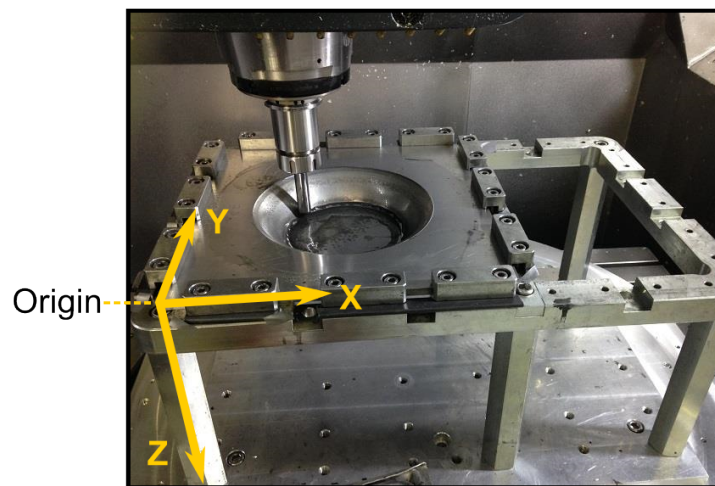


Figure 3.3: The forming rig with the location of the coordinate system's origin and axes highlighted.

3.1.3 Preparation for SPIF process

SolidWorks was used for all computer-aided design (CAD) work in this thesis, including developing the surfaces suitable for forming the selected component with SPIF. The forming surfaces were either developed from scratch or based on an existing component model.

Because a SPIF part is formed from a flat sheet of material, the CAD model for a forming surface must have all edges connected to a single plane. A connection might be established using a support wall (Jeswiet, Micari, et al., 2005) that will be removed after forming to reveal the final component. In addition, the total size of the surface could not exceed the capacity of the forming rig.

The walls of the forming surface could also not exceed 90° from horizontal while 3 axes of movement and standard forming tools were utilised. It should be noted, greater than 90° (undercut) walls are theoretically possible if additional forming axes are used on the CNC machine, or through the use of an undercutting forming tool. This type of tool is one where the forming end has a larger diameter than the shaft, and could, for example, form underneath a backing plate. However, undercut walls were not used in the components from this thesis.

The computer-aided manufacturing (CAM) system used to develop toolpaths was the program HyperMILL, embedded within SolidWorks. HyperMILL is able to export generated toolpaths in the appropriate format to run on the CNC machine. This included both machining and SPIF toolpaths.

Machining toolpaths for backing plates or other applications were programmed according to standard guidelines for the material type. The backing plate programs, for example, were based on mild steel guidelines and typically used a 12 mm endmill for cutting.

Developing the SPIF toolpath program required selection of the values for the process parameters listed in Chapter 2. These included tool shape and size, feed rate, spindle speed, step down, and material thickness, though the latter parameter is not programmed into the toolpath.

In addition, the toolpath type must be specified at this stage, selected from those standard machining toolpath types in HyperMILL that were appropriate for SPIF. The relevant options were generally a 'finishing' toolpath, including spiral, constant Z-level, and equidistant.

The Equidistant toolpath is identical to a spiral toolpath, with the requirement that the step over of the tool never exceeds a given distance. In other words, no matter the geometry of the part or the steepness of a wall, the absolute distance between one pass of the tool and the next is the same (or smaller). This toolpath has its origins in machining where it is important for the cutting tool to remove all material and leave a smooth surface. It has the same benefits in SPIF, ensuring the tool forms the entire surface of the sheet and leaves a good surface finish by eliminating individual tool marks that might stand out.

Examples of spiral and constant Z-level toolpaths are shown in Figure 3.4 (adapted from Jeswiet, Micari, et al. (2005)).

All toolpaths used the coordinate system shown in Figure 3.3, with the Z-axis origin defined by the top surface of the sheet material.

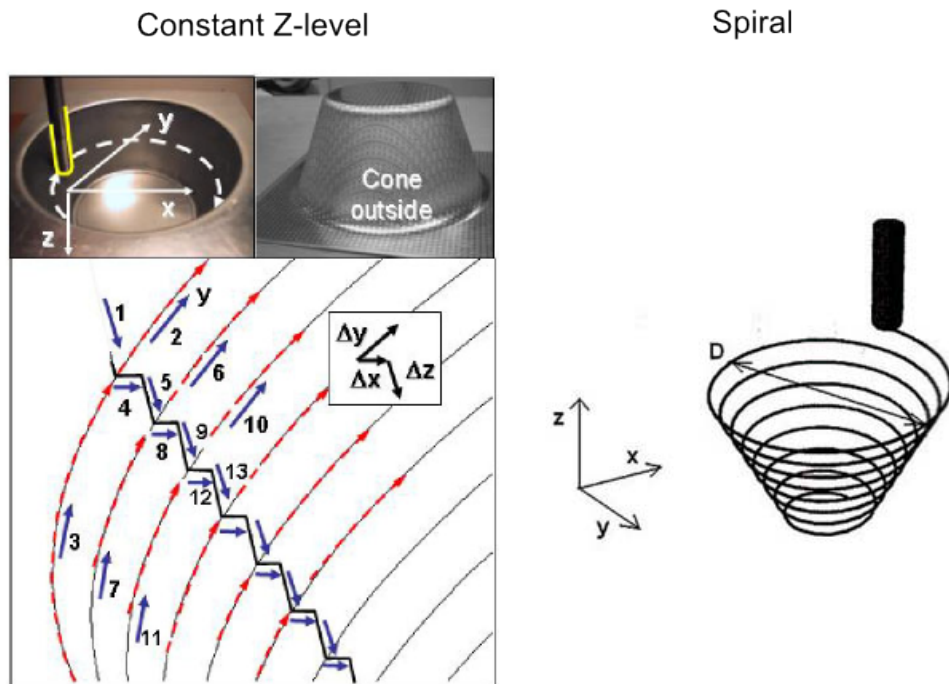


Figure 3.4: Two examples of toolpath types used in SPIF. Adapted from Jeswiet, Micari, et al. (2005) and Filice, Fratini, and Micari (2002).

3.1.4 SPIF process

When a SPIF toolpath is ready to be run, the equipment must be set up as discussed in §3.1.2. Lubrication is applied to the sheet just prior to initiating the toolpath operation, and in some cases was redistributed or reapplied during forming to maintain a constant layer between tool and sheet.

Each toolpath was initiated through the CNC machine and monitored for issues until forming was complete. If fracture occurred, whether unexpectedly or as part of formability experiments (§3.2), the program was manually stopped.

All lubrication was removed before unclamping the component from the frame.

3.1.5 Finishing operations

Finishing operations refers to any processes carried out on the sheet material after all SPIF programs have been finalised. These are designed to turn the formed sheet material blank into a finished component. Finishing operations can happen before or after the sheet is unclamped from the forming rig, and can include removing excess material, or adding details such as holes into the part. Before unclamping the part, machining toolpaths can be run on the CNC mill using small ballmills, for example.

After unclamping, operations could include cutting or welding.

3.2 Formability assessment

To determine the formability of a parameter combination in SPIF, variable wall angle conical frustum (VWACF) parts are used. These parts are an efficient and effective way to assess formability, moreso than other methods including flat-walled conical frustums, as discussed in the Literature Review, §2.3.1.

VWACFs are designed as a conical frustum with a constantly-increasing wall angle, and will fail when the material becomes too thin and fracture occurs. The shape is described in Figure 3.5 with relevant dimensions. The fracture depth, measured by a height gauge, is a reliable and comparable measure of formability.

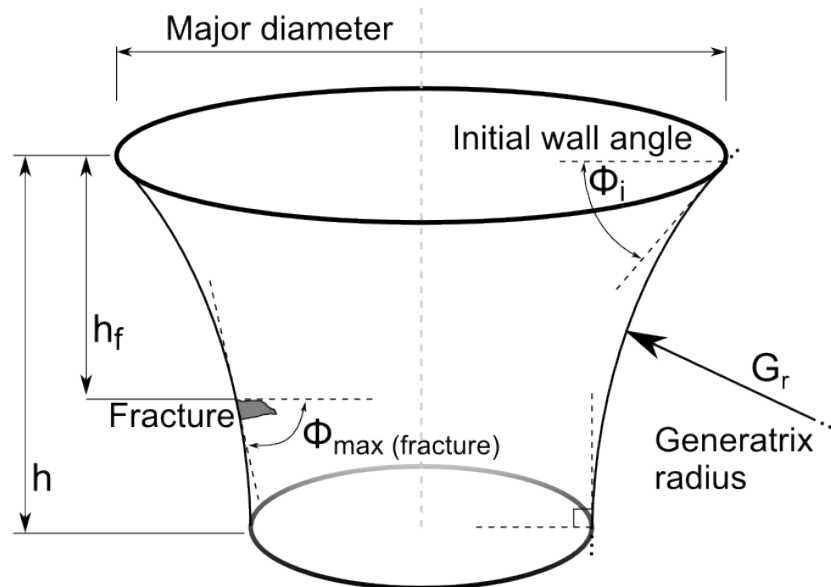


Figure 3.5: VWACF test shape with generic parameters

The simple equation to convert fracture depth to a wall angle at fracture value is shown in Equation 3.1. Fracture angle can be used as a wall angle limit in other applications.

$$\Phi_{max} = \cos^{-1} \frac{h - h_f}{G_r} \quad (3.1)$$

3.3 Geometric accuracy measurement

To determine the geometric accuracy of prototype components and other SPIF parts, a coordinate-measuring machine (CMM) was used. The CMM allowed a 3D surface model to be recorded, and compared to the original CAD models for deviation analysis over the whole part.

The CMM used to measure geometric accuracy was a FARO Laser ScanArm V3 ('Faro Arm'), consisting of a 7-axis FaroArm Platinum and a FARO Laser Line Probe. The Faro Arm is shown in Figure 3.6. The flexible arm allows a wide range of components of different sizes to be scanned for analysis.

The accuracy of the Laser Line Probe is ± 0.035 mm. The performance of the FaroArm Platinum, at its maximum extension of 1.8 m, is 0.081 mm.

The Faro Arm was calibrated to specifications outlined in the user manual before every scanning activity (FARO Technologies, 2010). The calibration procedure, data collection, and data analysis was conducted through the Geomagic Qualify 2012 software package Geomagic (2013). Various types of deviation data could be exported for publishing or further analysis.

3.4 Chapter summary

This chapter has presented the methodology which will be utilised in this thesis to answer the research question. Each component formed with SPIF for this research will be run using the procedure described in §3.1. Consistent equipment and some constant process parameters are specified.

The aims of this thesis involve assessing the formability and geometric accuracy effects of some SPIF process parameters. §3.2 and §3.3, respectively, lay out the methods which will be used to test formed components and allow comparisons between the process parameters.



Figure 3.6: FARO Laser ScanArm V3 used to scan the surface of components for geometric accuracy analysis (FARO Technologies, 2012).

Case studies in prototyping parts using SPIF

This chapter uses case studies of prototype components manufactured with single point incremental forming to investigate the challenges likely to be faced by industry when applying this method.

A review of SPIF case studies in the literature has been presented in Chapter 2. The review showed that researchers have used SPIF to form a number of prototype components, custom components, or representative geometries. The two main application areas for these parts were automotive and medical. The automotive industry in particular sees a wide range of examples of curved sheet metal surfaces which are potentially feasible to form with SPIF.

Furthermore, in the literature review the issues of geometric accuracy and formability were apparent, with components failing due to fracture or unacceptable geometric error. Useful insights can be gained from these case studies, particularly the examples of automotive components. However, specific sectors of the automotive industry may have characteristic component geometries which present unique challenges.

The two case studies in this chapter aim to understand any unique challenges which might be faced when forming components from the industry sponsor of this research. Futuris is a company in the automotive industry specialising in the design and manufacture of interior automotive components, such as seats and interior trim for cars, buses and other vehicles. Futuris develops components from start to finish, following the cycle shown in Chapter 1, Figure 1.1.

Focusing on the prototyping phase of the product development cycle, the components described in this chapter are prototypes of car seat components. These parts are mass-produced by Futuris and for this investigation are formed using SPIF. The forming process is set out in Chapter 3, Research Methodology.

The production steps, outcomes and observations are discussed for each of the two case studies. Connections are then drawn to the two key challenges of SPIF

mentioned, formability and geometric accuracy.

4.1 Case study: Seat base

The current and following section describe components produced for Futuris Automotive. The methodology behind the production of the components is presented with significant outcomes highlighted.

The first case study in this chapter was a proof-of-concept part formed for the industry sponsor. They wanted to determine whether it was possible to manufacture prototypes for their sheet metal components using SPIF. This component was the subject of an Honours thesis by the author (McAnulty, 2013).

The component, shown in Figure 4.1, was a part from the base of a car seat, measuring $470 * 245 \text{ mm}^2$.

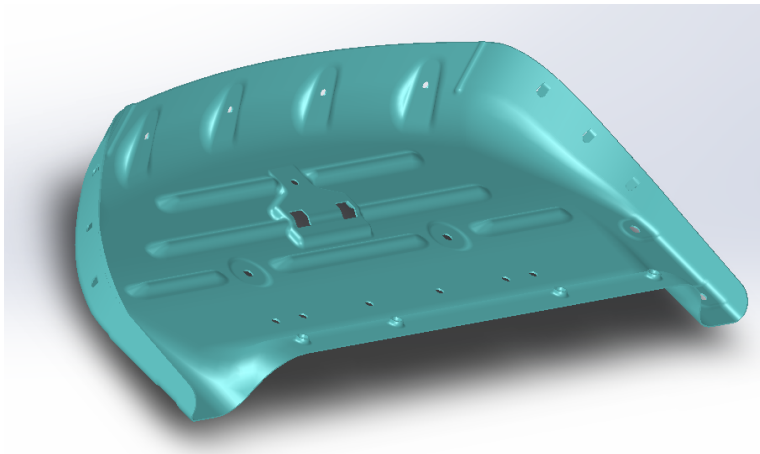


Figure 4.1: CAD model of the seat base component.

Forming the seat base with SPIF proved more of a challenge than initially expected, and it was only after three different forming approaches were tried that the part formed without fracture. The next section, §4.1.1 runs through these strategies and the reasoning behind them, followed by an analysis of the outcomes in §4.1.2.

4.1.1 Forming strategies

To prepare the CAD model for forming with SPIF, it was necessary to remove the features and details that would be impossible to form. These included the ridges and the hole flanges, which were flattened. Holes were also patched to make the de-featured surface shown in Figure 4.2.

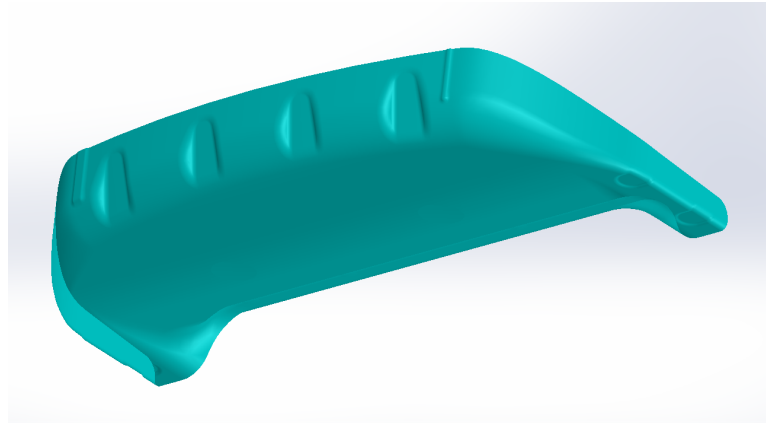


Figure 4.2: CAD model of the seat base SPIF surface, with holes and some features removed from the original to make it suitable for forming.

The approach for orienting the part within the forming space focused on the central back wall, ensuring its wall angle was within safe formability limits. For the AA6061-T0 used in these initial tests, the largest safe wall angle was 70° from the horizontal sheet plane (Nagy-Sochacki, 2009). With the orientation of the part set to 70° for the central back wall, the edges had to be extended up to the sheet plane to create a surface that can be formed from a flat sheet. The resulting forming surface is shown in Figure 4.3.

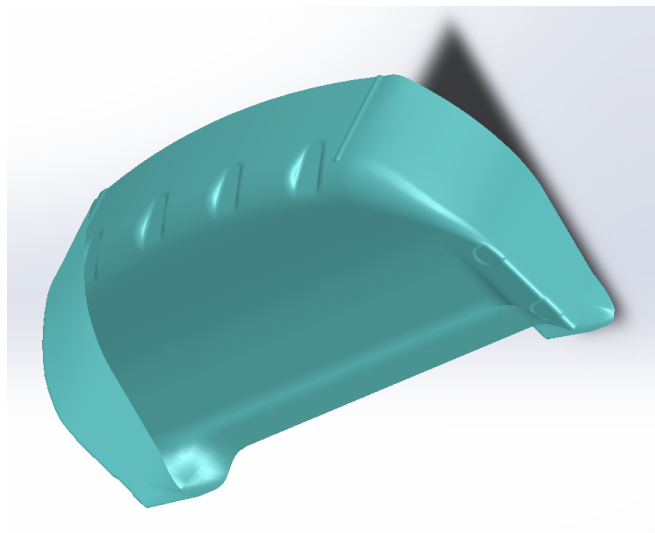


Figure 4.3: CAD model of the forming surface for the initial seat base test.

A backing plate was used to support the flange of the part, and a 12 mm hemispherical tool incrementally formed the part shape, but failure occurred at a depth of only a few centimetres. The sides of the part experienced tearing, where the walls

remained at an angle of close to 90°. Figure 4.4 shows an example of this tearing.



Figure 4.4: Tearing of the walls of the seat base when using single pass forming

To overcome the high wall angles at the sides of the part, an approach from Young and Jeswiet (2004) was used called multiple pass ('multi-pass') SPIF. One or more interim shapes are formed into the sheet before the final geometry is formed as usual. Interim shapes allow the material to progressively deform to a steeper wall angle, up to 90°, where it would be impossible to form in one go. The tool is always moving from the top of the sheet towards the bottom of the part, following the forming surface.

The first version of an interim shape model for the seat base component is shown in Figure 4.5. This surface was created by designing a virtual wireframe within the CAD model, reducing the depth of the part and the maximum wall angles to ensure the interim pass would be successful. Key metrics of the first interim pass surface are presented in Figure 4.6. This model formed to completion, but the final pass once again had tears along both sides of the part as a result of fold-over failure, which is an issue that had been noted in Young and Jeswiet (2004). This type of error seemed to be caused by too large a distance between the first interim pass surface and the final shape surface. The result was a lack of material flow leading to the type of fold and failure shown in Figure 4.7.

Even a second interim pass surface was not sufficient to avoid fold-over failure when forming the final pass. This second interim pass surface was structured between the first and final passes to reduce the forming distance even further, and did form to completion. The surface and its key dimensions are also shown in Figure 4.6. However, fractures occurred on the final pass at the locations shown in Figure 4.7.

The strategy of multiple passes used in this instance was unable to produce a successful component due to the persistent occurrence of fold-over failure when forming from the top to the bottom of the part.

To form the part geometry and overcome the previous issues, a revised approach

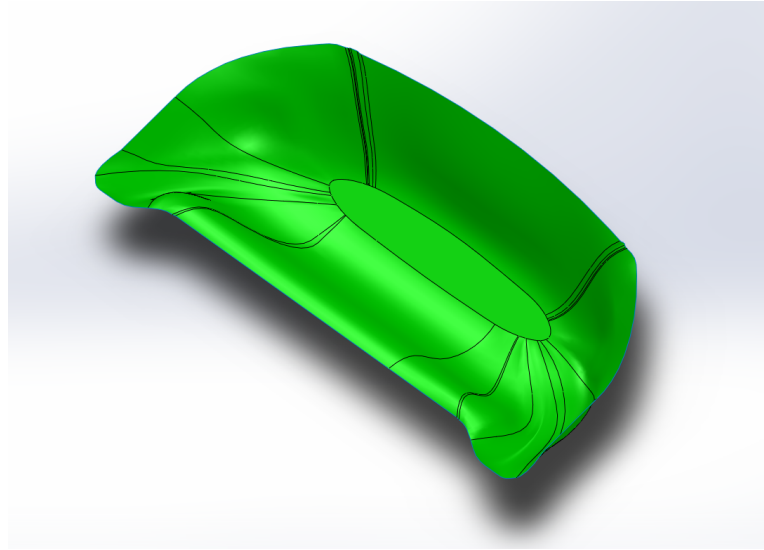


Figure 4.5: CAD model of the interim pass for the first attempt at forming the seat base.

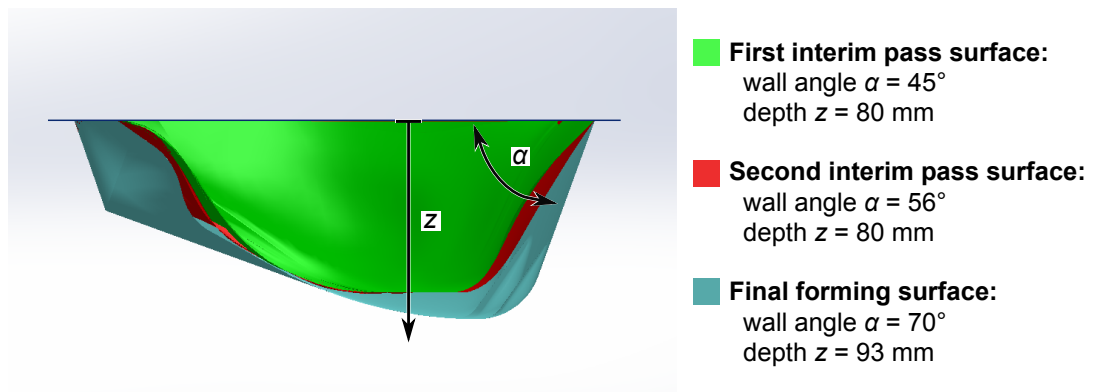


Figure 4.6: Cross sectional CAD model of the interim and final passes for the seat base, showing key dimensions.

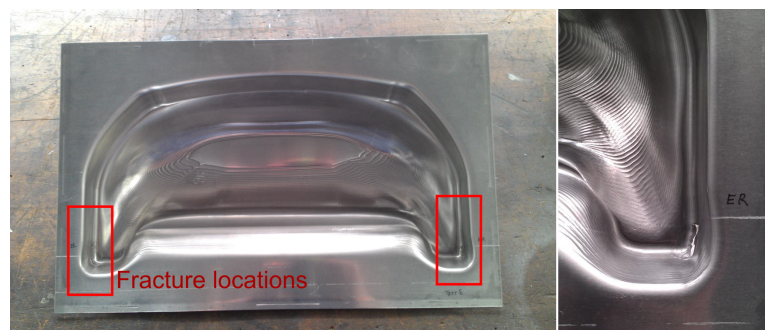


Figure 4.7: Left: Photograph of the component after two successful interim passes and 30% of the final pass, with fractures highlighted in red. Right: A close up of the fold-over failure.

was used based on the work of Skjoedt et al. (2008) and Adams and Jeswiet (2014a).

Skjoedt et al. (2008) successfully formed a vertical-walled (90°) cup by changing the overall forming direction of the tool from top-down to bottom-up for some of the passes in their multi-pass SPIF process. They noted an important difference in the contact conditions between the tool and the sheet for these two multi-pass methods. In top-down forming, only the tip of the tool contacts the sheet, while bottom-up forming can often result in the shaft of the tool, in addition to the end, contacting and therefore forming the sheet.

It should be reiterated that it is necessary for the first pass to be formed from the top of the sheet downwards.

In a paper by Adams and Jeswiet (2014a), the authors suggest identifying problem areas for targeted multi-pass SPIF, for example walls which are above the safe maximum wall angle. These areas could be re-formed using top-down or bottom-up multi-pass SPIF.

The revised strategy for the seat base component focused on preventing two issues: fold-over failure and geometric error in part depth. The strategy involved designing interim forming surfaces over the areas with the highest wall angles, such as the highlighted sections in Figure 4.7 that previously failed. These areas were too steep to form in a single pass, so five interim forming surfaces were designed with 3 mm gaps between each, starting from the final forming surface.

The strategy also made use of the bottom-up multi-pass forming technique, meaning that the first interim surface was formed from the top down, but the remaining five forming surfaces were formed from the bottom up. This prevents fold-over failure (only seen with multi-pass top-down forming) and undesirable increases in part depth that occurred in Skjoedt et al. (2008).

This strategy was more successful than the previous iteration, as the part was formed to completion. However, small cracks were produced in the areas with the steepest wall angles, meaning more work was required.

Clear problems were identified in the first two iterations of the seat base, and therefore some lessons on how to approach future parts. Firstly, it is not necessary for support walls to be a direct extension of the component. Secondly, the maximum forming area within the frame should be utilised to ensure the support walls are designed within safe formability limits. Finally, minimising the depth of the part might reduce the total deformation required and therefore the likelihood of failure due to thinning.

Insight was also gained from the literature, where Araujo et al. (2014) found that re-designing, or re-positioning, the SPIF surface made it possible to form a part which had previously exhibited fracture during forming.

Starting with the defeatured seat base surface (Figure 4.2) and applying this new knowledge, a new forming surface was designed and is shown in Figure 4.8. The depth (Z-dimension) was able to be reduced from 100 mm to 60 mm compared to the first component (Figure 4.3). While the angles on the side and back walls of the actual component are above the safe forming limit, the maximum depth of the part was reduced. This effectively reduced the distance that the sheet material had to move, and decreased the amount of thinning in the sheet. By maximising the sheet thickness in this way, the likelihood of fracture was reduced. In the X-dimension, the width of the forming surface (excluding backing plate) was increased from 470 mm in the first seat base attempt to 505 mm in this third attempt. The length (Y-dimension) increased from 245 mm to 285 mm. The support walls were also, where possible, maintained at angles around 55° , well within safe limits.

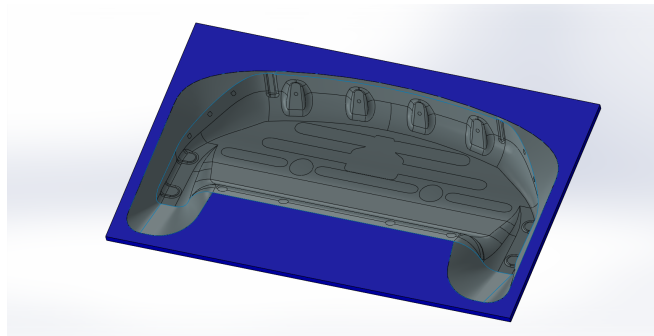


Figure 4.8: CAD model of the forming surface for the third seat base attempt. The backing plate is in blue.

A draft angle analysis was used to identify where the interim pass surfaces for multi-pass forming should be designed. In this respect, a draft angle of 75° was chosen based on the rough upper forming limit of aluminium alloy sheet specified in Jeswiet, Micari, et al. (2005) (78° maximum). The analysis result, shown in Figure 4.9, highlights in yellow the areas that are above 75° to guide the creation of the interim pass surfaces.

When designing the interim pass surfaces, the first pass, shown in Figure 4.10, aimed to form as much of the component as possible with wall angles under 60° . This surface (shown in red in the figure) covered the steep areas identified from the draft angle analysis in Figure 4.9. Subsequently, interim passes were added in approximately 3.5 mm intervals to reach the final shape, resulting in a total of 4 interim passes which are highlighted in a cross-section in Figure 4.11.

The first pass used top-down multi-pass forming, and the remaining passes were formed from the bottom up. This forming strategy was ultimately successful, with every pass forming to completion and no fractures occurring in the final part

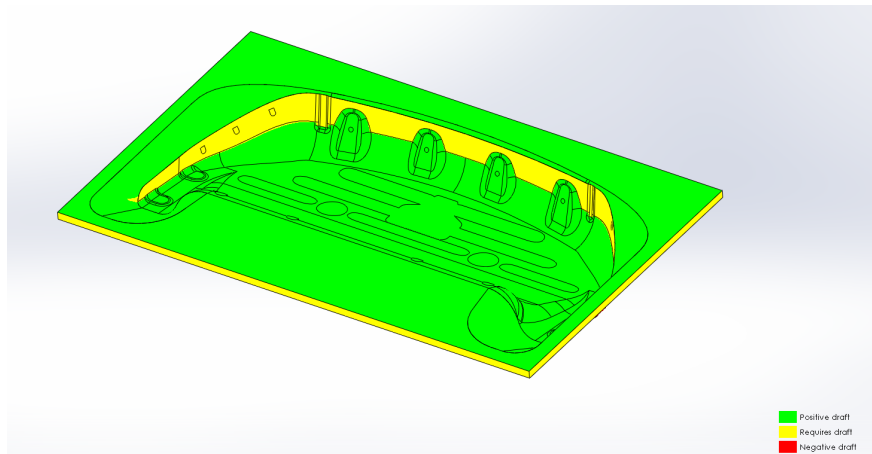


Figure 4.9: CAD model of the forming surface for the third seat base attempt, including the backing plate model. The draft angle analysis highlights in yellow the areas that are greater than 75° from the horizontal plane.

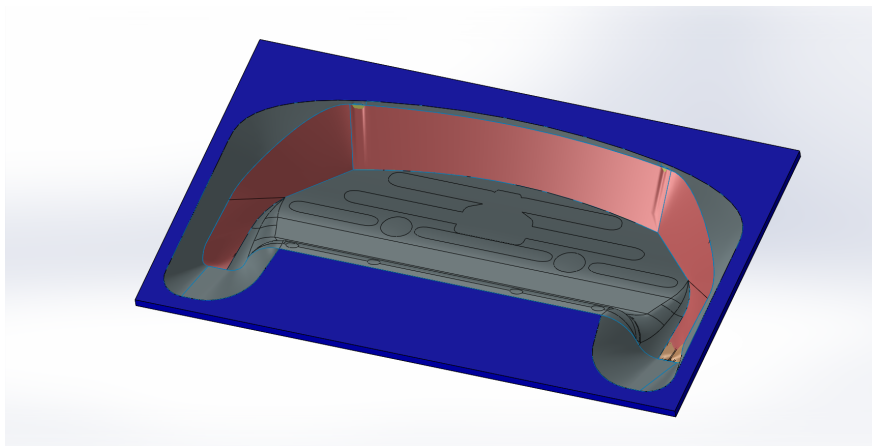


Figure 4.10: CAD model of the seat base highlighting the additions in red that became part of the forming surface for the first pass, where the part was formed from the top down.

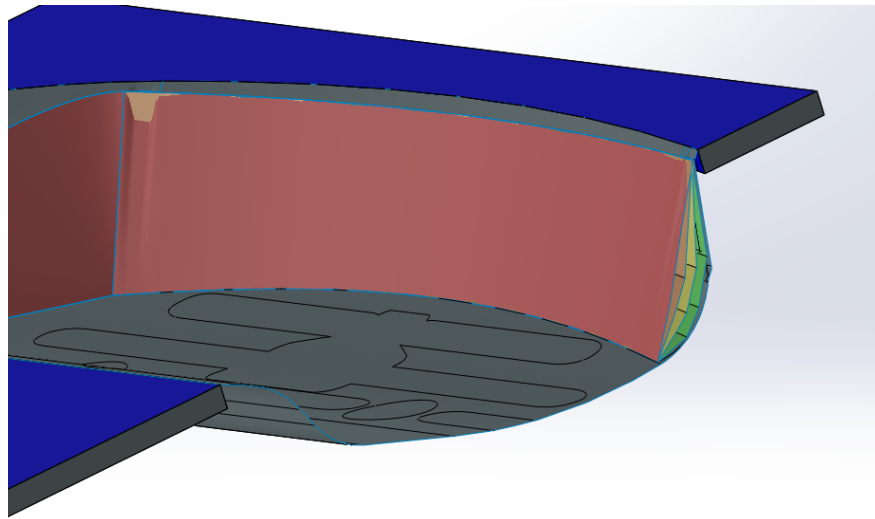


Figure 4.11: Cross section of the CAD model showing the four interim passes used to progressively form the final geometry for the third attempt at the seat base. All but the red surface were formed with bottom-up multi-pass forming.

(Figure 4.12). Appendix A details the values of the process parameters for this case study.

4.1.2 Observations

The cracks in the corners of the second iteration component were likely to be a result of biaxial stretching, such as is seen in the components in Bagudanch, Garcia-Romeu, et al. (2015). Plane strain is seen in flat surfaces formed by SPIF, but biaxial strain generated in edges and corners can increase the thickness strain and subsequently the likelihood of failure due to excessive thinning. Single and multi-pass toolpaths should be designed to ensure the material in corner features does not undergo thinning to the point of failure.

A major change which directly contributed to the success of the final part was improving the orientation of the model within the forming space. Part orientation was noted as an important consideration in Jeswiet, Micari, et al. (2005), and must be carefully evaluated for any component formed with SPIF. The resulting wall angles of the part surface in a particular orientation should be taken into account, as well as facilitating support walls with optimal design to support the forming process.

A particular type of error seen in the first iteration was wrinkling in a convex section of the geometry, shown in the photograph in Figure 4.13. The wrinkle was perpendicular to the toolpath direction and was attributed to undesirable flexing of



Figure 4.12: Photograph of the third attempt of the seat base component, successfully formed without cracks using bottom-up multi-pass SPIF

the entire part, rather than localised deformation only under the tool. The whole convex section was seen to flex each time the tool moved over the area. This shows the importance of stiffness in a part design, to support plastic forming rather than only elastic springback.

The second major change to the forming surface in the third iteration involved the support walls. Primarily, it was seen as important to ensure that the wall angles were in a mid range ($40^\circ - 60^\circ$) so they would form effectively and therefore be stiff enough to support forming the remainder of the part. The reasoning is as follows:

- Ensure the wall angles are well below the forming limit to eliminate any chance of failure by thinning.
- Ensure the wall angles are not too low, to minimise springback and encourage plastic deformation.
- Evaluate the trade off between wall angle and final thickness, because a lower wall angle means a greater final thickness, and a stronger support wall.

When designing the toolpaths, it was necessary to use a constant Z-level type for the first pass, as the tool must form the material at an even rate. However, bottom-up multi-pass toolpaths do not have this restriction, so an Equidistant Finishing type was selected. Equidistant Finishing generates a toolpath where each loop of the tool is a constant distance (equidistant) to the previous loop, resulting in a superior surface finish compared to Z-level. This also means the tool does not necessarily maintain a



Figure 4.13: Detail of wrinkling resulting from the multi-pass forming of the first attempt for the seat base component.

consistent increase or decrease in depth, leading to toolpath features such as the peak shown in Figure 4.14.

An interesting material flow pattern was observed in the completed part as a consequence of the multiple bottom-up re-forming passes. A lip developed around the part at the transition between the original model and the support walls, shown in the photograph in Figure 4.15. The previously discussed toolpath shape (from Figure 4.14) may have also exacerbated the situation.

In any case, the lip of material did not prohibit the usefulness of the component.

4.1.2.1 Geometric accuracy

For this case study, access was provided to a stamped version of the original component shown in Figure 4.1. To determine a benchmark level of geometric accuracy, or a maximum allowable deviation, the stamped component was scanned with a Faro Arm and laser attachment. The analysis suggested a benchmark maximum deviation of 1.5 mm, as more than 95% of the scanned points were within this margin of error.

Geometric accuracy of the final part from Figure 4.12 was measured using a Faro Arm with a laser scanning attachment. The results, shown in Figure 4.16 are in the form of a colour scale on the surface with areas of positive and negative

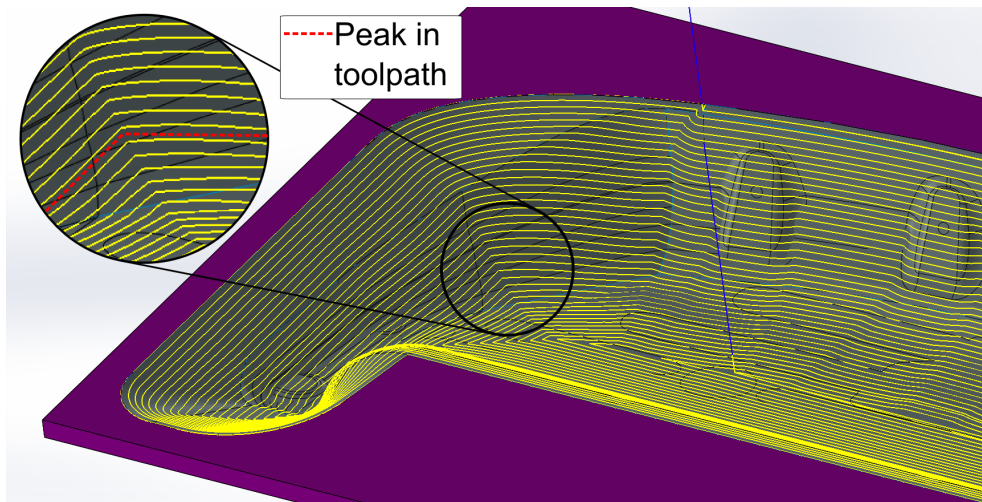


Figure 4.14: CAD model of the second-last forming pass, with overlaid toolpath in yellow showing the peak in the trajectory of the tool.

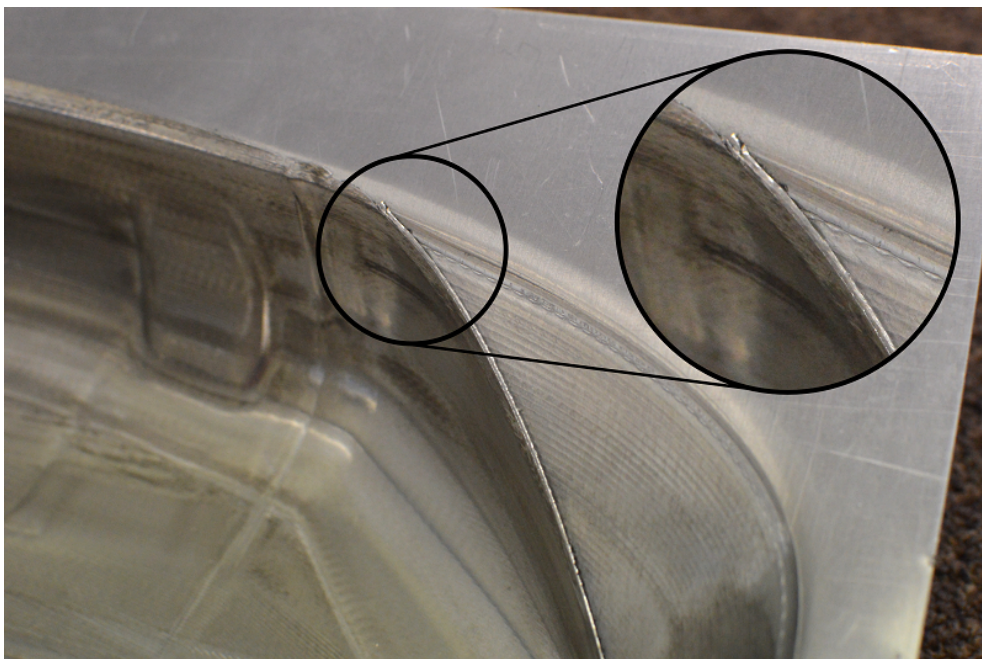


Figure 4.15: Detail of the final formed seat base component, showing the folded-over lip created as a result of the multiple bottom-up re-forming passes.

geometric error. Red indicates +5 mm error and blue represents -5 mm, with the scale distributed in between. This final component did not fulfil the benchmark error of 1.5 mm, with much of the surface showing ± 2 mm deviation.

Comparatively large deviations are seen in areas of the flange, which would have occurred after unclamping from the forming rig (Figure 4.16 (a)). This is a known issue in SPIF, mentioned in Micari, Ambrogio, and Filice (2007) and Behera, B. Lu, and Ou (2016). It indicates that there is some residual stress in the flange which may translate to inaccuracies in the component if it is cut away from the flange.

The bosses on the large central wall (Figure 4.16 (a)) are not accurately defined. Acute and obtuse edges over the part also have issues with accuracy (Figure 4.16 (b)). Furthermore, the shallow mid-section bulged downwards compared to the model, presenting a type of error to be monitored in future components.

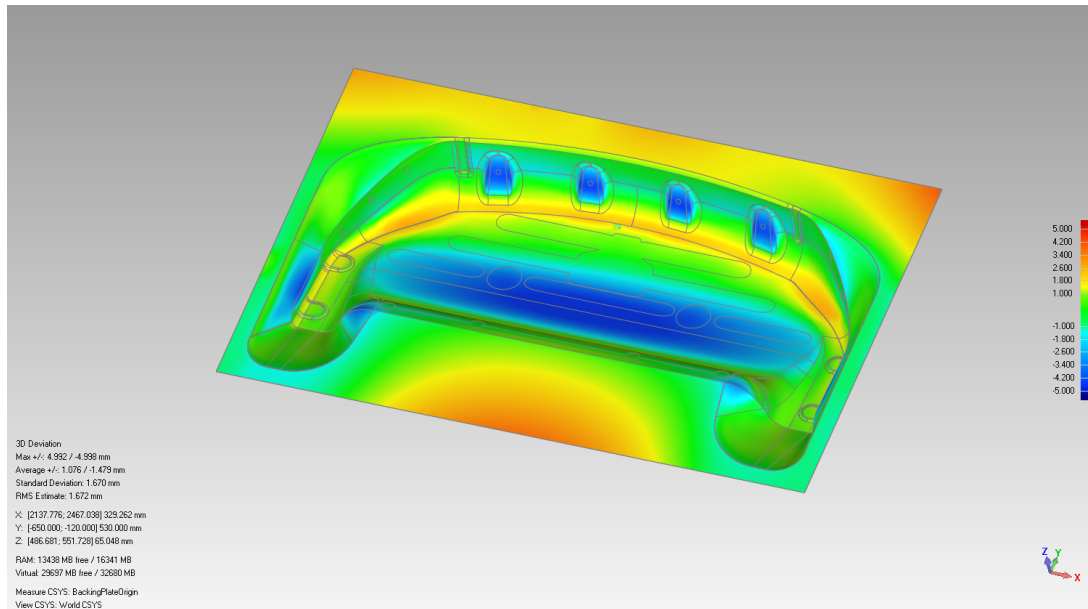
4.1.3 Conclusions

The success of this seat base component was due to a number of factors which improved the process enough to allow the challenging geometry to form without failure. These are listed below.

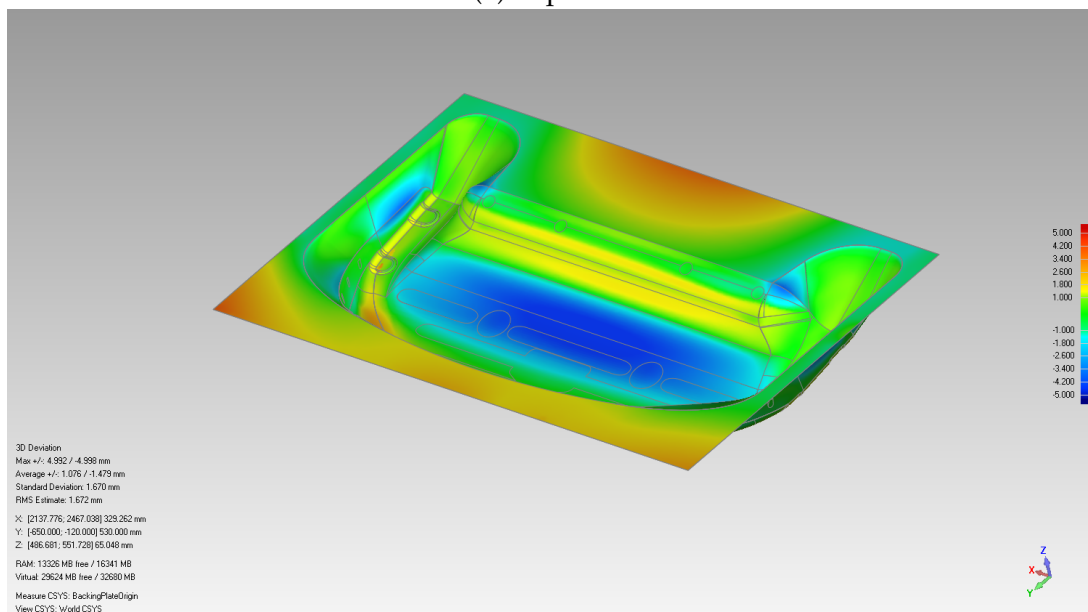
- Bottom-up multi-pass forming was a vital process improvement that eliminated fold-over failure and prevented unwanted depth increases.
- The first two iterations provided insight into the challenges of forming large SPIF components. This informed the process for the third iteration, where the part orientation within the forming space was improved.

The support walls were also re-designed to have greater stiffness through surface curvature and more ideal wall angles. As a result the support walls promoted plastic forming, rather than elastic forming, and reduced springback.

- Re-orienting the part presented a trade-off between reducing the wall angle of the back section, or reducing the total depth. In this case success was due to minimising the depth and using multi-pass SPIF to form the 90° walls.
- The corners of a SPIF surface require special consideration in toolpath design - whether that is single or multi-pass toolpaths. The biaxial strain that occurs in corners increases the thickness strain and likelihood of failure, and the toolpath design must ensure that there is appropriate material flow to avoid the excessive thinning which leads to fracture.



(a) Top view



(b) Back view

Figure 4.16: Laser scanning results of the third iteration of the SPIF seat base, shown as a colour scale of positive (red) and negative (blue) deviations compared to the CAD model in the figure.

4.2 Case study: Cushion pan

A prototype cushion pan for a car seat is the second case study in this chapter, made for use by the industry sponsor. The component measured 470 mm * 230 mm, and is shown in Figure 4.17.

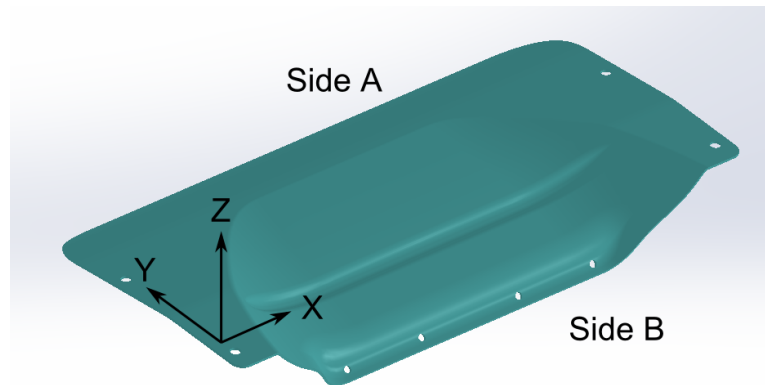


Figure 4.17: CAD model of the original cushion pan component.

4.2.1 Forming strategies

The original component required the addition of support walls to create a surface which could be incrementally formed from a sheet of material. There was some flexibility in how the cushion pan was oriented in the forming space, and this could be adjusted to change the upper dimensions and the wall angles over the surface of the part.

If any wall sections of the component were too steep, multi-pass forming would be required, adding further complexity to the process. To prevent the need for multi-pass forming, the cushion pan was oriented to reduce the wall angle of a section along Side B (as per Figure 4.17).

The final SPIF surface was also required to fit within the dimensional constraints of the forming rig, noting that the original part length was already close to the X-axis size limit of 500 mm.

Figure 4.18 shows the forming surface, with added support walls connecting the part to the plane of the flat sheet. The axes shown in Figure 4.17 correspond to those in Figure 4.18 to demonstrate the orientation of the original part in the forming surface.

As a result of the dimensional constraints and the large part, it was necessary for the support walls to have steep wall angles. Furthermore, the specific geometry of the cushion pan component meant that the support wall on Side B was much larger

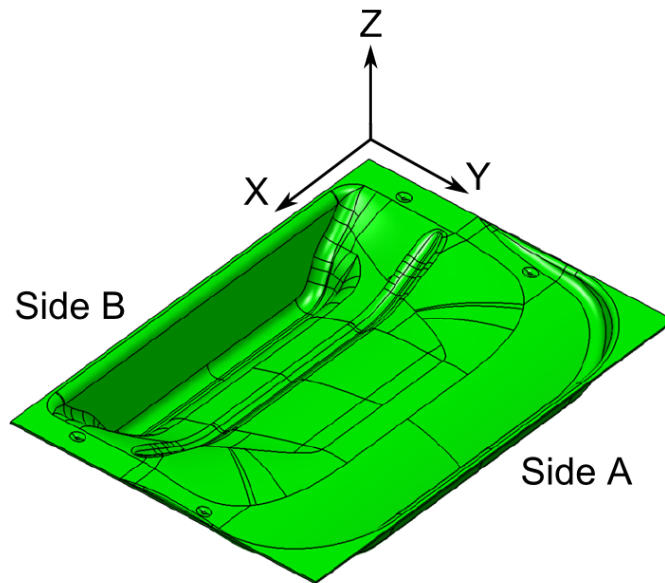


Figure 4.18: CAD model of the cushion pan forming surface prior to removal of the central groove feature.

than on Side A, and was also a perfectly flat surface. However, the support walls were not angled more than 75° from horizontal, and wall angles of 78° had been achieved in aluminium alloys in research from the literature (Jeswiet, Micari, et al., 2005). Therefore, this design was tested as an initial trial with an understanding of the risk of fracture.

A groove in the middle of the part, visible in Figure 4.18, was removed to simplify the formed component. The resulting model used to form the part is shown with the backing plate and forming rig frame in Figure 4.19.

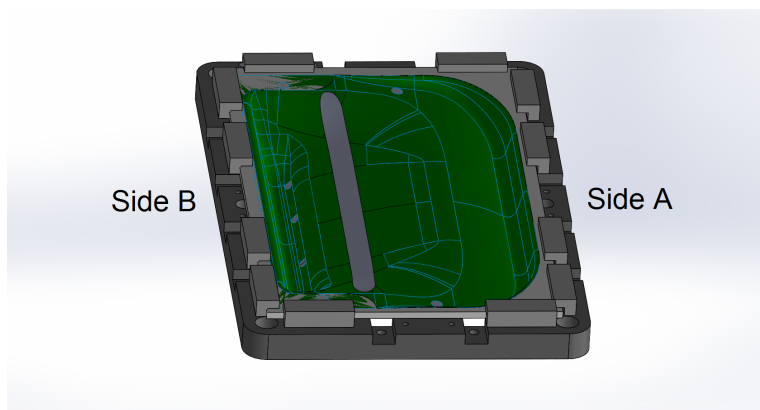


Figure 4.19: CAD model of the first design for the cushion pan SPIF surface.

The initial attempt at forming was not successful, as fractures occurred against support walls on Side A and Side B. Figure 4.20 shows a photograph of the failed part, outlining the fracture locations.

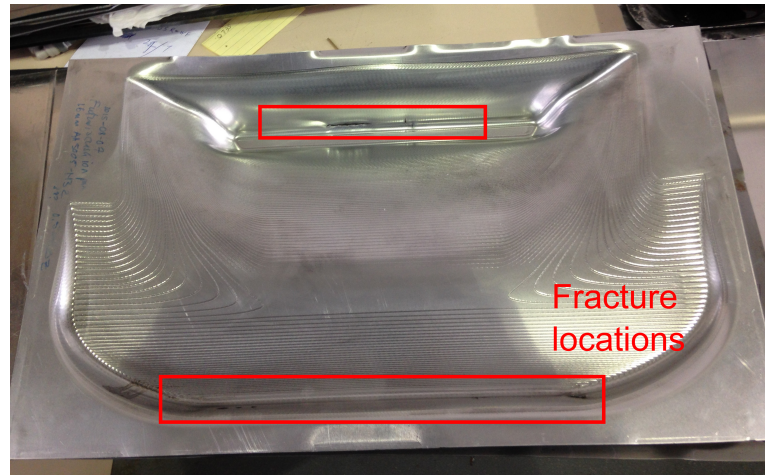


Figure 4.20: Photograph of a failed cushion pan part highlighting the fracture locations in red.

As simple next step before investing time to adjust the forming surface, the forming tool was changed from a hemispherical to a flat-ended tool. Research has indicated that flat-ended tools can improve the formability limits (Ziran et al., 2010), which possibly could have allowed the part to form successfully. However, fracture still occurred alongside the large support wall on Side B and bulging was observed on its flat surface.

The subsequent forming strategy involved adjusting the geometry to reduce the maximum wall angle of the support walls (highlighted in Figure 4.20 where fractures occurred) to less than 70° . Additionally, minor adjustments were made to the model to change the surfaces directly adjacent to the backing plate. Previously, some edges next to the backing plate had a convex radius, such as can be seen on Side B in Figure 4.18. These were all changed to a sharp edge for the subsequent forming surface, shown in Figure 4.21. Side B in this figure, for example, no longer has a convex radius. This change was intended to increase the stiffness of the geometry due to better support from the backing plate - promoting plastic rather than elastic bending deformation.

These two improvements in the SPIF surface - reducing the maximum wall angle and improving wall stiffness - were effective. The component formed successfully from the adjusted model, and a photograph of the cushion pan is shown in Figure 4.22.

Details of process parameters used in this case study are summarised in Appendix A.

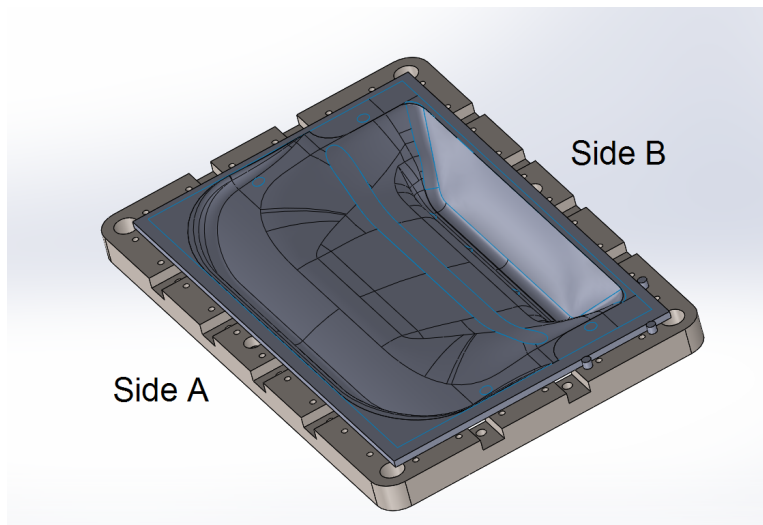


Figure 4.21: CAD model of the final design of the cushion pan which successfully formed with SPIF.



Figure 4.22: The cushion pan component, successfully formed with SPIF.

4.2.2 Observations

Fracture occurred at the large flat support wall on Side B (see Figure 4.18), and this flat surface exhibited inwards bulging. The final version of the cushion pan, despite forming completely without fracture, still showed a bulge in the flat Side B support wall.

Geometric accuracy of the final part, including the surface bulge, was quantified using the laser scanning attachment on the Faro Arm and the 3D compare function in Geomagic Qualify. Full details of this process are described in Chapter 3.

The deviation results generated from Geomagic Qualify are shown in Figure 4.23. The bulge was quite severe and caused a maximum deviation of 7 mm error compared to the CAD model.

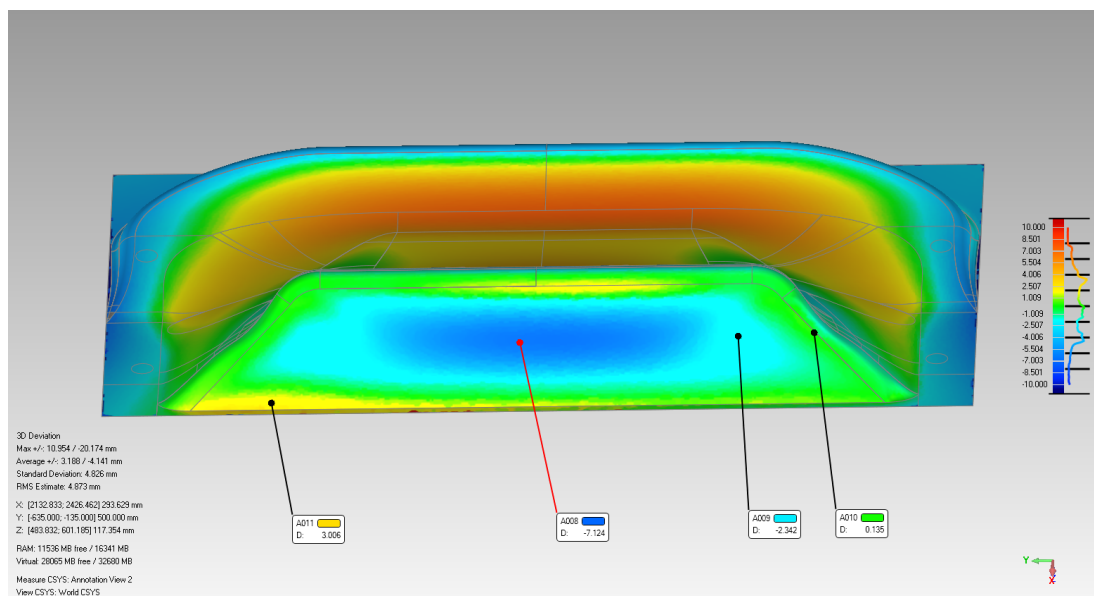


Figure 4.23: View of the large support wall (Side B) where inwards bulging (negative error) occurred.

Wall bulge in this section of the part could have caused the unexpected fracture as a result of increasing the apparent wall angle compared to the intended model. Figure 4.24 explains this concept, where severe bulging increases Φ and consequently the thickness strain. The material is formed further than the formability limit and consequently fails.

While in this case study the severe bulge was observed in a support wall for the cushion pan component, the observation in Figure 4.24 may be relevant for other SPIF parts with large straight walls.

Furthermore, the thin, channel-like geometry Side B was interesting as the walls

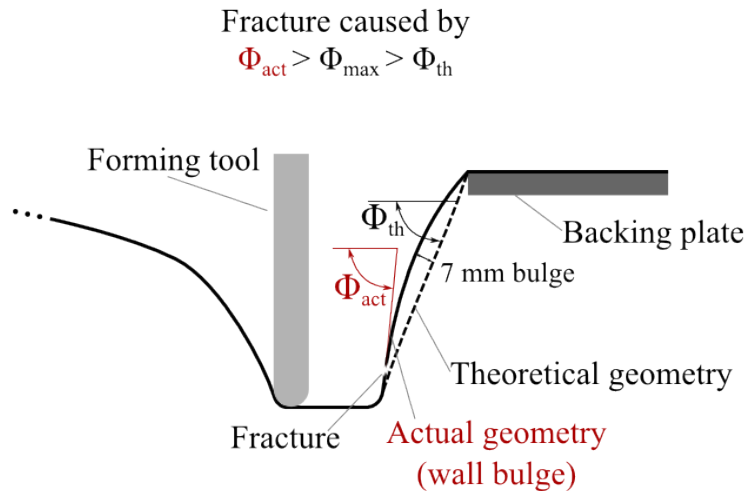


Figure 4.24: Bulging in the wall of the cushion pan as a proposed cause of unexpected fracture during forming.

on either side were forming very close to one another. This may have affected how much undeformed material was available for forming, and increased the likelihood of fracture due to thinning. In contrast, a standard truncated cone has a large base area where the tool is forming.

Another view of the Geomagic results can be seen in Figure 4.25 where the shallow central surface flexed downwards, away from the forming tool. The most severe area of deviation here was 7 mm away from the CAD model. Error in a large area with shallow curvature was also seen in the seat base component case study.

In an ideal situation, a larger forming rig would be used to improve the success of the formed cushion pan component. With a larger forming area, the support walls could have been designed at much lower wall angles, potentially reducing the wall bulge issues observed in this case. Reducing the wall bulge may have also solved the issue of premature failure by fracture.

This component had similar characteristics to a case study from Bambach, Taleb Araghi, and Hirt (2009) where a car fender section with a double curvature was formed. In their paper, the best geometric accuracy outcomes came from a part that had been heat treated before trimming from the flange and support walls. Heat treatment was outside the scope of this case study but future work could look at how to make heat treatment more accessible to standard workshops with non-specialised heating equipment, and dealing with large components. One possible investigative angle could involve heating the clamped part with an oxy-acetylene torch.

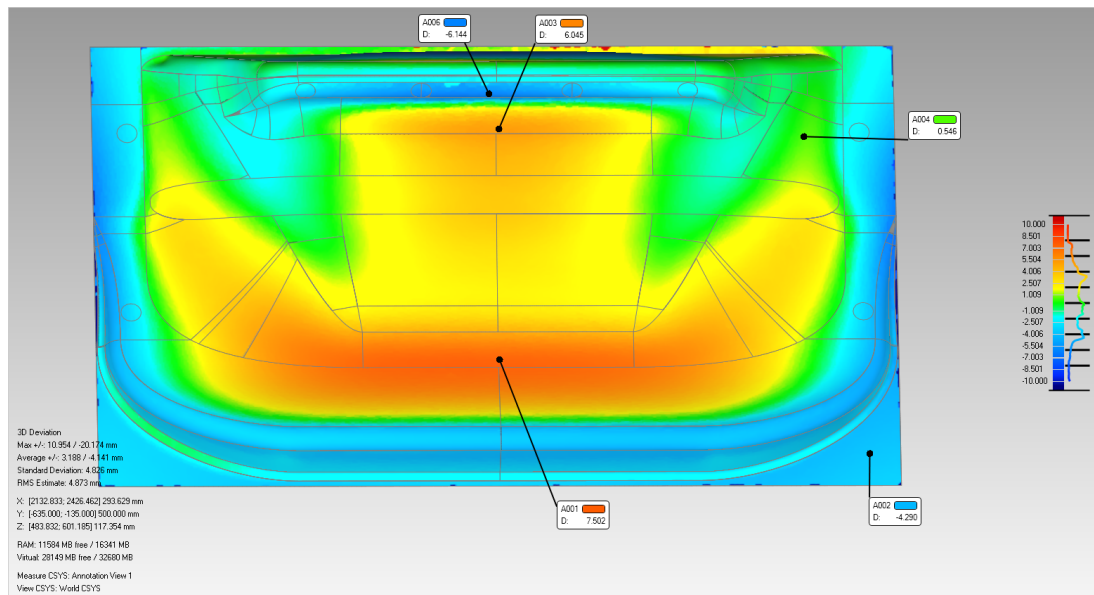


Figure 4.25: Top view of geometric accuracy results after laser scanning and comparison with the CAD model. Note the inaccuracy in the large shallow area.

4.2.3 Conclusions

- Wall bulge was observed in the flat wall on Side B (Figure 4.18). It is proposed that this inwards bulging contributed to the unexpected fracture by increasing the apparent wall angle, explained by the diagram in Figure 4.24.

Any SPIF component with a similar geometry section (large, flat, high wall angle) would likely be at risk of the same premature failure due to bulging error.

- Reducing the severity of, and ideally eliminating, the wall bulge in this and other components would be beneficial. For the cushion pan prototype, it may have removed the need to adjust the forming surface CAD model in order to achieve a successful part. In any SPIF component, reducing bulging error would bring the geometric accuracy closer to the required benchmark, as discussed in §4.1.2.1.
- Further work includes finding effective methods to reduce or remove bulging in the walls of SPIF parts. Chapter 7 presents original research on wall bulge as a characteristic SPIF error type, and how it might be improved.
- Another area of inaccuracy was a large shallow area shown in Figure 4.25. The forming mechanism in this area is possibly dominated by elastic or bending deformation due to low stiffness, rather than desirable plastic deformation.

Elastic deformation results in springback and higher geometric error, and is therefore undesirable in SPIF.

4.3 Chapter summary

This chapter presents two case studies of forming prototype components with single point incremental forming, based on parts from the Futuris, the industry sponsor of this research. These case studies have provided specific context for the challenges that may be encountered during industrial production of sheet metal prototypes with SPIF. The research follows on from the general insights seen in the literature review in Chapter 2, §2.2. The context developed in this chapter informs the work of the experimental investigations in this thesis, which aim to overcome issues from formability and geometric accuracy.

Both formability and geometric accuracy have been shown in this chapter to be concerns for failure in SPIF components. Fracture can occur in the sheet material when the formability limit is exceeded, or the geometric accuracy of the formed part is outside Futuris' requirements.

Neither of the case study components fell within the benchmark requirements for geometric accuracy, based on a comparison between the final formed part and the designed model. This is consistent with findings from the literature review. A particular type of geometric error was observed in the cushion pan component, where a flat wall exhibited 7 mm peak springback error due to an inwards bulge.

The process of manufacturing the prototypes also revealed general insights. These include points on developing an optimal forming surface, and avoiding failure in particular situations, as outlined below.

During the initial development of a forming surface, two things are important to consider. Firstly, the orientation of the unedited component shape within the forming space can have a large effect on the success of the part, as seen in the seat base case study in §4.1. Secondly, the design of any required support walls will influence the outcome and should be structured to maximise their stiffness and provide support to the original part geometry.

Corner features in SPIF parts require special consideration as they experience biaxial strain to a larger degree than a straight or slightly-curved wall feature. Biaxial strain will cause the thickness strain to increase which consequently increases the likelihood of fracture and failure of the component.

Bottom-up multi-pass forming was used to successfully form a part which had failed with the approaches of single-pass and top-down multi-pass SPIF. Where a high wall angle cannot be avoided by careful part orientation, bottom-up multi-pass

forming is a useful, though complex, forming technique.

As discussed in the literature review in Chapter 2, process parameters affect both the material formability and the geometric accuracy of a component. Understanding their specific effects in order to select the optimal process parameters may provide a straightforward solution to eliminate the modes of failure which are caused by these two aspects. The following experimental chapters in this thesis aim to accomplish this goal.

The thickness distribution of VWACF parts

When developing forming surfaces for components that will be manufactured with SPIF, the maximum wall angle to which a material can be formed (Φ_{\max}) is a helpful limit during the design process. Materials such as steel, aluminium, titanium or polymer sheets can have various levels of Φ_{\max} .

For the case study prototypes manufactured for this work, aluminium alloy sheet was used. An understanding of the value of Φ_{\max} for this material can be gained by looking at the academic literature, for example the formability research papers that were analysed in Chapter 2. From this data, the highest wall angle formed for aluminium alloy, Φ_{\max} , was 83° (Al-Ghamdi and Hussain, 2014). Therefore, the fracture of the cushion pan prototype in a section with a designed wall angle of only 75° was unexpected.

To minimise the likelihood of failure for SPIF prototypes and other components, a safer wall angle limit is worth considering. Unfortunately, neither of the two main methods of determining Φ_{\max} result in a 'safe' wall angle. These methods do not incorporate any margin of allowable error to the fracture point to account for variation in formability through part geometry or other factors.

The first method, using straight-walled conical frustums, involves forming parts with increasing wall angles until one part fails (Ham and Jeswiet, 2006). The value of Φ_{\max} is specified as the largest wall angle that formed without failure, and is arbitrarily close to the wall angle at which fracture occurs.

The second main method is variable wall angle conical frustum (VWACF) tests, which measure the wall angle at fracture (Hussain, Gao, and Dar, 2007). While this formability assessment test is efficient, the VWACF and the straight-walled cone method do not allow for a margin of safety which would assist a designed to prepare a SPIF forming surface. In addition, forming close to the fracture point may result in weaknesses within the material due to excessive thinning.

Developing a surface which is unlikely to fracture due to unsafe wall angles means that the part is more likely to form on the first attempt. This eliminates the need for subsequent iterations that delay the product development timeline.

Hussain and Gao (2007) proposed a safe wall angle limit which is based off the strain within the material after forming. Rather than using a binary fracture/no fracture result, this marker may allow a designer to avoid causing weaknesses in the material which would increase the likelihood of fracture.

This chapter aims to understand the Hussain and Gao (2007) safe wall angle limit such that it can be used for general SPIF applications, reducing the occurrence of fracture and increasing the feasibility of SPIF in industrial contexts.

5.1 Background

Hussain and Gao (2007) proposed a marker for safe forming limit that they called the intersection point. The marker was found by forming an aluminium VWACF part to the point of fracture and measuring the thickness along a cross-section of the cone. The measured thickness was plotted against the sine law prediction with good agreement between the two except where the part was bending around the backing plate, and in a short section just before fracture. Close to the fracture point the material seemed to undergo excessive thinning before it eventually failed. Figure 5.1 outlines the above process, showing the VWACF with depth markers and how results are plotted to determine the intersection point.

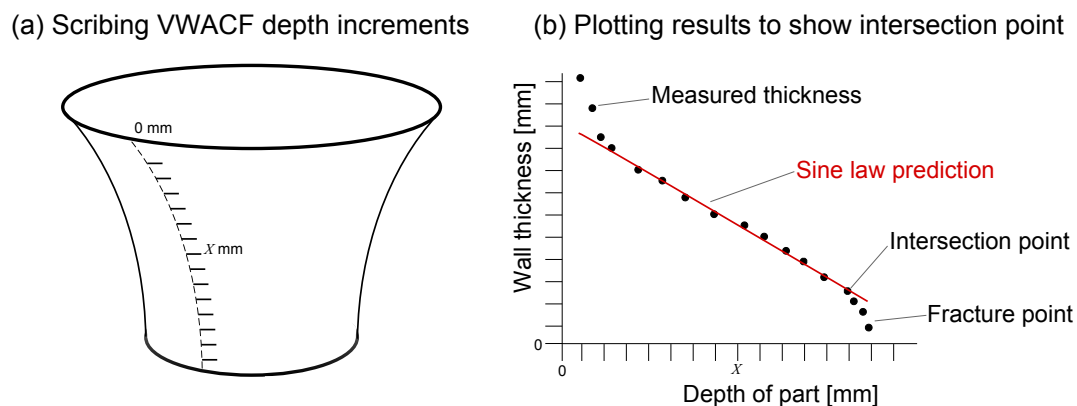


Figure 5.1: Explanation of the intersection point and how it is determined from the measured thickness of a VWACF part. (b) adapted from Figure 8, Hussain and Gao (2007).

The last point of agreement between the two curves before fracture occurred was termed the intersection point (see Figure 5.1 (b)). In subsequent papers the authors

renamed this point and referred to it as the transition point (Hussain, Gao, and Dar, 2007; Hussain, Gao, Hayat, and Qijian, 2007).

Hussain and Gao (2007) proposed that the intersection point represented the thinning limit, or the maximum wall angle to which the material could safely be formed. After this point, they found instabilities (microcracks) in the material which seemed to cause the measured thickness to deviate from the sine law prediction.

The intersection point (or transition point) was used in later research as the marker for maximum safe wall angle. For example, the formability of TRIP steel in SPIF was evaluated in Jin et al. (2012) using a VWACF test part. The authors reported the forming limit for the material as the wall angle corresponding to the intersection point. Excessive thinning of the material compared to the sine law prediction was also observed close to the point of fracture.

Further research on aluminium VWACF geometries and other test parts was conducted in Hussain, Gao, and Dar (2007) and Hussain, Gao, Hayat, and Qijian (2007). In both papers, the dimensions of various test parts were altered and the effect on the formability limit was reported using the wall angle corresponding to the ‘transition point’ of each component.

The observation of the intersection point (‘transition point’) varied in papers by Hussain, Gao, and Zhang (2008) and Kurra and Regalla (2014). Using titanium and extra-deep-drawing steel sheets respectively, the measured thickness distribution did not undergo significant deviation at the fracture point when compared to the sine law thickness prediction. These results suggest that material properties have an influence on the behaviour of the thickness distribution of SPIF parts, though investigating a range of materials is outside the scope of this study.

The intersection point has been applied as a useful indicator for a formability limit, or safe maximum wall angle limit. However, the process to determine the intersection point involves forming the VWACF part, scribing depth increments from the top to the bottom, cutting out the scribed section, and measuring the thickness at the end of all of the scribed lines. Not only does the procedure have multiple steps, but each step is time consuming which results in a long overall lead time for each individual part.

Conversely, the fracture depth of a VWACF is quick to measure with a height gauge, and the corresponding wall angle can easily be calculated. Therefore, a method to predict the intersection point from the wall angle at the fracture point would save considerable time. The benefits of the intersection point could be obtained without the associated time-consuming procedure.

To achieve this aim, the experiments in this chapter will compare the wall angles for the intersection point and the fracture point for a substantial number of VWACF test parts formed from aluminium sheet. The test parts will be formed using a design

of experiments to understand the effect of some process parameters on this forming limit.

The process parameters are selected based on insights gained from the literature review. Firstly, step down and sheet thickness were shown to be parameters with significant effects on formability in SPIF. Secondly, not only is tool size also a key parameter with an influence on formability, but tool shape is an aspect that has not been extensively studied. Some research has been carried out on the formability of different tool shapes. However, tool shape has not previously been studied in conjunction with other key SPIF parameters.

Therefore, the parameters of sheet thickness, step down, tool shaft radius, and tool end-shape (hemispherical or flat-ended) were varied in a design of experiments to determine the effect on the wall angle at the intersection point.

An empirical equation developed from the measured intersection point wall angle results would incorporate the process parameters and a measured wall angle at fracture as inputs to estimate the wall angle at the intersection point.

The equation would provide a safety margin for the wall angle at fracture, estimating a practical maximum wall angle limit to apply when modelling the forming surfaces for a SPIF component or prototype.

5.2 Method

The aim of the experiments described in this section is to generate results for the wall angles at fracture and at the intersection point. This will allow an empirical equation to be developed that will estimate the wall angle of the intersection point (a safe maximum wall angle limit) using the input of the wall angle at fracture.

The equation will assist in the design of components to be formed with SPIF by specifying a safe maximum wall angle for the CAD model. Ensuring the maximum wall angle limit is adhered to will increase the likelihood that the part will form successfully on the first attempt, and not fracture due to the material exceeding the formability limit.

To achieve this, VWACF tests were formed using a design of experiments (DOE) and for each part, the fracture depth and the thickness distribution were measured.

5.2.1 Design of experiments

Four SPIF parameters were varied in a factorial design of experiments. These parameters were step down, sheet thickness, and two tool geometry parameters – shaft radius and end shape. Four tools and two levels each of step down and sheet thickness were

used, resulting in 16 different tests. For statistical significance, the tests were repeated 3 times each, resulting in a total of 48 VWACF components. The full list of tests is shown in Table 5.1.

The process parameters - step down and sheet thickness - were chosen because it was likely that they would show a strong effect on formability based on the results of the literature review.

The tool parameters were also selected for the DOE based on the literature review because they are an area with minimal research, but potential to significantly influence the SPIF process. Solid tools were used as the end-shape of ball-bearing tools can only be hemispherical.

Four forming tools were used in the experiments, commercially made from tungsten carbide and ground to a smooth surface. Cross sections of these tools are shown in Figure 5.2. A dimple is present in the base of the flat-ended tools to attempt to eliminate any detrimental effects due to a stationary point on the flat contact surface of tool and sheet. While hemispherical tools also have this stationary point, the contact surface on the base of the tool is not flat and therefore not as likely to cause the same detrimental effects from a large contact area.

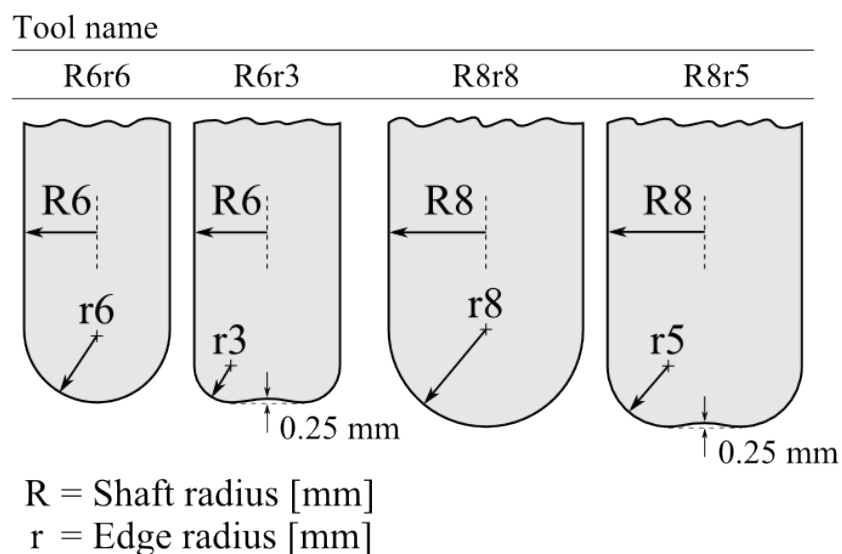


Figure 5.2: Hemispherical and flat-ended tools used in the study.

5.2.2 Test shape

As in the original research by Hussain and Gao (2007), VWACF test shapes were used. However, to make the VWACF results more applicable to the types of components

seen in the case studies (Chapter 4), the VWACF part size was increased.

The revised test shape design took advantage of the full area of the forming rig, which had a maximum size of 300 mm * 500 mm. The major (upper) diameter was set at 200 mm to allow for a minimum 50 mm flange around the edge. The flange was supported by a backing plate measuring 300 mm * 300 mm. The backing plate was designed with 1 mm of clearance for the VWACF parts, making the diameter of the hole 202 mm.

Consistent with Hussain and Gao (2007), the initial wall angle of the VWACF was set at 40°. To prevent issues with insufficient tool length, the depth was limited to 100 mm, resulting in a generatrix radius of approximately 130 mm.

The VWACF test shape dimensions are defined in Figure 5.3, and full details of the geometrical parameters are provided in Table 5.2.

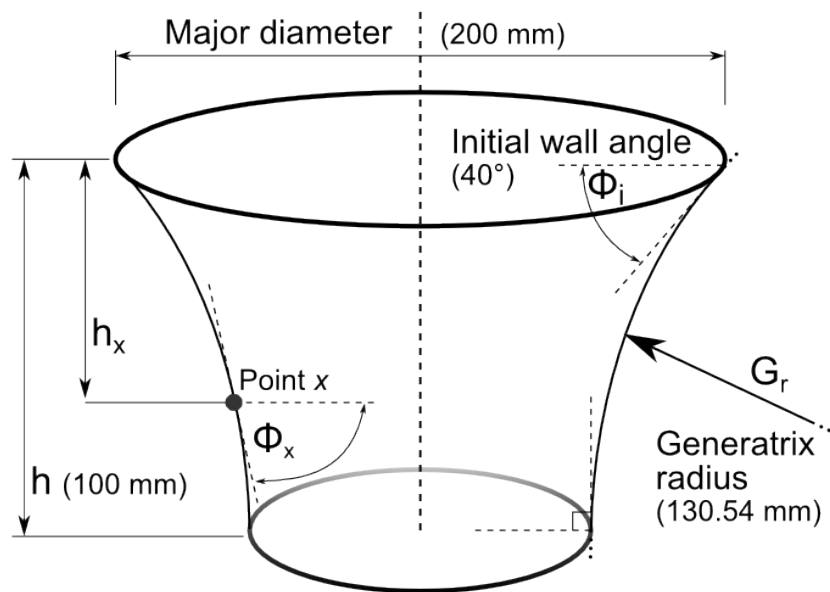


Figure 5.3: VWACF test shape with geometric parameters

From Hussain and Gao (2007), the equation to determine the wall angle of any point on the wall of the part is shown in Equation 5.1. Figure 5.3 defines the variables in the equation.

$$\Phi_x = \cos^{-1} \frac{h - h_x}{G_r} \quad (5.1)$$

Table 5.1: Parameter combinations for VWACF tests

Test No.	Thickness t_0 [mm]	Shaft radius R [mm]	Edge radius r [mm]	Tool end-shape S_t	Step down Δz [mm]
1	1	6	3	flat	0.5
2	1	6	3	flat	2
3	1	6	6	hemi	0.5
4	1	6	6	hemi	2
5	1	8	5	flat	0.5
6	1	8	5	flat	2
7	1	8	8	hemi	0.5
8	1	8	8	hemi	2
9	2	6	3	flat	0.5
10	2	6	3	flat	2
11	2	6	6	hemi	0.5
12	2	6	6	hemi	2
13	2	8	5	flat	0.5
14	2	8	5	flat	2
15	2	8	8	hemi	0.5
16	2	8	8	hemi	2

5.2.3 Experimental procedure

All test parts were formed with Aluminium Alloy AA5005-H34 sheet material on the CNC machine, using the standard SPIF procedure outlined in Chapter 3, Research Methodology.

Progress of the parts were monitored through the viewing window, allowing the program to be manually stopped when failure was observed. The toolpath type was constant Z-level, meaning each loop of the tool was at a constant depth (Z-value). Successive loops were connected by 5 mm-long lead-out and lead-in tool movements to minimise the impact of the tool plunge on the thickness distribution or surface finish.

The experimental details, including the SPIF process parameters that were held constant throughout the investigation, are given in Table 5.2. The stress–strain curve for AA5005-H34 can be found in the research literature in Shen et al. (2010).

5.2.4 Measuring the thickness distribution

To measure the thickness distribution of the VWACF test parts, the same procedure from Hussain and Gao (2007) was applied. The VWACF part and a height gauge were placed on a precise flat surface to minimise height measurement error. All measurements were recorded away from the seam in the VWACF part where the tool

Table 5.2: Constant experimental parameters

Parameter	Value
Test geometry dimensions	
Designed cone depth (h)	100 mm
Initial wall angle (Φ_i)	40°
Final wall angle	90°
Generatrix radius (G_r)	130.54 mm
Major diameter	200 mm
Process settings	
Spindle speed	2000 rpm
Feed rate	5000 mm/min
Tool material	Tungsten carbide
Milling mode	Climb (rolling)
Toolpath type	Constant Z-level
Test repeats	3
Material properties	
Material type	AA5005-H34
Yield strength	133 MPa
Ultimate tensile strength	153 MPa

made the step down transition during forming.

Using the height gauge, lines were scribed along a cross section of each part, starting at 10 mm apart close to the flange and increasing to 1 mm intervals leading up to the fracture point. The thickness distribution close to the flange was not of interest in this experiment, so the intervals were only small close to the fracture point. The precise fracture depth (h_f) was recorded to within 0.1 mm using the height gauge. The typical set up of the VWACF part and the height gauge is shown in Figure 5.4.

The scribed slice of the VWACF was cut out and a calibrated dial gauge indicator was used to manually record the thickness at the scribed lines. The measurement was taken just off to the side of the scribed lines so the indent did not affect the measurement. The dial gauge indicator setup is shown in Figure 5.5. Initial sheet thickness (t_0) was also recorded by measuring the thickness of the undeformed flange of each component slice. The value of t_0 was used to calculate the sine law thickness prediction and plot the measured and predicted thickness distributions for each test part.

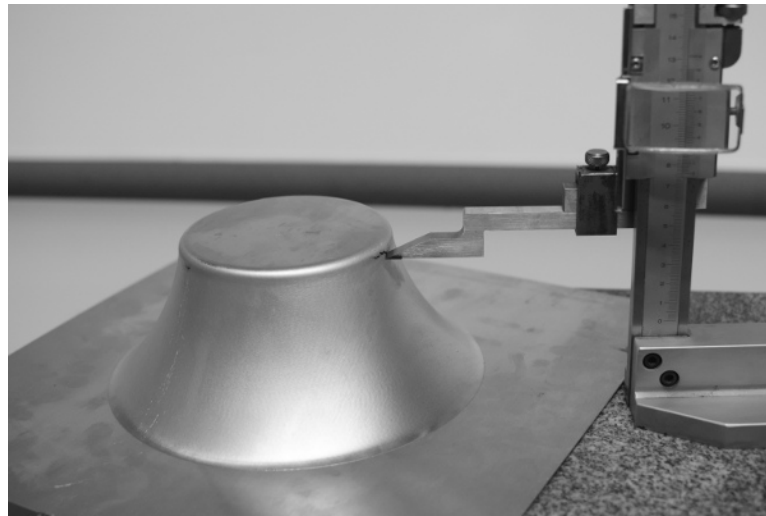


Figure 5.4: Set up of a height gauge and VWACF part used to measure depth increments and the fracture point.

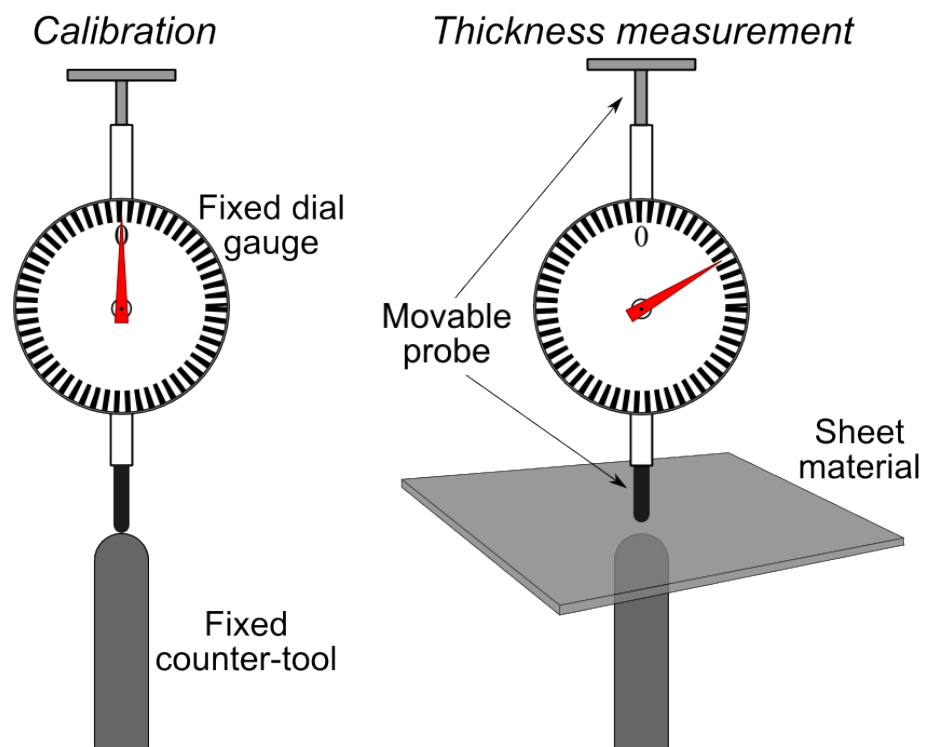
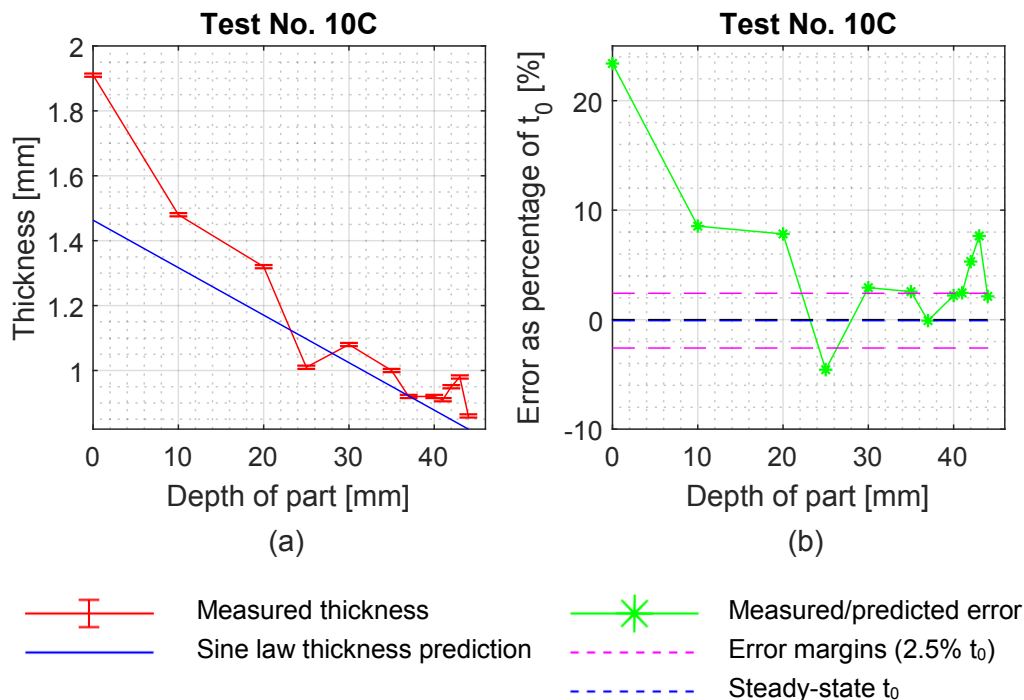


Figure 5.5: Diagram showing the dial gauge setup used to measure the thickness along the cross section of the VWACF parts.

5.3 Results and analysis

The 48 VWACF parts were all formed to the point of failure. Plots were generated for each component where the measured thickness distribution was compared to the predicted sine law thickness. Graphed results for all tests can be found in Appendix B.

While the intended data outcome of the experiments was to find wall angles corresponding to both the fracture point and the intersection point for all parts, this was not possible. The fracture depth was obtained for every component, but analysis of the graphed thickness distribution results revealed that an intersection point did not exist in the majority of parts. An example where no intersection point could be determined is shown in Figure 5.6 (a). Therefore, the empirical equation to predict the intersection point from the fracture depth was not able to be developed.



Parameters: 2 mm sheet thickness, 2 mm step down, R6r3 tool.

Figure 5.6: The thickness distribution of this test varies along the length of the part by more than $\pm 2.5\%$ compared to the sine law prediction. (a) Thickness distribution data, (b) Error plot including $\pm 2.5\% t_0$ margins.

Compared to the results from Hussain and Gao (2007) where the intersection point was originally proposed, none of the results from this study were as unambiguously clear. Instead, the error between the measured and predicted thickness close to the

fracture point was not as consistent or significant. A comparison between all the results is made using deviation as a percentage of the initial thickness of the sheet ($\% t_0$), to take into account different sheet thicknesses in Hussain and Gao (2007) and this work. Figure 5.6 (b) shows the $\% t_0$ error plotted on the Y-axis against depth of part.

In Hussain and Gao (2007), at the fracture point of the VWACF, the measured thickness was less than the predicted thickness by nearly $5\% t_0$. An error margin was applied to the deviation plots in this experiment to analyse the results. However, instead of $5\% t_0$, the margin was halved to $2.5\% t_0$ in order to better characterise the trends of the thickness distributions. A majority of tests in this experiment did not show any deviation outside these $2.5\% t_0$ margins.

Due to an unexplained offset between the measured and predicted thickness data, possibly from consistent error in depth measurement, a 'steady state' zero point was calculated for each individual test. This zero point was used for specifying the $\pm 2.5\% t_0$ error margins and is denoted by a blue dashed line in Figures 5.6 - 5.9 (b). The sine law prediction is shown in these figures as a black dashed line through the Y-axis origin.

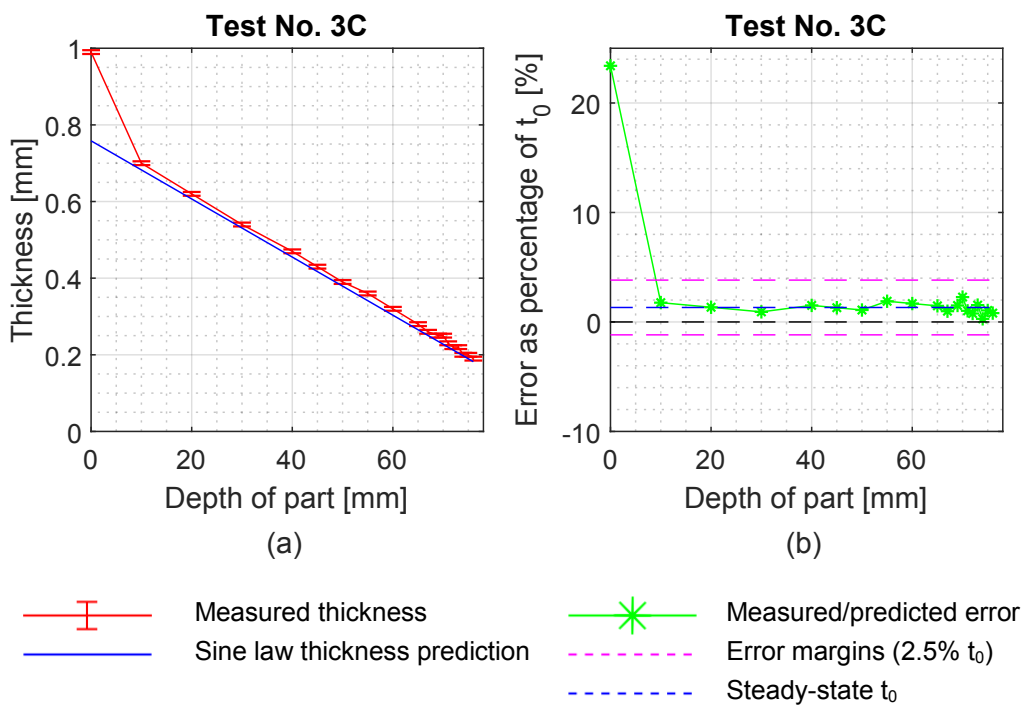
The 'steady state' zero point offset was calculated by taking an average of the error at 10, 20, 25, and 30 mm depth, representing the first four measured points on the wall of the part. This does not include the value plotted at 0 mm depth which represents the thickness of the original blank.

Though the results had significant variation, as seen in Figure 5.6 and Figure 5.7, specific trends were identified among the thickness distributions results from the 48 VWACF parts. For example, a few results showed a similar trend to the results from Hussain and Gao (2007) and Jin et al. (2012), where thinning occurred and the authors identified an intersection point.

Others showed almost identical results to Hussain, Gao, and Zhang (2008) and Kurra and Regalla (2014), where the trend of the measured thickness distribution was straight with no thinning close to fracture.

Furthermore, new behaviour of the thickness distribution was seen that had not been mentioned in any of the previous papers. This was the phenomenon of positive deviation close to the fracture point, mentioned in the list below along with an example plot.

Using the calculation of $\% t_0$ error and the $2.5\% t_0$ margins, the results were separated into specific classifications based on the behaviour of the thickness distribution. Each classification is described below with a corresponding example. Table 5.3 lists results for all tests.



Parameters: 1 mm sheet thickness, 0.5 mm step down, R6r6 tool.

Figure 5.7: The measured thickness distribution closely follows the sine law prediction until the final fracture point. (a) Thickness distribution data, (b) Error plot including $\pm 2.5\% t_0$ margins.

Straight (STR) No significant deviation is observed between the measured and predicted thickness distributions. The error lies within a $\pm 2.5\%$ margin.

Representative example: Figure 5.7.

Increase (INC) The deviation close to the fracture point is greater than $+2.5\%$.

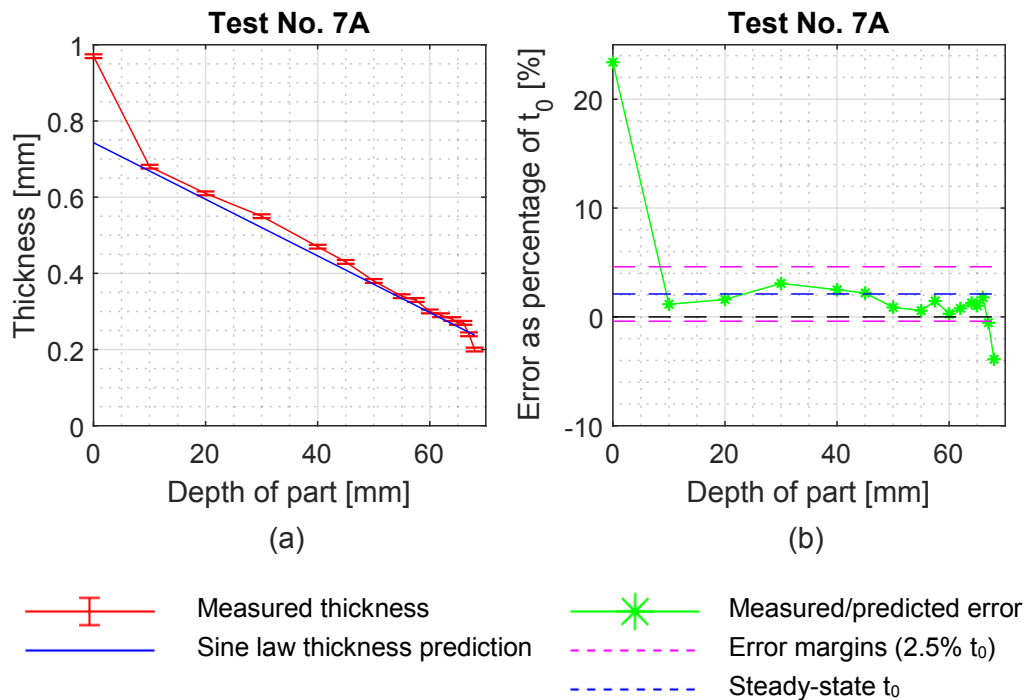
Representative example: Figure 5.9.

Decrease (DEC) The deviation close to the fracture point is lower than -2.5% .

Representative example: Figure 5.8.

Irregular (IRR) The thickness distribution does not follow a regular trend and fluctuates with more than $\pm 2.5\%$ error at multiple points.

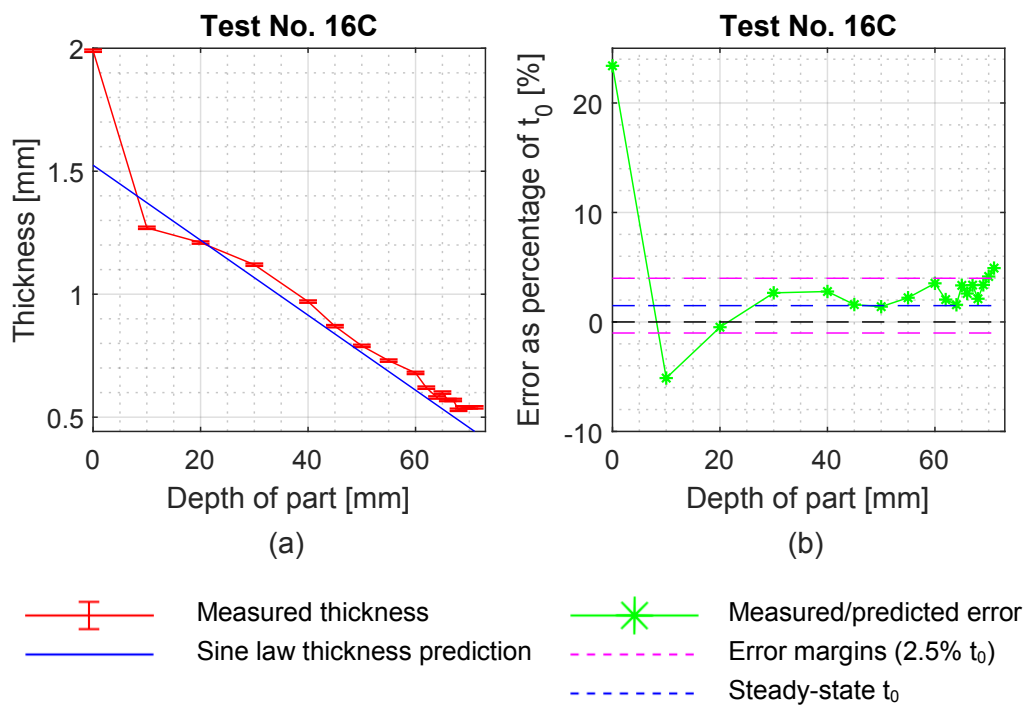
Representative example: Figure 5.6.



Parameters: 1 mm sheet thickness, 0.5 mm step down, R8r8 tool.

Figure 5.8: The measured cross-sectional thickness is decreased at the fracture point when compared to the sine law prediction. (a) Thickness distribution data, (b) Error plot including $\pm 2.5\% t_0$ margins.

The majority of parts (60%, Table 5.3) had thickness distributions that were in close alignment with the trend of the predicted thickness, and no significant deviation (greater than $2.5\% t_0$) was observed around the fracture point.



Parameters: 2 mm sheet thickness, 2 mm step down, R8r8 tool.

Figure 5.9: The measured thickness follows the prediction until approximately 5 mm before the fracture point, where positive deviation occurs. (a) Thickness distribution data, (b) Error plot including $\pm 2.5\% t_0$ margins.

Table 5.3: Classification of results for VWACF tests

Test No.	Rpt A	Rpt B	Rpt C
1	STR	STR	STR
2	DEC	STR	IRR
3	STR	INC	STR
4	STR	STR	INC
5	STR	DEC	STR
6	STR	STR	STR
7	DEC	INC	STR
8	STR	STR	IRR
9	STR	STR	STR
10	IRR	IRR	IRR
11	STR	IRR	STR
12	STR	DEC	INC
13	STR	STR	STR
14	IRR	IRR	IRR
15	STR	STR	STR
16	STR	INC	INC
% Totals			
STR	INC	DEC	IRR
60%	13%	8%	19%

Those tests classified as 'Irregular' were also identifiable in most cases by the surface damage which had occurred due to the poor combination of process parameters. Figure 5.10 shows photographs of the surface damage which caused the 'Irregular' classification for some tests. Intersection points were unable to be determined in these parts as a result of the fluctuation in measured thickness.

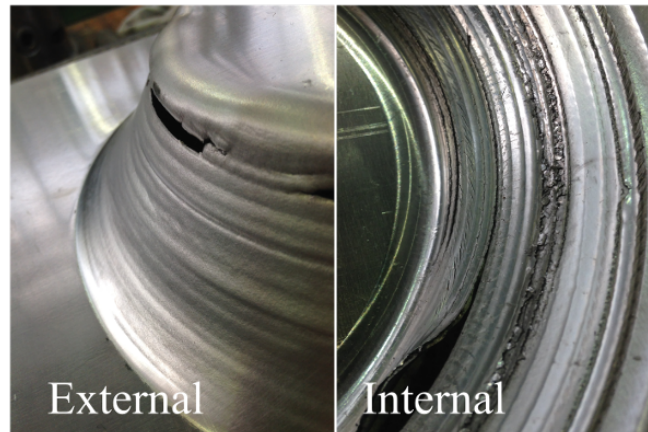


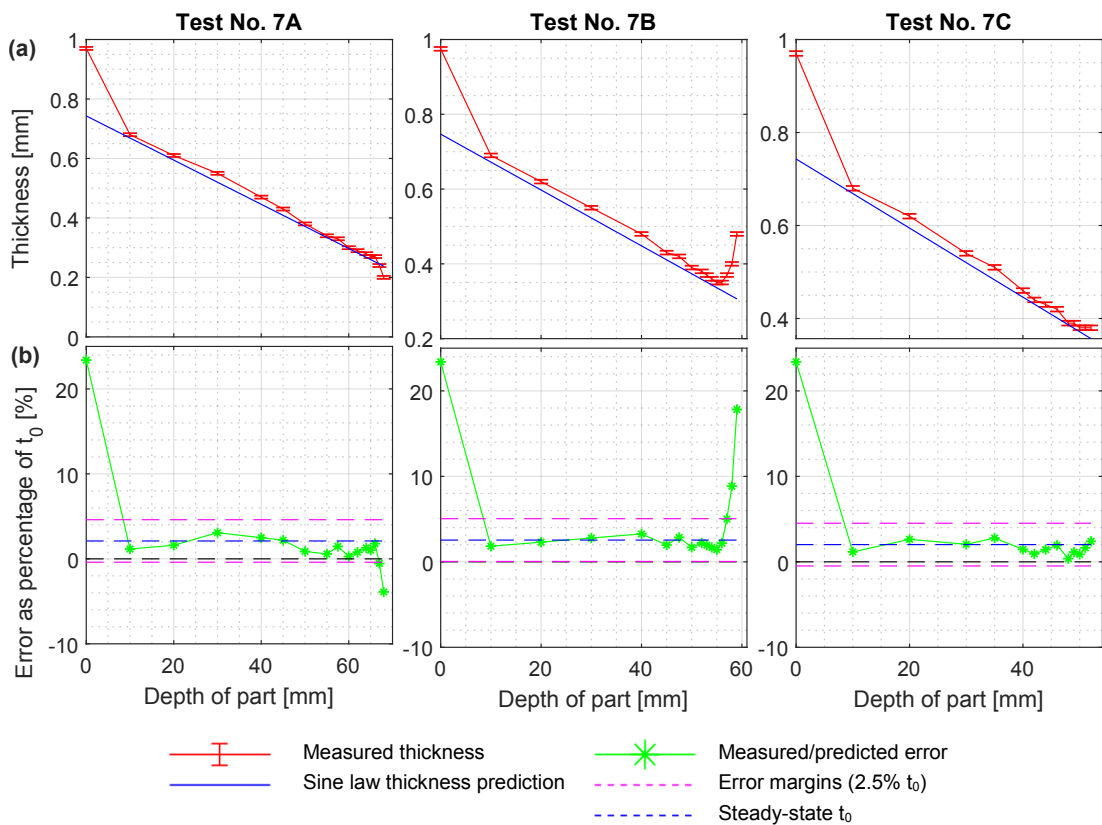
Figure 5.10: Rough external surface finish and internal galling of Test No. 10 and 14.

The behaviour of the measured thickness distribution close to the fracture point was, in most cases, inconsistent between the three test repeats with one test differing or all three having different classifications. This was sometimes in conjunction with a high repeatability of fracture depth. Examples are seen Table 5.3, for example Test No. 2, 7, and 12. The results for Test No. 7 are shown in Figure 5.11, specifically noting Row (a) where the thickness distribution varies widely between part A, B, and C.

This inconsistency raises questions about the use of trends within the thickness distribution as a basis for a formability marker, if identical process settings do not necessarily lead to identical thickness distribution results for all test repeats.

5.4 Discussion

While the results presented in this chapter did not allow the aim of the experiments to be fulfilled, it is nonetheless worth considering what insights can still be gained. The context of this discussion includes the other papers which considered the intersection point, and also the broader aims and themes of this thesis.



Parameters: 1 mm sheet thickness, 0.5 mm step down, R8r8 tool.

Figure 5.11: Results for Test No. 7 showing measured thickness distribution in Row (a) and corresponding error plots in Row (b). Note the variation between each test repeat.

5.4.1 General discussion

5.4.1.1 Impact on formability and geometric accuracy

Variation of the material thickness from the sine law may have an impact on the material's formability or the resulting geometric accuracy of the component.

If the material thickness deviates from the sine law close to fracture it may be seen as an instability that is equivalent to the necking phenomena from standard press forming or tensile tests (Kalpakjian and Schmid, 2010c). This is in contrast to a proposed 'noodle theory' (Malhotra et al., 2012), which says that during SPIF, multiple small necking instances develop within the sheet material. The necks are said to be a result of the incremental movement of the tool, and individually do not lead to fracture.

The necking-like instability could be an indicator that the formability limit of the material is approaching and the part will fail due to fracture. In fact, the overall inconsistency in the results from this chapter could reflect the variation in real-world forming situations that result in the need for a 'marginal zone' on a forming limit diagram (Keeler, 1965). Within the marginal zone, there is a possibility of failure as it takes into account the inevitable random differences between forming situations.

Instabilities such as the instance shown in Figure 5.9 could have an effect on geometric accuracy. This small section may present a weakness that reduces the overall stiffness of the part and leads to increased springback.

5.4.1.2 Part size and the thickness distribution

It is worth considering whether part size might be a factor for differing trends in the thickness distribution. The test part in Hussain and Gao (2007) had upper diameters of 110 mm, while the test parts from this experiment were roughly twice as large, with an upper diameter of 200 mm.

A repeat of a test from the present study (No. 7) did not show a clear intersection point when the part size was reduced to correspond with Hussain and Gao (2007). The thickness distribution from this test was classified as 'STR' (straight: no significant deviation of measured thickness from sine law predicted thickness).

Furthermore, two articles from the literature support the assertion that part size is not a factor in the existence of an intersection point. Kurra and Regalla (2014) and Hussain, Gao, and Zhang (2008) also formed VWACF parts of similar size to Hussain and Gao (2007). Neither of these results showed an intersection point and instead the measured and predicted thicknesses were in good agreement up to the fracture point. Therefore, the lack of intersection point in the results from this chapter is not due to

the larger size of test parts.

5.4.1.3 Microcracks causing instabilities

In Hussain and Gao (2007), microcracks were shown on the test parts, and the material thinning was said to be a result of these instabilities. If this is the case, microcracks should occur in other VWACF test parts.

Jin et al. (2012) did not mention microcracks. No microcracks were observed on the surface of any of the test parts from the current study, including where the part was classified as 'DEC' (decrease: The measured cross-sectional thickness is decreased at the fracture point when compared to the sine law prediction). Figure 5.12 shows a close up of the surface of one of the parts, free of microcracks. It is possible that microcracks are a phenomenon that is dependent on the specific material properties.



Figure 5.12: Close up of part near the point of fracture. The surface is regular and free of microcracks.

5.4.1.4 The trend of increasing thickness close to fracture

A new trend for the VWACF thickness distribution was presented in the results from this chapter. This was the situation where the measured thickness at the fracture point was greater than the sine law prediction, an example of which is shown in Figure 5.9. This may have been caused by material springback when a large fracture occurred. Material properties may affect this in the same way as they affect springback in other situations.

5.4.1.5 Material type and the intersection point

The types of material from the research papers discussed in the background (§5.1) included titanium, extra-deep drawing steel, and aluminium. Particular material properties, for example ductility, may increase the tendency of a material to undergo

significant thinning before fracture and therefore observe the occurrence of an intersection point. When the measured and predicted thickness distributions are in close alignment until the point of fracture, the material may be stiff and not ductile. Complete fracture may occur very soon after any small cracks begin in the material, with no resulting positive or negative deviation from the sine law prediction. However, based on the differing trends seen in the present results (Figures 5.6 - 5.9), use of a single material type does not ensure a predictable trend in deviation from the sine law.

5.4.2 Significance of the results

Discussion about the specifics of the intersection point is a side note to its applicability. This idea for a marker of safe formability is not a useful indicator because the thickness distribution close to fracture can be inconsistent (including between repeats of the same test), meaning the existence of an intersection point can be inconsistent. This reduces the usefulness of the intersection point in practical applications as it becomes a 'hit and miss' situation.

The intersection point seems to be present in some materials and not present in others, based on the present study and research by Hussain, Gao, and Zhang (2008) and Kurra and Regalla (2014). This suggests the material properties could have a significant effect, adding to the inconsistencies and the 'hit and miss' situation of attempting to utilise the intersection point in practical applications.

5.4.3 Conclusions

The indications from these results do not contradict any of the papers discussed in the literature review. These results simply show that the behaviour of a VWACF thickness distribution as it approaches fracture is different to the rest of the part, where the sine law successfully predicts the thickness of the material.

VWACF parts from this study had measured thickness distributions close to fracture which were greater than, equal to, less than, and entirely inconsistent with the sine law predicted thickness. Based on the analysis in this chapter it is not possible to predict the behaviour. Therefore, it is not helpful to use the thickness distribution as a basis for a marker such as the intersection point.

5.5 Chapter summary

This large-scale study showed that the concept of the intersection point presented in Hussain and Gao (2007) is not valid for all VWACF tests. Instead, variation was

observed in the behaviour of the thickness distribution close to the fracture point, and there was limited resemblance to the thickness distribution results from Hussain and Gao (2007).

The most practical and effective marker to assess and compare formability limits in SPIF is the point of fracture of a VWACF test. The fracture point has good reliability (failure will always occur) and repeatability.

In the following chapter, the fracture point of VWACF parts is used as a comparison method, rather than prescribing absolute formability limits. In comparison to the present chapter, this investigation will take a high-level approach to formability through the understanding of parameter effects and interactions.

Variation of formability results in SPIF and the non-linearity and interactions of process parameters

In this chapter, SPIF process parameters (tool shape and size, step down, and sheet thickness) are varied in a DOE to assess their effect on the formability limit of AA5005-H34 sheet. This work builds on previous chapters of this thesis and aims to support the hypotheses developed in the systematic quantitative literature review on formability in SPIF.

6.1 Background

This chapter experimentally investigates findings from the literature review (Chapter 2), the SPIF case studies (Chapter 4), and the previous chapter which looked at safe formability limits (Chapter 5). The case studies highlighted key issues encountered when forming automotive components, including the topic of formability and more specifically, preventing failure of the component by fracture.

Chapter 5 investigated the idea of a safe formability limit defined by the ‘intersection point’ (Hussain and Gao, 2007). The aim of the investigation was to develop a method for easily predicting the safe formability limit, applicable to practical SPIF situations such as the case studies in Chapter 4.

The results of the work in Chapter 5 were unclear, which meant the method was unable to be developed. However, insights were gained about the variability of the thickness distribution of SPIF parts close to fracture, even between repeats of the same test. This suggested an application-based approach – prescribing rules for specific situations – would not be as useful as a high-level investigative perspective.

In fact, the analysis of SPIF literature in Chapter 2 resulted in a number of high-

level ideas regarding the state of the formability literature and possible underlying factors which influence it. The findings showed that, throughout the literature, conflicting results exist about the effects of key process parameters on formability. This lack of consensus forms the basis of the high-level investigation in the present chapter. Specific hypotheses are as follows:

- The effect of most process parameters is non-linear, with an optimal value resulting in the highest level of formability.
- Interactions between parameters can have a significant effect on formability.

As a consequence of the two points above, different researchers can report different conclusions about parameter effects.

The effect of tool shape on formability has been the subject of a small amount of research, but interactions have not been studied. Tool shape may interact with other parameters, which would be important to understand for future applications.

In this chapter, experiments to test the hypotheses have been designed. Results from the experiments will allow conclusions to be drawn regarding parameter interactions and non-linearity.

6.2 Method

As mentioned in the introduction, this investigation developed from the results, or lack thereof, from the 'intersection point' investigation in Chapter 5. A key message from this chapter was that aiming for high-level insights about formability in SPIF will be more widely beneficial than application-based investigations.

The variable wall angle conical frustum (VWACF) tests formed in the previous chapter (Chapter 5) were also used in this chapter, with the fracture depth and corresponding wall angle at fracture analysed. This is in line with the recommendation given in the §5.5 that wall angle at fracture is the most efficient, effective, and reliable method to assess and compare formability in SPIF.

However, the experimental design from Chapter 5 was a simple factorial design with only two levels of each factor. At least one additional level of the factor was needed to test the hypothesis of non-linearity stated at the beginning of this chapter.

The factors tested for non-linearity were step down and thickness. These parameters were more feasible than the tool factors due to the ease of adding a 3rd factor level. Furthermore, indications from the literature review were that thickness and step down might show non-linearities, as a result of a number of 'Optimise' conclusions.

By adding a combined centre point for step down and thickness, the null hypothesis of linear response could be tested for both. Compared to adding a level for each parameter to the factorial experiment, this approach required only 12 additional VWACF parts rather than 60.

Interactions of the other factors with step down were anticipated to be strong due to the large range in values (0.5 mm and 2 mm step down), and previous examples in the literature (Shanmuganatan and Senthil Kumar, 2013). While this approach ensures that interactions, if they exist, will be clearly visible, the effect of step down may mask more subtle interactions between the other parameters.

Therefore, two sets of experiments were run for this investigation. Firstly, the experimental plan described in the preceding paragraphs was designated as Experimental Set 1 and examined all parameter effects.

Secondly, Experimental Set 2 eliminated the influence of step down by using a constant value of $\Delta z = 0.5$ mm. The experimental design was adjusted to incorporate additional tests for a $3^1 * 2^2$ factorial DOE with sheet thickness, shaft radius, and tool shape. The linearity of thickness effect on formability could then be studied more effectively.

Specific details are described in the following sections.

6.2.1 Experimental Set 1

Experimental Set 1 (ES1) is a fractional factorial DOE with 4^2 corner points and 2^1 centre point. Four tools were used at every thickness/step down combination, and each unique test was repeated three times for statistical significance. Table 6.1 shows the experiments that were carried out.

6.2.2 Experimental Set 2

Experimental Set 2 (ES2) is a $3^1 * 2^2$ factorial DOE with 3 levels of thickness and four tools incorporating 2 levels each of shaft radius and tool shape. The parameter combinations of the tests are set out in Table 6.2 and each was repeated three times for statistical significance.

6.2.3 Testing process

The production process for the VWACF test parts is in line with the method outlined in Chapters 3 and 5, though for this investigation fracture depth is the only response recorded.

Table 6.1: Tests and parameters for Experimental Set 1

Test No.	Thickness t [mm]	Shaft radius R [mm]	Edge radius r [mm]	Tool shape S_t	Step down Δz [mm]
1	1	6	3	flat	0.5
2	1	6	3	flat	2
3	1	6	6	hemi	0.5
4	1	6	6	hemi	2
5	1	8	5	flat	0.5
6	1	8	5	flat	2
7	1	8	8	hemi	0.5
8	1	8	8	hemi	2
9	1.6	6	3	flat	1
10	1.6	6	6	hemi	1
11	1.6	8	5	flat	1
12	1.6	8	8	hemi	1
13	2	6	3	flat	0.5
14	2	6	3	flat	2
15	2	6	6	hemi	0.5
16	2	6	6	hemi	2
17	2	8	5	flat	0.5
18	2	8	5	flat	2
19	2	8	8	hemi	0.5
20	2	8	8	hemi	2

Each VWACF part was formed from the AA5005-H34 sheet material in the CNC milling machine, and was monitored until fracture occurred so the machine could be manually stopped.

Fracture depth (h_f , specified in Figure 6.1), was recorded by placing each formed part upside down on a flat surface. A height gauge was used to measure the lowest point of fracture on the wall of the part. This setup is shown in Figure 6.2. The wall angle at fracture was calculated for each part from the depth measurement using the same from Chapter 5, restated below (Equation 6.1) specifically for the fracture point.

$$\Phi_{max} = \cos^{-1} \frac{h - h_f}{G_r} \quad (6.1)$$

6.2.4 Analysis process

Analysis of the results will use statistical methods to determine the significance of the parameter effects and interactions.

The non-linearity hypothesis will be discussed based on graphed results, as the use of non-linear statistical models is outside the scope of this work. Linear models,

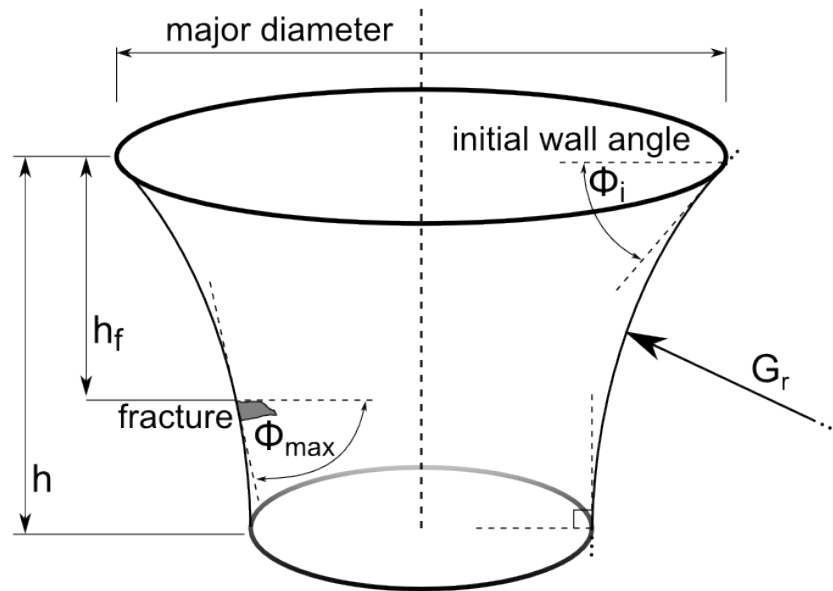


Figure 6.1: VWACF test shape with geometric parameters

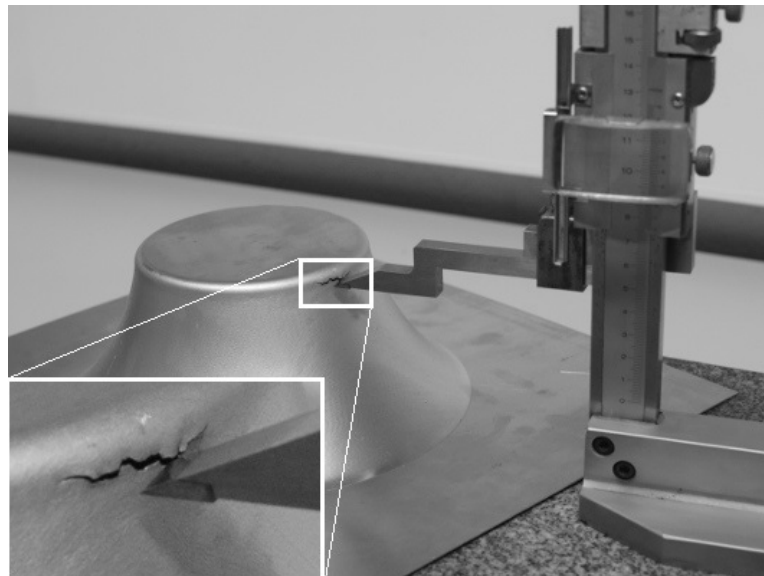


Figure 6.2: Height gauge measuring the lowest point of fracture on a VWACF part. Inset: detail of crack and gauge tip.

Table 6.2: Tests and parameters for Experimental Set 2.

Overlap of tests from Experimental Set 1 denoted by ‡.

Test No.	Thickness t [mm]	Shaft radius R [mm]	Edge radius r [mm]	Tool shape S_t	Step down Δz [mm]
1 ‡	1	6	3	flat	0.5
3 ‡	1	6	6	hemi	0.5
5 ‡	1	8	5	flat	0.5
7 ‡	1	8	8	hemi	0.5
21	1.6	6	3	flat	0.5
22	1.6	6	6	hemi	0.5
23	1.6	8	5	flat	0.5
24	1.6	8	8	hemi	0.5
13 ‡	2	6	3	flat	0.5
15 ‡	2	6	6	hemi	0.5
17 ‡	2	8	5	flat	0.5
19 ‡	2	8	8	hemi	0.5

outlined in this section, will be used to test for significant parameter interaction effects on formability.

To analyse the results of each experimental set, statistical computations were run in **R** (Team, 2008). Both sets of experiments in this chapter aim to determine the significance of the parameter main effects and interactions. Therefore, a criterion-based procedure (restricted maximum likelihood, REML) will be used to perform backward elimination on the maximum statistical model. This will reduce the initial model to only the terms which have a statistically significant influence and are able to effectively describe the response variable (i.e. wall angle at fracture).

The parameters varied for the experiments in this chapter, and their corresponding symbols, are step down (Δz), thickness (t), shaft radius (R), and tool shape (S_t). The wall angle at fracture will be denoted by Φ_{\max} .

6.2.4.1 Experimental Set 1

Due to the Z/t centre point of Experimental Set 1, the design is not balanced and therefore cannot be modelled with a standard model. Instead, the analysis will be carried out using a linear mixed model, which allows consideration of the random effect from the test repeats. The linear mixed model incorporates main effects and two-factor interactions only, as the DOE did not permit an assessment of the 3-factor interactions. The linear mixed model in **R** is calculated using the function `lmer`

from the `lme4` package (Bates et al., 2015). The final statistically significant model is determined by eliminating insignificant factors, in this instance using the step function (`R` package `lmerTest`).

All four factors varied in Experimental Set 1 are incorporated into the full linear mixed model which will be analysed. In addition, interaction terms, listed as $a * b$ and the random term for test repeats ($TestRpt$) are included in the model, Equation 6.2.

$$\Phi_{max} = R + t + S_t + \Delta z + R * t + R * S_t + R * \Delta z + t * S_t + t * \Delta z + S_t * \Delta z + TestRpt \quad (6.2)$$

6.2.4.2 Experimental Set 2

This experiment aims to test the linearity of thickness without the influence of step down, which is anticipated to be large. The same procedure as Experimental Set 1 will be carried out using the full statistical model in Equation 6.3, which includes parameter main effects and interactions, as well as the random term $TestRpt$ to account for multiple repeats of the same test. The model will be reduced to its most significant terms with backwards elimination.

$$\Phi_{max} = R + t + S_t + R * t + R * S_t + t * S_t + TestRpt \quad (6.3)$$

6.3 Results

The VWACF parts, an example of which is shown in Figure 6.2, were formed for the two experimental sets. Average maximum wall angle and the standard deviation for each test are recorded in Table 6.3.

Overall, the tests had good repeatability between the three repeats. However, three tests from the results in Table 6.3 have larger sample variances than the rest of the tests.

Test ID 14 and 18 used flat-ended tools to form 2 mm sheet with a 2 mm step down. Significant variation was seen between the failure depths of the three repeats due to severe galling on the sheet, previously discussed in Chapter 5 (Figure 5.10).

Test ID 7 also had large sample variance, though an explanation was not obvious. Investigating further, three extra repeats of Test ID 7 were conducted (making a total of six) but the results confirmed the large variation of fracture depth. Excessive heat generation for this particular combination of parameters is a possible reason for the variation. However, confirmation of this theory would require further experimentation

Table 6.3: Maximum wall angle results

Test ID	$\Phi_{\max} \pm s^2$	Test ID	$\Phi_{\max} \pm s^2$
1	77.81 \pm 1.57	13	82.59 \pm 0.13
2	66.08 \pm 0.28	14	67.87 \pm 4.69
3	79.75 \pm 1.05	15	79.06 \pm 0.90
4	72.43 \pm 0.49	16	78.06 \pm 1.84
5	77.90 \pm 0.32	17	83.18 \pm 0.38
6	67.89 \pm 1.45	18	60.05 \pm 3.79
7	74.43 \pm 3.39	19	80.76 \pm 0.65
8	71.49 \pm 1.00	20	78.51 \pm 0.78
9	77.97 \pm 0.99	21	81.45 \pm 0.20
10	82.53 \pm 0.95	22	82.65 \pm 1.25
11	79.00 \pm 0.27	23	82.40 \pm 0.20
12	80.67 \pm 0.97	24	81.45 \pm 0.51

into the forming mechanisms which is not within the scope of this investigation.

6.4 Analysis

This section presents results of the analysis process described in §6.2.4.

6.4.1 Experimental Set 1 parameter interactions

The four parameters used in Experimental Set 1 were step down (Δz), thickness (t), shaft radius (R), and tool shape (S_t).

As discussed in §6.2.4, the initial experimental design was not balanced. In addition, the further three test repeats conducted for Test ID 7 (see §6.3) also cause an imbalance in the results of the experiment. The linear mixed model is able to account for the extra test repeats. After the backward elimination function was run, the final reduced model incorporated only the statistically significant terms. Performing an Analysis of Variance (ANOVA) on the final model shows the probability of each term's significance. The final model and ANOVA results are shown below in Equation 6.4 and Table 6.4.

$$\Phi_{\max} = S_t + \Delta z + S_t * \Delta z + TestRpt \quad (6.4)$$

The full **R** code and output is shown in Appendix C.2.

Consistent with established research literature, as summarised in Chapter 2, step down has been shown to significantly affect the fracture angle (wall angle at fracture)

Table 6.4: Experimental Set 1 ANOVA results

Parameter	SS	MS	DF	DDF	F value	Probability
S_t	22.765	22.765	1	14.191	6.0911	0.026887
Δz	162.309	81.155	2	14.178	21.7139	4.83×10^{-5}
$S_t * \Delta z$	52.473	26.236	2	14.178	7.0199	0.007604

SS: Sum of Squares

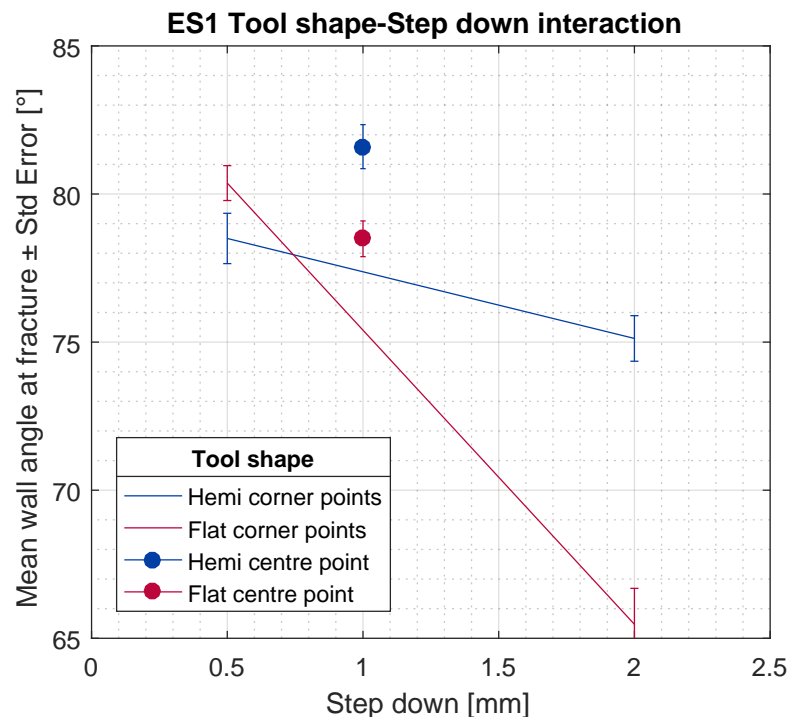
MS: Mean Squares

DF: Degrees of Freedom

DDF: Denominator Degrees of Freedom

in SPIF. In fact, in these experiments, the fracture angle could be improved by 10° by using 0.5 mm instead of 2 mm step down.

The tool shape and the interaction between these two variables are also significant factors affecting formability in SPIF. The interaction is plotted in Figure 6.3. The plot emphasises the strong negative effect on formability that occurs when a flat-ended tool is used with a large (2 mm) step down.

**Figure 6.3:** Effect of step down with varying tool shape: Experimental Set 1

The analysis of Experimental Set 1 using a linear mixed model determined that the main effects of tool shape and step down had a significant effect on the formability.

Importantly, the interaction between the two was also significant. All other parameters from the maximum statistical model were not significant based on this analysis.

6.4.2 Experimental Set 2 parameter interactions

The three parameters used in Experimental Set 2 were thickness (t), shaft radius (R), and tool shape (S_t).

The method of analysis has been previously set out in §6.2.4. However, due to collinearity the interaction terms $R * S_t$ and $R * t$ were unable to be in a model at the same time, meaning there were two equal valid options for modelling the experiment. These are shown in Equations 6.5 and 6.6 below (Φ_{max}^1 and Φ_{max}^2). Both have the random term $TestRpt$ to account for multiple repeats of each parameter combination.

$$\Phi_{max}^1 = R + t + S_t + R * S_t + S_t * t + TestRpt \quad (6.5)$$

$$\Phi_{max}^2 = R + t + S_t + R * t + S_t * t + TestRpt \quad (6.6)$$

Both Φ_{max}^1 and Φ_{max}^2 resulted in the same final model, which did not include any interaction terms. The model is shown below in Equation 6.7, along with an ANOVA assessment of the significance of the terms in the final model in Table 6.5. Full **R** codes and outputs for all functions are given in Appendix C.3.

$$\Phi_{max} = t + TestRpt \quad (6.7)$$

Table 6.5: Experimental Set 2 ANOVA results

Parameter	SS	MS	DF	DDF	F-value	Probability
t	42.36	21.18	2	9.7536	8.1105	0.008423

SS: Sum of Squares

MS: Mean Squares

DF: Degrees of Freedom

DDF: Denominator Degrees of Freedom

The results of Experimental Set 2 show that the main effect of sheet thickness has a significant effect on fracture angle. The other parameters varied in this DOE, and their interactions were not statistically significant.

6.4.3 Non-linearity of parameters

The results of Experimental Set 1 and 2 allow the non-linearity hypothesis to be tested for the step down and sheet thickness parameters.

Figure 6.4 presents the interaction plot for both these parameters, using the data from Experimental Set 1. The centre point of 1 mm step down and 1.6 mm thickness suggests that non-linearity for both parameters is a possibility by its position in line with the trend of 0.5 mm step down.

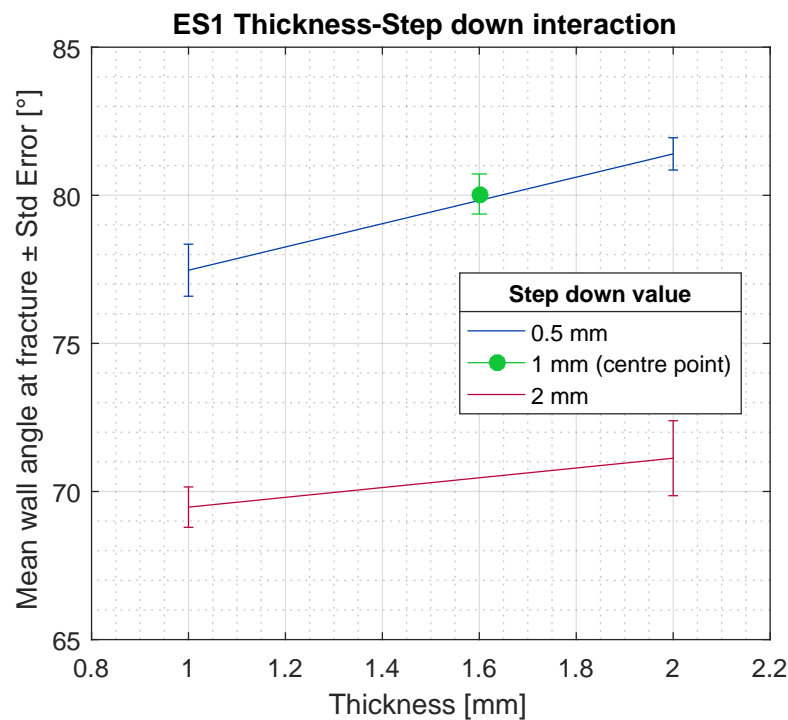


Figure 6.4: The effect of thickness for different values of step down

Looking at the separate main effect plots in Figure 6.5, it seems likely that the majority of the non-linearity in Figure 6.4 originates from the thickness results. A sheet thickness of 1.6 mm shows a large improvement in formability compared to both 1 mm and 2 mm thicknesses. The centre point on the step down main effect plot does not appear to be as significantly deviated from the trend set by the 0.5 mm and 2 mm step down results.

Without the influence of a centre point, the main effect of thickness from Experimental Set 2 has a more linear trend. However, the average wall angle at fracture results for the 1.6 mm sheet and the 2 mm sheet are not significantly different. This statement is based on a Student's *t*-test for heteroscedastic data, giving a probability of $0.15 > 0.05$ significance level.

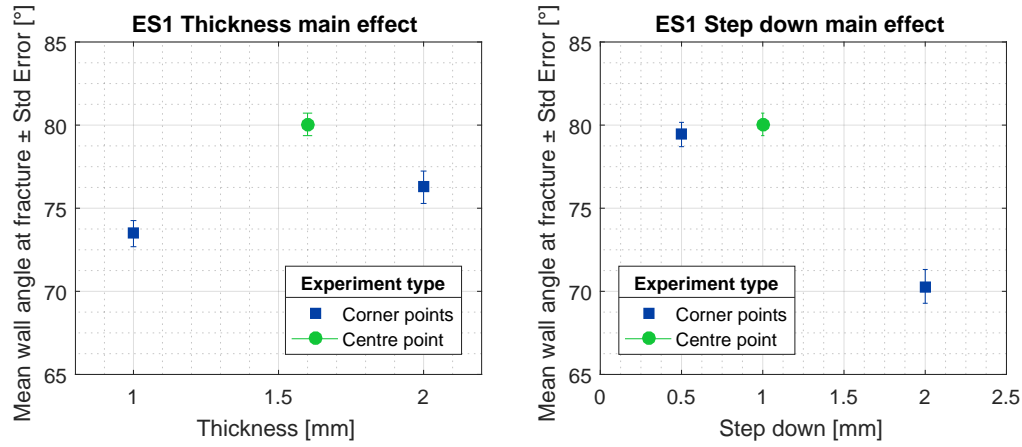


Figure 6.5: The main effects of thickness and step down from Experimental Set 1

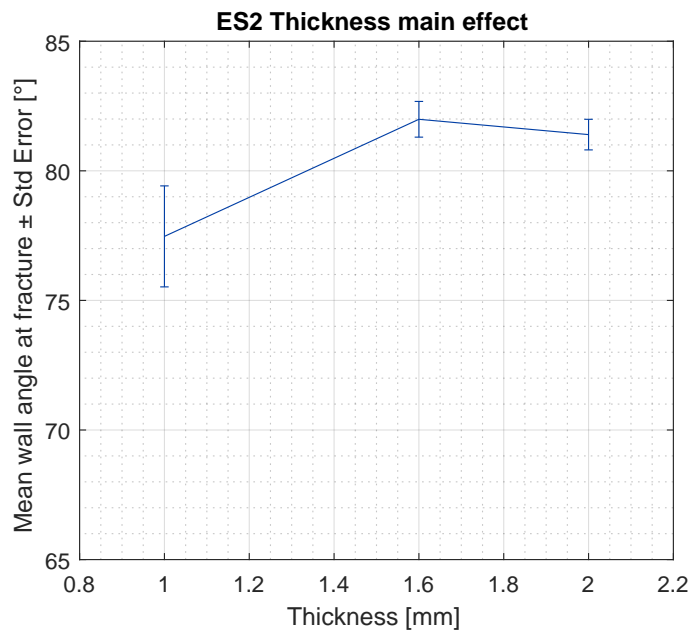


Figure 6.6: The effect of varying thickness on formability in Experimental Set 2

Indistinguishable wall angle results for 1.6 mm and 2 mm sheet support the non-linearity hypothesis for thickness, as both are significantly greater than the results for the 1 mm sheet. Linearity for this parameter would mean the linear trend between 1 and 1.6, or 1.6 and 2 mm sheet was reflected in the remaining result, which is not the case.

Eliminating the 2 mm step down tests from Experimental Set 1 in Experimental Set 2 changed the average response for some of the forming tools. Figure 6.7 and 6.8 shows individual forming tools and the average wall angle at fracture results plotted against thickness.

In Experimental Set 1 (Figure 6.7), the R8r5 tool had the lowest average fracture angle when forming a 2 mm sheet. However, the opposite is true for Experimental Set 2.

In fact the two flat-ended tools exhibit an apparent linear response in their interaction with thickness. This causes the two flat-ended tools to have the highest wall angle at fracture at 2 mm thickness. The flat tools may allow better distribution of the forming force and reducing the pressure as a consequence of their larger base contact area. Reduction of pressure may result in more ideal forming conditions. However, confirmation of this theory is outside the scope of this research.

The R6r6 tool performs optimally at 1.6 mm rather than 1 or 2 mm sheet thickness. Therefore, the response of wall angle at fracture may be affected by the specific forming tool, and assessing the results as simply groups of ‘flat’ or ‘hemispherical’ tools does not provide the highest level of insight.

6.5 Discussion

6.5.1 Parameter interactions

Not all parameter interactions significantly affected the formability. The only significant interaction was between step down and tool shape, shown in Figure 6.3. In these results, the tool shape with the highest formability was different depending on the value of step down. Specifically, flat-ended tools were better at 0.5 mm step down, but hemispherical tools were better when either the 1 mm or 2 mm step down was used.

This interaction alone does not account for the discrepancies outlined in Chapter 2 seen between the results in the literature.

In Experimental Set 1 the factor of tool shape was found to affect formability. This seemed to be primarily because of its interaction with step down. Some parts had particularly bad outcomes as a result of the combination of large step down and flat-ended tool, where galling of the sheet occurred.

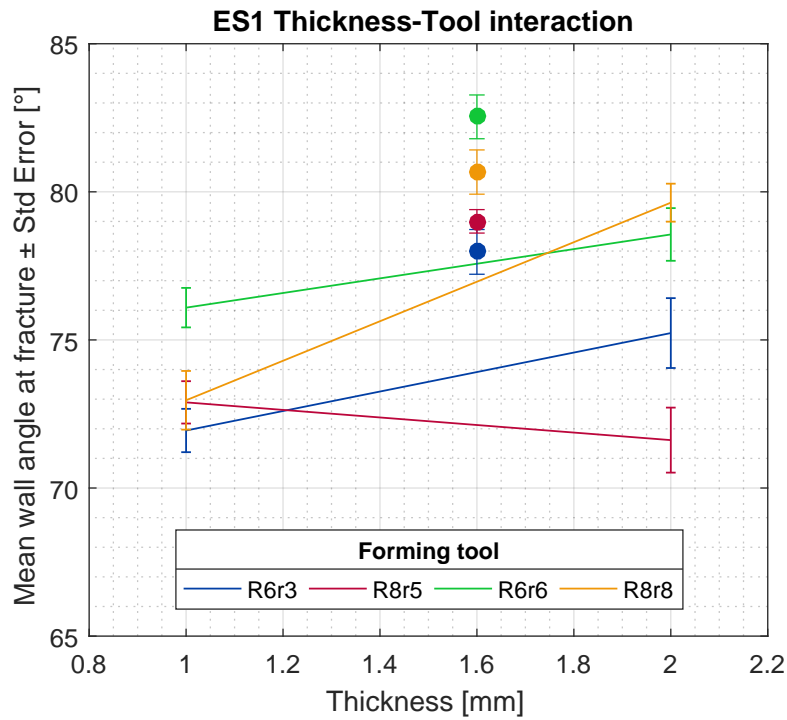


Figure 6.7: Effect of thickness with different tools for Experimental Set 1

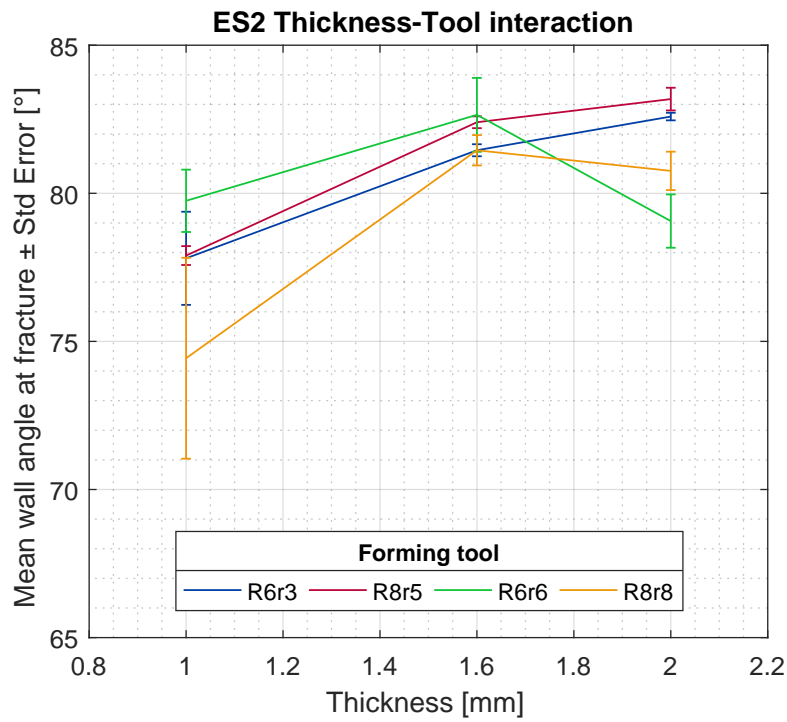


Figure 6.8: Effect of thickness with different tools for Experimental Set 2

In Experimental Set 2, where the step down was maintained constant at 0.5 mm, tool shape was not a significant factor. If tool shape does not have a significant effect on formability in the absence of large values of step down, it may still be a significant factor for geometric accuracy. Along with formability, geometric accuracy was identified in the case studies as a key aspect of forming successful SPIF components.

In fact, the use of a flat versus hemispherical tool seemed to increase the severity of the wall bulge seen in the cushion pan case study (Chapter 4). This observation was not tested more rigorously, so would need further experimentation to draw any conclusions.

6.5.2 Non-linear parameter effects

The effect of thickness is non-linear, though for the results in Experimental Set 2 some tools emphasised this non-linearity more than others. For example, in both sets of experiments the R6r6 tool had greater formability, by a statistically significant margin, at 1.6 mm compared to 1 mm and 2 mm sheet thicknesses. This response is non-linear, visible in both Figure 6.7 and Figure 6.8. On the other hand, in Experimental Set 2 both the flat-ended tools performed best at 2 mm thickness and the worst at 1 mm thickness, demonstrating a linear response (Figure 6.8).

Interestingly, based on the mean wall angle at fracture for each tool, the 'best' tool at 1 mm thickness was the 'worst' tool at 2 mm thickness. From a practical perspective, this highlights a challenge with choosing tools where the formability may be superior in one situation, but poor in another.

It can be concluded that across the specific tools and thicknesses studied the responses have varying degrees of linearity. Furthermore, at each level of thickness there was no pattern to the results when tool shape or tool shaft radius are considered which means more complex effects exist.

If some parameters have non-linear effects on formability this means that there will be an optimal range of values to achieve the best formability. However, this optimal range may change with adjustments in other process parameters because of interaction effects also observed in this chapter.

Moreover, for future attempts at modelling the effect of process parameters, researchers may want to consider non-linear statistical models to determine their correlation with formability results. However, the usefulness of empirical models in SPIF is limited, as indicated by the present results and those from Chapter 5. It is clear that formability in SPIF is influenced by a number of aspects from parameter interactions that produce outliers as a result of severe galling, to non-linearities in the effect of thickness observed with some tools but not others.

6.5.3 Part failure and Contact Pressure

This section discusses the poor outcomes for a small number of the VWACF parts where a flat-ended tool, the largest sheet thickness, and a large step down was used. This parameter combination resulted in grinding (galling) of the sheet, extremely poor surface finish, and correspondingly low formability.

The contact pressure between the tool and the sheet is proposed as an explanation for this. Pressure is a function of force per area, and the flat-ended tools provide a significantly larger contact surface on the sheet compared to hemispherical tools. The step down also changes the contact area somewhat, as it defines how much of the edge of the tool is in contact with the sheet while forming. Furthermore, increased thickness will increase the force required for forming, and the shaft radius of the tool will change the contact area.

Therefore, all the parameters studied in this experiment would affect the contact pressure. The question that follows is to what degree do they affect contact pressure and what are the consequences.

In Tests 14 and 18, where severe galling occurred, the contact pressure would be higher around the small edge radius (r , see Figure 5.2), and lower on the flat base of the tool. This pressure concentration could have increased the friction and initiated galling, which in turn increases friction further and exacerbates the problem.

To understand any relationship between maximum formability and some level or optimisation of contact pressure, further experiments involving force measurement and contact area modelling would need to be conducted.

6.6 Conclusion

This chapter sets out a large-scale investigation into formability in SPIF, based on findings from the literature review. The systematic literature review (§2.3) showed a lack of consensus about the effects of select process parameters, including sheet thickness.

In this chapter, experiments were designed to test two hypotheses: the non-linearity of parameter effects and the significance of parameter interactions. It was proposed that these phenomenon could go some way to explaining the different conclusions seen across the literature around formability in SPIF.

The method of formability comparison was to use the fracture point of variable wall angle conical frustum (VWACF) parts. In the previous chapter these test parts were found to be the most efficient and consistent measure of formability level.

The results from the two experimental sets in this chapter have led to a number

of insights: firstly, a strong effect of step down on formability, where a smaller value of step down will increase the fracture angle. In this case an increase of 10° was the result when the step down was decreased from 2 mm to 0.5 mm. This conclusion is in line with the majority of papers from the literature review (Chapter 2) that studied the effect of step down.

Secondly, both tool shape, and the interaction of tool shape and step down, were significant in their effect on formability in Experimental Set 1. No precedent has been set for this finding in the literature as tool shape has not been the study of interactions in the past.

The effect of step down and tool shape was that the flat-ended tools performed significantly worse than hemispherical tools when a larger value of step down was used (1 mm or 2 mm). However, in Experimental Set 1 the flat-ended tools showed higher average formability with the minimum step down (0.5 mm). This is an important consideration for future work when selecting the tool shape and process parameters.

The results from this investigation suggest the idea that contact pressure plays a role in the success or failure of parts in SPIF, discussed in §6.5.3. Contact pressure is a process factor that changes in response to a number of parameters including tool size, step down, sheet thickness, and particularly tool shape.

Tool shape was a significant factor in the presence of a poor interaction with step down, but without this effect it was not found to have a strong effect on formability. However, it has been noted in §4.2 of the case studies chapter that tool shape may influence the geometric accuracy outcome of a SPIF component or prototype. This concept forms the basis of the investigation carried out in the following chapter, *The impact of tool shape on wall bulge in flat-walled SPIF parts*, Chapter 7.

The impact of tool shape on wall bulge in flat-walled SPIF parts

This chapter looks at wall bulge in flat-walled SPIF parts, based on insights from the literature review (Chapter 2) and the case studies (Chapter 4). The literature showed that pillowing in the flat base of SPIF parts was the subject of a number of studies. However, a similar mode of error of bulging in flat walls had not been extensively investigated. Tool shape was identified as having a significant effect on pillowing, but no corresponding research on wall bulge had been carried out.

The wall bulge phenomenon was identified in the cushion pan component (§4.2), where a flat section of the part showed a peak of 7 mm deviation error. The novel research in this chapter aims to investigate whether the choice of flat or hemispherical tool shape could improve or eliminate the the wall bulge error in SPIF parts.

7.1 Background

Prototypes in a production context should, among other requirements, accurately reflect the geometry of the final component. While SPIF is a promising method of prototyping, geometric accuracy is a continuing issue. A significant factor in this is springback, which occurs in any sheet forming operation. Springback may even be exacerbated in SPIF by the incremental process and small tool (Micari, Ambrogio, and Filice, 2007).

Improving geometric accuracy is a priority for using SPIF in practical applications such as prototyping. Allowing designers and engineers to rapidly form a geometrically accurate prototype of the final part will help determine whether the design is correct or whether it needs further revision to meet requirements. Furthermore, the flexibility of SPIF means that revisions can be implemented to the CAD model and a new prototype can be quickly produced.

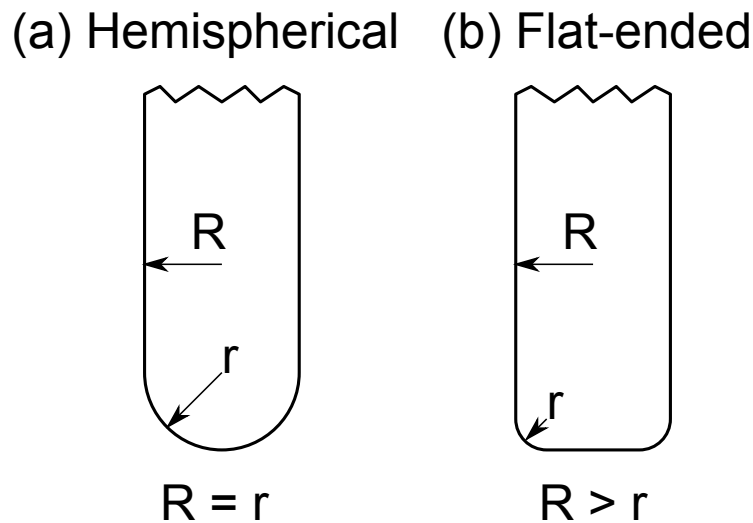


Figure 7.1: Hemispherical and flat-ended tool cross-sections, including dimensions.

While multiple types of forming tools have been used for SPIF in the past, by far the most common tool is a solid, hemispherical-ended tool (McAnulty, Jeswiet, and Doolan, 2016). Figure 7.1 (a) shows the profile of this type of tool. Other types include non-hemispherical-ended tools such as the flat-ended tool in Figure 7.1 (b), and ball-bearing tools.

7.1.1 Hypothesis

Based on the literature review (§2.4) and the observations from the cushion pan case study (§4.2.2), the hypothesis for the results of this work is outlined below.

Flat-ended tools reduce pillowing in the flat base of SPIF parts compared to hemispherical tools (Isidore et al., 2016), but concurrently increase the bulging in flat walls. This is due to the manifestation of springback and related build-up of stress in the part. Differently shaped tools allow different material flow trajectories, for example a flat-ended tool without a lower point allows greater material flow from the base to the wall of a part.

7.1.2 This work

At a high level, this research looks at the effect of tool shape and size on the geometric accuracy of SPIF parts. The differences in geometric error between test parts are analysed to determine this effect.

More specifically, the characteristic wall bulge error observed in the cushion pan case study is studied by forming flat-walled parts with different tools. This type of

error is directly relevant for prototyping components, especially if the part is large with significant flat-walled areas.

7.2 Method

A set of nine tools were used in this study and two repeats of a truncated pyramid shape were formed using each tool. The level of wall bulge in the truncated pyramids was measured by scanning the interior formed surface of the parts using a Faro Arm, and calculating deviation from the CAD model.

7.2.1 Tool design

This study uses hemispherical and flat-ended tools, previously defined in Figure 2.4.

No initial limitations existed for the specific sizes of these tools, or how many should be tested. Requirements were developed based off the hypothesis and the fact that the tools would also need to be appropriate for a parallel investigation into formability. Final requirements are laid out in Table 7.1. It was important to design a well-distributed set of tools, so no two tools were too similar such that no useful comparative information would be generated.










Table 7.2 lists the tools designed for the experiments. A metric for ‘flatness’ was defined to allow a comparison between tools of different sizes. This was the edge radius divided by the shaft radius, r/R . Examples of flatness for different shaped tools are shown in Table 7.2. Consistent with the tools used for the study in Chapter 6, as described in §6.2, a small dimple was machined into the base of the flat-ended tools to eliminate the stationary point.

Table 7.1: Requirements for tool designs

Geometric accuracy
Multiple shaft radii (R)
3 different edge radii (r) for each shaft radius (R)
The difference in flatness of the tools for a single shaft radius will not be less than $0.15 * r/R$
Formability
At least 2 pairs of tools with identical r , but different R .
The difference in flatness of the two tools within a pair will not be less than $0.1 * r/R$

The tools were manufactured from AISI O1 silver steel on a CNC lathe and polished after turning. The tip of each tool was hardened by heating to cherry red and quenching in oil. Final polishing of the tools with 1200 grit wet sandpaper and

Table 7.2: Hemispherical and flat-ended tools

Tool #	Tool name	Shaft radius R [mm]	Edge radius r [mm]	Flatness r/R	Tool shape	Cross section
T1	R5r1	5	1	0.2	Flat-ended	
T2	R5r3.5	5	3.5	0.7	Flat-ended	
T3	R5r5	5	5	1	Hemispherical	
T4	R7r2	7	2	0.29	Flat-ended	
T5	R7r3.5	7	3.5	0.5	Flat-ended	
T6	R7r7	7	7	1	Hemispherical	
T7	R10r2	10	2	0.2	Flat-ended	
T8	R10r5	10	5	0.5	Flat-ended	
T9	R10r10	10	10	1	Hemispherical	

scotch-brite was carried out before they were used to remove the carbon coating left by the quenching process and ensure an adequately smooth surface.

7.2.2 Test shape design

In the literature (§2.4) and in the Case Studies chapter of this thesis (§4.2.2), bulging has been shown to occur in flat walls of SPIF parts. To induce wall bulge in the tests, a pyramidal frustum shape was chosen as it has four flat walls. Bambach, Taleb Araghi, and Hirt (2009) showed larger parts had larger geometric error due to wall bulge, so the major dimensions of the pyramid were set to 200 mm squared.

Consistent with a number of previous test parts in the literature, the wall angle of the test shape was 55° (Behera, Verbert, et al., 2013; Bambach, Taleb Araghi, and Hirt, 2009; Al-Ghamdi and Hussain, 2015). This wall angle is also within the safe forming limit of this material to avoid the possibility of fracture.

A depth of 75 mm was chosen for the truncated pyramid to optimise the area of the walls and the base. To prevent a sharp corner in the toolpath which would

prevent smooth movement of the tool from one side to another, the edge radius of the model was 15 mm in the horizontal plane. This radius was slightly larger than the minimum 10 mm radius required to accommodate the 10 mm radius tools. All parameters for the test geometry are presented in Table 7.3.

7.2.3 Experimental method

The SPIF process used for this investigation is consistent with the methodology outlined in Chapter 3. Specific details of the process and experimental parameters for the tests are covered in this following section. The key material properties for the 1 mm sheet were obtained from tensile tests. Results are shown in Table 7.3 under ‘Material properties’.

Process settings were chosen based on past experience and knowledge of the literature. For example, 0.5 mm step down results in a quality surface finish but reduces forming time compared to a smaller value such as 0.1 mm. A spindle speed of 1000 RPM can provide heating benefits to formability but is not high enough to risk galling on the sheet surface. The lubricant was mineral gearbox oil as it has a high viscosity and adheres to the sheet metal during forming.

A spiral toolpath was selected as it eliminates the ‘seam’ that is seen in constant Z-level toolpaths where the tool steps downwards. A ‘seam’ on the interior of the part may show up on the scanned surface and interfere with the results. Climb milling direction was used as it involves the tool rolling over the sheet, which reduces the sliding distance and generated friction (Eyckens et al., 2010).

SPIF has been found to have high repeatability in past studies including Buffa, Campanella, and Fratini (2013) and Centeno et al. (2014), so tests were only repeated twice for time efficiency.

As described in §3.3, a surface mesh of the inside of each test part was recorded using a Faro Arm laser scanning probe and the Geomagic Qualify software package. The surface mesh was aligned with the CAD model in Geomagic so a 3D comparison could be carried out. An example of the output of this comparison is shown in Figure 7.4, where the colour scale indicates the degree of positive and negative geometric error. Deviation data along each wall and the base was exported for the analysis presented in the following section.

It is worth noting that the raw formed surface of the parts was too reflective for the laser scanner and produced erroneous spikes or gaps in the scan data. This issue was identified in Ham and Jeswiet (2008) and the authors investigated several options for surface treatments to solve the problem. They found that aerosol deodorant facilitated the best result for the laser scanning data, so this also applied to the current wall

Table 7.3: Constant experimental parameters

Parameter	Value
Test geometry dimensions	
Part shape	Truncated square pyramid
Upper part size	200 mm x 200 mm
Wall angle	55°
Depth of pyramid	75 mm
Radius of edges	15 mm
Process settings	
Step down	0.5 mm
Spindle speed	1000 rpm
Feed rate	5000 mm/min
Milling mode	Climb (rolling)
Toolpath type	Spiral
Lubrication type	Mineral gearbox oil
Tool material	Hardened silver steel
Test repeats	2
Material properties	
Material type	AA5005-H34
Material thickness	1 mm
Modulus of Elasticity	69 GPa
Yield Stress	133 MPa
Ultimate Tensile Strength	153 MPa

bulge test.

The aerosol deodorant is sprayed in an even layer on the internal area of the truncated pyramid, which dries into a thin, frosted, and highly unreflective layer. This treatment successfully eliminated all reflection issues with the laser scanner.

7.2.4 Strain analysis

To study any differences in the thickness strain across the walls of the test parts, a digital image correlation system (DIC) called ARAMIS was used on selected tests. Those parts with the highest and lowest wall bulge results were repeated in order to carry out the strain analysis process.

ARAMIS uses stereoscopic cameras to detect changes in a stochastic pattern on the surface of a material, translating to surface strain. The setup and required stochastic pattern are shown in Figure 7.2. The cameras are calibrated before any experiments are undertaken.

The process to measure strain on a SPIF part is as follows.

- Clean material and roughen surface slightly to reduce shine.
- Coat material in white silicon-based spray paint, allow to dry for 5 minutes.
- Spray black paint over white to create optimal speckle pattern.
- Capture image of material in set location using ARAMIS cameras.
- Immediately form SPIF part with painted side of material facing down.
- Remove formed component and capture second image of material in same location using ARAMIS cameras.
- Calculate strain over photographed surface.
- Export strain data from cross-sections of surface.

This method is in contrast with the designed application of ARAMIS, which is to capture regular images of a deformation process such as a tensile test. So while larger strains (large deformation of the stochastic pattern) in a SPIF part are unable to be associated with the pre-formed sheet, moderate strains such as those seen in this 55° truncated pyramid are detectable.

Strain grids were an alternative method to find surface strain, but the resolution and accuracy is not as high as ARAMIS. This is due to manual measurement of the circles and large diameters (e.g. 2 mm) compared to the size of the speckles on ARAMIS' stochastic pattern.

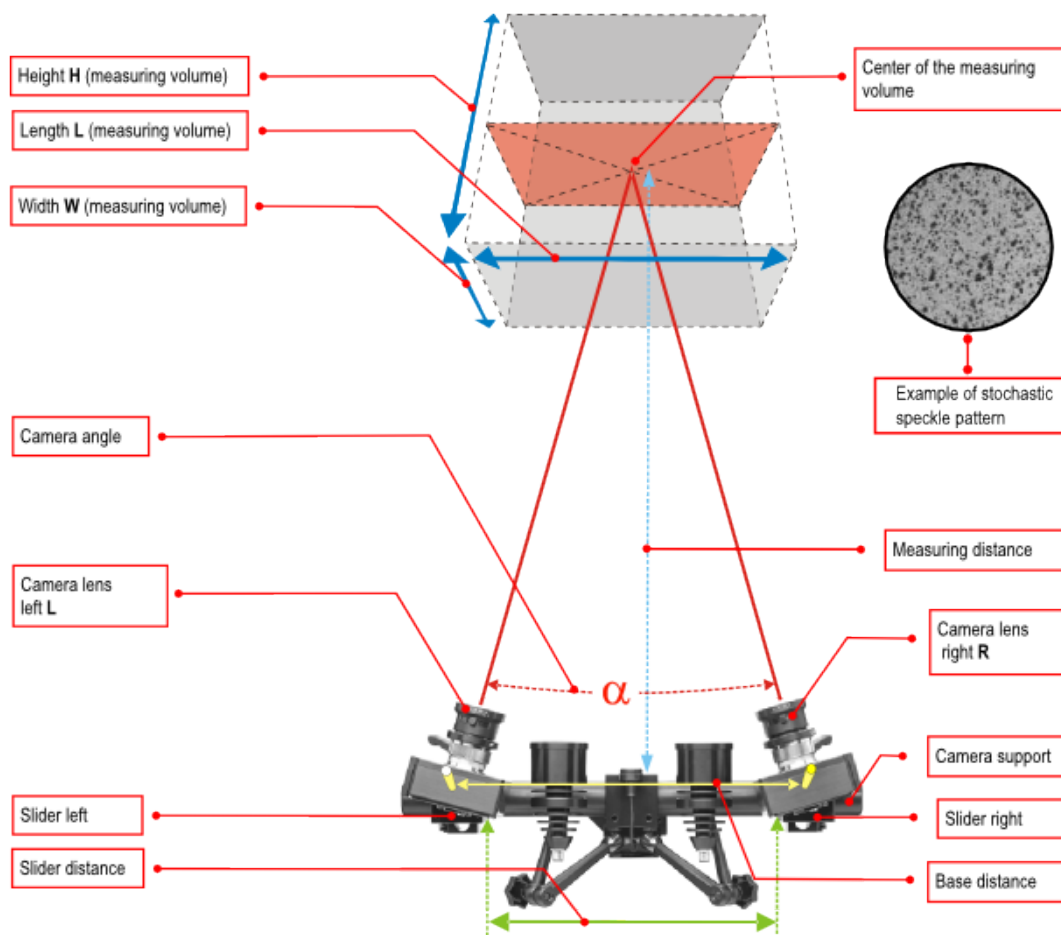


Figure 7.2: Schematic of the ARAMIS digital image correlation system for determining surface strain.

7.2.5 Statistical analysis method

The results generated from the experiments in this chapter are statistically analysed to determine the significance of the parameter effects. A correlation function is used for this purpose. The significance of correlation between the designated response data and the tool parameters (tool shaft radius, edge radius and flatness ratio) is run in **R** using the Pearson coefficient. The correlation function is `cor.test` which shows the correlation coefficient and the statistical significance of the correlation for the response variable and the selected tool parameter.

7.2.6 Formability assessment

To assess the material formability with each tool, VWACF test parts were formed alongside each truncated pyramid test. The method for producing the VWACF parts is consistent with §3.2. Fracture depth results are converted into wall angle at fracture values to allow statistical analyses to be carried out, as described in §7.2.5. The response data for formability is the wall angle at fracture.

7.3 Results and discussion

In this section, the results of the laser scanning are presented and analysed. Data was obtained from all 18 test parts, an example of which is shown in Figure 7.3 with the deodorant-covered matte internal surface clearly visible.

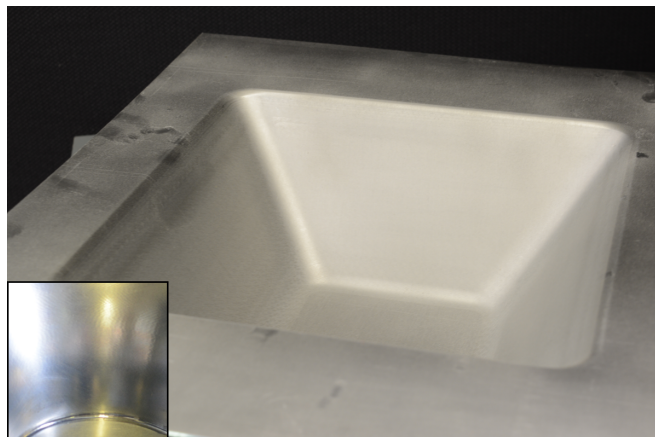


Figure 7.3: Photo of a formed truncated pyramid component showing matted internal surface. Inset: a reflective incrementally formed surface before treatment.

Geometric deviation results were exported in the form of 3D surfaces and 2D cross sections, shown in Figures 7.4 and 7.5 respectively.

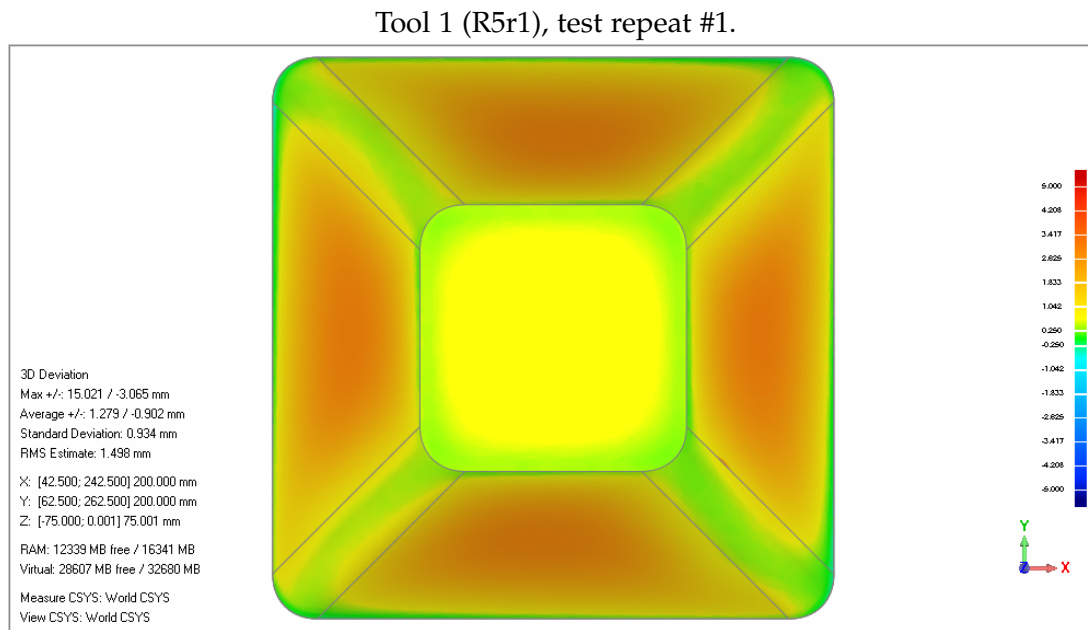


Figure 7.4: Top view of truncated pyramid test part. Colour scale from +5 mm (red) to -5mm (blue)

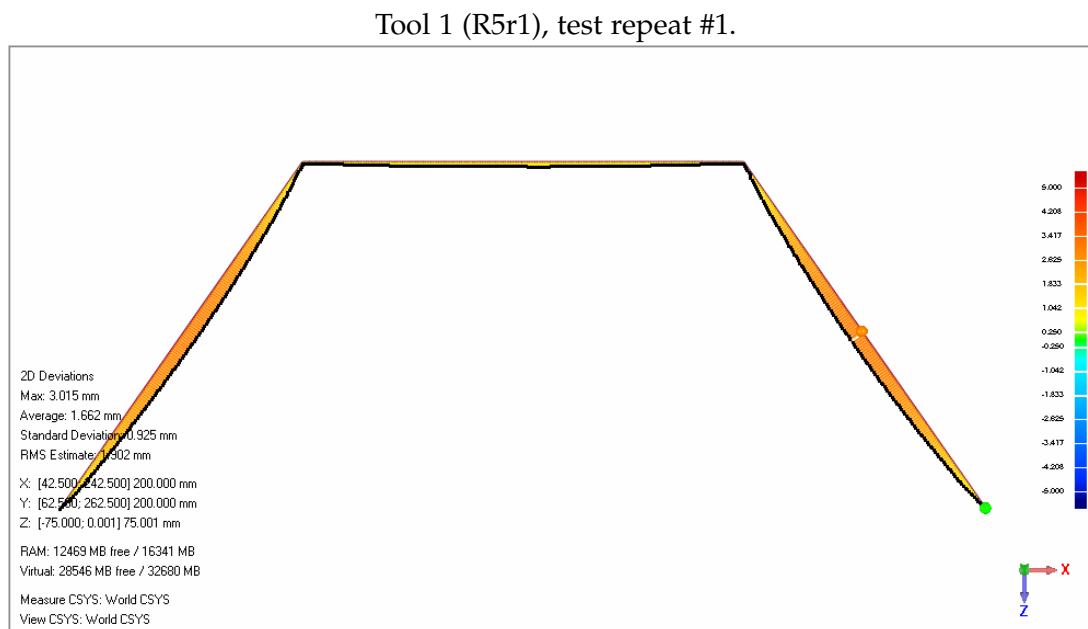


Figure 7.5: Cross-section deviation view of truncated pyramid test part. Colour scale from +5 mm (red) to -5mm (blue)

The areas with the largest geometric error were the four walls of the truncated pyramid. In Figure 7.4, the maximum deviation is 3.02 mm. The colour scale shown is from +5 mm (red) to -5mm (blue), however no negative error, or bulging away from the internal surface, was observed in any of the test parts.

The 3D surfaces appeared to show twisting of the part compared to the CAD model. The twisting does not extend into the walls of the truncated pyramid, so does not affect the maximum wall bulge results. This is an interesting phenomenon, and similar types of error have been reported in the literature (Vanhove, Verbert, et al., 2010), but it is outside the scope of the present study to investigate further (see §7.4.1).

7.3.1 Wall bulge

The results from each test repeat show good repeatability for each tool. The maximum deviation for each wall of every test part is plotted in Figures 7.6 and 7.7, along with an average result for each tool. The repeatability for the maximum wall bulge results is high. The data are plotted against tool flatness (r/R) and shaft radius (R) respectively. The results in Figure 7.6 have been scattered slightly on the x-axis to differentiate clustered points. The points are colour-coded based on shaft radius and each point is labelled with the tool name.

These results show a trend between deviation and tool shaft radius, clearly shown in Figure 7.7. As R increases, so too does the variation in results between the respective trio of tools. Overall variation for the average wall bulge is only 0.6 mm for R5 tools, 1.12 mm for R7 tools, and 2.43 mm for R10 tools.

As a consequence of the large overall variation between the R10 results, both maximum and minimum wall bulge results are produced by 10 mm shaft radius tools - R10r5 and R10r10 respectively. The hypothesis is supported with this result, as a flat-ended tool has the largest wall bulge result by a significant margin.

7.3.1.1 Statistical analysis

Determination of the significance of parameter effects was carried out using the method described in §7.2.5. The **R** analysis results in Table 7.4 showed that there is a significant linear correlation between the wall bulge results and both edge radius and tool flatness ratio.

There is a significant difference between the wall bulge which resulted from using hemispherical tools compared to flat-ended tools. The p-value for a t-test between the two samples returned a p-value of $9.307 * 10^{-15}$.

Based on t-tests, the wall bulge results for all tools are significantly different to one another with a significance level of 99.9% or greater, except for one pair. This exception

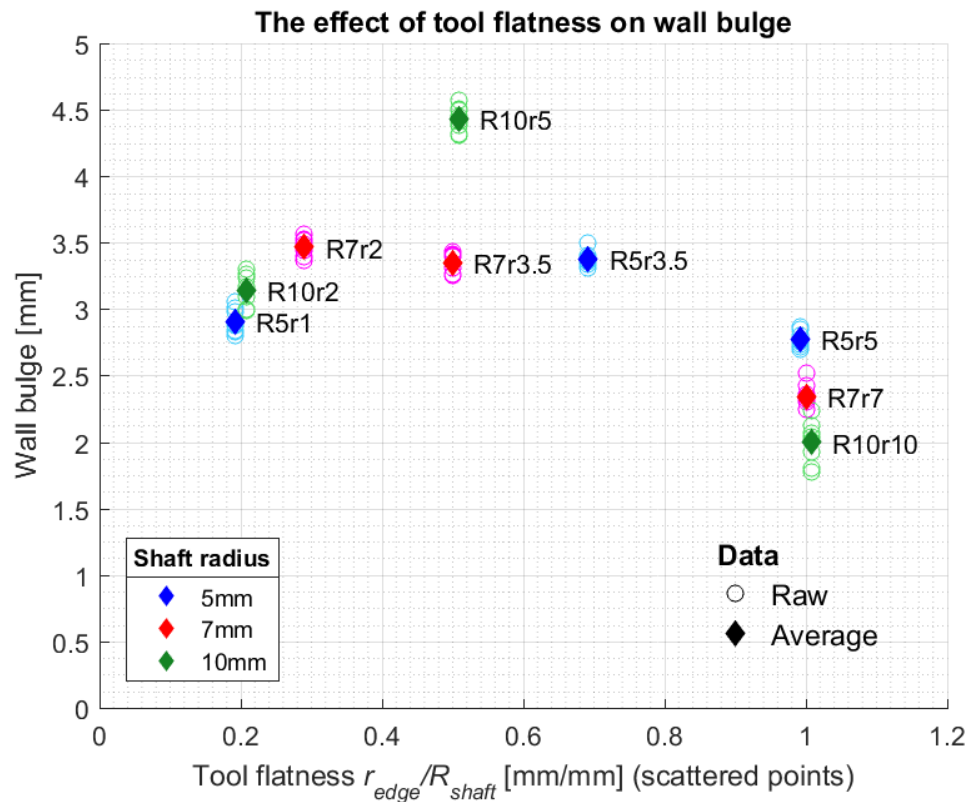


Figure 7.6: Maximum wall bulge plotted against tool flatness ratio

Table 7.4: Linear correlations of parameters and maximum wall bulge

Parameter	Correlation p-value	Significance (0.05 sig. level)
Shaft radius	0.3676	Not significant
Edge radius	$2.784 * 10^6$	Significant
Flatness ratio	$6.77 * 10^7$	Significant

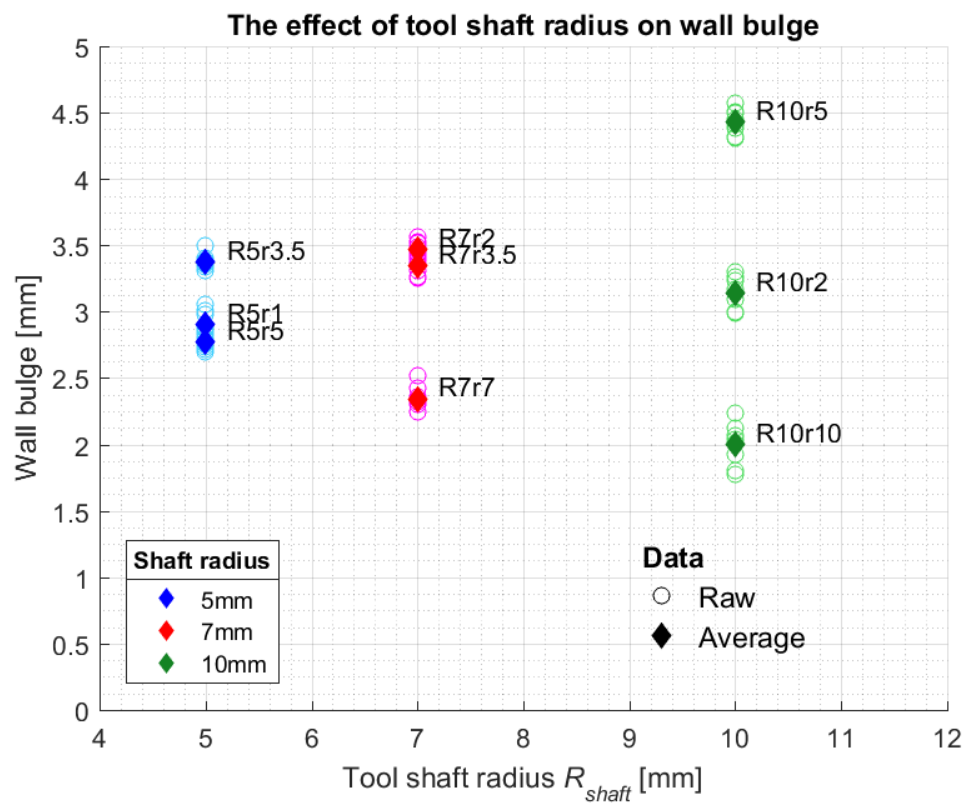


Figure 7.7: Maximum wall bulge plotted against tool shaft radius

is the two tools R7r2 and R5r3.5, which are only 98.87% likely to be significantly different.

As the results for each tool are significantly different, it is worth noting some trends in the data. The highest average wall bulge for each R set is produced by a flat-ended tool, and the three hemispherical tools generated the lowest average wall bulge.

Only in the R7 set of tools was the highest wall bulge result caused by the flattest tool, R7r2. For the other two shaft radius sets it was the mid-range flatness tool, most significantly with R10r5 which caused the most severe wall bulge. It may, therefore, be an unacceptable trade off to use this large shaft radius, mid-range flatness tool. It causes such large geometric error in the walls that any benefits such as minimum pillowing may not be worthwhile.

From the results presented in this section, it can be concluded that as shaft radius increases, the potential impact of the use of a flatter tool becomes more significant.

7.3.2 Pillowing

The maximum deviation in the base of each part ('pillow' height), is plotted against tool edge radius (r) in Figure 7.8. The points have been scattered horizontally to differentiate between clustered points.

Pillowing was observed in the truncated pyramids, but mostly smaller than 1 mm pillow height. The magnitude was less than the maximum wall bulge, and also less than other instances of pillowing from the literature, for example in Al-Ghamdi and Hussain (2015) with a pillow height of 3.5 mm.

7.3.2.1 Statistical analysis

Consistent with the wall bulge results, the pillow height data was analysed using the method in §7.2.5. The **R** statistical analysis results in Table 7.5 show the significance of each parameter effect. There is a significant linear correlation between the pillow height and both edge radius and shaft radius, using a 0.05 significance level. Decreasing both edge radius and shaft radius caused an increase in pillow height, a finding which agrees with the conclusion from Hussain (2014). In their work, which only looked at hemispherical tools, a smaller shaft radius increased the pillow height. The present research indicates that the edge radius of the tool is the underlying reason for their results.

Based on a Student's t-Test, there is no significant difference between the pillow height in the tests formed with hemispherical tools compared to flat-ended tools. However, previous research by Isidore et al. (2016) has shown that flat tools decrease

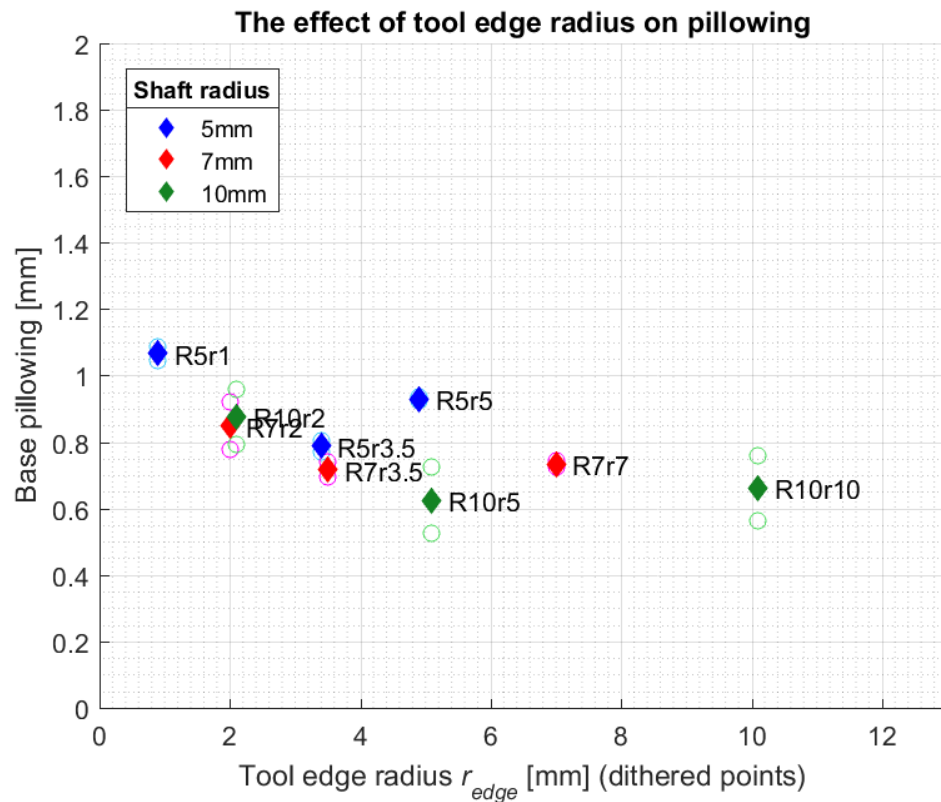


Figure 7.8: Maximum base deviation (‘pillow height’) plotted against tool edge radius

Table 7.5: Linear correlations of parameters and maximum pillow height

Parameter	Correlation p-value	Significance (0.05 sig. level)
Shaft radius	0.01621	Significant
Edge radius	0.00828	Significant
Flatness ratio	0.126	Not significant

pillowing compared to hemispherical tools. The current results do not specifically agree with their findings but neither is there conflict.

7.3.3 Strains and material flow

A new strain model for SPIF was presented in Bambach (2010). Prior to this model, the sine law presented an effective but simplistic way of predicting the strain in SPIF. This new model from Bambach accounted for the existence of some minor strain in SPIF parts, rather than pure major strain based on the material movement principle behind the sine law. Through experiments, it was demonstrated to be more reflective of actual strain profiles in SPIF parts.

Figure 7.9 and Figure 7.10 present concepts which go some way to explaining the pillowing phenomenon as it occurs with the use of hemispherical tools, and how the use of flat-ended tools does not cause pillowing to the same degree. Figure 7.10 suggests increased material flow from the base to the wall of the SPIF part, which may explain the increased wall bulge error.

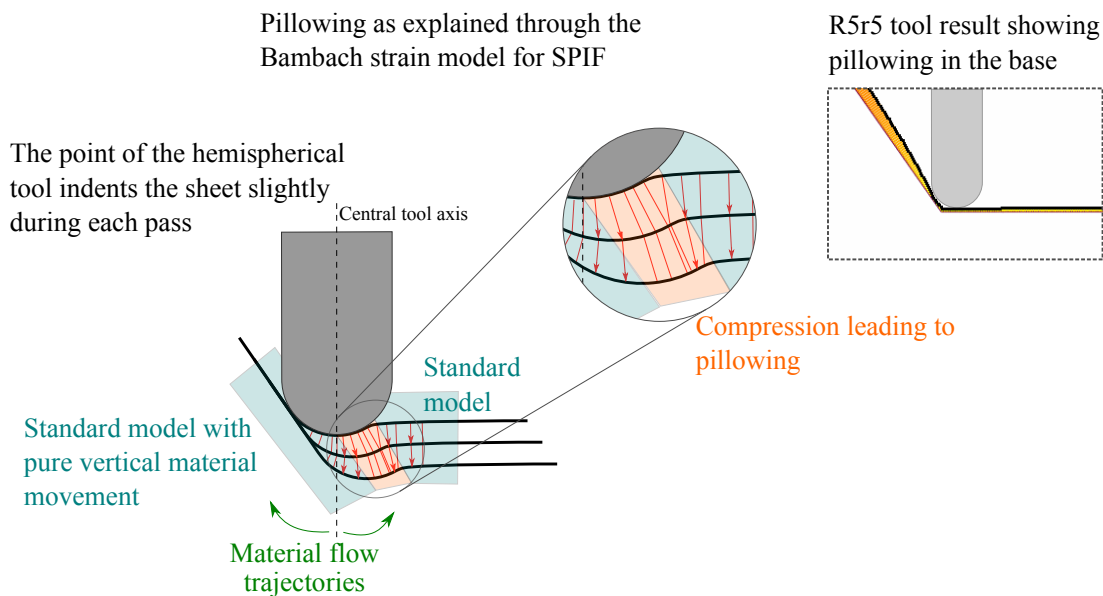
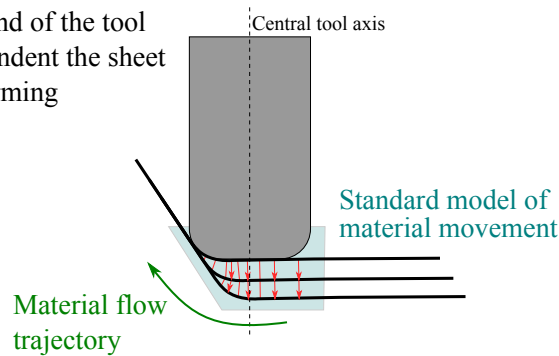


Figure 7.9: Interpretation of Bambach SPIF strain model to explain pillowing using a hemispherical tool.

To investigate the mechanism of wall bulge, selected tests were repeated in order to measure the cross-sectional thickness strain along the flat walls. Surface strain results were obtained using ARAMIS, described in §7.2.4, which allowed cross-sectional data to be exported for analysis. Figure 7.11 shows one of the tests after forming.

The reduction of pillowing and increase in wall bulge with flat-ended tools explained through Bambach strain model for SPIF

The flat end of the tool does not indent the sheet during forming



R10r5 tool result with reduced pillowing in the base and a larger degree of wall bulge

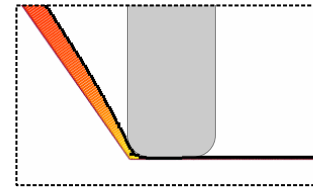


Figure 7.10: Translation of Bambach SPIF strain model to a flat-ended tool scenario.

The recorded cross sections were perpendicular to the undeformed sheet and the base of the wall, as shown in Figure 7.12. Predicted strain was calculated for the truncated pyramid geometry and compared to the measured strain.

The repeated tests used the tools that had induced maximum and minimum wall bulge, R10r5 and R10r10 respectively. This was to ensure any difference in thickness strain would be more likely to show clearly on the plots.

In addition, a tool with the same edge radius as R10r5 was used to form a third strain test. This test, using the R5r5 tool, aimed to look for any difference or similarity between tools with constant edge radius (r) but varying shaft radius (R).

Figure 7.13 shows the thickness strain obtained by the ARAMIS system from the three additional tests. Multiple sections were used for each strain surface, resulting in multiple lines plotted for each test. The thickness strain prediction, calculated using the sine law, is also shown on the graph. There is good agreement between the measured strain in steady-state and the predicted strain for all tests.

Also in Figure 7.13 is a cross-sectional representation of the truncated pyramid part. This is correlated vertically with the strain measurements such that the strain features correspond to the geometry features.

For all three tests a thinning band was observed, as described in Young and Jeswiet (2004), where the thickness strain peaks during the initial stages of forming. In this case, the thinning band occurred at a depth of approximately 7 – 17 mm. Figure 7.14 shows a closeup, delineated by the grey box in Figure 7.13.

The section of the plot showing negative thickness strain is due to compression of

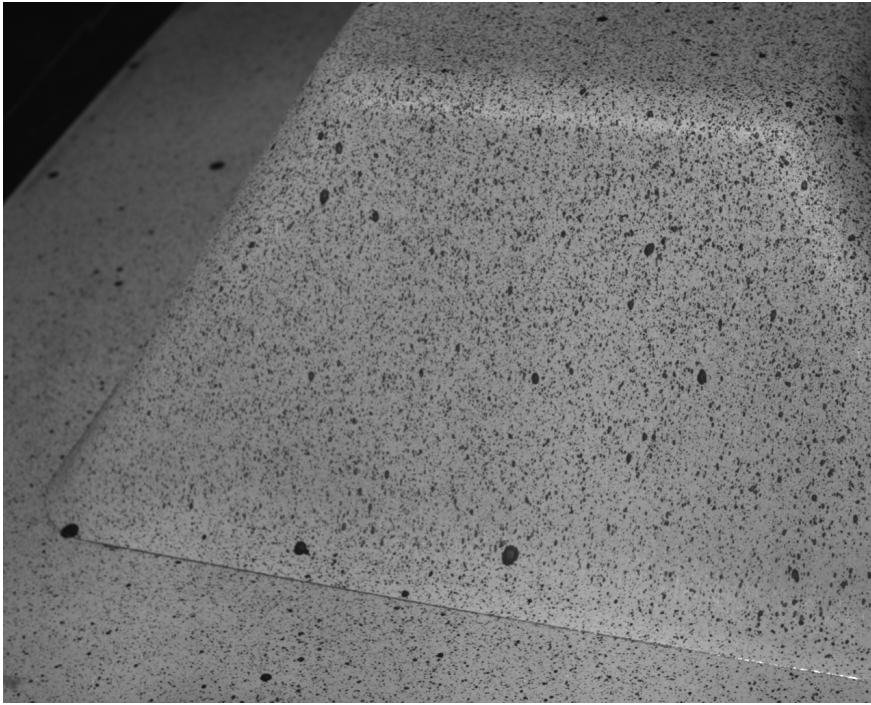


Figure 7.11: Image from the stereoscopic camera in the ARAMIS system showing the stochastic pattern on the final formed T9 part.

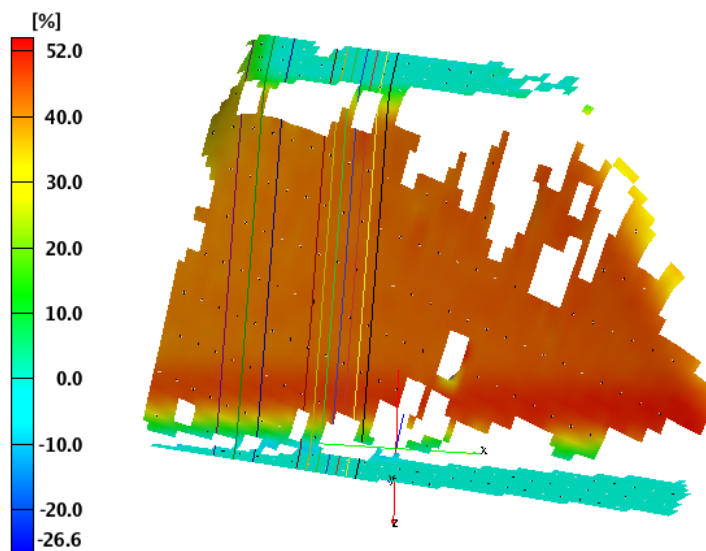


Figure 7.12: Strain surface generated from the ARAMIS system showing sections which were exported. Thickness strain colour scale is shown on the left.

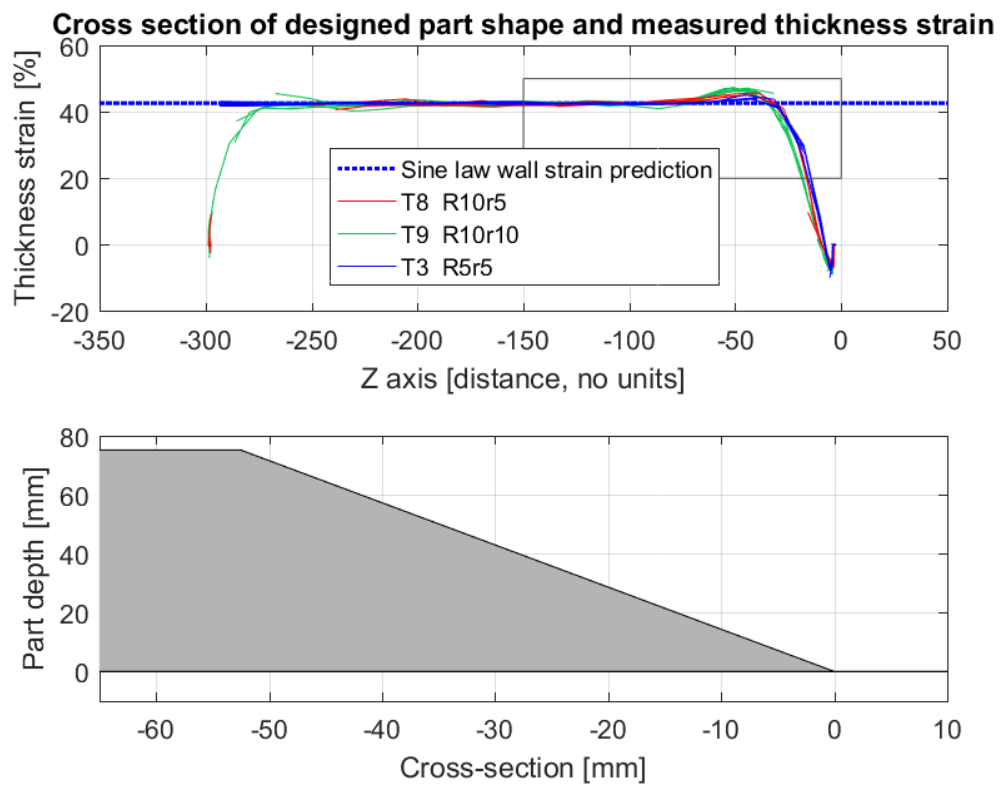


Figure 7.13: Cross-sectional strain for Tool 3 (R5r5) Tool 8 (R10r5), and Tool 9 (R10r10). The top graph of measured thickness does not have distance units because the ARAMIS strain data export cannot triangulate physical distance on the photographed part.

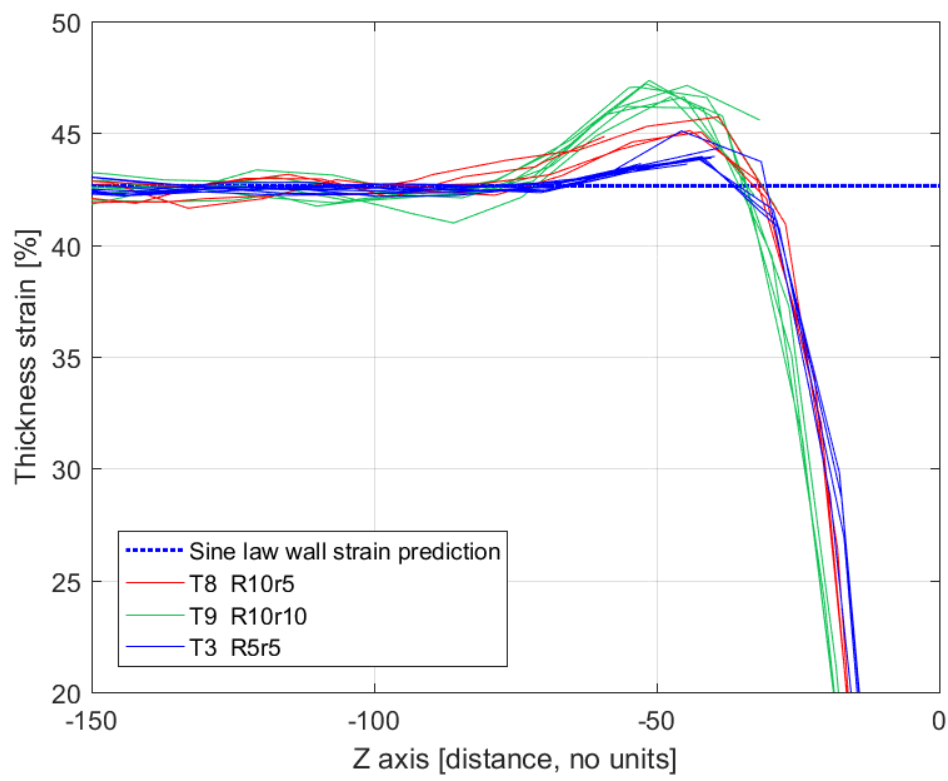


Figure 7.14: Cross-sectional strain for Tool 8, R10r5, and Tool 9, R10r10

the sheet material where it bends around the backing plate.

The strain results showed consistent strain in the walls of the part, aligning with the sine law predictions. The differentiating factor between the three tool results was the peak in thickness strain in the initial phases of forming (the thinning band).

The largest wall bulge tool (R10r5) did not definitively have the highest or lowest peak in thickness strain. However, the tool that caused the least amount of wall bulge (R10r10) had the highest thickness strain peak.

The other two tools, R10r5 and R5r5, have lower peak strains. From this data, the smallest tool appears to have the lowest peak strain in the thinning band. While the two 'r5' tools have somewhat similar strain distributions, they are not identical and therefore edge radius (r) is not an independent factor in determining the characteristics of the thinning band.

Proposing a reason that a more severe thinning band leads to a higher pillow in the base of the part, the stretch may lead to more material being pushed towards the base of the part. Concurrently, increased thickness strain in the thinning band leads to less wall bulge because the wall is less stiff - it is weakened as a result of the thinning band.

The limitations of the ARAMIS setup meant that it was not possible to obtain good strain data around the bottom edge of the parts. It is possible that interesting strain features may have been visible in this area, in the same way that the thinning band is clearly visible in Figure 7.13. This is proposed as further work in §7.4.1.

7.3.4 Formability analysis

In addition to the wall bulge tests, the tools for this experiment were designed to allow pair-wise comparisons of formability to be made between tools with the same flatness ratio or edge radius. The formability results are plotted in Figure 7.15.

As described in §7.2.5, a process of statistical analysis was carried out using the fracture angle results. The correlations and significance are shown for each parameter in Table 7.6.

Table 7.6: Linear correlations of parameters and fracture angle

Parameter	Correlation p-value	Significance (0.05 sig. level)
Shaft radius	0.01169	Significant
Edge radius	0.9656	Not significant
Flatness ratio	0.07758	Not significant

No significant difference was found between the fracture angle results of the combined flat-ended tools compared to the hemispherical tools.

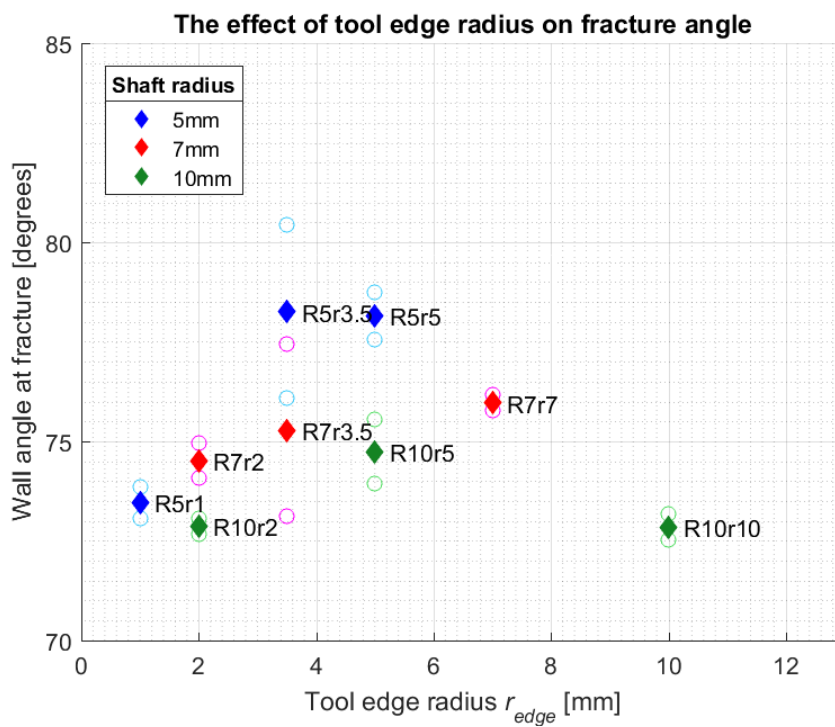


Figure 7.15: Wall angle at fracture results from the VWACF formability tests, plotted against the tool flatness ratio (r/R). Raw data indicated by circles, average by diamond.

As shown in the research discussed in the literature review (Chapter 2), the shaft radius (R) has a significant effect on formability. However, neither edge radius (r) or flatness ratio (r/R) show any significant linear correlation to the fracture angle. Therefore, based on this experiment and analysis, no conclusions can be drawn about the effect of these latter two parameters on the formability of VWACF parts.

7.4 Chapter summary

This chapter has investigated the effect of parameters on geometric accuracy in SPIF. Specifically, truncated pyramid test parts were formed with flat-ended and hemispherical tools of different sizes to determine their impact on wall bulge.

The highest level of deviation in the walls of the truncated pyramid test parts was seen when flat-ended tools were used. The three hemispherical tools induced the lowest amount of wall bulge. This result supports the hypothesis presented in §7.1.1.

The interaction between tool shaft radius and the flatness ratio indicates that a wider range of wall bulge is seen with different tool shapes when the shaft radius is larger. Tools with 10 mm shaft radius showed more variation in wall bulge results with different flatness ratios. Conversely, the flatness of a tool was seen to make little difference to the amount of wall bulge error when the shaft radius was small, for example 5 mm.

Pillowing was observed in the base of the parts, with a statistical analysis showing a significant correlation between the pillow height and the tool edge and shaft radii (r and R). Smaller values of both these parameters resulted in a greater pillow height, consistent with previous pillowing research.

The combined result of these findings is that a larger flat tool may reduce the pillowing but could result in severe wall bulge. This was seen specifically with the parts formed using the R10r5 flat-ended tool. Therefore, a trade off between pillowing and wall bulge exists. This result has not been previously shown in the research literature.

An explanation of the mechanisms behind pillowing and wall bulge has been proposed based on the strain model from Bambach (2010). It suggests that material compression from the hemispherical tools leads to pillowing, whereas material flow is facilitated by the large flat surface area of the flat-ended tools.

A VWACF formability assessment of each tool was carried out, and statistical analysis showed a correlation between the fracture angle and the shaft radius. Overall, tools with a smaller shaft radius showed increased formability and fractured at a larger wall angle.

7.4.1 Further work

Directions for future work in this space are outlined below.

- Assess the trade-off between wall bulge and pillow height in further detail, including the effects of metallic and non-metallic material type or other process parameters.
- Investigate the relationship between wall bulge and wall angle. Research has shown an increase in pillowing in conical frustums as the wall angle Φ decreases (Hussain, 2014). This understanding could help in situations such as forming surface design for a SPIF part, where a designer has flexibility in the orientation of the original component. Optimising the wall angle of features such as large flat walls may provide an effective method to increase the geometric accuracy.
- Understand the twisting observed in the geometric accuracy results of the truncated pyramid components. The choice of tool or the toolpath direction may have an effect on the twisting in the centre stage of forming. There may also be an effect of deformation rate or feed rate, where a slower feed rate could reduce the amount of twisting.
- Conduct work to verify the strain model by Bambach (2010) as relates to, and possibly explains, the variation in wall bulge with different degrees of tool flatness. This would include measuring strain around the bottom edge of the part to look for any pillowing or wall bulge indicators.

Discussion

This chapter discusses the findings of this thesis, with the aim of placing the results in context with the broader understanding of SPIF. Firstly, the results described in the previous chapters are briefly reiterated. Secondly, the implications of these findings are discussed with respect to the aim of the thesis. The chapter concludes with a summary of the significant insights from this work.

To reiterate from Chapter 1, this thesis aimed to progress SPIF towards an industrially viable process. This is one where effective components can be produced that will not fail due to fracture and that will have an acceptable final geometric accuracy. To achieve this, the work carried out in this thesis looked at the effect of process parameters on material formability and geometric accuracy. A greater understanding would allow the best parameters to be selected for the situation to eliminate the aforementioned issues.

8.1 Summary of findings in this thesis

The case studies in Chapter 4 emphasised issues which might occur for a SPIF prototype in an industrial context. These include having to form multiple iterations of a component before success is achieved, leading to time lost in the production cycle. This issue arose in the case studies due to the material exceeding the formability limit and resulting in a fractured component.

Furthermore, obtaining the geometric accuracy tolerance required for a functional prototype part is hindered by typical modes of geometric error in SPIF, such as large deviations in flat sections of a part.

The aim of Chapter 5 was to understand parameter effects on the 'intersection point' to allow its use in generic situations where there is a need to identify a safe maximum wall angle. This is a wall angle below which fracture is unlikely to occur. However, the occurrence of the intersection point was inconsistent across the 48 VWACF parts formed in the experiments, showing that it is not valid as a useful

formability indicator.

Another indicator is required for investigations into formability limits, and the fracture depth of the VWACF parts is suggested. The research in this chapter supported the use of fracture depth as an indicator due to the consistency and reliability of the measurement. It is therefore an effective way to compare formability.

This research program around the intersection point did not solve the issue of 'safe' formability limits.

Chapter 6 aimed to investigate parameter effect hypotheses that were proposed in the conclusion of the quantitative literature review in Chapter 2. Specifically, the non-linearity of, and interactions between parameter effects on formability.

The results of this chapter were that tool shape was found to be a significant factor in the presence of step down. These two parameters, tool shape and step down, also interacted together to a significant degree. Thickness and step down showed non-linear main effects, supporting this hypothesis.

Particular VWACF parts also showed certain combinations of parameters that caused surface damage to the parts during forming. These examples were shown in Figure 5.10.

Chapter 7 investigated the effect of tool shape and size on wall bulge. The aim of the experiments was to understand how this mode of geometric error might be improved with careful choice of tools, in the same way that pillowing error can be reduced through the use of flat-ended tools.

Flat-ended tools caused a greater degree of wall bulge deviation compared to hemispherical tools. However, the test parts formed with hemispherical tools still demonstrated wall bulge error, so the choice of tool is unable to eliminate the issue.

8.2 Formability

Failure of a component by fracture was identified as a problem with the use of SPIF for part production, and preventing it was an aim of this thesis. The research undertaken on this topic, formability, has not led to a complete fix for the problem. Instead, wall angle values at which fracture will occur have been assessed for different process parameters, but a minimum safety margin on these values was not able to be determined. An arbitrary safety margin, potentially on the excessive side, can be added which can allow the design of a forming surface that does not fracture.

If a safety margin is further investigated, the usefulness of the thickness distribution (or thickness strain) as a basis for this is in question. As discussed, in Chapter 5 of this thesis a safety margin was not able to be determined due to varying levels of irregularity in the thickness distribution of VWACF parts formed with SPIF. It is

unclear how a generally-applicable safety margin could be developed. However, in preventing failure by fracture, multi-pass forming is likely to be the real solution - despite its complexity. The formability issue for the seat base component in §4.1 was resolved with a solution that involved multi-pass forming. Adding additional passes, or 'interim' surfaces, to a forming process eliminates the formability limits of single-pass SPIF.

The complexity of multi-pass SPIF is a barrier. Development of interim surfaces is more an art than a science due to the ambiguous choice of what to form, how far to form, how to shape the forming surface, and the forming toolpath - among other details. Based on this, a safe wall angle for single-pass SPIF would be beneficial.

As CAM programs become more sophisticated, dealing with more complex toolpaths such as those using 5 axes, an algorithm to generate multi-pass forming surfaces seems more feasible. It would require significant research and experimental data inputs, but allowing the everyday use of multi-pass SPIF would go a significant way to solving the problem of failure by fracture.

8.3 Geometric accuracy

In this thesis, Chapter 7 showed that hemispherical tools, compared to flat-ended tools, cause less geometric error from bulging in flat walls of SPIF components (§7.3). This novel result represents a small amount of progress towards achieving the aim of this thesis, i.e. forming a prototype within the required geometric accuracy margins. However, the Chapter 7 results ask more questions than they answer due to the geometric error trade-off identified with the use of flat or hemispherical tools. Namely, while hemispherical tools reduced wall bulge in the test part, the use of flat-ended tools are known to reduce pillowing error compared to hemispherical tools.

The mechanisms behind pillowing and wall bulge were discussed in §7.3.3, including the hypothesis that a higher level of strain in the thinning band might indicate the presence of a more severe pillow in the base of the part. However, the use of a material strain model to attempt to understand error mechanisms would likely lose validity as the material is formed close to fracture. As shown in Chapter 5, §5.3, the behaviour of thickness strain tends to be unpredictable as it approaches the formability limit. There is scope for further research in this area of tool shape and geometric error. It is, however, unlikely to be a complete solution to the requirement of geometric accuracy.

A complete solution for geometric accuracy is needed before SPIF can be used as a viable rapid prototyping process. Realistically, the primary requirement of a prototype is to be dimensionally accurate. This is because, unless they are manufactured with

the technique used for mass-production, other properties of the part are unlikely to be the same which precludes testing of those properties. For example, the thickness distribution, and therefore the strength, of a SPIF part will not be the same as a stamped part. Comparing to another rapid prototyping method, a 3D printed part would also not have the same results on a compression test as an injection-moulded part, even if they had identical shapes.

Though achieving geometric accuracy within the required tolerance is key to the success of a SPIF prototype, this thesis supports the research literature which characterises it as a significant challenge - or a 'wicked problem', as it might be called. A wicked problem is one that is challenging due to aspects such as interdependencies that cause a solution for one part to increase issues in another part (Churchman, 1967). There are several reasons for this, outlined below, which compound to ensure a simple solution would never be sufficient.

Firstly, as discussed by Allwood, Braun, and Music (2010), there are multiple stages of the SPIF process where geometric error is introduced. These are the 'clamped accuracy', after the part has been formed within the frame, 'unclamped accuracy', after the part has been removed from the frame, and 'final accuracy', after the support walls and flange sections have been removed to reveal the final intended component.

A second reason is the fundamental requirement for a flange in SPIF. Unless the flange is part of the design, this means it must be trimmed, inducing geometric error through springback. Furthermore, once the flange has been trimmed the part cannot be formed any further with SPIF. Compare this to stamping, which may have additional flange sections to facilitate ideal material flow, but can also continue to form material in a press after trimming.

The final reason discussed here is the forming time of SPIF, particularly when measured against the forming time of stamping. This adds to the complexity and computational intensity of modelling an entire SPIF process, for example using finite element analysis (FEA) (Jeswiet, Micari, et al., 2005). A SPIF modelling process such as the Bambach strain model (Bambach, 2010) discussed earlier is less computationally intensive and is accurate for single-pass SPIF (Adams, McAnulty, and Doolan, 2015). However, understanding strain does not necessarily help with understanding how to improve geometric accuracy.

Approaches to improving geometric accuracy in the literature were discussed in §2.4. These included heat treatment of the unclamped part to reduce the stress within the material and reduce geometric error after support walls were trimmed (Bambach, Taleb Araghi, and Hirt, 2009). A heat treatment process adds to the turnaround time and the required equipment, but annealing of sheet material is a well-established industrial technique. Though it would require a special forming rig, heat-treating the

formed component while it is still fully clamped may allow a significant reduction in springback error.

Multi-pass SPIF for improving geometric accuracy was also tested in Bambach, Taleb Araghi, and Hirt (2009). The design of interim passes for reducing geometric error may not be based on the same requirements as multi-pass forming that is used to overcome material formability limits. Furthermore, multi-pass with complex part shapes (i.e. typical industrial components) can introduce types of error such as channelling and wrinkling as seen in §4.1, Figures 4.7 and 4.13.

Complex algorithm-based methods of toolpath adjustment are also an approach investigated by SPIF researchers (Behera, Verbert, et al., 2013). However, the amount and nature of toolpath adjustment would be material dependent, meaning it may be difficult to translate an algorithm from one material type to another. Furthermore, if multi-pass SPIF is used for formability reasons, the toolpath adjustment could be applied to the final pass but may not behave as expected due to aspects such as work hardening in the material.

In the results from Chapter 6, the key message is not to do with the specific wall angle (Φ_{\max}) results, but more about the general finding of non-linear and interaction effects of process parameters. The direct results of how to increase formability are specific to the material type and other factors such that they will not apply more broadly.

On the other hand, in the geometric accuracy study from this thesis (Chapter 7), a specific finding is discussed. Namely, the increase in wall bulge with the use of flat-ended tools compared to hemispherical tools. However, this finding is supported by the proposed pillowing and wall bulge mechanism (§7.3.3), based on Bambach's strain model (Bambach, 2010). This proposed mechanism may apply regardless of other process parameters. Further work would be required to investigate whether the significant interaction of tool shape and step down (Figure 6.3) affects geometric accuracy in addition to influencing formability.

8.4 SPIF in industry

This thesis has focused on the problems that would be faced by technicians in industry using SPIF to manufacture prototypes from sheet metal. Specifically, failure by fracture (formability) and unacceptable geometric error were investigated. The aim of this thesis was to overcome these issues to allow a SPIF prototype to be successfully produced on the first attempt. Eliminating the need for two or more iterations before success is important in an industrial context, as time is money and a delay in prototyping would cause a delay in the overall production schedule.

Work remains to be done in achieving the aim, as the research in this thesis did not fully solve the issues. Geometric accuracy, as discussed in the previous section, is a ‘wicked problem’ and is unlikely to have a simple solution. Superceding formability issues with multi-pass SPIF is feasible but complex and requires more research into development of forming surfaces and the use of computer algorithms to model the process.

A subsequent consideration is that formability and geometric accuracy can be affected by the same process changes, such as choice of forming tool. For an industrial prototype, both aspects must fulfil the requirements. This may be complicated to achieve if a process change affects formability in a beneficial way and geometric accuracy in a detrimental way. Therefore, while focused academic research is important, synthesised studies should also look at combined effects to ensure relevancy to SPIF applications in industry.

8.5 Chapter summary

In this chapter, a cumulative discussion of the thesis findings has been presented in the context of the original research aim, and what is yet to be accomplished.

On the topic of formability, Chapter 5 looked at a ‘safety margin’ to incorporate on top of the fracture point of the material. While the intention of this research was to prevent failure by fracture in SPIF components, multi-pass is discussed as a method which supercedes the need for a safety margin. Multi-pass SPIF, however, adds an additional level of complexity to the forming process. To achieve the aim of this thesis and prevent unwanted fracture in the material, both these aspects could be addressed. A safety margin may be helpful when single-pass SPIF is used, but to simplify multi-pass SPIF, an automated algorithm would be helpful to develop interim forming surfaces.

Geometric accuracy is an essential requirement for prototypes. Results in this thesis have demonstrated novel findings on this topic, though the trade-off between forming tools and specific modes of error reveals scope for further understanding through research.

A significantly more sophisticated solution is required, beyond simply choosing the right forming tool, as prototypes are primarily utilised for their dimensional accuracy rather than for testing mechanical properties. The example discussed is an injection-moulded component being prototyped with 3D printing. Fundamental issues have been mentioned which lead to geometric accuracy being a ‘wicked problem’, and despite complex algorithms proposed in the literature, is still a barrier to industrial applicability.

Producing a prototype on the first attempt which meets all requirements is a necessary achievement for SPIF to be used in industry. However, the process settings affect both formability and geometric accuracy in ways which may not be positive for both at the same time. This finding emphasises the need for industrially-targeted research with nuanced experiments that look at the relationships between these traits.

With its positive traits discussed in Chapter 1, SPIF is the kind of rapid prototyping technique which could fill the gap in industrial sheet metal prototypes. However, with further understanding, it is arguably a more complex process than other rapid prototyping techniques including 3D printing or laser sintering.

The need for complex process development and, often, multiple iterations to form a successful part are negative traits. On balance, these do not present SPIF as the most useful rapid prototyping technique. Ideally, user-friendly modelling methods would be created that allow a SPIF component to meet all requirements including high geometric accuracy and first-time-around successful production.

Conclusion

This thesis aimed to progress SPIF towards an industrially viable process where effective components could be produced without fail due to fracture and with an acceptable final geometric accuracy.

To work towards this aim, the work undertaken looked at the effect of process parameters on material formability and geometric accuracy. With a greater understanding, the best parameters might have been selected for the situation to eliminate the aforementioned issues.

The research question was ‘What are the effects and interactions of SPIF process parameters on the material formability during forming and geometric accuracy after forming?’.

9.1 Formability

The review of the literature on formability in SPIF (§2.3) in this thesis has shown variation in conclusions regarding the effect of process parameters on material formability. A hypothesis was developed in the literature review that the variation could be attributed to non-linear parameter effects and interactions. Both aspects were supported by the experimental work in Chapter 6 which varied four process parameters in a DOE.

The conclusions from the formability literature review in §2.3, mentioned above, were a significant outcome of this thesis. They were found using the methodology of a systematic quantitative literature review (SQLR) process as described in Pickering and Byrne (2014). The SQLR was well suited for this application due to the multiple parameter effects studied, which would have been challenging to compare with a less-quantitative analysis. This process allowed a thorough understanding of the state of the art to be developed, though there were limitations in the results due to journal access restrictions and unreported parameters in research papers.

The research in Chapter 5 has demonstrated that the behaviour of the material

thickness close to fracture in VWACF parts is unpredictable. A consequence of this is that a 'safety margin' for the fracture limit (intersection point) could not be determined, which would have been a beneficial tool for applying SPIF in industry.

Unique case studies of forming automotive components with SPIF have been presented in Chapter 4. Multi-pass SPIF was successfully applied to one of the components (§4.1) after failure had occurred with a single-pass approach. Forming the material with progressive forming surfaces using multi-pass SPIF was able to overcome the regular formability limit of the material. Success was only achieved, however, after a number of attempts. Developing the forming surfaces was based largely on a trial and error process, including trialling top-down multi-pass and moving on to bottom-up multi-pass for the ultimately-successful component. Multi-pass SPIF somewhat supercedes the need for a 'safety margin' (mentioned above) as it can allow a material to form further than with single-pass SPIF. However, based on the time-consuming process of developing several iterations of the seat base part, more work is needed achieve industrial viability.

9.2 Geometric accuracy

A review of the literature in §2.4 highlighted research which found that flat-ended forming tools, compared to hemispherical tools, reduce 'pillowing' in the flat base of a SPIF part, improving the geometric accuracy. However, the experiments in Chapter 7 have shown that flat-ended tools increase bulging in flat walls compared to hemispherical tools, which cause significant dimensional error in the part. Therefore, a trade-off exists between these two types of errors. This is a novel finding for geometric accuracy in SPIF.

Significantly, the strain model by Bambach (2010) was mapped to the wall bulge and pillowing errors and appears to correlate well. Further work in this space could compare measured and modelled strain to determine whether the validity of this prediction. An accurate strain model could assist in understanding the forming mechanisms which lead to these errors.

The simple change of forming tools tested in Chapter 7 of this thesis did not have a significant enough effect to improve the geometric accuracy to within the benchmark requirements. Though more complex solutions, as discussed in §2.4, could add to the turnaround time of a prototype, they are more likely to address the geometric accuracy of the whole surface rather than just a particular wall feature. However, complex solutions could also make the industrial application of SPIF less feasible. Not only does it extensively complicate the prototype development, but the effect of these process adjustments on formability, surface finish, and other aspects should not be

ignored.

Through the case studies in Chapter 4 and experimentation in Chapter 7, this thesis has highlighted the challenge of forming both test parts and automotive components which meet the benchmark geometric accuracy requirements for industrial prototypes. The case study components were formed without process adjustments to improve the geometric accuracy, but in an industrial situation work would be required to ensure the prototypes were within the allowable error margins for their dimensional accuracy.

9.3 Other insights from this work

A contribution of this thesis stems from a finding in the formability SQLR (§2.3) that many journal articles did not thoroughly report the process parameters used for SPIF experiments. Therefore, a suggested list of parameters for the basic SPIF process is presented for future authors to reference. Even if a parameter is not specifically varied in experiments, comprehensive reporting of exact settings will facilitate accurate comparison and benchmarking between research studies in SPIF.

The work in this thesis has shown the interactive effect of formability and geometric accuracy, which were investigated as two significant causes of part failure. With formability, failure by fracture occurs when the formability limit is exceeded, and geometric accuracy failure is when the dimensional error of the part falls outside the required margins. The case studies in Chapter 4, which were representative of typical parts produced by Futuris, demonstrated these failure modes. Fracture in a section of the cushion pan part (§4.2) was likely caused by bulging error in that section, as proposed in Figure 4.24. These sorts of compounding issues add hurdles to the industrial viability of SPIF, and emphasise the need for research which evaluates whole-of-part impacts from process changes.

9.4 Future work

This section outlines the areas for future work that have been determined based on the results in this thesis. In general, the three themes of future work are formability, geometric accuracy, and the broader concerns surrounding SPIF and its applicability in industrial situations.

9.4.1 Formability

In Chapter 5, a potential safety marker for wall angle in SPIF (the intersection point) was investigated. However, it was based on the thickness distribution of VWACF parts

and results showed that this was not reliable enough and the intersection point was not valid. Future work could investigate alternative methods of developing a margin of safety which can be added to the wall angle at fracture of a VWACF test. For an industrial application, this would be helpful for a technician to be confident designing a part with a maximum wall angle that is not going to exceed the formability limit and lead to fracture.

Multi-pass forming in Chapter 4 allowed the single-pass SPIF formability limits to be superseded and the seat base (§4.1) to be successfully formed. Though not a major focus of this thesis, multi-pass is a promising technique for industrial use. However, it is not currently a user-friendly technique, so future work should focus on developing guidelines or similar for effective application of multi-pass SPIF in industry.

9.4.2 Geometric accuracy

Chapter 7 identified a trade-off between flat or hemispherical tools and the occurrence of wall bulge or pillowing that has not been previously reported in the literature. Future work in this space could involve testing this scenario with more complicated test shapes, such as a component with large flat and curved walls. Furthermore, forming different sections of the part with different tools is a promising solution, and could build on work such as Essa and Hartley (2011) by using a flat ended tool to remove the pillow in the base. While the optimal tool shape alone is unlikely to improve geometric accuracy to the level required for industry, in conjunction with other approaches such as toolpath compensation it may go some way towards success. As a continuation of this trade-off, further research could verify the proposed mapping of the Bambach (2010) strain model onto the wall bulge and pillowing situations.

Twisting in the mid-depth region of the truncated pyramid parts was observed in the geometric error surface scans from Chapter 7. This mode of SPIF error has been previously studied in works such as Vanhove, Verbert, et al. (2010) and Duflou, Vanhove, et al. (2010). However, in these papers the focus is on fundamental understanding rather than industrial solutions. While the authors mention solving twist error by alternating the toolpath direction, they also point out that the side-effect is usually an undesirable 'seam' on the surface of the part where the tool changes direction. Therefore, scope exists for future research into solutions for twist that are particularly applicable in an industrial situation.

9.4.3 Broader research in SPIF

In Chapter 4, §4.1, well-designed support walls were a key aspect of improving the seat base forming surface so it would form successfully. Both case studies in this thesis also

highlighted the inaccuracy which tends to occur in sections with a shallow wall angle. Conversely, high wall angles were a cause of failure from exceeding the formability limit. Therefore, a question is whether an optimal value or range in between these two extremes is ideal for support walls to ensure they provide maximum stiffness and accuracy to the component. A study considering the severity of wall bulge or springback for different wall angles would also inform the development of an ideal wall angle range for support walls.

A number of the VWACF test parts from Chapter 6 experienced severe surface damage during forming. The particular combinations of thickness, step down, tool size, and tool shape caused the tool to grind into the sheet, despite lubrication on the surface. Furthermore, the formability result, Φ_{\max} , was reduced by nearly 30° compared to the most successful VWACF part (Table C.1). As discussed in Chapter 6, all the tested parameters affected either the contact force (F) or the contact area (A) between the tool and sheet. Therefore, contact pressure ($P = F/A$) may correlate with this kind of failure where too much pressure causes surface damage instead of deforming as usual. Contact area models have been established in the literature, for example in Adams and Jeswiet (2015). Forces in SPIF can be measured using a specialised forming rig. Therefore, future work could examine this idea in more detail as a way to monitor, predict, or even maximise the success of a part formed with SPIF. Establishing an ideal range for contact pressure conditions between tool and sheet may give insights into optimisation for both surface finish and formability.

Bibliography

- Adams, D. and J. Jeswiet (2014a). "Design rules and applications of single-point incremental forming". In: *Proceedings of the Institution of Mechanical Engineers, Part B: Journal of Engineering Manufacture* 229.5, pp. 754–760. URL: <http://dx.doi.org/10.1177/0954405414531426>.
- (2014b). "Single-point incremental forming of 6061-T6 using electrically assisted forming methods". In: *Proceedings of the Institution of Mechanical Engineers, Part B: Journal of Engineering Manufacture* 228.7, pp. 757–764. URL: <http://dx.doi.org/10.1177/0954405413501670>.
- (2015). "A new model for contact geometry in single-point incremental forming". In: *Proceedings of the Institution of Mechanical Engineers* 229.6, p. 982. ISSN: 09544054.
- Adams, D., T. McAnulty, and M. Doolan (2015). "Experimental testing of an analytical model for membrane strains in single point incremental forming". In: *Key Engineering Materials*. Vol. 639. Trans Tech Publications, pp. 187–194. URL: <http://dx.doi.org/10.4028/www.scientific.net/KEM.639.187>.
- Allwood, J. M., D. Braun, and O. Music (2010). "The effect of partially cut-out blanks on geometric accuracy in incremental sheet forming". In: *Journal of Materials Processing Technology* 210.11, pp. 1501–1510. ISSN: 0924-0136. DOI: <http://dx.doi.org/10.1016/j.jmatprotec.2010.04.008>. URL: <http://www.sciencedirect.com/science/article/pii/S092401361000124X>.
- Ambrogio, G., I. Costantino, et al. (2004). "Influence of some relevant process parameters on the dimensional accuracy in incremental forming: A numerical and experimental investigation". In: *Journal of Materials Processing Technology* 153-154.1-3, pp. 501–507. URL: <http://www.scopus.com/inward/record.url?eid=2-s2.0-8844225324&partnerID=40&md5=b52a383e924113c1f1191ffd772fd1a4>.
- Ambrogio, G., V. Cozza, et al. (2007). "An analytical model for improving precision in single point incremental forming". In: *Journal of Materials Processing Technology* 191.1-3, pp. 92–95. URL: <http://www.scopus.com/inward/record.url?eid=2-s2.0-34249875974&partnerID=40&md5=f67a3e249e3fdef382445a625ddca37c>.
- Ambrogio, G., L. De Napoli, et al. (2005). "Application of Incremental Forming process for high customised medical product manufacturing". In: *Journal of Materials Processing Technology* 162-163.SPEC. ISS. Pp. 156–162. URL: <http://www>.

- scopus.com/inward/record.url?eid = 2-s2.0-17844371731&partnerID = 40&md5 = ffbbcf4d9f07a62824f575ca5c4e4999.
- Ambrogio, G., L. Filice, and F. Micari (2006). "A force measuring based strategy for failure prevention in incremental forming". In: *Journal of Materials Processing Technology* 177.1-3, pp. 413–416. URL: <http://dx.doi.org/10.1016/j.jmatprotec.2006.04.076>.
- Ambrogio, G. and F. Gagliardi (2015). "Temperature variation during high speed incremental forming on different lightweight alloys". In: *International Journal of Advanced Manufacturing Technology* 76.9-12, pp. 1819–1825. URL: <http://dx.doi.org/10.1007/s00170-014-6398-y>.
- Araujo, R. et al. (2014). "Single point incremental forming of a facial implant". In: *Prosthetics and Orthotics International* 38.5, pp. 369–378. URL: <http://dx.doi.org/10.1177/0309364613502071>.
- Arfa, H., R. Bahloul, and H. BelHadjSalah (2013). "Finite element modelling and experimental investigation of single point incremental forming process of aluminum sheets: Influence of process parameters on punch force monitoring and on mechanical and geometrical quality of parts". In: *International Journal of Material Forming* 6.4, pp. 483–510. URL: <http://dx.doi.org/10.1007/s12289-012-1101-z>.
- Bagudanch, I., M. L. Garcia-Romeu, et al. (2015). "Forming force and temperature effects on single point incremental forming of polyvinylchloride". In: *Journal of Materials Processing Technology* 219, pp. 221–229. URL: <http://dx.doi.org/10.1016/j.jmatprotec.2014.12.004>.
- Bagudanch, I., L. M. Lozano-Sánchez, et al. (2015). "Manufacturing of Polymeric Biocompatible Cranial Geometry by Single Point Incremental Forming". In: *Procedia Engineering* 132, pp. 267–273. ISSN: 1877-7058. DOI: <http://dx.doi.org/10.1016/j.proeng.2015.12.494>. URL: <http://www.sciencedirect.com/science/article/pii/S1877705815044057>.
- Bambach, M. (2010). "A geometrical model of the kinematics of incremental sheet forming for the prediction of membrane strains and sheet thickness". In: *Journal of Materials Processing Technology* 210.12, pp. 1562–1573. URL: <http://dx.doi.org/10.1016/j.jmatprotec.2010.05.003>.
- Bambach, M., B. Taleb Araghi, and G. Hirt (2009). "Strategies to improve the geometric accuracy in asymmetric single point incremental forming". In: *Production Engineering* 3.2, pp. 145–156. URL: <http://www.scopus.com/inward/record.url?eid = 2-s2.0-67651154174&partnerID = 40&md5 = cbc3645cee65d6f1eb840e3e1be31ad7>.
- Bates, D. et al. (2015). "Fitting Linear Mixed-Effects Models Using lme4". In: *2015* 67.1, p. 48. ISSN: 1548-7660. DOI: 10.18637/jss.v067.i01. URL: <https://www.jstatsoft.org/v067/i01>.

-
- Behera, A. K., B. Lauwers, and J. R. Duflou (2014). "Tool path generation framework for accurate manufacture of complex 3D sheet metal parts using single point incremental forming". In: *Computers in Industry* 65.4, pp. 563–584. ISSN: 0166-3615. DOI: <http://dx.doi.org/10.1016/j.compind.2014.01.002>. URL: <http://www.sciencedirect.com/science/article/pii/S0166361514000189>.
- Behera, A. K., B. Lu, and H. Ou (2016). "Characterization of shape and dimensional accuracy of incrementally formed titanium sheet parts with intermediate curvatures between two feature types". In: *The International Journal of Advanced Manufacturing Technology* 83.5, pp. 1099–1111. ISSN: 1433-3015. DOI: 10.1007/s00170-015-7649-2. URL: <http://dx.doi.org/10.1007/s00170-015-7649-2>.
- Behera, A. K., R. A. de Sousa, et al. (2017). "Single point incremental forming: An assessment of the progress and technology trends from 2005 to 2015". In: *Journal of Manufacturing Processes* 27, pp. 37–62. ISSN: 1526-6125. DOI: <http://dx.doi.org/10.1016/j.jmapro.2017.03.014>. URL: <http://www.sciencedirect.com/science/article/pii/S1526612517300713>.
- Behera, A. K., J. Verbert, et al. (2013). "Tool path compensation strategies for single point incremental sheet forming using multivariate adaptive regression splines". In: *CAD Computer Aided Design* 45.3, pp. 575–590. DOI: 10.1016/j.cad.2012.10.045. URL: <https://www.scopus.com/inward/record.uri?eid=2-s2.0-84868551118&partnerID=40&md5=7b03bb368390b3dd425bdb8ac91dbc61>.
- Buffa, G., D. Campanella, and L. Fratini (2013). "On the improvement of material formability in SPIF operation through tool stirring action". In: *International Journal of Advanced Manufacturing Technology* 66.9-12, pp. 1343–1351. URL: <http://dx.doi.org/10.1007/s00170-012-4412-9>.
- Cavaler, L. C. C. et al. (2010). "Surface roughness in the incremental forming of AISI 304L stainless steel sheets". In: *Far East Journal of Mechanical Engineering and Physics* 1.2, pp. 87–98. URL: <http://pphmj.com/journals/fjmep.htm>.
- Cawley, B., D. Adams, and J. Jeswiet (2013). *Examining tool shapes in single point incremental forming*. Conference Paper. URL: <http://www.scopus.com/inward/record.url?eid=2-s2.0-84892776270&partnerID=40&md5=eba53430e17474f0d9574448fbb335a4>.
- Centeno, G. et al. (2014). "Critical analysis of necking and fracture limit strains and forming forces in single-point incremental forming". In: *Materials and Design* 63, pp. 20–29. URL: <http://dx.doi.org/10.1016/j.matdes.2014.05.066>.
- Churchman, C. West (1967). "Free for All: Wicked Problems". In: *Management Science* 14.4, B-141-B-146. URL: <https://doi.org/10.1287/mnsc.14.4.B141>.
- Davarpanah, M. A. et al. (2015). "Effects of incremental depth and tool rotation on failure modes and microstructural properties in Single Point Incremental Forming

- of polymers". In: *Journal of Materials Processing Technology* 222, pp. 287–300. URL: <http://dx.doi.org/10.1016/j.jmatprotec.2015.03.014>.
- Duflou, J. R., A. K. Behera, et al. (2013). "Manufacture of accurate titanium cranio-facial implants with high forming angle using single point incremental forming". In: *Key Engineering Materials*. Vol. 549, pp. 223–230. DOI: 10.4028/www.scientific.net/KEM.549.223. URL: <https://www.scopus.com/inward/record.uri?eid=2-s2.0-84877847813&doi=10.4028%2fwww.scientific.net%2fKEM.549.223&partnerID=40&md5=0736a4acb10c016f65a0a2063b79b955>.
- Duflou, J. R., B. Callebaut, et al. (2007). "Laser assisted incremental forming: Formability and accuracy improvement". In: *CIRP Annals - Manufacturing Technology* 56.1, pp. 273–276. URL: <http://dx.doi.org/10.1016/j.cirp.2007.05.063>.
- Duflou, J. R., H. Vanhove, et al. (2010). "Twist revisited: Twist phenomena in single point incremental forming". In: *CIRP Annals - Manufacturing Technology* 59.1, pp. 307–310. DOI: 10.1016/j.cirp.2010.03.018. URL: <http://www.scopus.com/inward/record.url?eid=2-s2.0-77955310724&partnerID=40&md5=a0dbded3af02e717c8df2454eaf84928>.
- Durante, M., A. Formisano, and A. Langella (2011). "Observations on the influence of tool-sheet contact conditions on an incremental forming process". In: *Journal of Materials Engineering and Performance* 20.6, pp. 941–946. URL: <http://dx.doi.org/10.1007/s11665-010-9742-x>.
- Durante, M., A. Formisano, A. Langella, and F. M. Capece Minutolo (2009). "The influence of tool rotation on an incremental forming process". In: *Journal of Materials Processing Technology* 209.9, pp. 4621–4626. URL: <http://dx.doi.org/10.1016/j.jmatprotec.2008.11.028>.
- Echrif, S. B. M. and M. Hrairi (2011). "Research and progress in incremental sheet forming processes". In: *Materials and Manufacturing Processes* 26.11, pp. 1404–1414. URL: <http://dx.doi.org/10.1080/10426914.2010.544817>.
- Essa, K. and P. Hartley (2011). "An assessment of various process strategies for improving precision in single point incremental forming". In: *International Journal of Material Forming* 4.4, pp. 401–412. DOI: 10.1007/s12289-010-1004-9. URL: <https://www.scopus.com/inward/record.uri?eid=2-s2.0-81755176717&partnerID=40&md5=3839bdabddea44c1c0ee4990612ae1f6>.
- Eyckens, P. et al. (2010). "The significance of friction in the single point incremental forming process". In: *International Journal of Material Forming* 3.SUPPL. 1, pp. 947–950. URL: <http://dx.doi.org/10.1007/s12289-010-0925-7>.
- Fan, G. et al. (2010). "Electric hot incremental forming of Ti-6Al-4V titanium sheet". In: *International Journal of Advanced Manufacturing Technology* 49.9-12, pp. 941–947. URL: <http://dx.doi.org/10.1007/s00170-009-2472-2>.

- Fang, Y. et al. (2014). "Analytical and experimental investigations on deformation mechanism and fracture behavior in single point incremental forming". In: *Journal of Materials Processing Technology* 214.8, pp. 1503–1515. URL: <http://dx.doi.org/10.1016/j.jmatprotec.2014.02.019>.
- FARO Technologies, Inc. (2010). *FaroArm Manual*. Generic.
- (2012). *Faro Laser ScanArm V3*. Figure.
- Filice, L., L. Fratini, and F. Micari (2002). "Analysis of Material Formability in Incremental Forming". In: *CIRP Annals - Manufacturing Technology* 51.1, pp. 199–202. URL: [http://dx.doi.org/10.1016/S0007-8506\(07\)61499-1](http://dx.doi.org/10.1016/S0007-8506(07)61499-1).
- Franzen, V. et al. (2009). "Single point incremental forming of PVC". In: *Journal of Materials Processing Technology* 209.1, pp. 462–469. URL: <http://dx.doi.org/10.1016/j.jmatprotec.2008.02.013>.
- Fratini, L. et al. (2004). "Influence of mechanical properties of the sheet material on formability in single point incremental forming". In: *CIRP Annals - Manufacturing Technology* 53.1, pp. 207–210. URL: <http://www.scopus.com/inward/record.url?eid=2-s2.0-3142706601&partnerID=40&md5=f8b3cf733b850f876ef442fcdd63d816>.
- Gatea, S., H. Ou, and G. McCartney (2016). "Review on the influence of process parameters in incremental sheet forming". In: *The International Journal of Advanced Manufacturing Technology* 87.1, pp. 479–499. ISSN: 1433-3015. DOI: 10.1007/s00170-016-8426-6. URL: <http://dx.doi.org/10.1007/s00170-016-8426-6>.
- Geomagic, Inc (2013). *Geomagic Qualify Interactive User Guide*. Generic.
- Al-Ghamdi, K. A. and G. Hussain (2014). "Threshold tool-radius condition maximizing the formability in SPIF considering a variety of materials: Experimental and FE investigations". In: *International Journal of Machine Tools and Manufacture* 88, pp. 82–94. URL: <http://dx.doi.org/10.1016/j.ijmachtools.2014.09.005>.
- (2015). "The pillowing tendency of materials in single-point incremental forming: Experimental and finite element analyses". In: *Proceedings of the Institution of Mechanical Engineers, Part B: Journal of Engineering Manufacture* 229.5, pp. 744–753. DOI: 10.1177/0954405414530906. URL: <https://www.scopus.com/inward/record.uri?eid=2-s2.0-84955284867&partnerID=40&md5=0c5458157192f1e34b24e7b97845b46e>.
- Golabi, S. and H. Khazaali (2014). "Determining frustum depth of 304 stainless steel plates with various diameters and thicknesses by incremental forming". In: *Journal of Mechanical Science and Technology* 28.8, pp. 3273–3278. URL: <http://dx.doi.org/10.1007/s12206-014-0738-6>.
- Hagan, E. and J. Jeswiet (2003). "A review of conventional and modern single-point sheet metal forming methods". In: *Proceedings of the Institution of Mechanical Engineers, Part B: Journal of Engineering Manufacture* 217.2, pp. 213–225. URL: <http://dx.doi.org/10.1243/095440503321148858>.

-
- Ham, M. and J. Jeswiet (2006). "Single Point Incremental Forming and the Forming Criteria for AA3003". In: *CIRP Annals - Manufacturing Technology* 55.1, pp. 241–244. URL: [http://dx.doi.org/10.1016/S0007-8506\(07\)60407-7](http://dx.doi.org/10.1016/S0007-8506(07)60407-7).
- (2007). "Forming limit curves in single point incremental forming". In: *CIRP Annals - Manufacturing Technology* 56.1, pp. 277–280. URL: <http://dx.doi.org/10.1016/j.cirp.2007.05.064>.
- (2008). "Dimensional accuracy of single point incremental forming". In: *International Journal of Material Forming* 1.SUPPL. 1, pp. 1171–1174. URL: <http://www.scopus.com/inward/record.url?eid=2-s2.0-78651580148&partnerID=40&md5=058dd4652281e18687345ee5d2789b4f>.
- Hussain, G. (2014). "Experimental investigations on the role of tool size in causing and controlling defects in single point incremental forming process". In: *Proceedings of the Institution of Mechanical Engineers, Part B: Journal of Engineering Manufacture* 228.2, pp. 266–277. DOI: 10.1177/0954405413498864. URL: <http://www.scopus.com/inward/record.url?eid=2-s2.0-84896777335&partnerID=40&md5=0971c56c28515ac8320124061596ad7d>.
- Hussain, G. and L. Gao (2007). "A novel method to test the thinning limits of sheet metals in negative incremental forming". In: *International Journal of Machine Tools and Manufacture* 47.3–4, pp. 419–435. URL: <http://dx.doi.org/10.1016/j.ijmachtools.2006.06.015>.
- Hussain, G., L. Gao, and N. U. Dar (2007). "An experimental study on some formability evaluation methods in negative incremental forming". In: *Journal of Materials Processing Technology* 186.1-3, pp. 45–53. URL: <http://dx.doi.org/10.1016/j.jmatprotec.2006.12.005>.
- Hussain, G., L. Gao, and N. Hayat (2011a). "Forming parameters and forming defects in incremental forming of an aluminum sheet: Correlation, empirical modeling, and optimization: Part A". In: *Materials and Manufacturing Processes* 26.12, pp. 1546–1553. URL: <http://dx.doi.org/10.1080/10426914.2011.552017>.
- (2011b). "Improving profile accuracy in SPIF process through statistical optimization of forming parameters". In: *Journal of Mechanical Science and Technology* 25.1, pp. 177–182.
- Hussain, G., L. Gao, N. Hayat, and N. U. Dar (2010). "The formability of annealed and pre-aged AA-2024 sheets in single-point incremental forming". In: *International Journal of Advanced Manufacturing Technology* 46.5-8, pp. 543–549. URL: <http://dx.doi.org/10.1007/s00170-009-2120-x>.
- Hussain, G., L. Gao, N. Hayat, and L. Qijian (2007). "The effect of variation in the curvature of part on the formability in incremental forming: An experimental

- investigation". In: *International Journal of Machine Tools and Manufacture* 47.14, pp. 2177–2181. URL: <http://dx.doi.org/10.1016/j.ijmachtools.2007.05.001>.
- Hussain, G., L. Gao, and Z. Y. Zhang (2008). "Formability evaluation of a pure titanium sheet in the cold incremental forming process". In: *International Journal of Advanced Manufacturing Technology* 37.9-10, pp. 920–926. URL: <http://dx.doi.org/10.1007/s00170-007-1043-7>.
- Hussain, G., H. R. Khan, et al. (2013). "Guidelines for tool-size selection for single-point incremental forming of an aerospace alloy". In: *Materials and Manufacturing Processes* 28.3, pp. 324–329. URL: <http://dx.doi.org/10.1080/10426914.2012.700151>.
- Isidore, B. B. Lemopi et al. (2016). "Prediction and control of pillow defect in single point incremental forming using numerical simulations". In: *Journal of Mechanical Science and Technology* 30.5, pp. 2151–2161. ISSN: 1976-3824. DOI: 10.1007/s12206-016-0422-0. URL: <http://dx.doi.org/10.1007/s12206-016-0422-0>.
- Jackson, K. P., J. M. Allwood, and M. Landert (2008). "Incremental forming of sandwich panels". In: *Journal of Materials Processing Technology* 204.1-3, pp. 290–303. URL: <http://dx.doi.org/10.1016/j.jmatprotec.2007.11.117>.
- Jeswiet, J., J. R. Duflou, et al. (2005). "Custom Manufacture of a Solar Cooker – A Case Study". In: *Advanced Materials Research* 6-8, pp. 487–492.
- Jeswiet, J., E. Hagan, and A. Szekeres (2002). "Forming parameters for incremental forming of aluminium alloy sheet metal". In: *Proceedings of the Institution of Mechanical Engineers, Part B: Journal of Engineering Manufacture* 216.10, pp. 1367–1371. URL: <http://dx.doi.org/10.1243/095440502320405458>.
- Jeswiet, J., F. Micari, et al. (2005). "Asymmetric Single Point Incremental Forming of Sheet Metal". In: *CIRP Annals - Manufacturing Technology* 54.2, pp. 623–649. URL: [http://dx.doi.org/10.1016/S0007-8506\(07\)60021-3](http://dx.doi.org/10.1016/S0007-8506(07)60021-3).
- Jeswiet, J. and D. Young (2005). "Forming limit diagrams for single point incremental forming of aluminium sheet". In: *Proceedings of the Institution of Mechanical Engineers, Part B: Journal of Engineering Manufacture* 219.4, pp. 359–364. URL: <http://www.scopus.com/inward/record.url?eid=2-s2.0-32844465974&partnerID=40&md5=9cd56d7971c1041086fc046cf3a69e4f>.
- Jin, W. et al. (2012). *Study on Possibility of Processing TRIP Steel Sheet by Single Point Incremental Forming*. Conference Paper. URL: http://www.atlantis-press.com/php/download_paper.php?id=3818.
- Kalpajian, Serope and Steven R. Schmid (2010a). "General Introduction". In: *Manufacturing Engineering and Technology*. 6th ed. New Jersey, U.S.A: Prentice Hall. Chap. 33. ISBN: 978-0-13-608168-5.

-
- Kalpakjian, Serope and Steven R. Schmid (2010b). "Rapid-Prototyping Processes and Operations". In: *Manufacturing Engineering and Technology*. 6th ed. New Jersey, U.S.A: Prentice Hall. Chap. 20. ISBN: 978-0-13-608168-5.
- (2010c). "Sheet-Metal Forming Processes and Equipment". In: *Manufacturing Engineering and Technology*. 6th ed. New Jersey, U.S.A: Prentice Hall. Chap. 16. ISBN: 978-0-13-608168-5.
- Keeler, Stuart P. (1965). *Determination of Forming Limits in Automotive Stampings*. Conference Paper. DOI: 10.4271/650535. URL: <https://doi.org/10.4271/650535>.
- Kim, T. J. and D. Y. Yang (2000). "Improvement of formability for the incremental sheet metal forming process". In: *International Journal of Mechanical Sciences* 42.7, pp. 1271–1286. URL: [http://dx.doi.org/10.1016/S0020-7403\(99\)00047-8](http://dx.doi.org/10.1016/S0020-7403(99)00047-8).
- Kim, Y. H. and J. J. Park (2002). "Effect of process parameters on formability in incremental forming of sheet metal". In: *Journal of Materials Processing Technology* 130–131.0, pp. 42–46. URL: [http://dx.doi.org/10.1016/S0924-0136\(02\)00788-4](http://dx.doi.org/10.1016/S0924-0136(02)00788-4).
- Kurra, S. and S. P. Regalla (2014). "Experimental and numerical studies on formability of extra-deep drawing steel in incremental sheet metal forming". In: *Journal of Materials Research and Technology* 3.2, pp. 158–171. DOI: 10.1016/j.jmrt.2014.03.009. URL: <http://www.scopus.com/inward/record.url?eid=2-s2.0-84926240569&partnerID=40&md5=1cf3cbf4117463ab85a34c0d7b1037e5>.
- Le, V. S., A. Ghiotti, and G. Lucchetta (2008). "Preliminary Studies on Single Point Incremental Forming for Thermoplastic Materials". In: *International Journal of Material Forming* 1.1, pp. 1179–1182. URL: <http://dx.doi.org/10.1007/s12289-008-0191-0>.
- Li, Y. et al. (2014). "Simulation and experimental observations of effect of different contact interfaces on the incremental sheet forming process". In: *Materials and Manufacturing Processes* 29.2, pp. 121–128. URL: <http://dx.doi.org/10.1080/10426914.2013.822977>.
- Liu, Z., Y. Li, and P. A. Meehan (2013). "Experimental investigation of mechanical properties, formability and force measurement for AA7075-O aluminum alloy sheets formed by incremental forming". In: *International Journal of Precision Engineering and Manufacturing* 14.11, pp. 1891–1899. URL: <http://dx.doi.org/10.1007/s12541-013-0255-z>.
- Lu, B., Y. Fang, et al. (2014). "Mechanism investigation of friction-related effects in single point incremental forming using a developed oblique roller-ball tool". In: *International Journal of Machine Tools and Manufacture* 85, pp. 14–29. URL: <http://dx.doi.org/10.1016/j.ijmachtools.2014.04.007>.
- Lu, B., H. Ou, et al. (2016). "Titanium based cranial reconstruction using incremental sheet forming". In: *International Journal of Material Forming* 9.3, pp. 361–370. DOI:

- 10.1007/s12289-014-1205-8. URL: <https://www.scopus.com/inward/record.uri?eid=2-s2.0-84916920300&doi=10.1007%2fs12289-014-1205-8&partnerID=40&md5=055f6fcc7a5e61b7dfc47bdb1c0e9495>.
- Lu, H. et al. (2016). "Two-directional toolpath correction in single-point incremental forming using model predictive control". In: *International Journal of Advanced Manufacturing Technology*, pp. 1–16. DOI: 10.1007/s00170-016-9672-3. URL: <https://www.scopus.com/inward/record.uri?eid=2-s2.0-84996917459&doi=10.1007%2fs00170-016-9672-3&partnerID=40&md5=367b8dea01b50789d2f16927f5ee8c26>.
- Malhotra, R. et al. (2012). "Mechanics of fracture in single point incremental forming". In: *Journal of Materials Processing Technology* 212.7, pp. 1573–1590. URL: <http://dx.doi.org/10.1016/j.jmatprotec.2012.02.021>.
- Manco, G. L. and G. Ambrogio (2010). "Influence of thickness on formability in 6082-T6". In: *International Journal of Material Forming* 3.SUPPL. 1, pp. 983–986. URL: <http://dx.doi.org/10.1007/s12289-010-0934-6>.
- Marques, T. A., M. B. Silva, and P. A. F. Martins (2012). "On the potential of single point incremental forming of sheet polymer parts". In: *International Journal of Advanced Manufacturing Technology* 60.1-4, pp. 75–86. URL: <http://dx.doi.org/10.1007/s00170-011-3585-y>.
- Martins, P. A. F. et al. (2009). "Single point incremental forming of polymers". In: *CIRP Annals - Manufacturing Technology* 58.1, pp. 229–232. URL: <http://dx.doi.org/10.1016/j.cirp.2009.03.095>.
- McAnulty, T. (2013). "Single point incremental forming as a method for rapid prototyping of interior automotive components". Thesis.
- McAnulty, T., J. Jeswiet, and M. Doolan (2016). "Formability in single point incremental forming: A comparative analysis of the state of the art". In: *CIRP Journal of Manufacturing Science and Technology*. ISSN: 1755-5817. URL: <http://dx.doi.org/10.1016/j.cirpj.2016.07.003>.
- Micari, F., G. Ambrogio, and L. Filice (2007). "Shape and dimensional accuracy in Single Point Incremental Forming: State of the art and future trends". In: *Journal of Materials Processing Technology* 191.1-3, pp. 390–395. URL: <http://dx.doi.org/10.1016/j.jmatprotec.2007.03.066>.
- Nagy-Sochacki, A. (2009). "The effects of process and part parameters on single point incrementally formed parts". Thesis.
- Obikawa, Toshiyuki, Shunsuke Satou, and Tomomi Hakutani (2009). "Dieless incremental micro-forming of miniature shell objects of aluminum foils". In: *International Journal of Machine Tools and Manufacture* 49.12–13, pp. 906–915. URL: <http://dx.doi.org/10.1016/j.ijmachtools.2009.07.001>.

-
- Palumbo, G. and M. Brandizzi (2012). "Experimental investigations on the single point incremental forming of a titanium alloy component combining static heating with high tool rotation speed". In: *Materials and Design* 40, pp. 43–51. URL: <http://dx.doi.org/10.1016/j.matdes.2012.03.031>.
- Petek, A., K. Kuzman, and J. Kopac (2009). "Deformations and forces analysis of single point incremental sheet metal forming". In: *Archives of Materials science and Engineering* 35.2, pp. 35–42. URL: <http://www.scopus.com/inward/record.url?eid=2-s2.0-77952507216&partnerID=40&md5=7d456f1e2d1b1c9237670f34db0f43>.
- Pickering, C. M. and J. A. Byrne (2014). "The benefits of publishing systematic quantitative literature reviews for PhD candidates and other early-career researchers". In: *Higher Education Research and Development* 33.3, pp. 534–548. URL: <http://dx.doi.org/10.1080/07294360.2013.841651>.
- Russell, C. (2008). "The design and analysis of flexible fixtures for implementation of single point incremental sheet forming in conjunction with three axis CNC mills". Thesis.
- Shanmuganatan, S. P. and V. S. Senthil Kumar (2013). "Metallurgical analysis and finite element modelling for thinning characteristics of profile forming on circular cup". In: *Materials and Design* 44.0, pp. 208–215. URL: <http://dx.doi.org/10.1016/j.matdes.2012.07.042>.
- Shen, Jianhu et al. (2010). "Experiments on curved sandwich panels under blast loading". In: *International Journal of Impact Engineering* 37.9, pp. 960–970. ISSN: 0734-743X. URL: <https://doi.org/10.1016/j.ijimpeng.2010.03.002>.
- Shim, M. S. and J. J. Park (2001). "The formability of aluminum sheet in incremental forming". In: *Journal of Materials Processing Technology* 113.1-3, pp. 654–658. URL: [http://dx.doi.org/10.1016/S0924-0136\(01\)00679-3](http://dx.doi.org/10.1016/S0924-0136(01)00679-3).
- Silva, M. B., L. M. Alves, and P. A. F. Martins (2010). "Single point incremental forming of PVC: Experimental findings and theoretical interpretation". In: *European Journal of Mechanics, A/Solids* 29.4, pp. 557–566. URL: <http://dx.doi.org/10.1016/j.euromechsol.2010.03.008>.
- Silva, M. B., P. S. Nielsen, et al. (2011). "Failure mechanisms in single-point incremental forming of metals". In: *International Journal of Advanced Manufacturing Technology* 56.9-12, pp. 893–903. URL: <http://dx.doi.org/10.1007/s00170-011-3254-1>.
- Silva, M. B., M. Skjoedt, et al. (2008). "Single-point incremental forming and formability-failure diagrams". In: *Journal of Strain Analysis for Engineering Design* 43.1, pp. 15–35. URL: <http://dx.doi.org/10.1243/03093247JSA340>.
- Skjoedt, M. et al. (2008). "Multi stage strategies for single point incremental forming of a cup". In: *International Journal of Material Forming* 1.SUPPL. 1, pp. 1199–1202. URL:

- <http://www.scopus.com/inward/record.url?eid=2-s2.0-77950689660&partnerID=40&md5=760c1d5c8963c4940390f4b45f8df8af>.
- Strano, M. (2005). "Technological representation of forming limits for negative incremental forming of thin aluminum sheets". In: *Journal of Manufacturing Processes* 7.2, pp. 122–129. URL: [http://dx.doi.org/10.1016/S1526-6125\(05\)70089-X](http://dx.doi.org/10.1016/S1526-6125(05)70089-X).
- Team, R Development Core (2008). *R: A Language and Environment for Statistical Computing*. Vienna, Austria: R Foundation for Statistical Computing. ISBN: 3-900051-07-0. URL: <http://www.R-project.org>.
- Vanhove, H. and J. R. Dufloy (2015). "Negative bulge formation in high speed incremental forming". In: *Key Engineering Materials*. Vol. 639. Trans Tech Publications, pp. 173–178. DOI: 10.4028/www.scientific.net/KEM.639.173. URL: <https://www.scopus.com/inward/record.uri?eid=2-s2.0-84930171574&partnerID=40&md5=962580b98b370f3b9c075934bc92f233>.
- Vanhove, H., J. Verbert, et al. (2010). "An experimental study of twist phenomena in single point incremental forming". In: *International Journal of Material Forming* 3.SUPPL. 1, pp. 975–978. DOI: 10.1007/s12289-010-0932-8. URL: <http://www.scopus.com/inward/record.url?eid=2-s2.0-78651560501&partnerID=40&md5=5fbab8844b4018a99dc313c5f00f8d42>.
- Verbert, J., J. R. Dufloy, and B. Lauwers (2007). "Feature based approach for increasing the accuracy of the SPIF process". In: *Key Engineering Materials*. Vol. 344. Trans Tech Publications, pp. 527–534. DOI: 10.4028/0-87849-437-5.527. URL: <http://www.scopus.com/inward/record.url?eid=2-s2.0-34248539371&partnerID=40&md5=ceec089ef09c06479136f568b1f27fb6>.
- Xu, D. et al. (2013). "Mechanism investigation for the influence of tool rotation and laser surface texturing (LST) on formability in single point incremental forming". In: *International Journal of Machine Tools and Manufacture* 73, pp. 37–46. URL: <http://dx.doi.org/10.1016/j.ijmachtools.2013.06.007>.
- Young, D. and J. Jeswiet (2004). "Wall thickness variations in single-point incremental forming". In: *Proceedings of the Institution of Mechanical Engineers, Part B: Journal of Engineering Manufacture* 218.11, pp. 1453–1459.
- Ziran, X. et al. (2010). "The performance of flat end and hemispherical end tools in single-point incremental forming". In: *International Journal of Advanced Manufacturing Technology* 46.9-12, pp. 1113–1118. URL: <http://dx.doi.org/10.1007/s00170-009-2179-4>.

Case studies process parameters

Additional experimental details

- All tools used have a hemispherical end except where otherwise specified.
- All tools are made from tungsten carbide.
- The tool rotation was climb (rolling) milling.
- The toolpath type for all case studies was spiral, eliminating the visible step-down point.
- Lubricant used for all case study components was deep drawing oil.

Table A.1: Process parameters used for forming the seat base (SB) and cushion pan (CP) components.

Parameter	SB1	SB2	SB3	CP
Aluminium alloy [AA]	6061-T0	6061-T0	5005-H34	5005-H34
Material thickness [mm]	2	2	2	1
Tool diameter [mm]	12	12	12	12
Step down [mm]	1	0.5	0.5	0.5
Spindle speed [rpm]	1000	1000	1000	1000
Feed rate [mm/min]	3000	3000	3000	5000

Thickness distribution results of VWACF parts

This appendix presents the full set of data for Chapter 5. Each page shows the results for a single test, which includes the three repeats. The measured VWACF thickness distribution compared to the sine law prediction is shown in the first column, and the corresponding error between measured and predicted thickness is shown to the right.

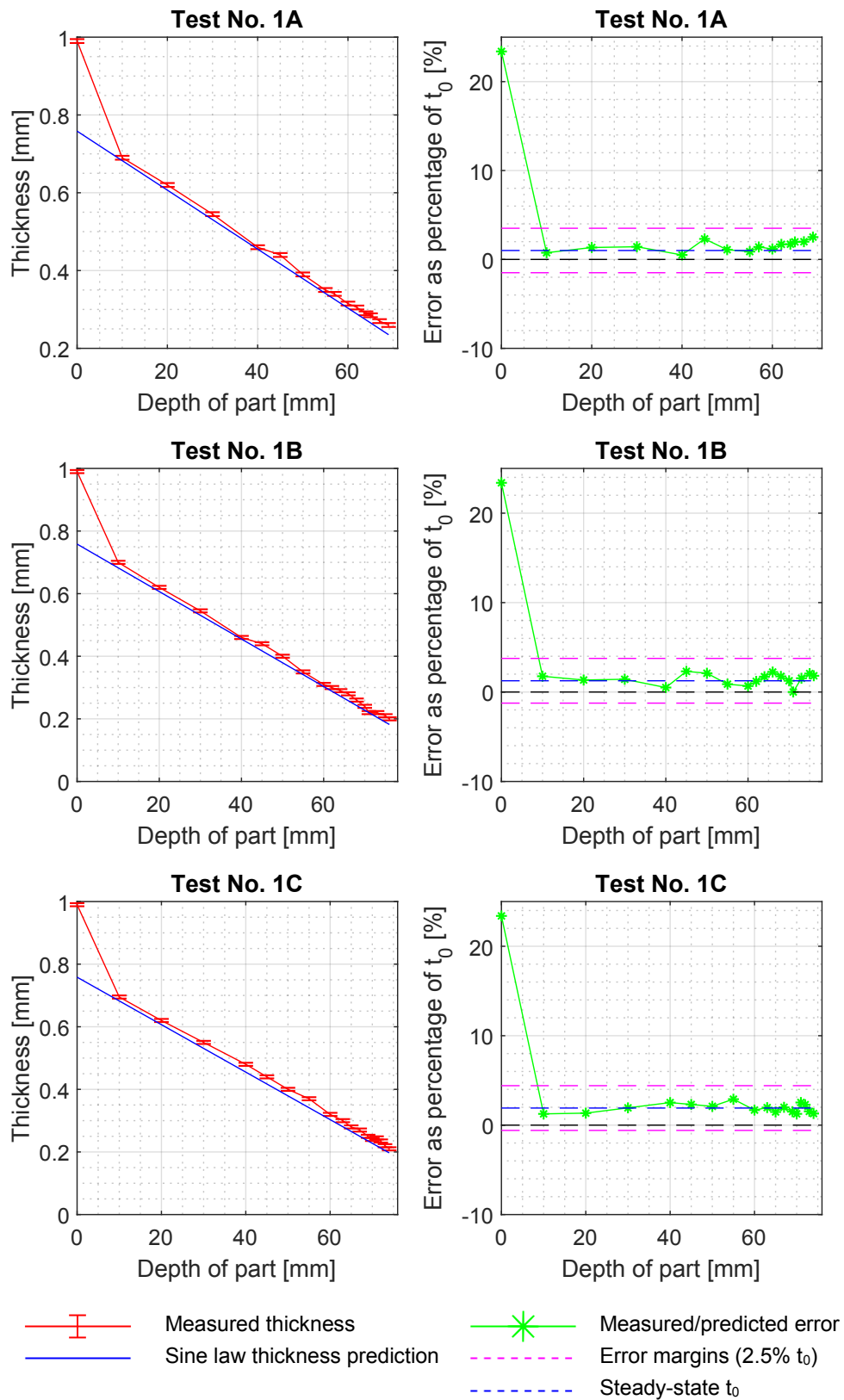


Figure B.1: Test No. 1 - measured thickness distribution results and error plots for each test repeat.

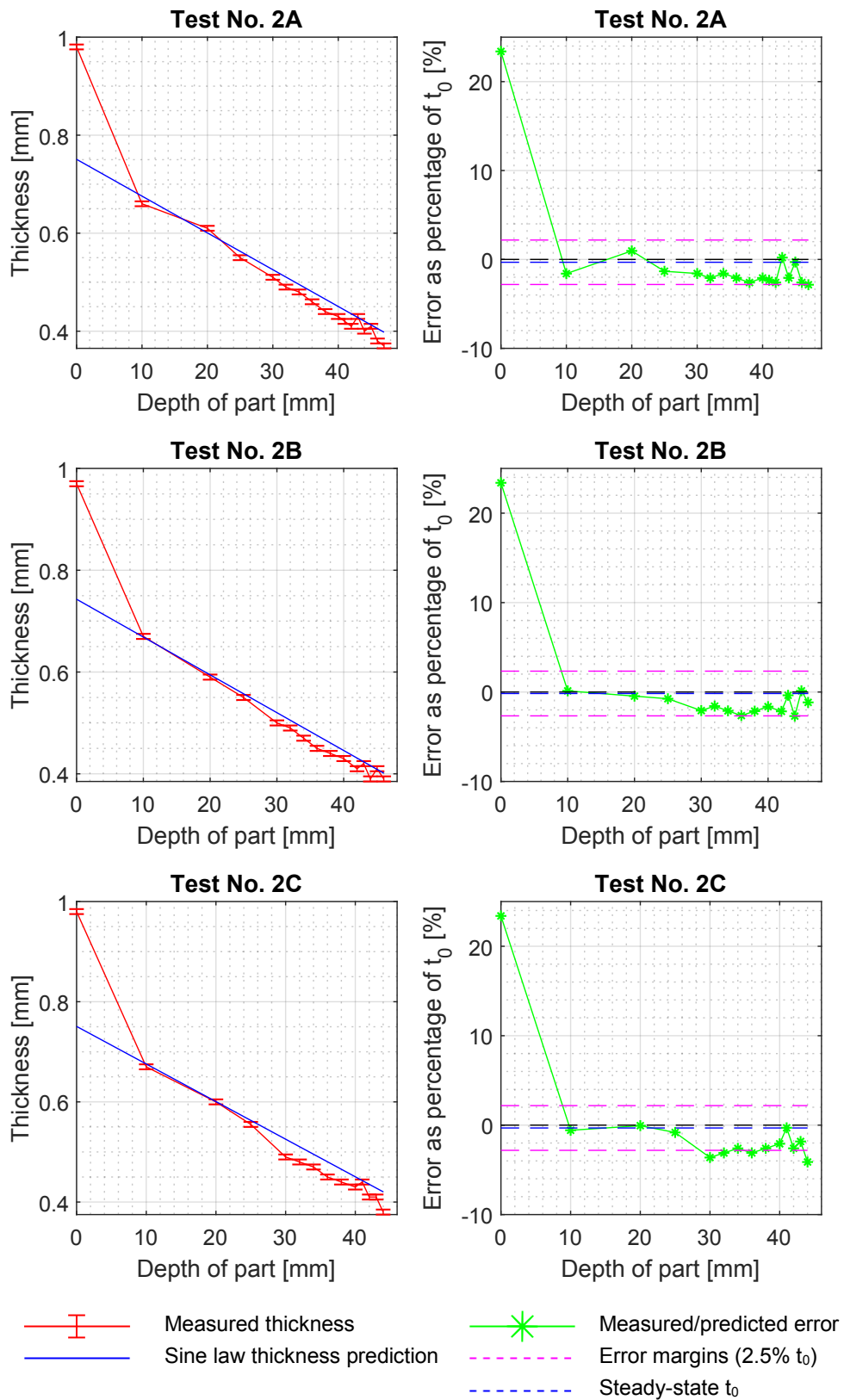


Figure B.2: Test No. 2 - measured thickness distribution results and error plots for each test repeat.

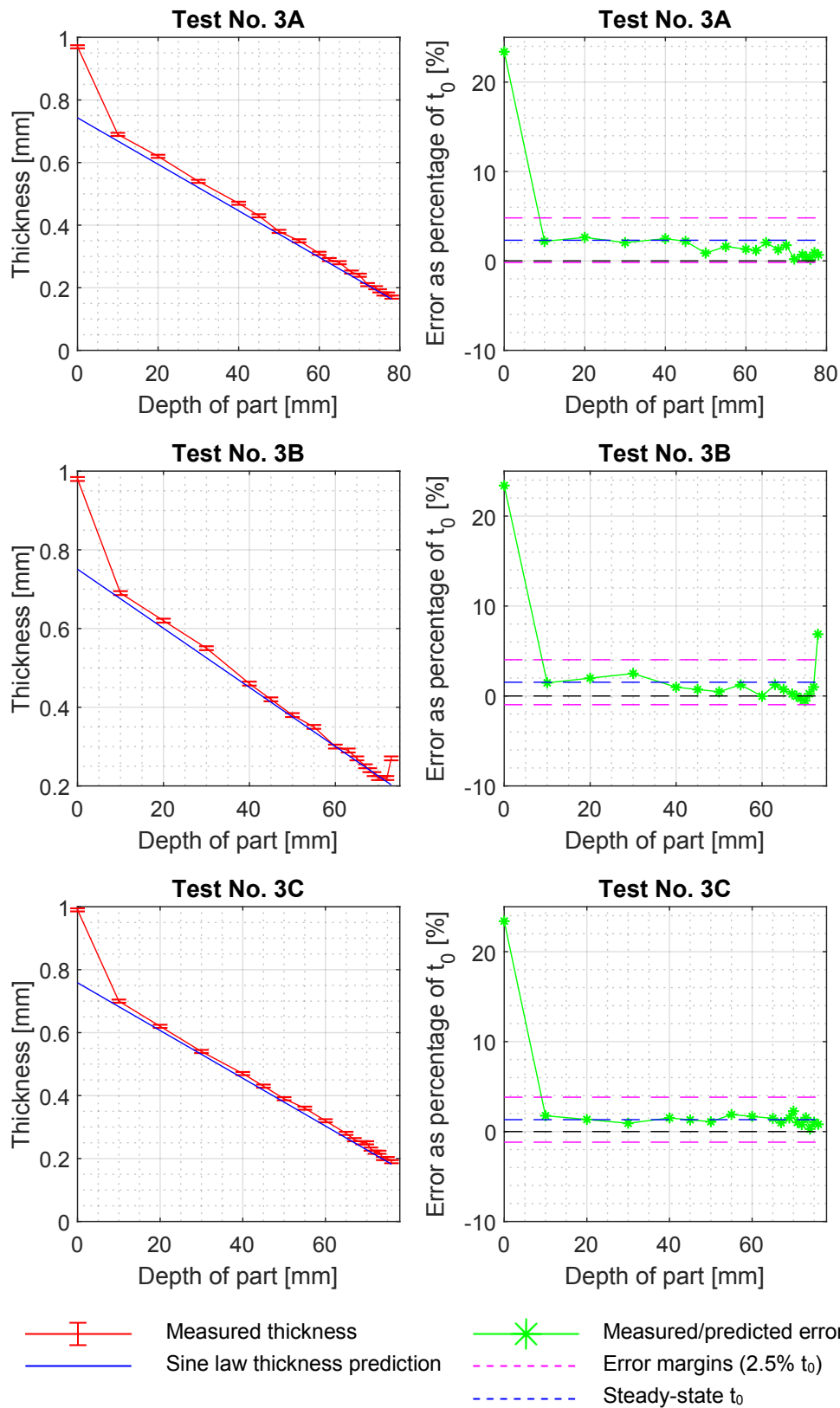


Figure B.3: Test No. 3 - measured thickness distribution results and error plots for each test repeat.

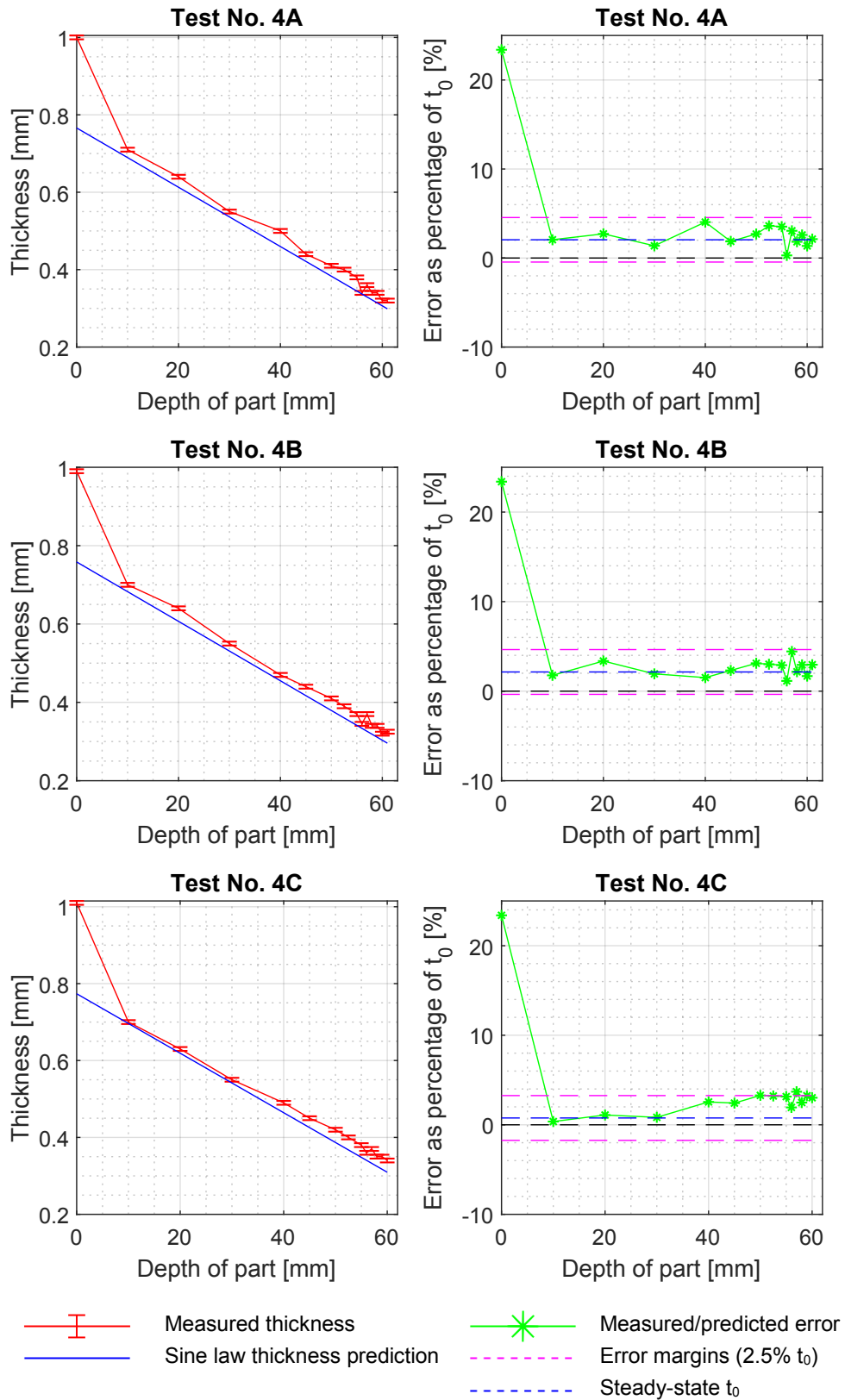


Figure B.4: Test No. 4 - measured thickness distribution results and error plots for each test repeat.

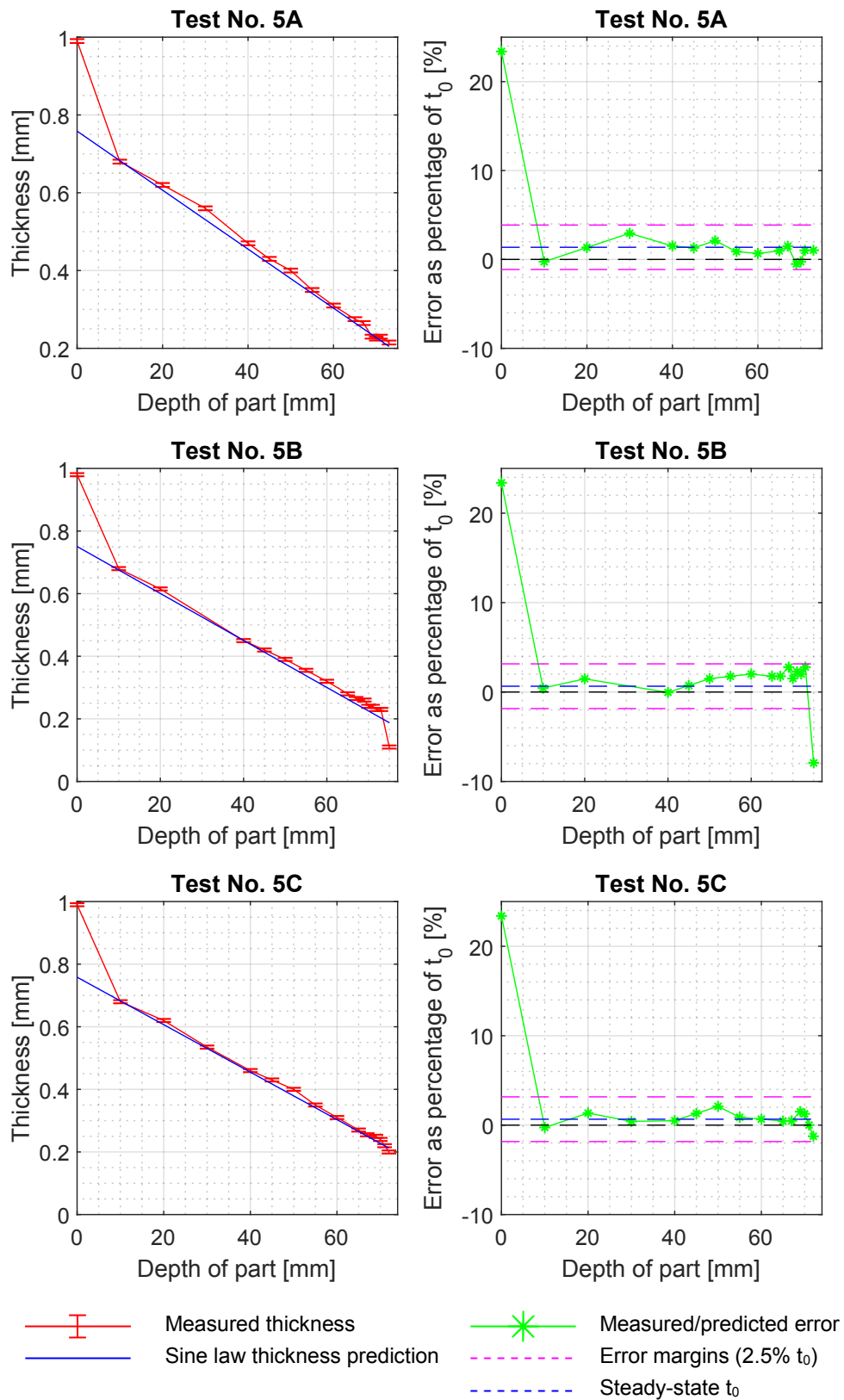


Figure B.5: Test No. 5 - measured thickness distribution results and error plots for each test repeat.

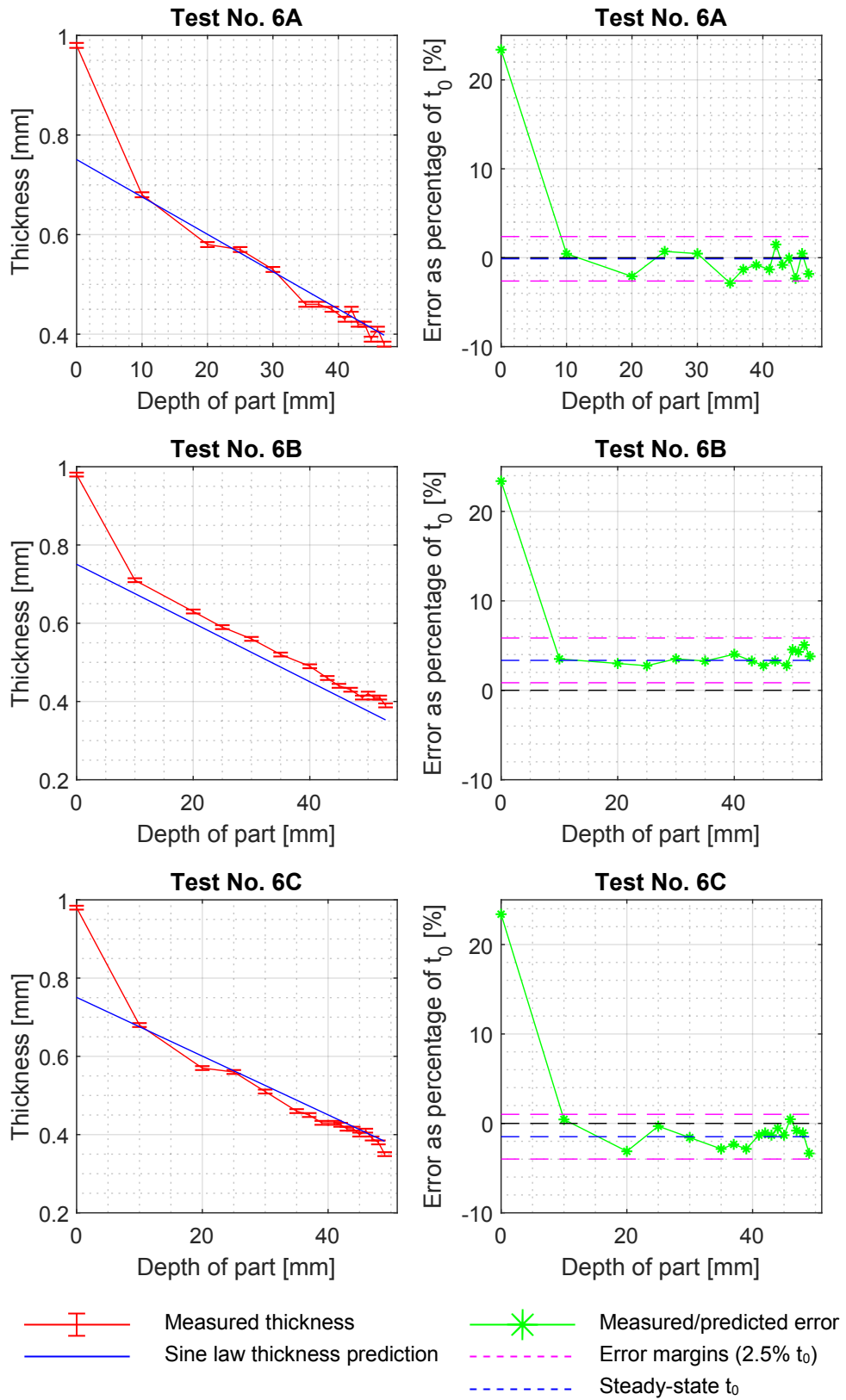


Figure B.6: Test No. 6 - measured thickness distribution results and error plots for each test repeat.

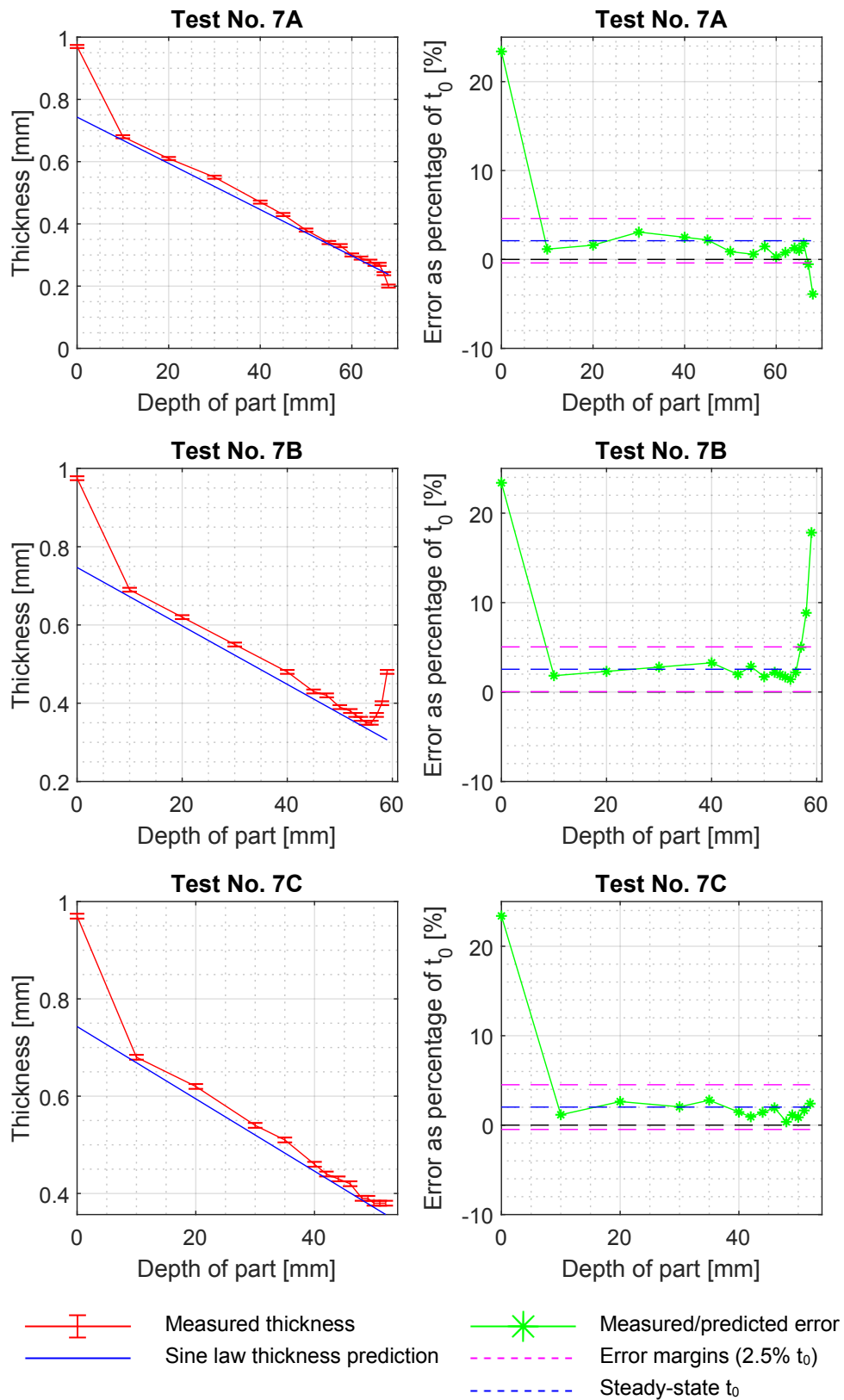


Figure B.7: Test No. 7 - measured thickness distribution results and error plots for each test repeat.

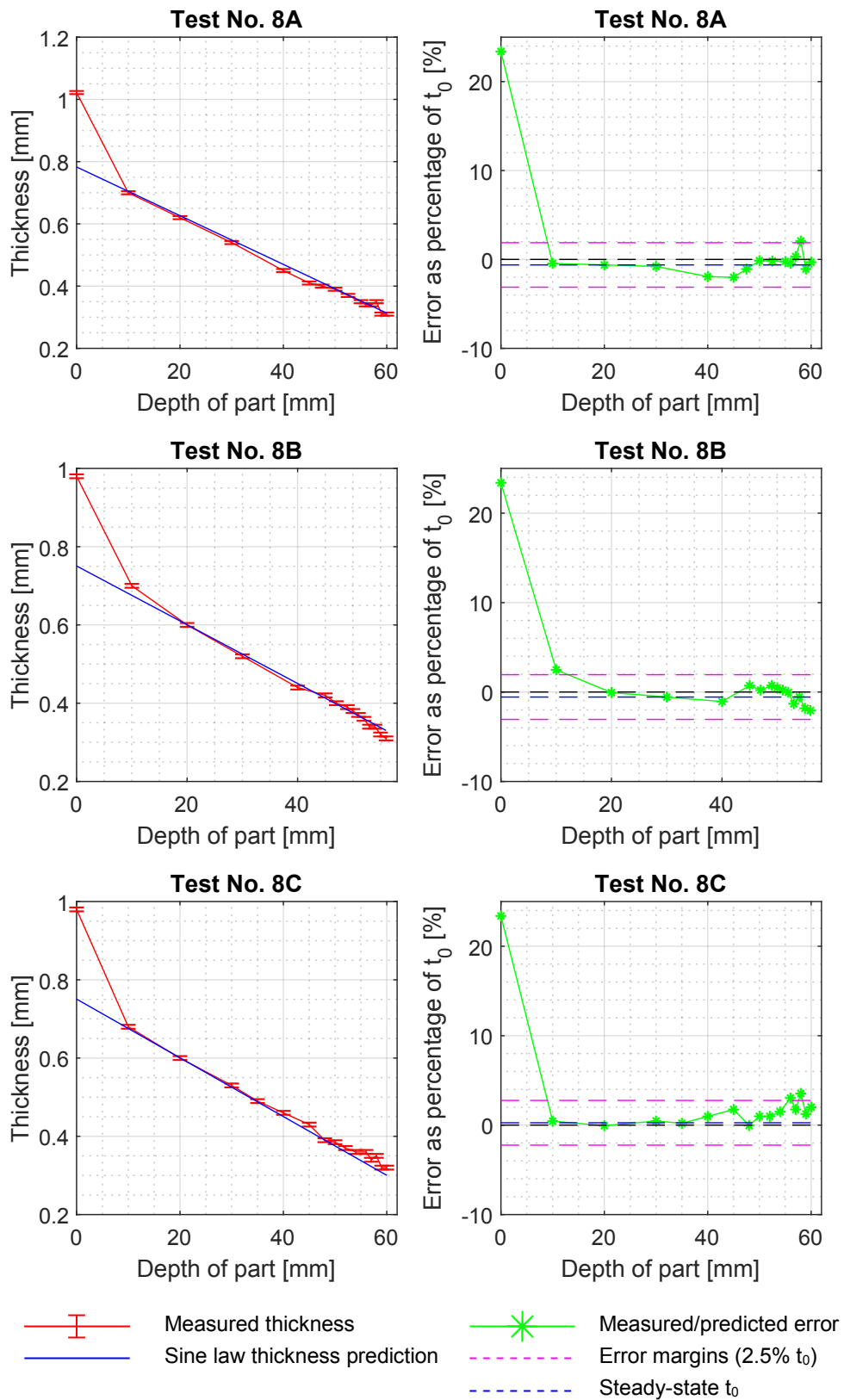


Figure B.8: Test No. 8 - measured thickness distribution results and error plots for each test repeat.

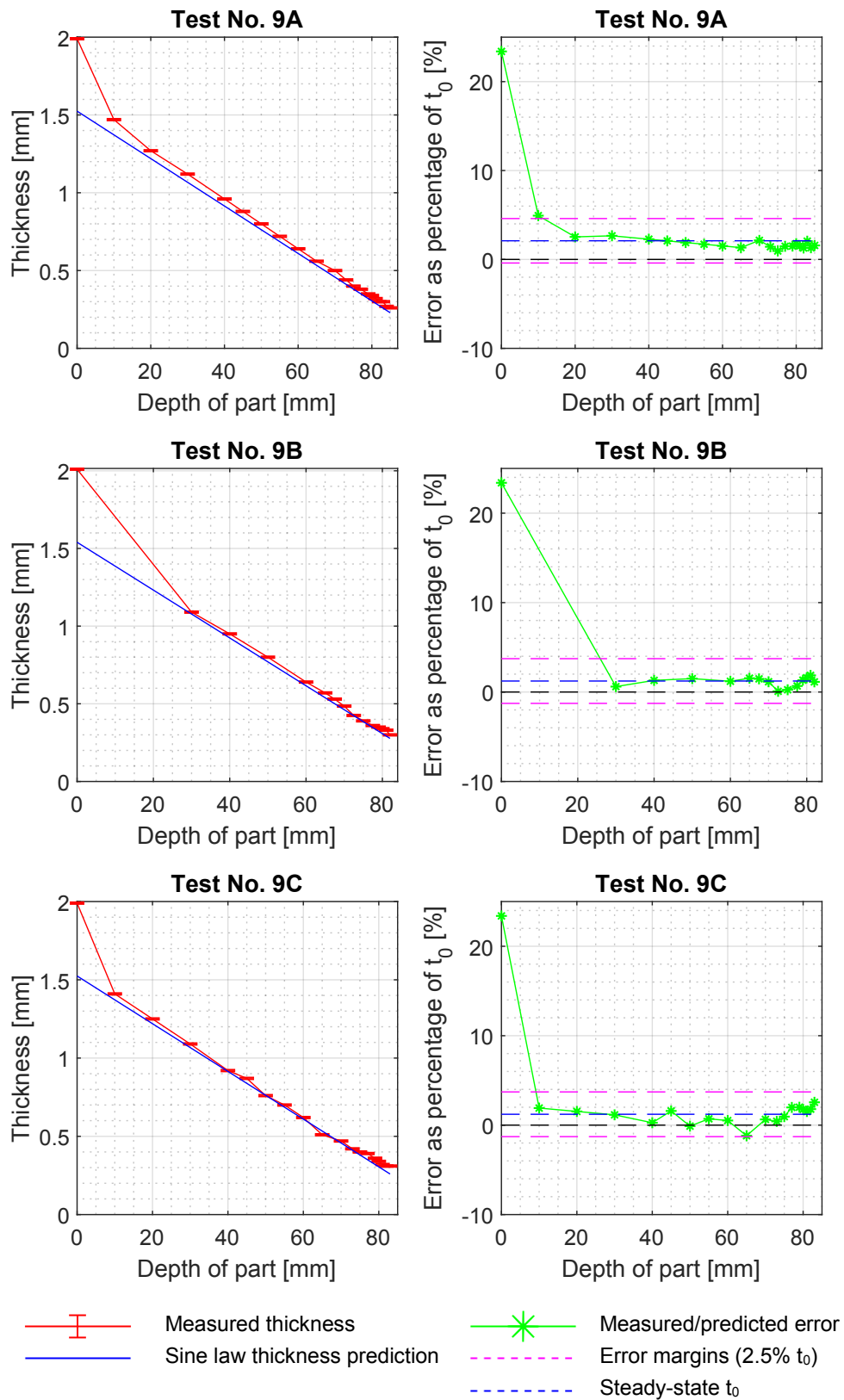


Figure B.9: Test No. 9 - measured thickness distribution results and error plots for each test repeat.

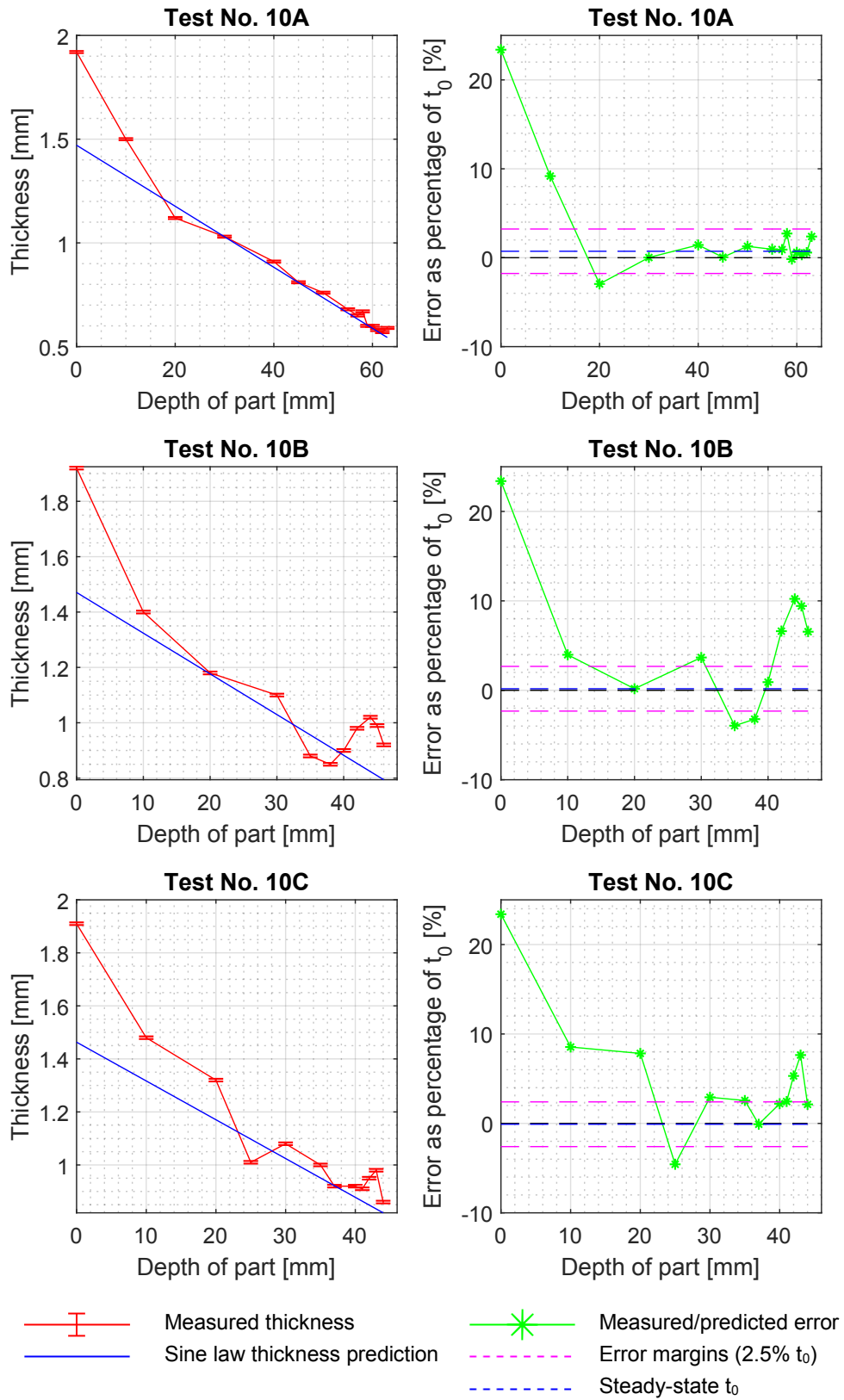


Figure B.10: Test No. 10 - measured thickness distribution results and error plots for each test repeat.

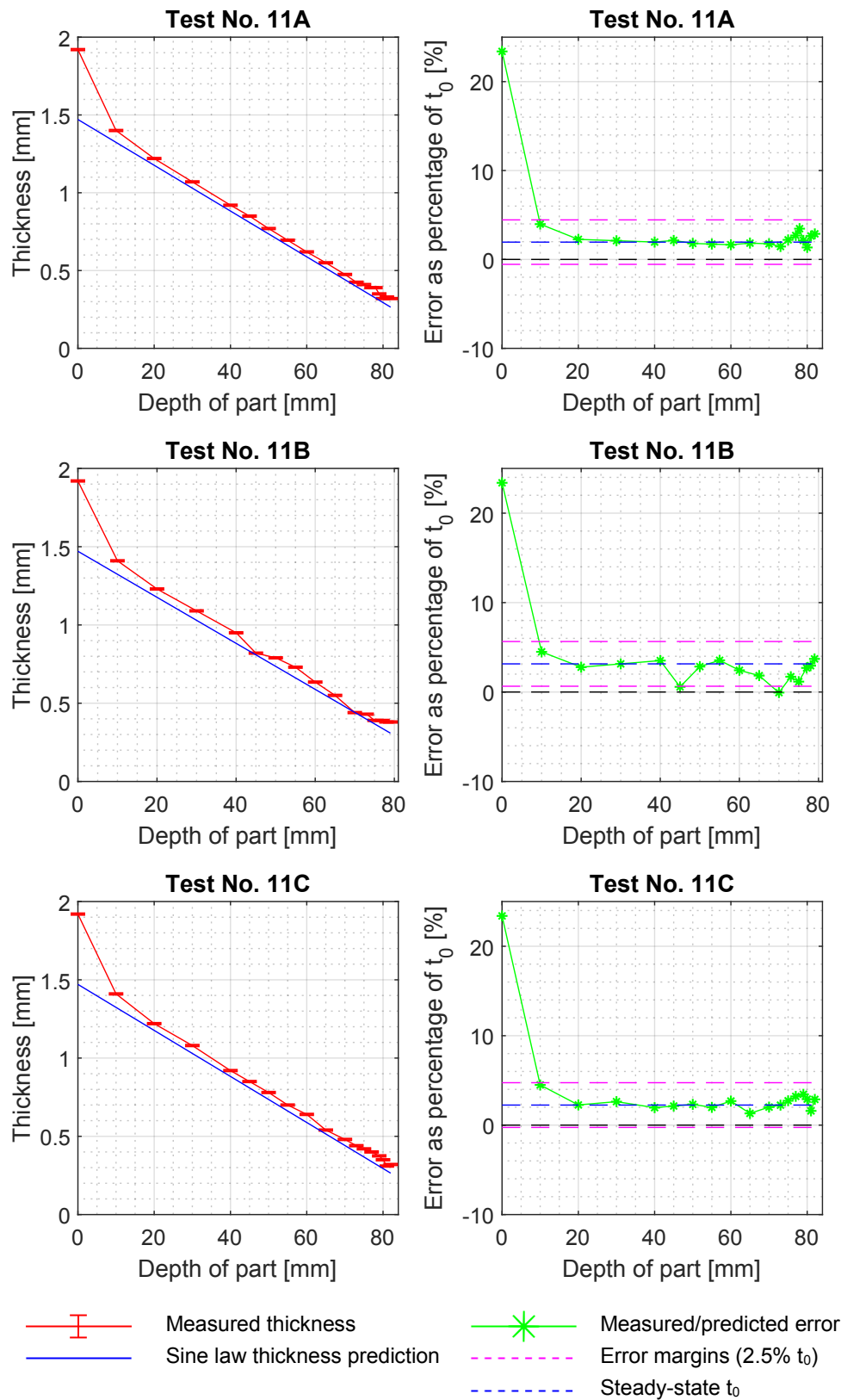


Figure B.11: Test No. 11 - measured thickness distribution results and error plots for each test repeat.

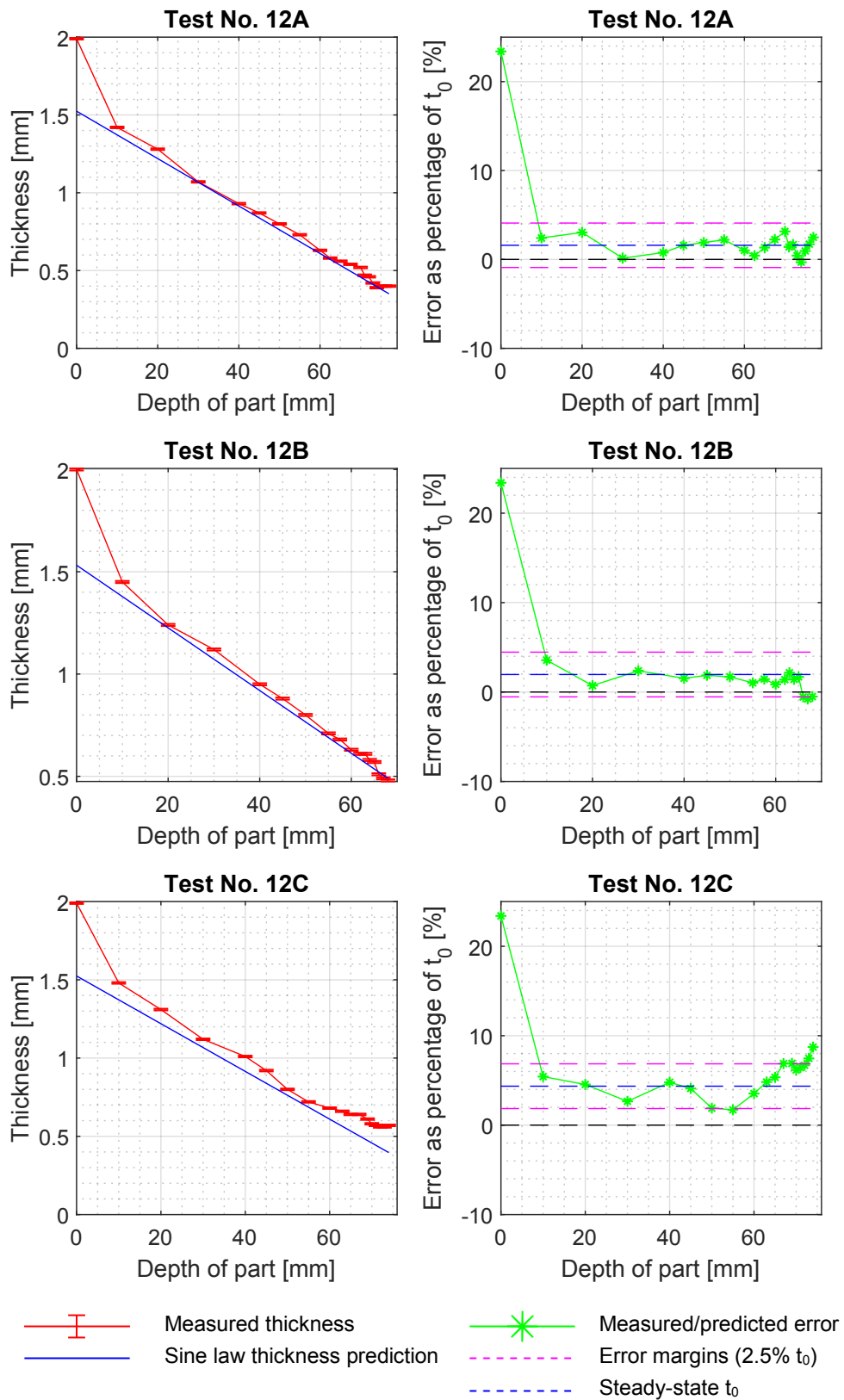


Figure B.12: Test No. 12 - measured thickness distribution results and error plots for each test repeat.

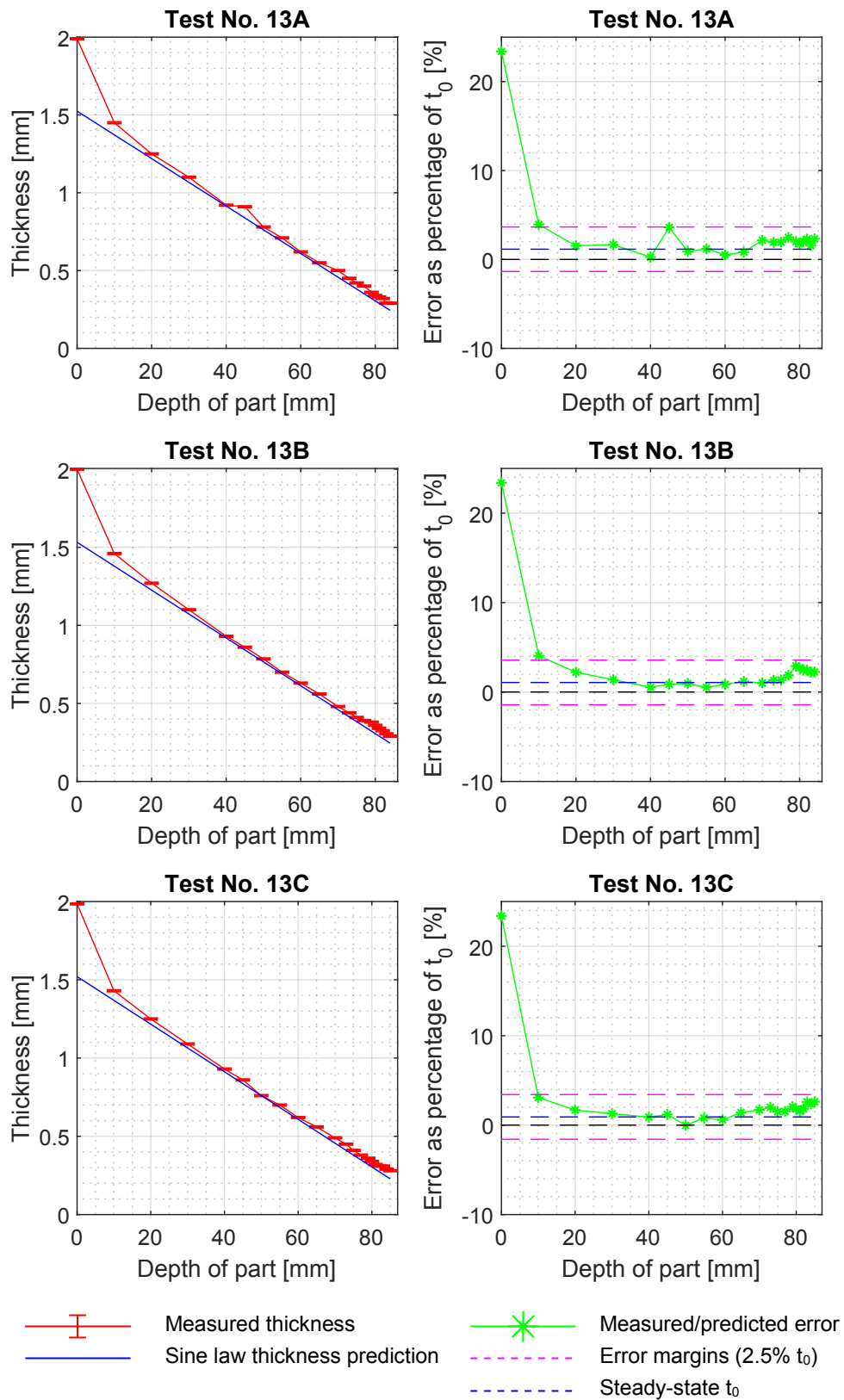


Figure B.13: Test No. 13 - measured thickness distribution results and error plots for each test repeat.

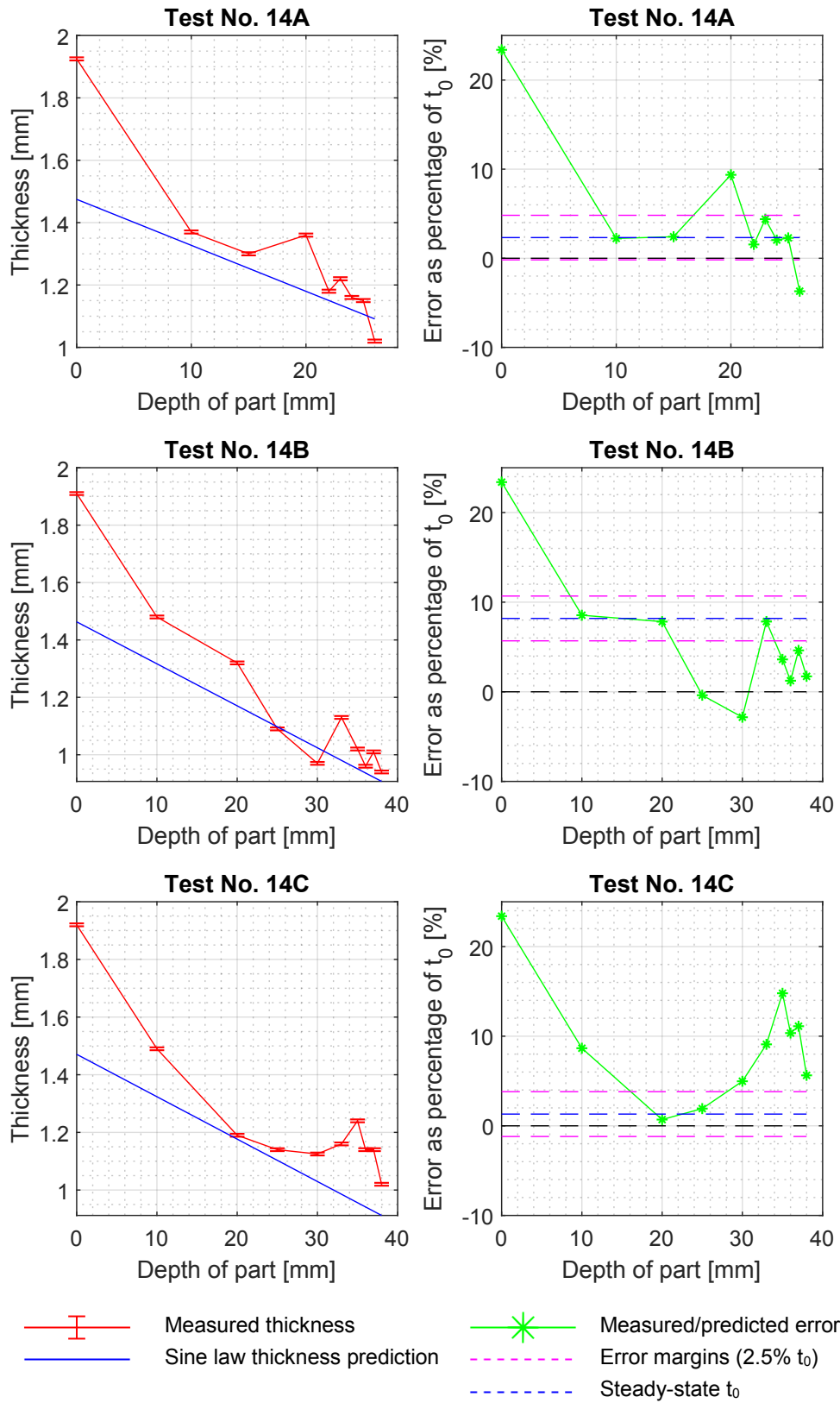


Figure B.14: Test No. 14 - measured thickness distribution results and error plots for each test repeat.

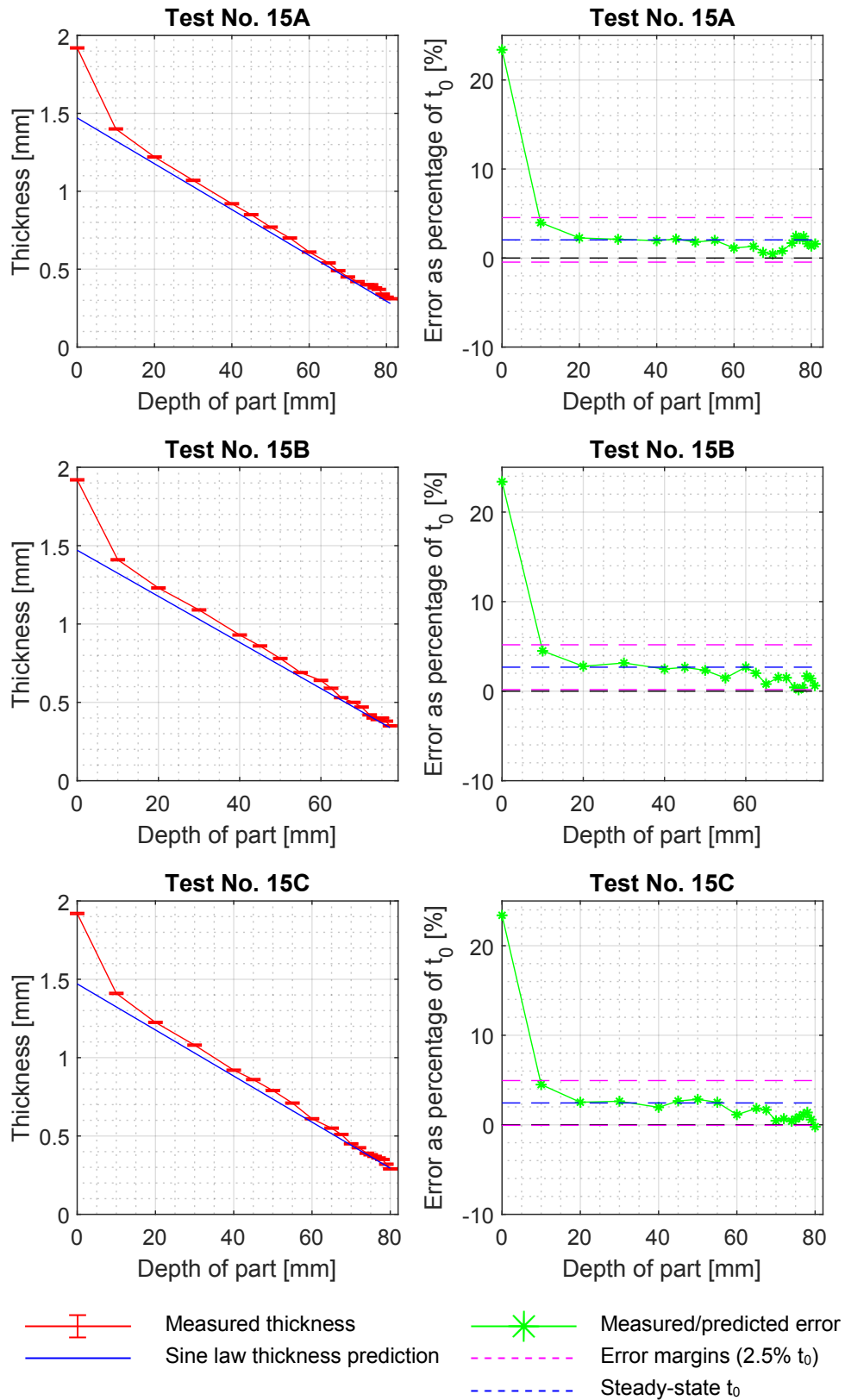


Figure B.15: Test No. 15 - measured thickness distribution results and error plots for each test repeat.

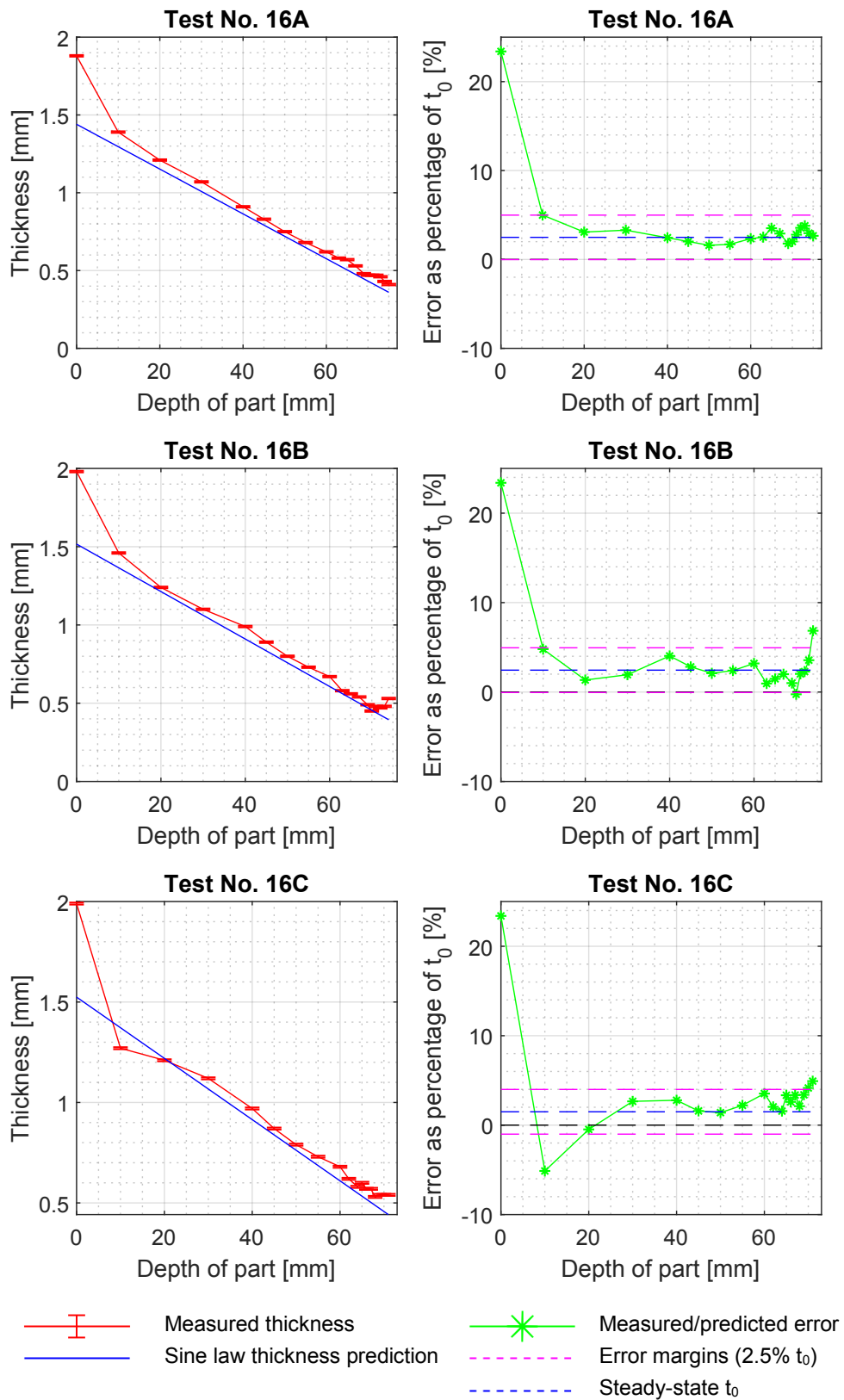


Figure B.16: Test No. 16 - measured thickness distribution results and error plots for each test repeat.

Formability of VWACF test parts and statistical data analysis

The following pages present additional information regarding the study in Chapter 6. Firstly, the raw data from the VWACF parts is given, followed by the full statistical analysis carried out in **R** with this data.

C.1 Fracture depth of VWACF parts

Table C.1: Raw data of the fracture depth of the VWACF parts

Test No.	Fracture depth [mm]	Wall angle [°]
1	84.5, 84.0, 84.0	82.74, 82.52, 82.52
2	48.3, 48.5, 47.4	66.19, 66.29, 65.76
3	80.0, 75.3, 78.0	80.74, 78.65, 79.85
4	77.5, 69.5, 75.0	79.63, 76.04, 78.51
5	85.0, 85.0, 86.5	82.96, 82.96, 83.62
6	49.0, 55.1, 51.5	66.53, 69.41, 67.72
7	71.6, 62.0, 54.0, 61.0, 72.7, 70.8	77.43, 72.62, 69.37, 72.62, 77.48, 77.07
8	76.0, 76.0, 73.0	78.96, 78.96, 77.61
9	69.9, 76.9, 73.5	76.22, 79.36, 77.84
10	63.4, 47.2, 45.2	73.26, 65.66, 64.69
11	78.1, 76.5, 74.1	79.90, 79.18, 78.11
12	62.0, 62.4, 60.4	72.62, 72.80, 71.88
13	73.5, 74.4, 73.0	77.84, 78.24, 77.61
14	27.4, 40.0, 40.4	55.68, 62.14, 62.34
15	81.4, 78.5, 80.2	81.36, 80.07, 80.83
16	61.1, 57.1, 60.5	72.20, 70.35, 71.93
17	75.0, 70.6, 72.8	78.96, 76.98, 77.97
18	84.6, 80.6, 83.9	83.22, 81.45, 82.92
19	75.8, 74.8, 74.7	79.32, 78.87, 78.82
20	79.2, 76.5, 80.8	80.83, 79.63, 81.54
21	80.5, 81.1, 80.2	81.41, 81.68, 81.28
22	84.0, 85.7, 80.2	82.96, 83.71, 81.28
23	82.3, 82.7, 83.2	82.21, 82.38, 82.61
24	79.4, 81.7, 80.7	80.92, 81.94, 81.50

C.2 Experimental Set 1 - R code

```
# Wall angle at fracture = Fr_A
# Shaft radius = R
# Sheet thickness = t
# Tool shape = flat
# Step down = Z

> fit = lmer(Fr_A ~ R+t+flat+Z+ R:t + R:flat+ t:flat +
+ Z:t + Z:flat+ Z:R + (1|TestID), data = esn, REML=TRUE)
```

fixed-effect model matrix is rank deficient
so dropping 6 columns / coefficients

```
>
> s_fit <- step(fit, type = 3,
+ alpha.random = 0.1, alpha.fixed = 0.05,
+ reduce.fixed = TRUE, reduce.random = TRUE,
+ fixed.calc = TRUE, lsmeans.calc = TRUE,
+ keep.effs = NULL)
> print(s_fit)
```

Random effects:

Chi.sq	Chi.DF	elim.num	p.value
TestID	23.33	1	kept
			0

Fixed effects:

Sum Sq	Mean Sq	NumDF	DenDF	F.value	elim.num	Pr(>F)
R:t	0.0086	0.0086	2	5.97	0.0023	1 0.9634
R:Z	0.4231	0.2115	2	6.97	0.0565	2 0.9455
R:flat	0.0639	0.0639	1	8.94	0.0171	3 0.8989
t:Z	2.5124	2.5124	1	9.90	0.6705	4 0.4321
R	2.6556	2.6556	1	10.94	0.7088	5 0.4179
t:fl	6.5587	6.5587	2	11.94	1.7513	6 0.2105
t	15.1066	15.1066	2	13.02	4.0373	7 0.0657
flat	22.7653	22.7653	1	14.19	6.0911	kept 0.0269
Z	162.3093	81.1546	2	14.18	21.7139	kept 0
flat:Z	52.4727	26.2364	2	14.18	7.0199	kept 0.0076

(...)

Final model:

```
lme4::lmer(formula = Fr_A ~ flat + Z + flat:Z + (1 | TestID),
data = esn, contrasts = list(flat = "contr.SAS", Z = "contr.SAS"))
```

```
>
```

Analysis of Variance Table of type III with Satterthwaite approximation for degrees of freedom

Sum Sq	Mean Sq	NumDF	DenDF	F.value	Pr(>F)
flat	22.765	22.765	1	14.191	6.0911 0.026887 *
Z	162.309	81.155	2	14.178	21.7139 4.829e-05 ***

```
flat:Z  52.473  26.236      2 14.178  7.0199  0.007604 **
---
Signif. codes:  0 '***' 0.001 '**' 0.01 '*' 0.05 '.' 0.1 ' ' 1
```

C.3 Experimental Set 2 - R code

```
# Wall angle at fracture = Fr_A
# Shaft radius = R
# Sheet thickness = t
# Tool shape = flat

> # Models which are able to successfully be applied in the step function
> # (other models did not generate a result and produced a NULL response)
> model1 = Fr_A ~ R+t+flat+ R:flat + flat:t + (1|TestID)
> model2 = Fr_A ~ R+t+flat+ R:t + flat:t + (1|TestID)
> es2_m1 = lmer(model1, data = esn, REML=TRUE)
> es2_m2 = lmer(model2, data = esn, REML=TRUE)
> summary(es2_m1)
Linear mixed model fit by REML t-tests use Satterthwaite
approximations to degrees of freedom [lmerMod]
Formula: Fr_A ~ R + t + flat + R:flat + flat:t + (1 | TestID)
Data: esn

REML criterion at convergence: 137.8

Scaled residuals:
Min      1Q  Median      3Q      Max
-3.2753 -0.1730  0.0235  0.2976  1.7202

Random effects:
Groups   Name          Variance Std.Dev.
TestID   (Intercept)  2.473    1.572
Residual                2.637    1.624
Number of obs: 39, groups: TestID, 12

Fixed effects:
Estimate Std. Error      df t value Pr(>|t|)
(Intercept)  77.5807      1.4948  4.3030  51.901 3.48e-07 ***
```

```

R8          0.5427    1.4948  4.3030   0.363   0.7337
t1.6        4.0741    1.8307  4.3030   2.225   0.0853 .
t2          5.0337    1.8307  4.3030   2.750   0.0474 *
flat1       0.2263    2.1018  4.2020   0.108   0.9192
R8:flat1    -2.2330    2.1018  4.2020  -1.062   0.3453
t1.6:flat1  1.0149    2.5668  4.1520   0.395   0.7120
t2:flat1    -2.0860    2.5668  4.1520  -0.813   0.4604
---
Signif. codes:  0 '***' 0.001 '**' 0.01 '*' 0.05 '.' 0.1 ' ' 1

```

(...)

```
> summary(es2_m2)
```

```

Linear mixed model fit by REML t-tests use Satterthwaite
approximations to degrees of freedom [lmerMod]
Formula: Fr_A ~ R + t + flat + R:t + flat:t + (1 | TestID)
Data: esn

```

```
REML criterion at convergence: 132.7
```

```
Scaled residuals:
```

```

Min      1Q  Median      3Q      Max
-3.2398 -0.2155  0.0420  0.2991  1.7514

```

```
Random effects:
```

```

Groups   Name          Variance Std.Dev.
TestID   (Intercept)  2.187   1.479
Residual                2.642   1.625
Number of obs: 39, groups: TestID, 12

```

```
Fixed effects:
```

```

Estimate Std. Error      df t value Pr(>|t|)
(Intercept)  79.2081    1.5074  3.1075 52.545 1.09e-05 ***
R8           -2.7119    1.7186  2.9483 -1.578  0.214
t1.6         2.7807    2.1385  3.1479  1.300  0.281
t2           3.1067    2.1385  3.1479  1.453  0.238
flat1        -0.8636    1.7186  2.9483 -0.502  0.650
R8:t1.6      2.5870    2.4539  3.0673  1.054  0.368

```

```
R8:t2      3.8541    2.4539  3.0673   1.571    0.212
t1.6:flat1 0.9884    2.4539  3.0673   0.403    0.714
t2:flat1   -2.1125    2.4539  3.0673  -0.861    0.451
```

```
---
```

```
Signif. codes:  0 '***' 0.001 '**' 0.01 '*' 0.05 '.' 0.1 ' ' 1
```

```
(...)
```

```
> es2_s1 <- step(es2_m1, type = 3, alpha.random = 0.1, alpha.fixed = 0.05,
+   reduce.fixed = TRUE, reduce.random = TRUE, fixed.calc = TRUE,
+   lsmeans.calc = TRUE, keep.offs = NULL)
> es2_s2 <- step(es2_m2, type = 3, alpha.random = 0.1, alpha.fixed = 0.05,
+   reduce.fixed = TRUE, reduce.random = TRUE, fixed.calc = TRUE,
+   lsmeans.calc = TRUE, keep.offs = NULL)
> print(es2_s1)
```

```
Random effects:
```

```
Chi.sq Chi.DF elim.num p.value
```

```
TestID  5.21    1    kept  0.0225
```

```
Fixed effects:
```

```
Sum Sq Mean Sq NumDF DenDF F.value elim.num Pr(>F)
```

```
t:flat  3.9368  1.9684    2  4.20  0.7464    1 0.5280
```

```
R:flat  3.2757  3.2757    1  6.13  1.2406    2 0.3071
```

```
R        0.8584  0.8584    1  7.31  0.3261    3 0.5851
```

```
flat    4.3455  4.3455    1  8.52  1.6571    4 0.2319
```

```
t       42.3601 21.1801    2  9.75  8.1105    kept 0.0084
```

```
(...)
```

```
Final model:
```

```
lme4::lmer(formula = Fr_A ~ t + (1 | TestID), data = esn, REML = TRUE,
contrasts = list(t = "contr.SAS"))
```

```
> print(es2_s2)
```

```
Random effects:
```

```
Chi.sq Chi.DF elim.num p.value
```

```
TestID  3.4    1    kept  0.0651
```

Fixed effects:

	Sum Sq	Mean Sq	NumDF	DenDF	F.value	elim.num	Pr(>F)
t:flat	4.3259	2.1629	2	3.11	0.8188	1	0.5181
R:t	7.3964	3.6982	2	5.01	1.3977	2	0.3293
R	0.8584	0.8584	1	7.31	0.3261	3	0.5851
flat	4.3455	4.3455	1	8.52	1.6571	4	0.2319
t	42.3601	21.1801	2	9.75	8.1105	kept	0.0084

(...)

Final model:

```
lme4::lmer(formula = Fr_A ~ t + (1 | TestID), data = esn, REML = TRUE,
contrasts = list(t = "contr.SAS"))
```

```
>
```

```
> ##The Final Model from both results is identical.
```

```
> fmodel = Fr_A ~ t + (1 | TestID)
```

```
> es2_fmodel = lmer(fmodel, data = esn, REML=TRUE, contrasts =
list(t = "contr.SAS"))
```

```
> anova(es2_fmodel)
```

Analysis of Variance Table of type III with Satterthwaite approximation for degrees of freedom

	Sum Sq	Mean Sq	NumDF	DenDF	F.value	Pr(>F)
t	42.36	21.18	2	9.7536	8.1105	0.008423 **

```
---
```

```
Signif. codes:  0 '***' 0.001 '**' 0.01 '*' 0.05 '.' 0.1 ' ' 1
```

```
>
```


Geometric accuracy results of truncated pyramid test parts

The following pages present the geometric accuracy results for each truncated pyramid component formed for the experiments in Chapter 7. The results are grouped by component, firstly showing a top-view of the part with a colour scale of deviation, and secondly showing a cross sectional comparison of the measured and designed parts.

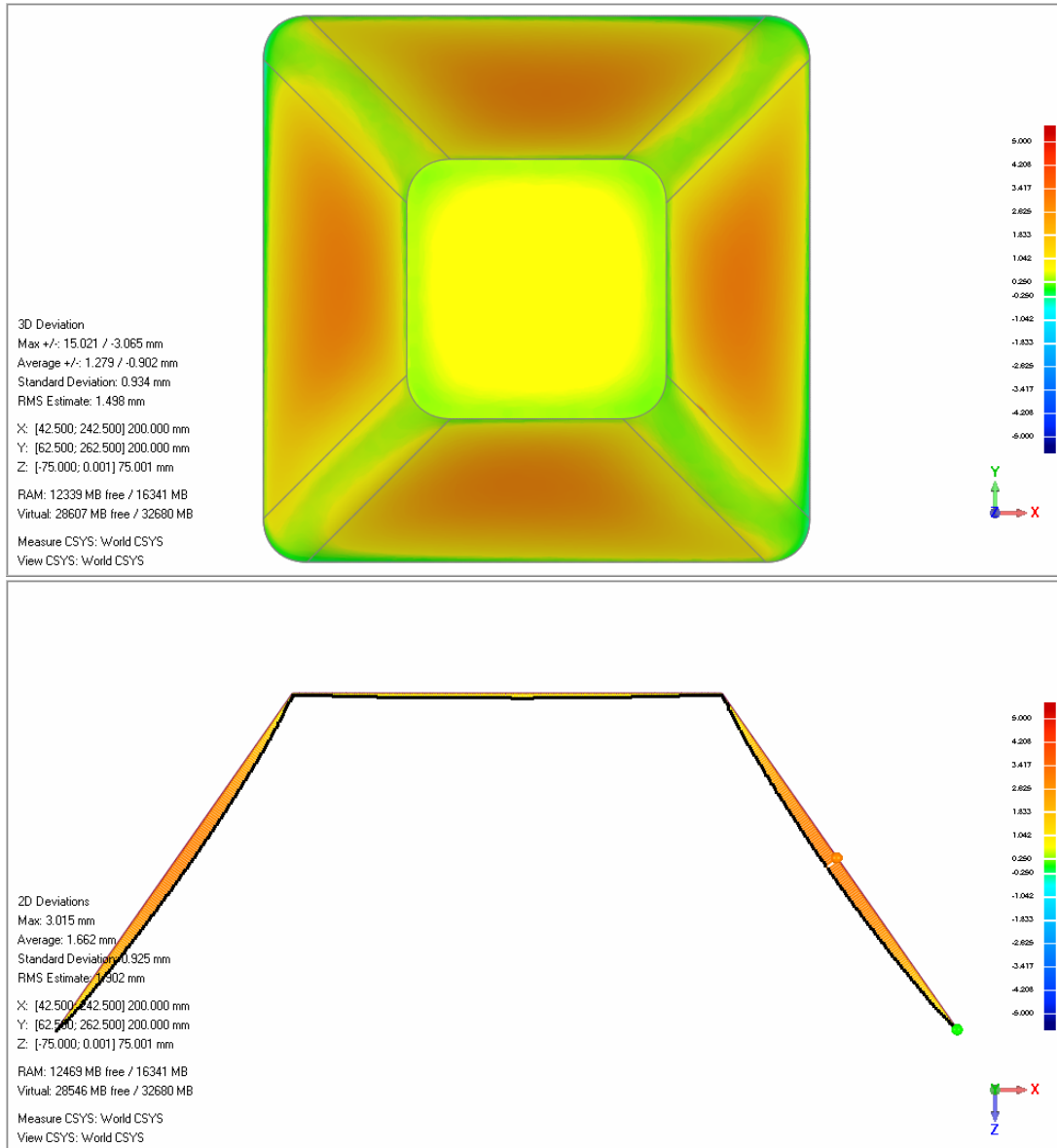


Figure D.1: Part T1A geometric accuracy results - top view and cross-section view

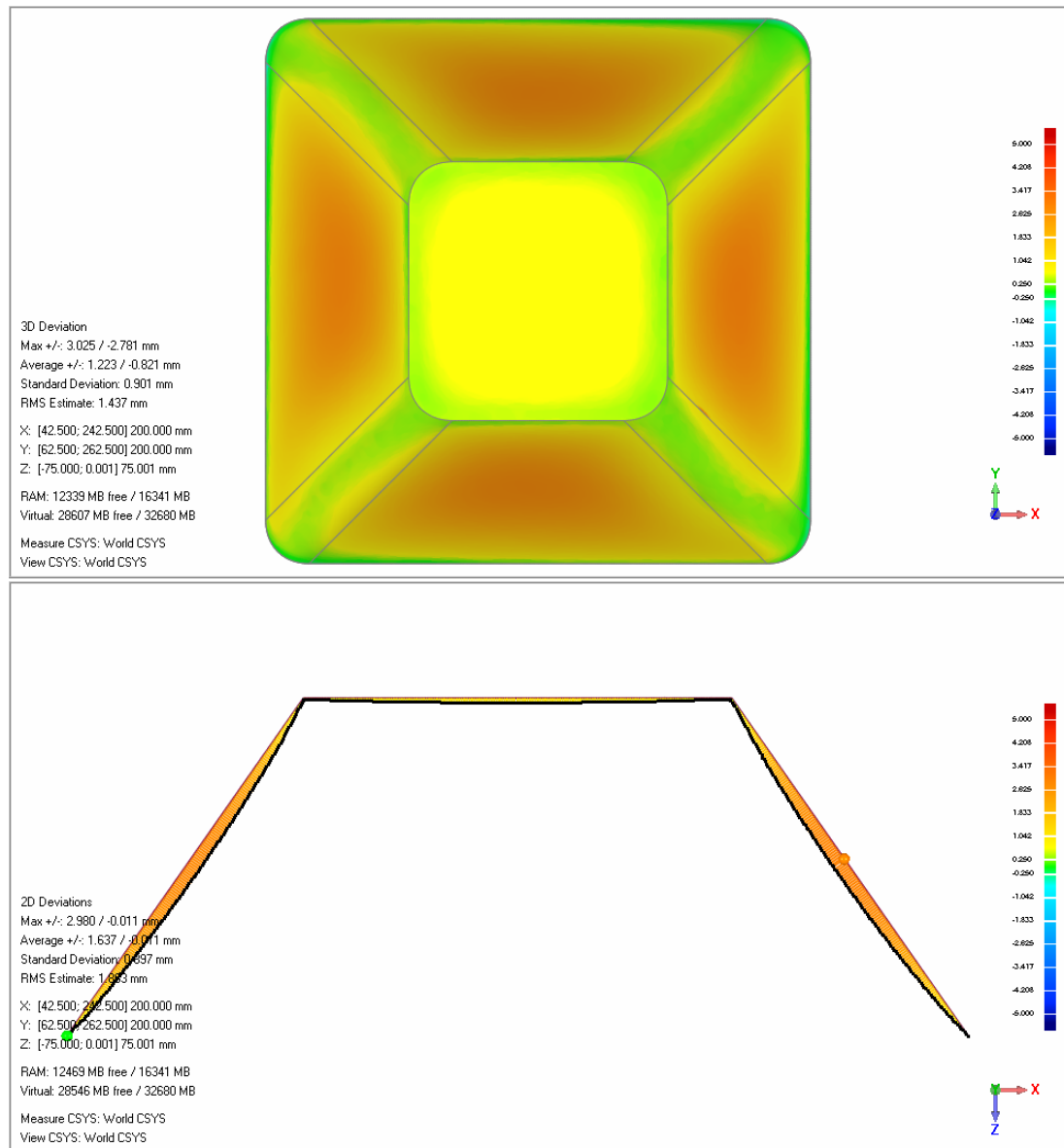


Figure D.2: Part T1B geometric accuracy results - top view and cross-section view

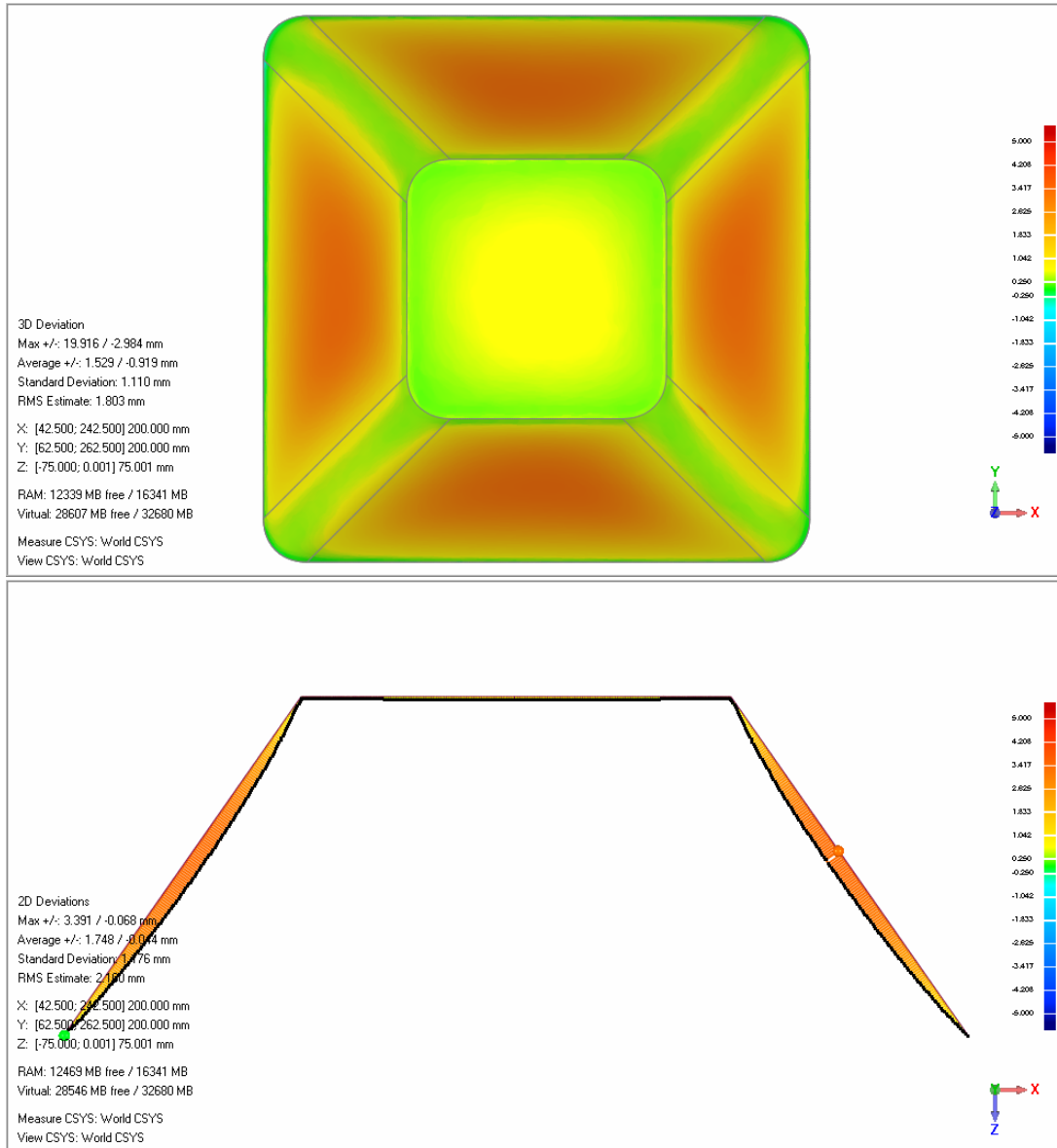


Figure D.3: Part T2A geometric accuracy results - top view and cross-section view

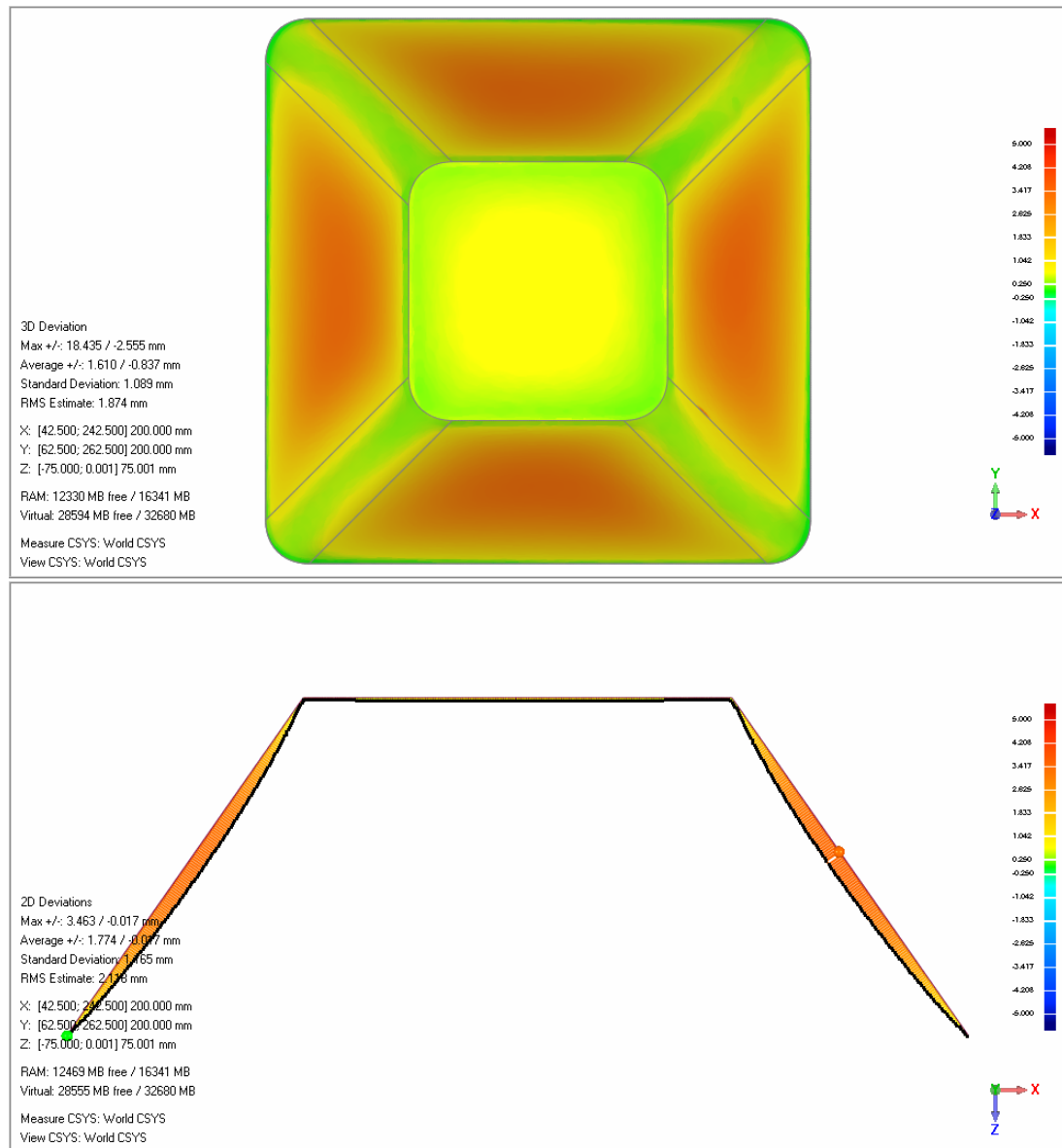


Figure D.4: Part T2B geometric accuracy results - top view and cross-section view

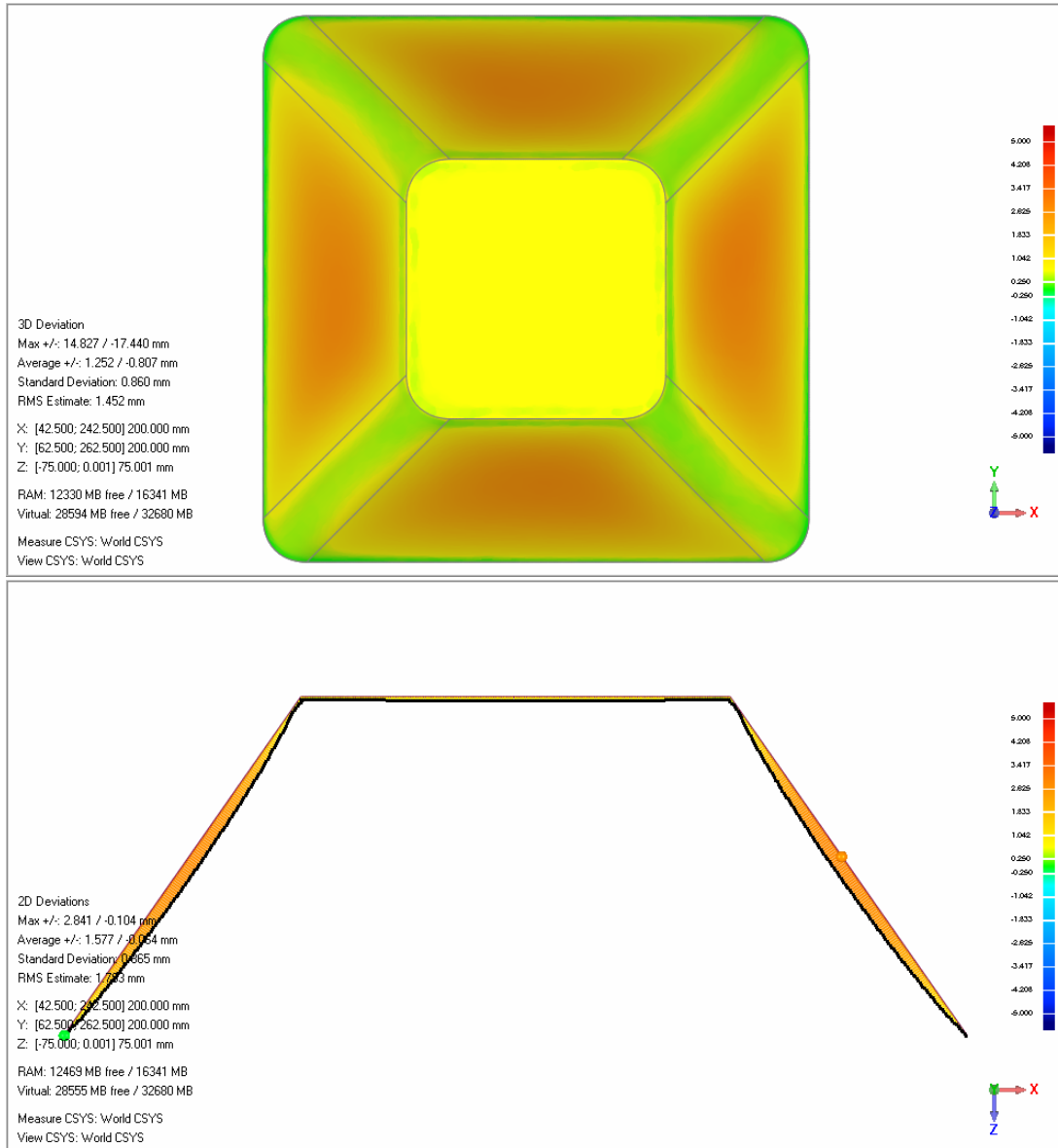


Figure D.5: Part T3A geometric accuracy results - top view and cross-section view

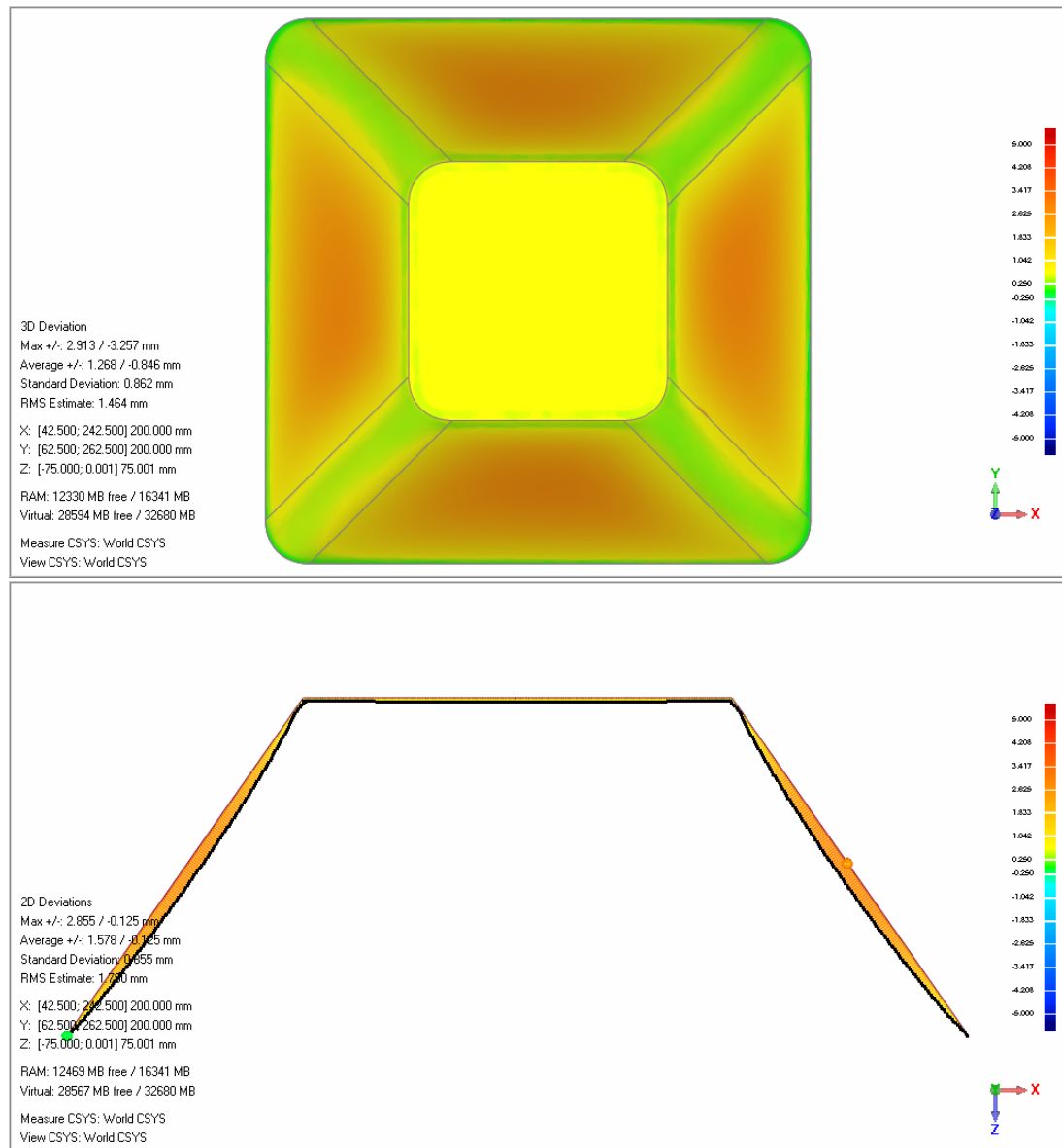


Figure D.6: Part T3B geometric accuracy results - top view and cross-section view

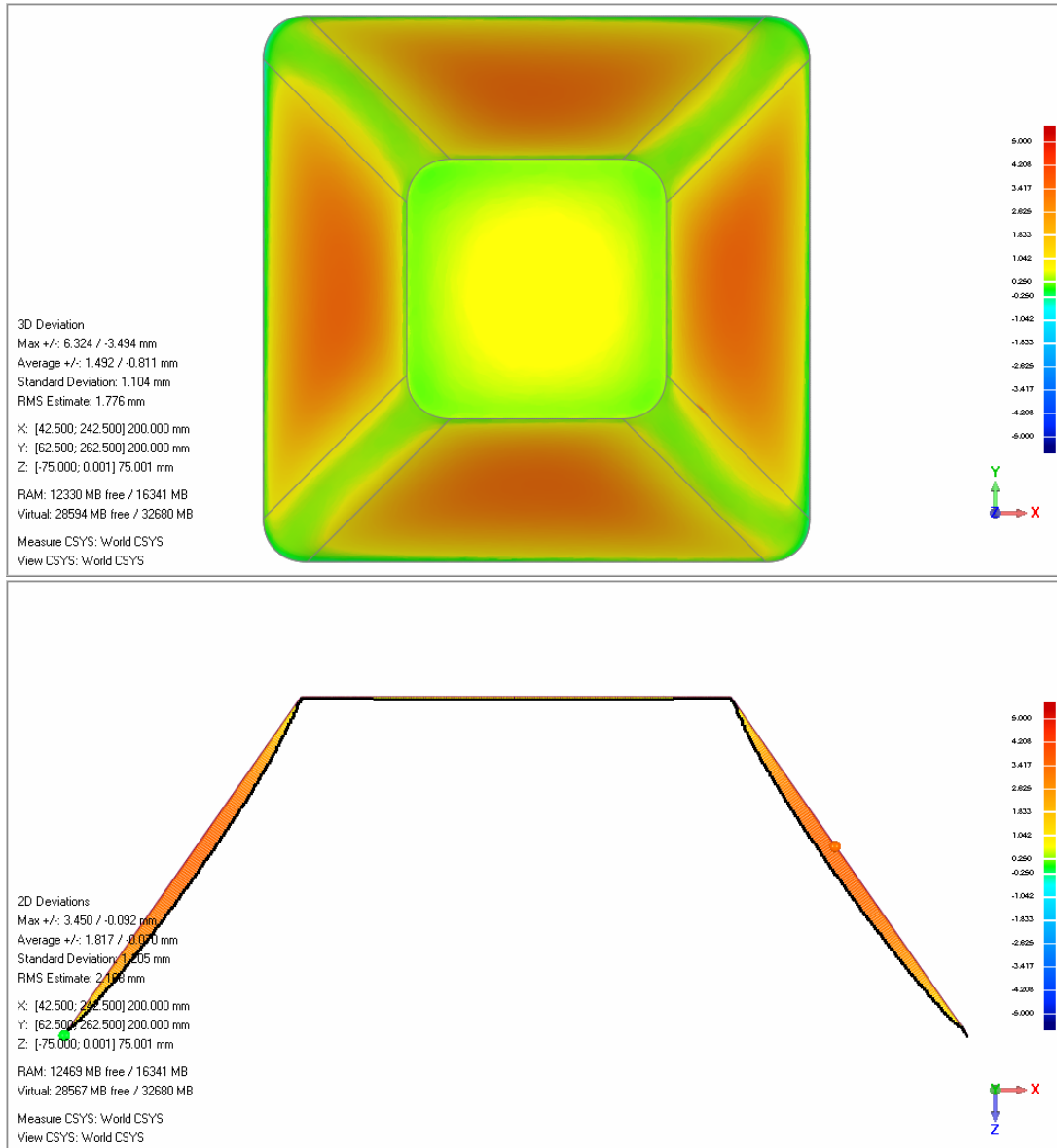


Figure D.7: Part T4A geometric accuracy results - top view and cross-section view

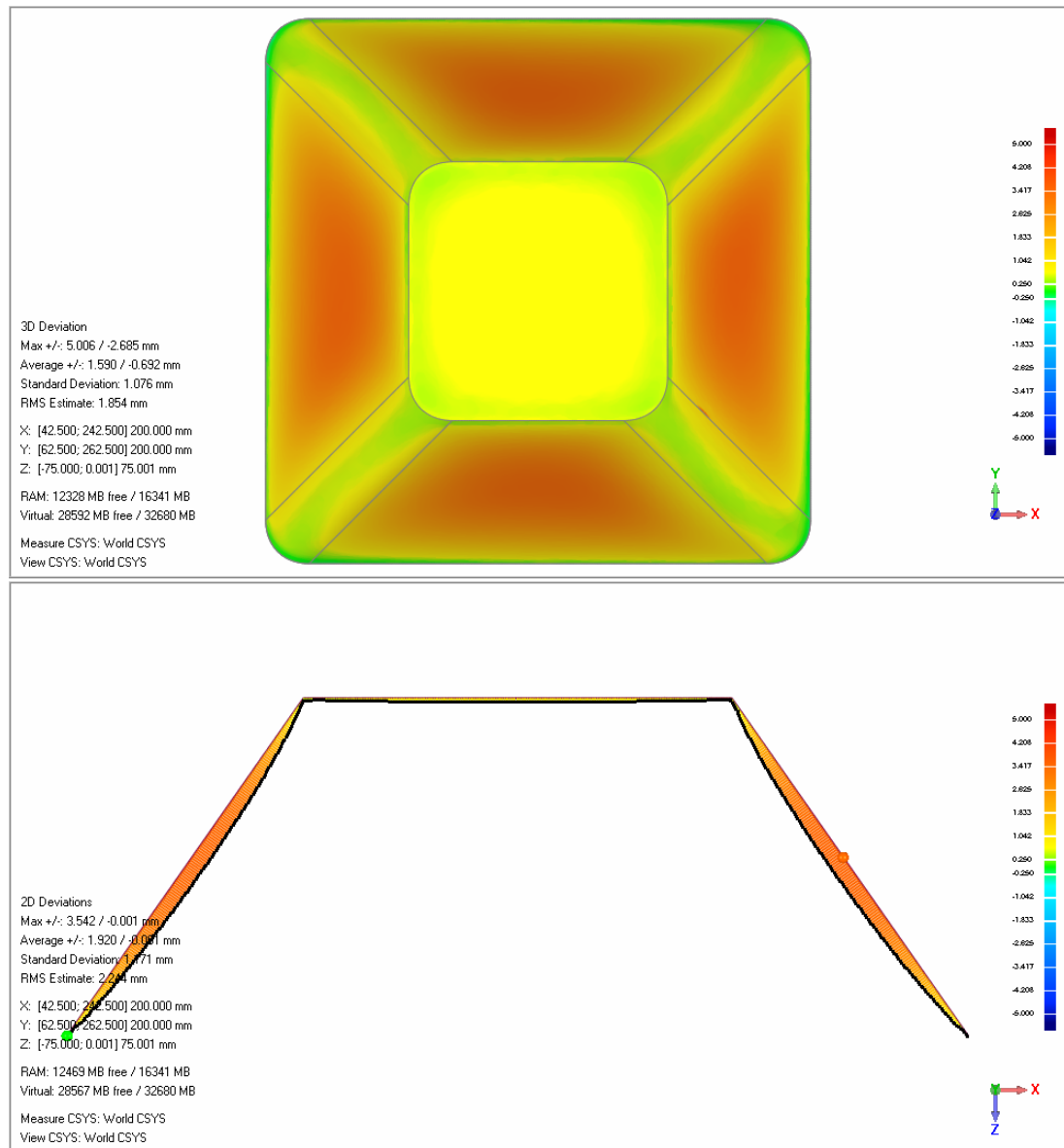


Figure D.8: Part T4B geometric accuracy results - top view and cross-section view

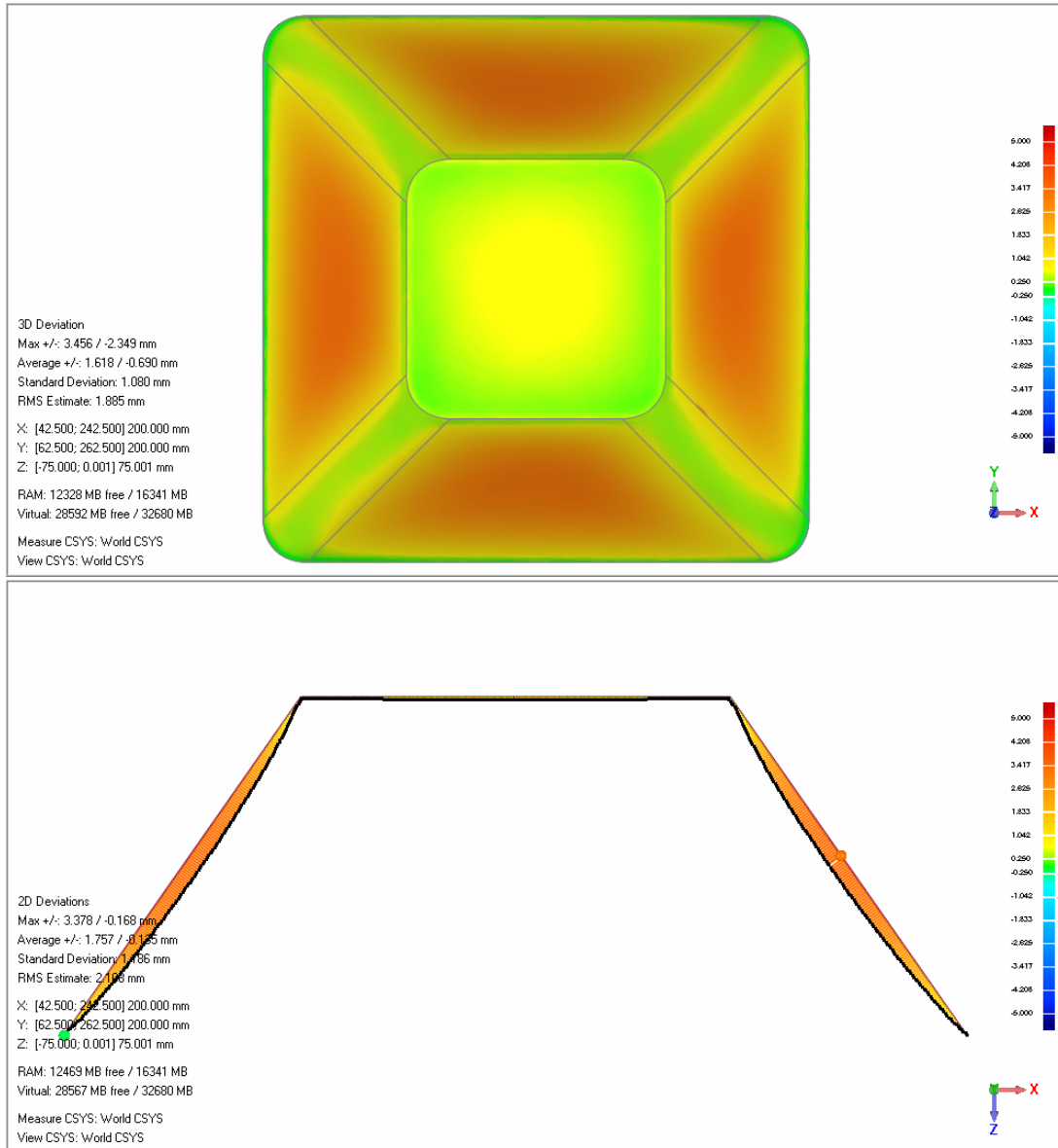


Figure D.9: Part T5A geometric accuracy results - top view and cross-section view

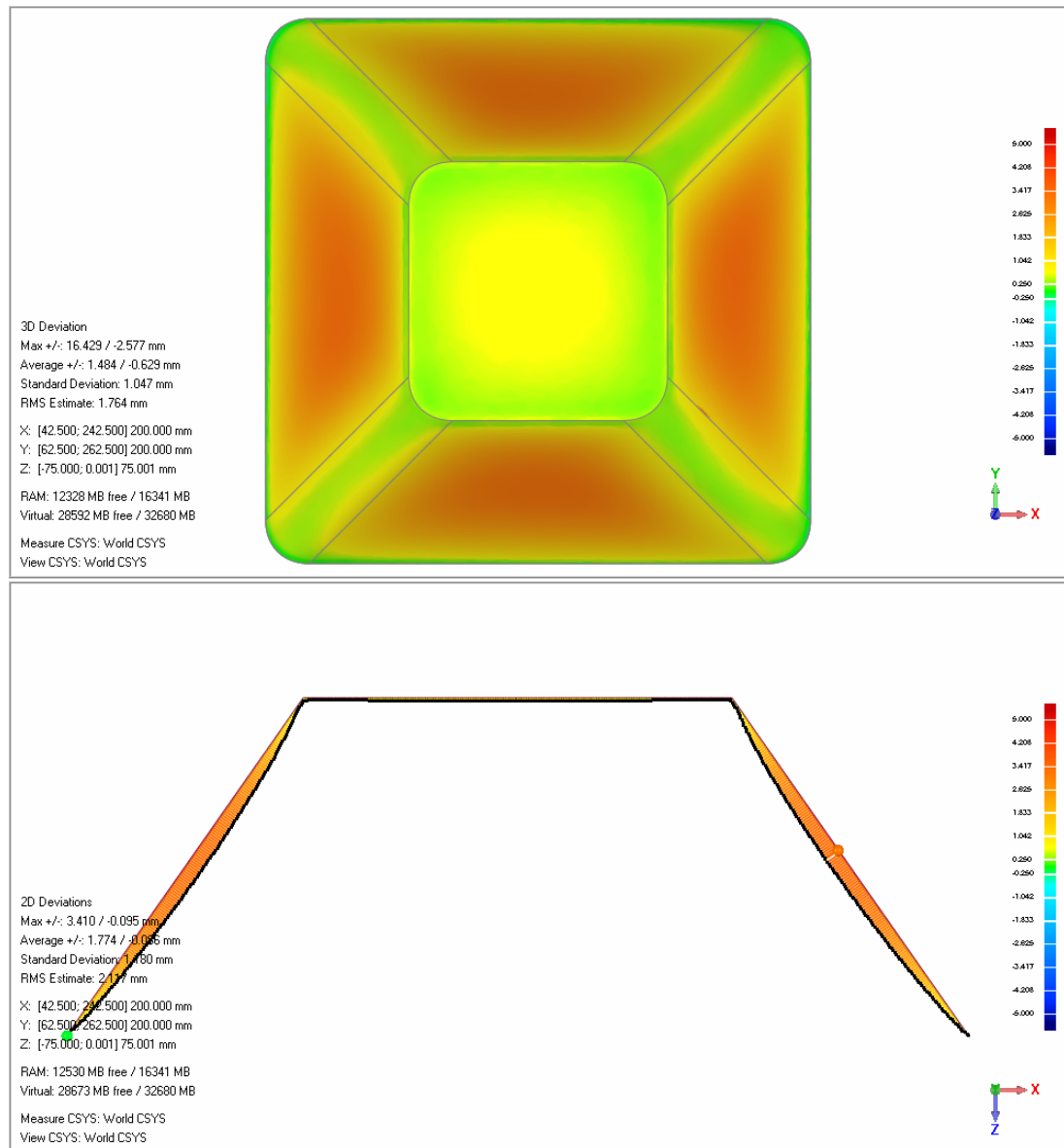


Figure D.10: Part T5B geometric accuracy results - top view and cross-section view

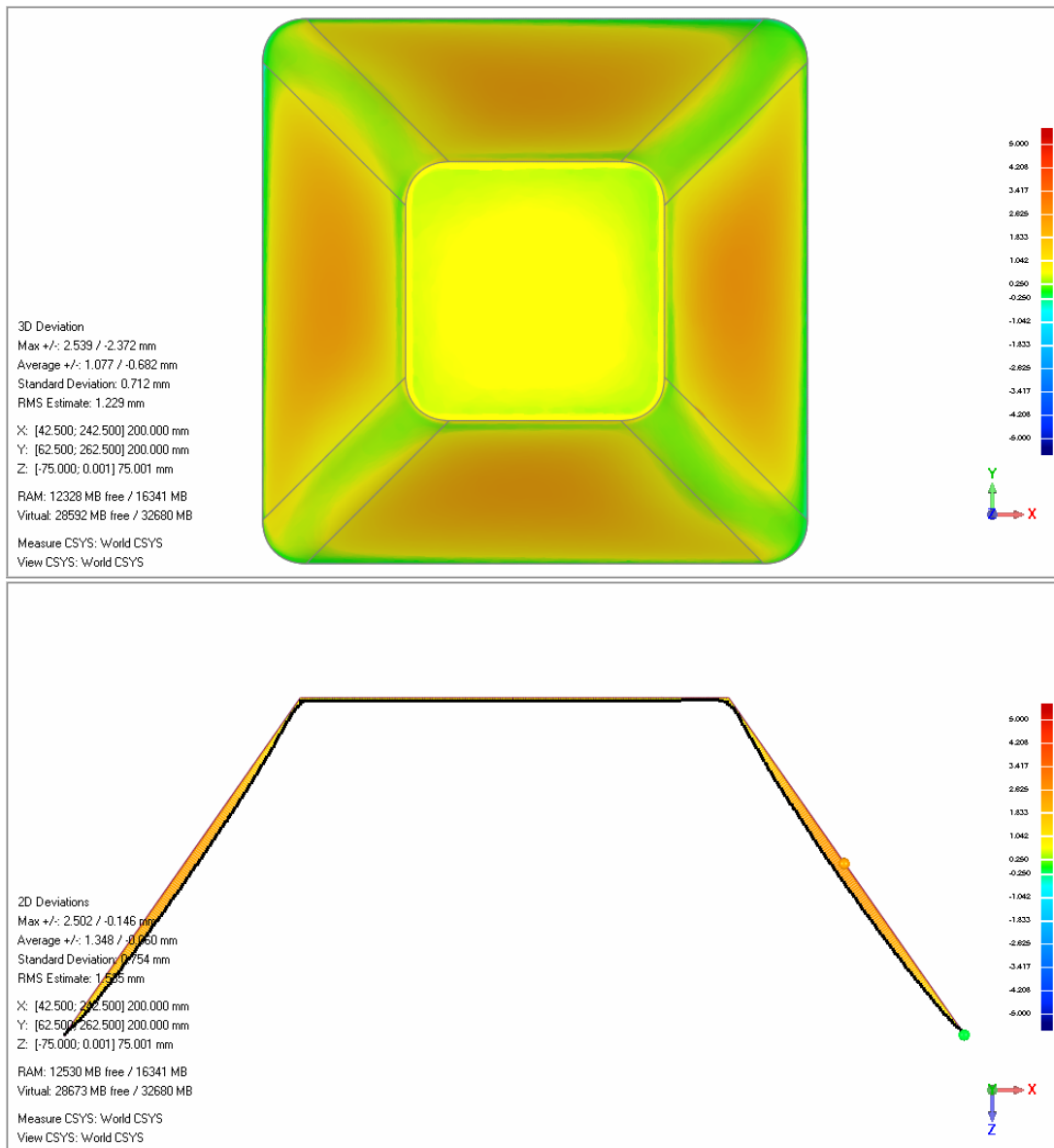


Figure D.11: Part T6A geometric accuracy results - top view and cross-section view

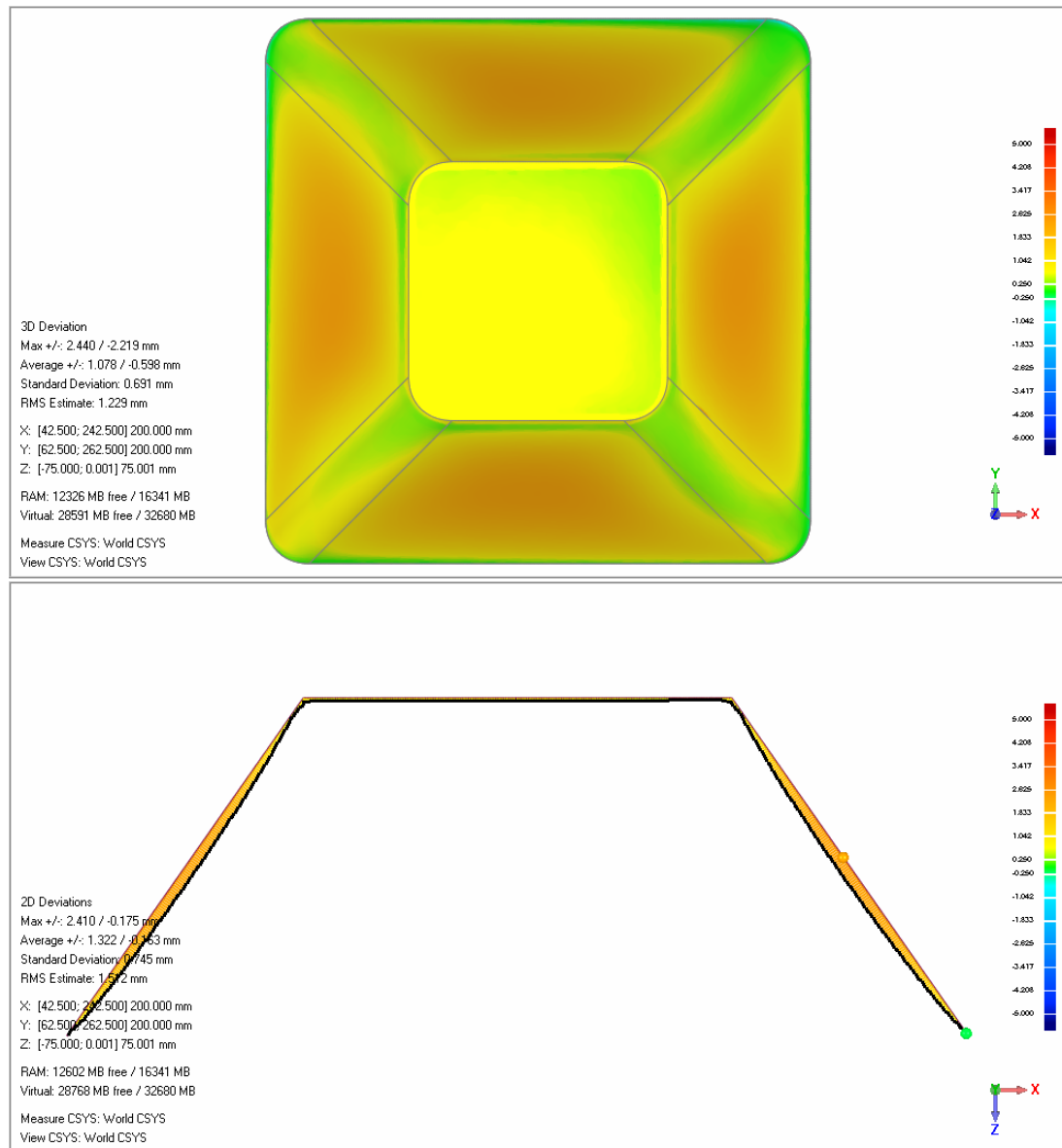


Figure D.12: Part T6B geometric accuracy results - top view and cross-section view

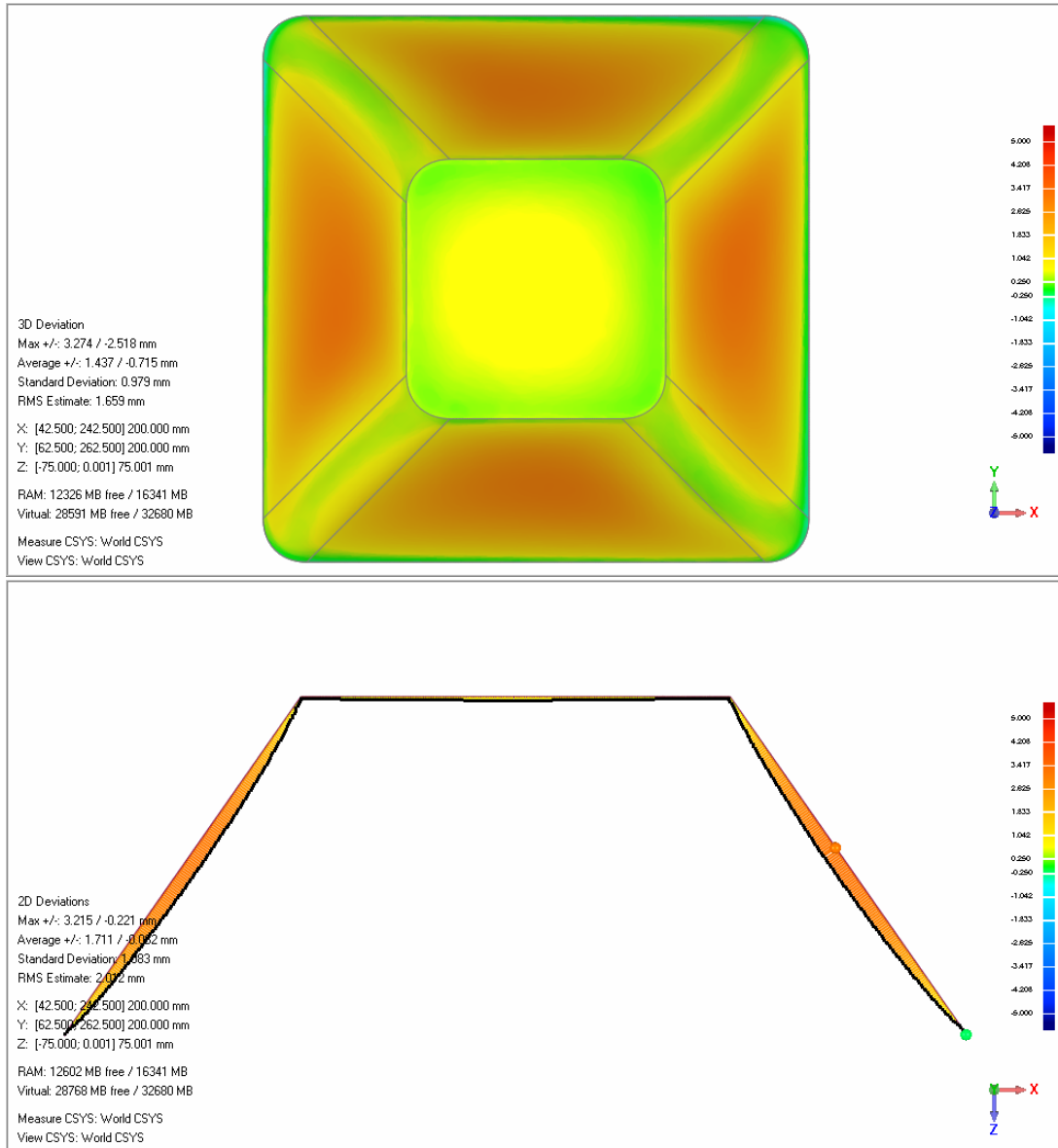


Figure D.13: Part T7A geometric accuracy results - top view and cross-section view

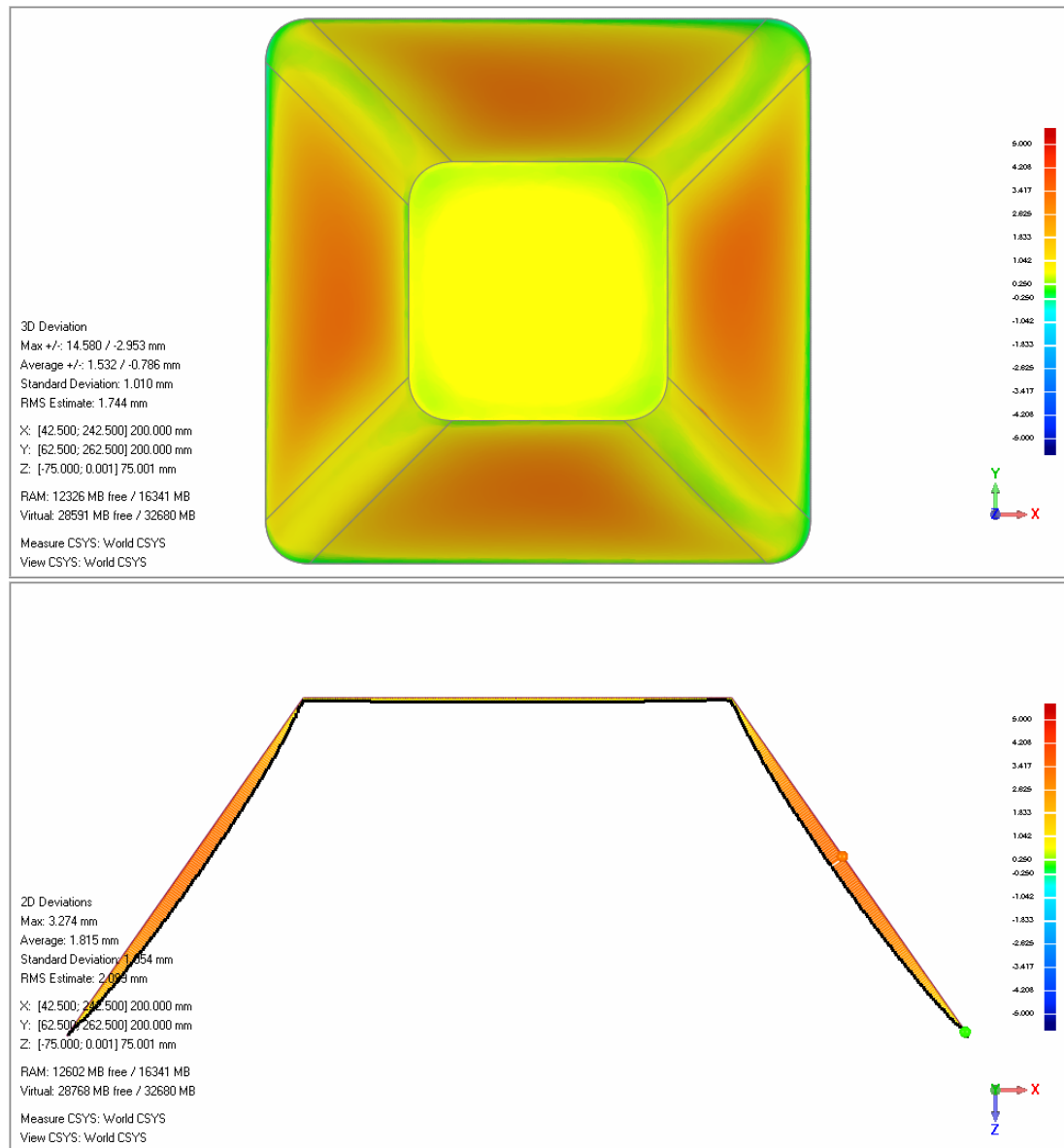


Figure D.14: Part T7B geometric accuracy results - top view and cross-section view

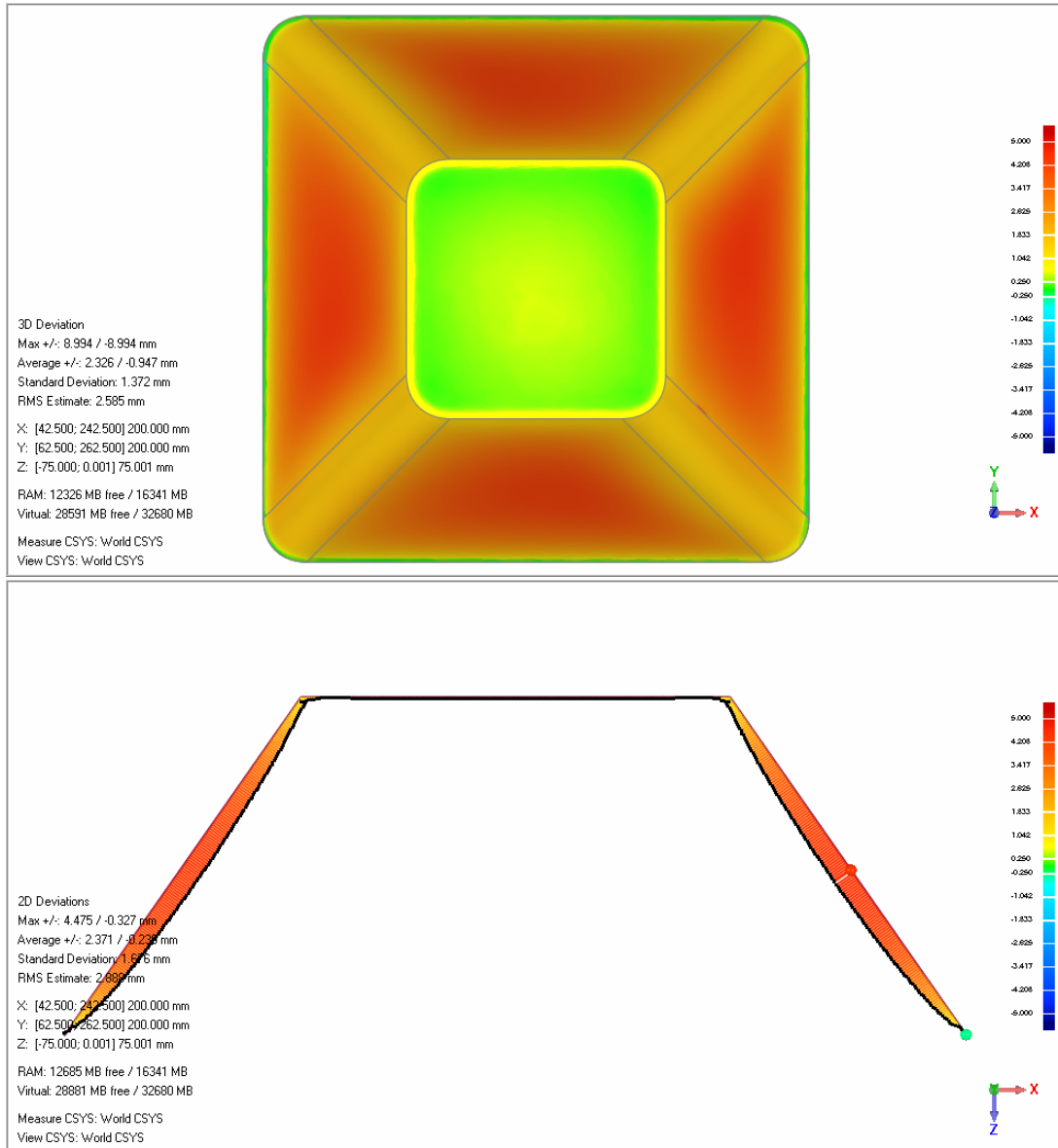


Figure D.15: Part T8A geometric accuracy results - top view and cross-section view

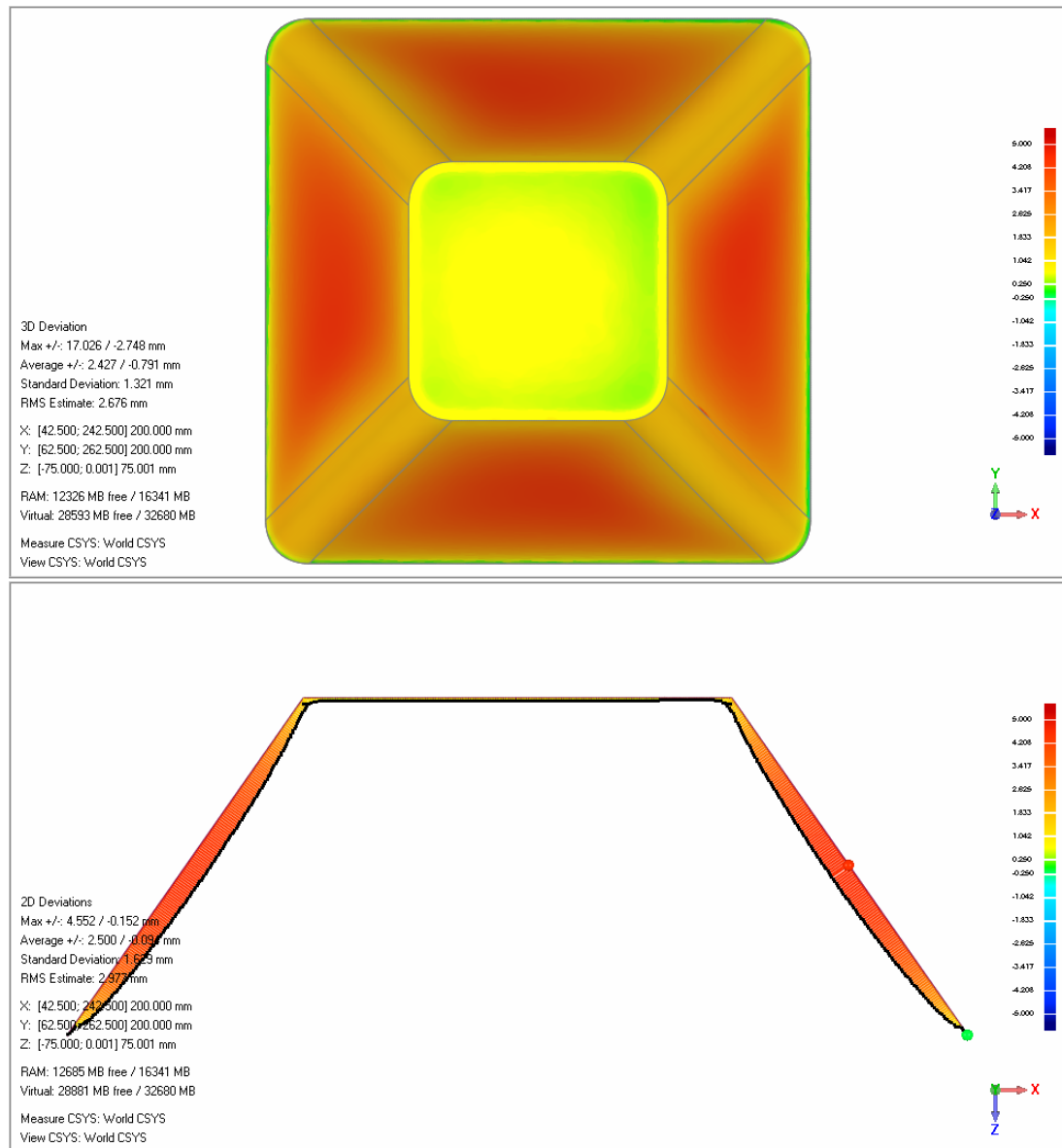


Figure D.16: Part T8B geometric accuracy results - top view and cross-section view

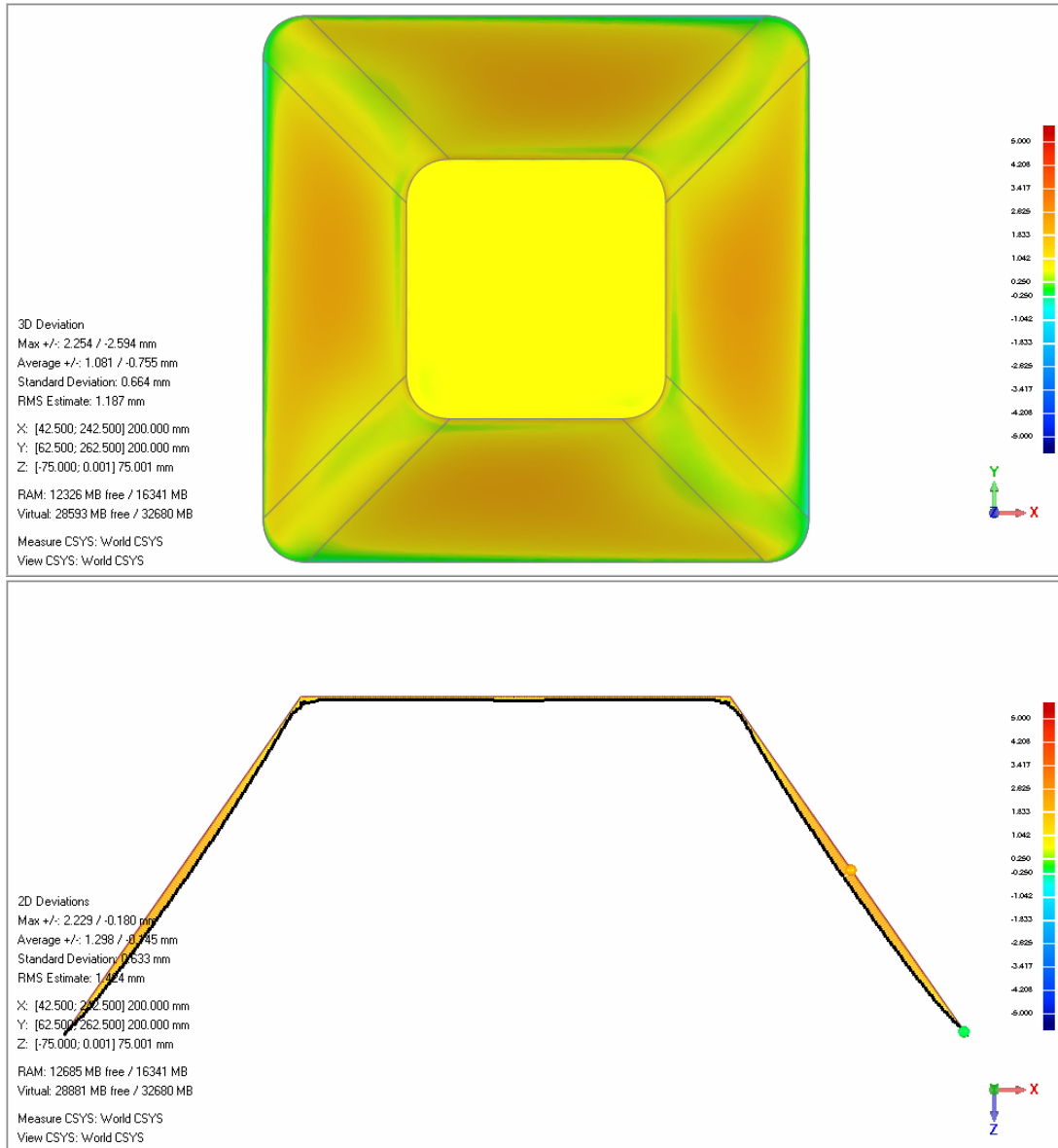


Figure D.17: Part T9A geometric accuracy results - top view and cross-section view

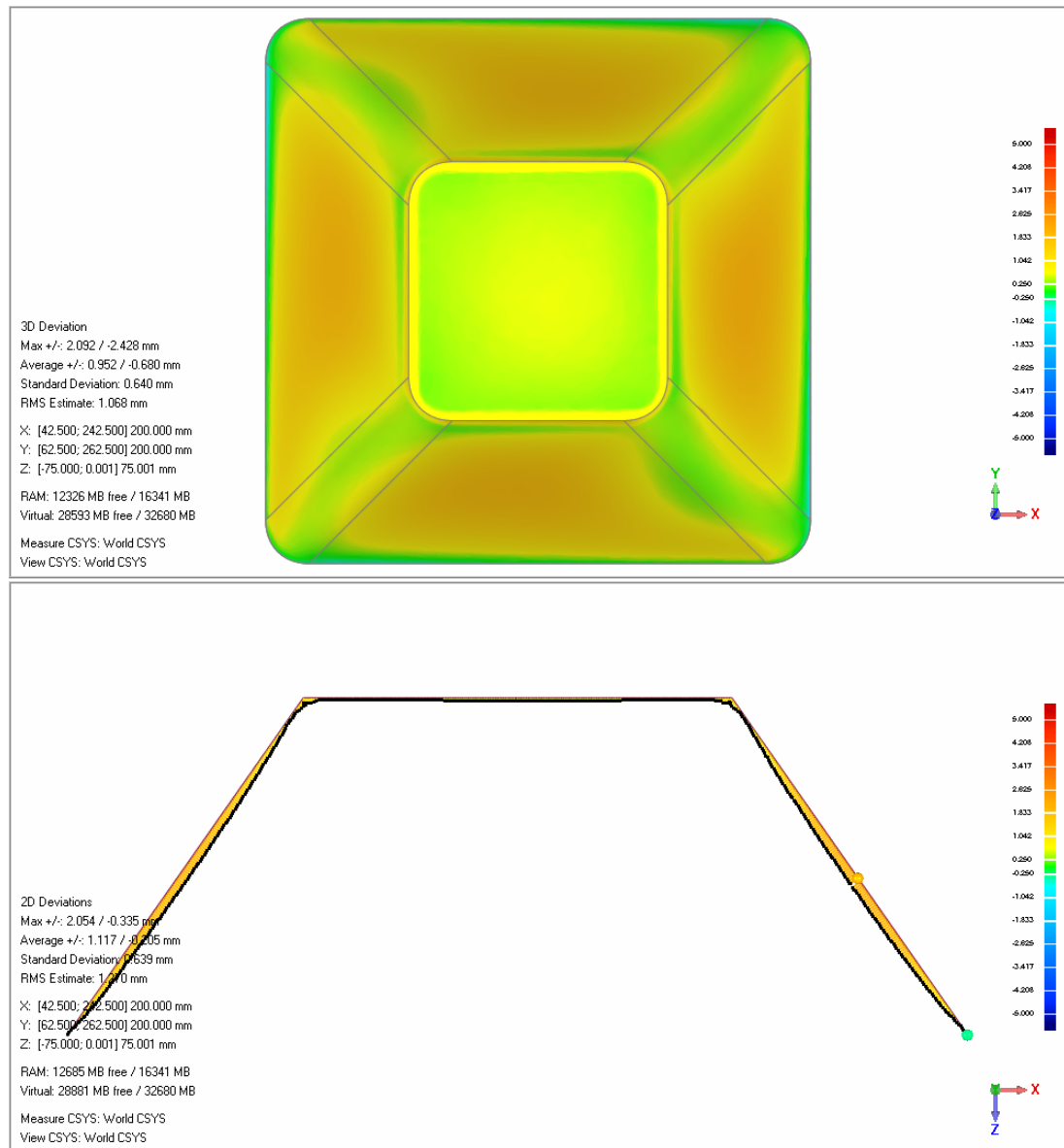


Figure D.18: Part T9B geometric accuracy results - top view and cross-section view

